Karlsruher Institut für Technologie

Schriftenreihe
Kontinuumsmechanik im Maschinenbau

29

Maximilian Krause

Local Stresses and Strains in Polycrystals

KIT Scientific Publishing

Maximilian Krause

Local Stresses and Strains in Polycrystals

Schriftenreihe
Kontinuumsmechanik im Maschinenbau
Band 29

Karlsruher Institut für Technologie (KIT)
Institut für Technische Mechanik
Bereich Kontinuumsmechanik

Hrsg. Prof. Dr.-Ing. habil. Thomas Böhlke

Eine Übersicht aller bisher in dieser Schriftenreihe erschienenen Bände finden Sie am Ende des Buchs.

Local Stresses and Strains in Polycrystals

by
Maximilian Krause

KIT Scientific Publishing

Karlsruher Institut für Technologie
Institut für Technische Mechanik
Bereich Kontinuumsmechanik

Local Stresses and Strains in Polycrystals

Zur Erlangung des akademischen Grades eines Doktor-Ingenieurs
von der KIT-Fakultät für Maschinenbau des
Karlsruher Instituts für Technologie (KIT) genehmigte Dissertation

von Maximilian Krause, M.Sc.

Tag der mündlichen Prüfung: 2. Dezember 2024
Hauptreferent: Prof. Dr.-Ing. Thomas Böhlke
Korreferent: Prof. Dr. Stéphane Berbenni

Impressum

Scientific Publishing

Karlsruher Institut für Technologie (KIT)
KIT Scientific Publishing
Straße am Forum 2
D-76131 Karlsruhe

KIT Scientific Publishing is a registered trademark
of Karlsruhe Institute of Technology.
Reprint using the book cover is not allowed.

www.bibliothek.kit.edu/ksp.php | E-Mail: info@ksp.kit.edu | Shop: www.ksp.kit.edu

Print on Demand 2025 – Gedruckt auf FSC-zertifiziertem Papier

ISSN 2192-693X
ISBN 978-3-7315-1411-4
DOI 10.5445/KSP1000178529

Publications and citations

This thesis is based on scientific publications in accordance with §12 (3) of the KIT doctoral regulations for mechanical engineering. These publications are put into context by means of a general introduction, three entirely new introductory method sections (section 2.1, chapter 3 and section 5.1), and chapter 7, which draws overall conclusions. Additionally, sections 5.4 and 6.3 contain unpublished results which are not part of those scientific publications.

Copyrighted content has been reproduced with permission of the respective rights holders for those publications for which the copyright licenses required permission. Whenever text sections from existing publications are used, this is indicated by a footnote in the corresponding chapter or section heading. To specify the manner in which text sections from publications is utilized, we define and use the clause *based on* as follows:

- Chapters or sections *based on* one or multiple publications include, but are not restricted to, selected content from the referenced publications. The sections from which the publication content was taken are given in the footnotes.
- Notation, spelling, grammar, and citation style of the publication content were adjusted to the requirements to this thesis, and references to other chapters of this thesis were introduced.
- Repeated content was omitted and replaced with references to other sections of this thesis as appropriate.
- The numbering of equations, figures and tables was adapted.

Additionally, the captions of figures and tables taken from the above publications are furnished with the clause *adapted from*. The formatting

of figures and tables *adapted from* publications may have been changed. The respective reference publication and the respective figure or table number are provided in the captions.

List of publications

Parts of the following publications have been incorporated into the thesis:

- **Krause, M.** and Böhlke, T., 2020. Maximum-entropy based estimates of stress and strain in thermoelastic random heterogeneous materials. Journal of Elasticity, 141, pp.321-348.
- **Krause, M.**, Pallicity, T.D. and Böhlke, T., 2023. Exact second moments of strain for composites with isotropic phases. European Journal of Mechanics-A/Solids, 97, p.104806.
- **Krause, M**. and Böhlke, T., 2024. Tensorial harmonic bases of arbitrary order with applications in elasticity, elastoviscoplasticity and texture-based modeling. Accepted at Mathematics and Mechanics of Solids.
- **Krause, M.**, Zürn, M., Gibmeier, J. and Böhlke, T., 2024. Determination of Diffraction Elastic Constants using the Maximum Entropy Method. Submitted.

Other published articles, which were *not* used in this thesis, are listed here according to the doctoral regulations for Mechanical Engineering (2017) §12 (1):

- **Krause, M.** and Böhlke, T., 2021. Stochastic evaluation of stress and strain distributions in duplex steel. Archive of Applied Mechanics, 91(8), pp.3527-3540.
- **Krause, M.** and Böhlke, T., 2022. Estimating stress fluctuations in polycrystals with an improved maximum entropy method. In: 8th European Congress on Computational Methods in Applied Sciences and Engineering. CIMNE.

- Simon, N., **Krause, M.**, Heinemann, P., Erdle, H., Böhlke, T. and Gibmeier, J., 2020. Phase-specific strain hardening and load partitioning of cold rolled duplex stainless steel X2CrNiN23-4. Crystals, 10(11), p.976.
- Gehrig, F., Wicht, D., **Krause, M.** and Böhlke, T., 2022. FFT-based investigation of the shear stress distribution in face-centered cubic polycrystals. International Journal of Plasticity, 157, p.103369.

Zusammenfassung

Auf der Mikroskala sind die meisten Strukturmaterialien heterogen. Sobald externe Lasten wirken, bilden sich daher heterogene Spannungs- und Dehnungsfelder aus. Diese Heterogenitäten können das Materialverhalten zu einem makroskopisch erkennbaren Grad beeinflussen, beispielsweise durch die Bildung von Mikrorissen oder mikroplastischen Verformungen. Die heterogenen Spannungs- und Dehnungsfelder zu quantifizieren erfordert im Allgemeinen Informationen zur vorliegenden Mikrostruktur, welche aufwändig zu erlangen sein können.

In dieser Dissertation untersuchen wir unterschiedliche Methoden zur Berechnung der Statistik lokaler Spannungen und Dehnungen mit besonderem Blick auf polykristalline Metalle. Die zentrale untersuchte Methode ist die mikromechanische Maximum-Entropie-Methode, eine Näherungsmethode auf Grundlage informationstheoretischer Erkenntnisse, welche lokale Spannungen und Dehungen basierend auf den makrokopischen Eigenschaften eines Materials vorhersagt ohne explizite Beschreibungen der Mikrostruktur zu benötigen. Auf Basis des allgemeinen Prinzips maximaler Entropie leiten wir verschiedene Versionen der Methode her, welche auf unterschiedlichen mikromechanischen Annahmen fußen, und bewerten diese Versionen in Bezug auf theoretische Konsistenz und Genauigkeit im Vergleich mit numerischen Vollfeldrechnungen. Um den Maximum-Entropie-Ansatz zu validieren und zu erweitern, leiten wir außerdem Spannungs- und Dehnungsstatistiken aus der Homogenisierungstheorie her, indem wir eine variationstheoretische Methode auf die Singulärapproximation

anwenden, und finden so explizite Formeln welche parametrisierbar sind um eine große Klasse an Mikrostrukturen beschreiben zu können.

Um eine effiziente numerische Implementierung dieser theoretischen Ansätze zu ermöglichen definieren wir eine Konvention für harmonische Basen für Tensorräume beliebiger Stufe, welche eine effiziente tensorielle Beschreibung von Wahrscheinlichkeitsverteilungen von Orientierungen in Polykristallen ermöglicht. Außerdem vereinfacht die harmonische Basiskonvention die Beschreibung von Materialeigenschaften, indem sie explizit Materialsymmetrien in die Basiswahl integriert, und verspricht so erhöhte numerische Effizienz in einer breiten Menge kontinuumsmechanischer Anwendungen.

Als Beispiel eines makroskopisch observablen physikalischen Phänomens, welches durch lokale Dehnungsstatistiken beeinflusst wird, untersuchen wir diffraktionsbasierte Verfahren zur Spannungsmessung in Polykristallen. Mithilfe der Maximum-Entropie-Methode formulieren wir einen neuen Ansatz zur Berechnung der röntgenograpischen Elastizitätskonstanten welche zur Interpretation von Diffraktionsmustern als Spannungen verwendet werden. Diesen Ansatz wenden wir sowohl auf statistisch isotrope als auch auf texturierte Polykristalle an.

Summary

On a microscopic scale, most structural materials are heterogeneous. Applying external loads therefore causes heterogeneous stress and strain fields. These heterogeneities can influence the behavior at a macroscopically noticeable level, for example, by inducing microcracks and microplasticity. Quantifying the heterogeneous stress and strain fields generally requires information about the exact microstructure, which can be difficult to acquire.

In this thesis, we investigate various methods of calculating local stress and strain statistics of heterogeneous materials with particular focus on polycrystalline metals. The main method under consideration is the micromechanical Maximum Entropy Method, an approximation technique based on results from information theory, which predicts local stress and strains based on the macroscopic properties of a material without explicit descriptions of the microstructure. Based on the general principle of maximum entropy, we derive different versions of the technique based on different micromechanical assumptions, and evaluate these versions in terms of theoretical consistency and accuracy compared to numerical full-field simulations. To validate and extend the maximum entropy approach, we furthermore derive stress and strain statistics from homogenization theories using a variational technique, which we apply to the Singular Approximation framework to find explicit formulas which are parameterized to describe a wide range of microstructures.

To facilitate efficient numerical implementations of the theoretical approaches, we define a harmonic basis convention for tensorial spaces of arbitrary order, which allows for an efficient tensorial description of

probability distributions of orientations in polycrystals. Furthermore, the harmonic basis convention simplifies the description of material properties by explicitly incorporating material symmetries into the choice of tensorial basis, which promises increased numerical efficiency in a wide range of continuum-mechanical applications.

As an example of a macroscopically observable physical effect which depends on local strain statistics, we investigate diffraction-based residual stress analysis in polycrystals. By applying the Maximum Entropy Method, we formulate a novel method to calculating diffraction elastic constants for use in the interpretation of diffraction patterns as residual stresses. This method is applied both to statistically isotropic and textured polycrystalline materials.

Acknowledgments

I would like thank Prof. Thomas Böhlke for providing guidance, feedback, and many valuable ideas throughout the process of writing this thesis. Furthermore, I would like to thank Prof. Stéphane Berbenni for reviewing the dissertation and his many constructive remarks.

Thanks are also due to my colleagues for many invaluable discussions and distractions, and to the support staff at the institute, for handling organizational hurdles.

Finally, I am deeply grateful for the support provided by my family and friends.

Elsevier, Springer and SAGE are gratefully acknowledged for providing the opportunity to incorporate my publications into this thesis.

The research documented in this doctoral thesis was partially funded by the German Research Foundation (DFG) (BO 1466/14-1) as part of project 512640977, 'Evaluation of non-linear $\sin^2\psi$ - distributions in residual stress analysis based on a scale-bridging mechanical modeling', and partially as part of the DFG priority programme 2013 "The utilization of residual stresses induced by metal forming". The support by the DFG is gratefully acknowledged.

Karlsruhe, January 2025 Maximilian Krause

Contents

Chapter 1

Introduction

1.1 Motivation

Under a microscope, many seemingly homogeneous materials are revealed to be composed of dissimilar components. Whether the heterogeneities are crystallites, fibers, or pores, their presence leads to an uneven distribution of local material properties. In most cases, the heterogeneous microstructure cannot be precisely controlled during the production process, such that the precise arrangement of mechanical properties at the microscopic scale is random. When the material is put under load, the heterogeneities induce fluctuations of the stress and strain fields which impact the overall properties. The search for simple macroscopic models which take into account all relevant features of the microstructure comprises the classical homogenization problem of micromechanics. Analytical homogenization approaches are particularly well-explored for linear elastic materials.

A suitable homogenized material model describes the interaction of macroscopic fields. However, the microscopic fluctuations may still be directly relevant when considering microscopic interactions such as crack initiation, local plasticity, and microstructure evolution. Even when the microscopic stresses are strictly within the linear regime, a condition which can itself only be ensured by investigating microscopic fluctuations, there are physical effects which depend directly on the

local strain, such as diffraction in crystals. As accurate descriptions of the microstructure geometry may be difficult to obtain and expensive to utilize, the question becomes how the stochastic fluctuations on the microscale may be predicted from macroscopic properties.

In statistical thermodynamics, a well-established method to estimate fluctuations from average values is the Maximum Entropy Method (MEM) of Jaynes (1963). The MEM was first formulated for linear micromechanics by Kreher and Pompe (1985), who also introduced an alternative formulation in 1989. Since then, there have been very few works validating or extending the method. Compared to established micromechanical methods, many possible applications of the MEM are still unexplored. Furthermore, the presence of two different MEM formulations suggests that there are other variants still possible. Among the many open questions surrounding the MEM, we wish to highlight the following.

- Consistency: Considering that there are two different approaches, is there a general MEM framework which can serve as a basis for further extensions? What are the links to classical homogenization theory? Is the MEM consistent with established theoretical results?
- Accuracy: Assuming maximal entropy leads to a method which requires very little information about the microstructure under consideration. How accurate is this approximation for engineering-relevant heterogeneous materials such as polycrystalline metals and two-phase composites? How does it compare to full-field strain statistics obtained via simulation?
- Validation: Experimental measurements using diffraction methods are dependent on local strain statistics. How do experimental results compare to MEM predictions?
- Efficiency: The MEM is a purely analytical method, meaning that it does not inherently require the numerical expense of full-field

simulations. How can that advantage of the MEM be preserved when dealing with data-intensive materials such as textured polycrystals?

1.2 State of the art

1.2.1 Initial remarks

This summary of the state of the art is thematically divided into subsections, in order of their corresponding chapters. Section 1.2.2 deals with the state of the art of tensor algebra, in particular tensorial bases as used for efficient implementations of continuum-mechanical calculations. In Section 1.2.3, the state of the art of theoretical micromechanics is summarized. Particular emphasis is put on methods for the calculation of statistical second moments of local stress and strain distributions. Section 1.2.4 summarizes the state of the art on the micromechanical MEM. Finally, Section 1.2.5 deals with the application of micromechanical theory to X-ray diffraction stress analysis.

1.2.2 Tensorial bases[1]

Continuum mechanics deals with tensorial quantities in all subareas, i.e., kinematics, balance equations, constitutive theory. The tensorial quantities necessitate a higher-order tensor algebra; however, matrix-vector formulations are more accessible both numerically and didactically.

Depicting higher-order tensors as vectors is as simple as picking a set of higher-order basis tensors, but the choice is not obvious. The oldest and most common approach dates back to Voigt (1910). The Voigt notation renders symmetric second-order tensors as 6-dimensional component

[1] This section is based on section 1 of the publication *Tensorial harmonic bases of arbitrary order with applications in elasticity, elastoviscoplasticity and texture-based modeling* (Krause and Böhlke, 2024)

vectors by defining six orthogonal second-order basis tensors, not all of which are normalized. Therefore, co- and contravariant tensors need to be distinguished, leading to different notations for stress and strain tensors. Though this non-normalized basis requires special care (cf. Helnwein (2001)), it is commonly used in commercial computer codes such as Abaqus, Ansys and LS-DYNA.

The Voigt basis can be normalized, resulting in a factor of $\sqrt{2}$ for each of the shear basis tensors. Originally proposed by Voigt (1910), the normalized Voigt basis is often called Mandel basis (Mandel, 1965). As it is an orthonormal basis, results from elementary linear algebra can be applied to Mandel basis component vectors and matrices in a straightforward manner.

While Voigt's original decomposition into normal and shear tensors derives naturally from the standard basis of the underlying vector space, the normal tensors can be further split into a spherical part and two deviatoric parts. The deviatoric basis is due to Kocks et al. (1983), who denoted it the natural basis due to its particular usefulness in descriptions of cubic polycrystals. Kocks's original non-orthonormalized basis was followed by orthonormalized versions by, among others, Lequeu (1986) and Van Houtte (1988). A lucid description as an eigentensor basis of cubic stiffness tensors can be found in Kocks et al. (2000), Chapter 7.

Separately from stress and strain bases, texture description has undergone a number of evolutions. Roe (1965) and Bunge (1965) are generally credited with texture coefficient descriptions of the orientation distribution function based on spherical harmonics series. These scalar coefficients motivated a coordinate-independent tensorial depiction, introduced by Adams et al. (1992). In actual calculation these tensorial descriptions still necessitate a choice of basis tensors, cf. Lobos Fernández and Böhlke (2019). Man and Du (2022) recently proposed an orthonormal basis of harmonic tensor spaces which uses results from complexified tensor algebra.

1.2.3 Micromechanics[2]

Heterogeneous materials, owing to their fabrication process, generally possess random microstructures, allowing for the application of statistical continuum theories to mechanical problems, as described by e.g. Beran (1965). By using this framework to project the random heterogeneous material properties onto homogeneous effective properties, the "mean field" problem is obtained out of the more complex "full field" problem. This projection is achieved via homogenization methods, which can be numerical in nature, such as those used in FE (Guedes and Kikuchi, 1990), FFT (Moulinec and Suquet, 1998) or NTFA (Fritzen, 2010) approaches. These numerical methods depend on full-field calculations of representative volumes as an intermediate step, which requires detailed microstructure knowledge. Full-field calculations are generally more numerically expensive than analytical solutions, which offer explicit or implicit solutions in terms of straightforward formulas. Exact (i.e. precise to arbitrary tolerances) analytical homogenization approaches are known for special microstructures (Bensoussan et al., 1978), while analytical estimates such as self-consistent estimates, the Mori-Tanaka method (Mori and Tanaka, 1973) and differential schemes (Norris, 1985) suffice in many common applications. For an overview of these and other homogenization methods, see Nemat-Nasser and Hori (1993) or Torquato (2002) and the references therein. These methods generally require only the one-point probability function of material properties, along with some microstructural assumptions.

Statistics of local stress and strain fields are essential to the effective material behavior of composites, particularly in the nonlinear case. Mi-

[2] The first paragraph of this section is based on section 1 of the publication *Maximum-Entropy Based Estimates of Stress and Strain in Thermoelastic Random Heterogeneous Materials* (Krause and Böhlke, 2020), while subsequent paragraphs are based on section 1 of the publication *Exact second moments of strain for composites with isotropic phases* (Krause et al., 2023)

cromechanical estimates of onset of plasticity or failure depend to a large degree on the local fields, meaning that micromechanically motivated material models ought to consider as much information about the local stress and strain statistics as is available. In general, full statistical information about the local fields is available from full-field simulations. These simulations are however too computationally expensive for some contexts, such as material laws for numerical simulations which need to be evaluated at large numbers of material points. For these cases, analytical estimates of local field statistics are required.

Common analytical homogenization methods, often referred to as mean-field methods as they posit effective mean fields on the macroscale, predict the elastic stiffness on the macroscale based on assumptions about the local field statistics. For two-phase materials, the mean or first order statistical moment of the local field in a given phase can be evaluated from the homogenized effective stiffness alone (Levin, 1967). Methods based on Eshelby's single inclusion problem even explicitly assume the phase-wise means. However, when considering nonlinear phenomena, the fluctuations of local fields are of interest, which can be described by higher order statistical moments. Any mean-field based approach which provides an approximation for the effective energy also implicitly defines the second-order statistical moments for each phase by prescribing the partitioning of the energy onto the phases. These second-order statistical moments are fully described by minor- and major-symmetric fourth-order tensors.

Bobeth and Diener (1987) first derived an expression for second-order moments of local fields based on derivatives of the effective energy with respect to the phase stiffness, which was expanded to the affine or thermoelastic case by Kreher (1990). In a composite with isotropic phases, second-order moments of norms of the spherical and deviatoric parts of stresses can be computed particularly easily by numerical or analytical differentiation. This special case has been employed by various groups

in the homogenization of nonlinear composites (cf. Ponte Castañeda (2002); Lahellec and Suquet (2007); Badulescu et al. (2015)). The complete fourth order tensor form of the second moment is more rarely computed numerically, e.g. by Brenner et al. (2004) for the self-consistent method using a Gaussian quadrature method. Recently, Das and Castañeda (2021) have computed second moments of local fields in a large strain framework.

1.2.4 The Maximum-Entropy Method[3]

Solving the homogenized problem yields the mean or effective fields. Many homogenization methods additionally allow calculation of phase mean fields from the overall mean fields by providing phase averages of stress or strain localization tensors; in the two-phase case, they can even be calculated exactly. However, considering only the overall or phase mean fields is insufficient for problems in which local fluctuations determine the result, such as material failure, for which no homogenization theory is known to the authors (as discussed by e.g. Kröner (1963) and Dyskin (1999)). For these problems, it is necessary to extract information about local fluctuations from the effective field. While this is again possible by performing numerical simulations of fully known microstructures, as is generally done alongside numerical homogenization methods in two-scale simulations such as FE^2, the required microstructural data is not easily acquired.

Kreher and Pompe (1989) detail an approach to produce analytical approximations of first- and second-order statistical moments of stresses and strains in heterogeneous thermoelastic materials under consideration of effective material values obtained by homogenization methods

[3] This section is based on section 1 of the publication *Maximum-Entropy Based Estimates of Stress and Strain in Thermoelastic Random Heterogeneous Materials* (Krause and Böhlke, 2020)

or experiments. This approach employs the maximum entropy methods commonly seen in statistical thermodynamics and physics (see Jaynes (1963) and Jaynes (1978)), and is therefore often abbreviated as MEM in the following.

The statistical nature of this work is reminiscent of, but only tangentially related to, Uncertainty Quantification (UQ), described by Chernatynskiy et al. (2013) as the statistical study of models operating on uncertain parameters. In the language of UQ, the method considered here calculates the aleatoric uncertainty of the stress and strain values of a single randomly chosen point of the microstructure, if the effective properties of the continuum, the phase volume fractions, phase properties, and the effective load are known exactly, but the microstructure is entirely uncertain. As far as the authors are aware, there are no UQ works considering that particular problem.

1.2.5 X-Ray diffraction stress analysis[4]

Diffraction methods are an established technique to analyze residual stresses in polycrystalline materials. By Bragg's Law, information about the lattice strains can be extracted from diffraction measurements of X-rays impacting the material. Since for a given incident angle and wavelength, diffraction only occurs in grains with a particular orientation and lattice plane distance, the information acquired from a single diffraction measurement does not describe the entire polycrystal. Interpreting the measured diffraction data as an overall residual stress therefore requires microstructural assumptions on local strain distributions.

This work focuses on surface stress analysis using X-ray diffraction (XRD), which has its origins in the pioneering work by Lester and Aborn (1925). In particular, the $\sin^2(\psi)$ technique due to Macherauch and

[4] This section is based on section 1 of the publication *Determination of Diffraction Elastic Constants using the Maximum Entropy Method* (Krause et al., 2024).

Müller (1961) as portrayed by Noyan and Cohen (1987) is discussed. This well-established technique is among the most commonly used stress analysis techniques today (Guo et al., 2021). While other diffraction measurement approaches to XRD stress analysis such as the $\cos(\alpha)$ technique pioneered by Taira and Tanaka (1979) are not explicitly discussed, the fundamental micromechanical relations underlying the analysis are the same, and the micromechanical methods described in this work should be applicable.

In the texture-free case, the relationship between diffraction measurements and overall residual stresses can be described by diffraction elastic constants, which can be measured experimentally or calculated from single-crystal elastic constants. Initially the calculation of diffraction elastic constants was based on the simple micromechanical assumptions due to Voigt (1889) and Reuss (1929). A more accurate assumption is the self-consistent Eshelby-Kröner approximation formulated by Kröner (1958), which was applied to XRD stress analysis by Bollenrath et al. (1967), and is still widely used today.

In case of texture, the diffraction elastic constants are replaced by stress factors, which are orientation-dependent second-order tensors (Dölle and Hauk, 1976). Early attempts at calculating the stress factors used the Reuss model (Hauk et al., 1975; Barral et al., 1987), with later works extending the approach to the self-consistent approximation (Behnken and Hauk, 1991). In more recent developments, a number of other models such as the Modified Voigt model (Murray and Noyan, 1999) or Inverse Kröner model (Gnäupel-Herold et al., 2012) have been proposed, which are not yet as widely used according to Gnäupel-Herold (2012).

1.3 Contributions

In this section, the contributions of this thesis which extend the state of the art are summarized.

- A convention for tensorial harmonic bases is defined. These bases are real, not complex, can be extended to arbitrary tensor orders, and highlight the connection between material symmetries and tensorial Fourier coefficients.
- General formulas for the computation of second moments are applied to the Singular Approximation, yielding a set of formulas fit for a wide class of materials.
- The Single-Point MEM is extended to partially homogeneous materials. A validation for various material classes using full-field simulations shows that the MEM is particularly accurate for polycrystals.
- A novel MEM incorporating exact second moments is derived. In the process, another MEM formulation is shown to be related to the Singular Approximation.
- Diffraction-based stress measurement methods are formulated using the Singular Approximation, yielding a framework which describes and extends various existing models. For textured polycrystals, a formulation using tensorial texture coefficients is found. The effect of truncating the involved Fourier series is investigated.
- MEM methods are applied to diffraction-based stress measurement methods. A comparison with full-field simulations of generated microstructures shows them to yield similar results as the most accurate of the investigated existing methods, while also being comparatively simple to compute and adaptable to macroscopically measurable stiffness parameters.

1.4 Outline

In Section 2.1, mathematical foundations for the rest of the manuscript are laid down. After recapitulating relevant notions of tensor algebra, we define a novel harmonic basis formalism which is used to simplify

tensor representation and reduce the numerical expense of subsequent calculations.

In Chapter 3, essentials of continuum mechanics are briefly recapitulated. Particular focus is put on the mechanics of linear elastic materials with eigenstrains in the small deformation limit. For heterogeneous materials with random microstructures, fundamental relations are summarized. Various theoretical models of the mechanics of random heterogeneous materials such as the Voigt, Reuss and Hashin-Shtrikman bounds as well as the self-consistent method are summarized and recontextualized as special cases of the Singular Approximation.

Chapter 4 is concerned with the calculation of second statistical moments of strains in heterogeneous linear elastic materials. The variational approach of Bobeth and Diener (1987) is rederived and applied to the general Singular Approximation. We derive general expressions for the full tensorial second moments by calculating general anisotropic derivatives of Hill's polarization tensor. We then apply this theory to isotropic two-phase composites with isotropic phases. Various theoretical models are compared to finite element calculations.

Chapter 5 deals with the micromechanical Maximum Entropy Method (MEM). Following Kreher and Pompe (1989), we begin by re-deriving the single-point micromechanical MEM. In doing so, we find a more compact set of formulas than Kreher and Pompe's original formulation, which is more general particularly in dealing with partially homogeneous materials. The single-point MEM is then compared to full-field simulations of polycrystalline and composite microstructures. Next, we rederive Kreher and Pompe's "improved" MEM formulation, contextualizing it from the point of view of the Singular Approximation. This is followed by a comparison with the single-point MEM and exact second moment expressions.

In Chapter 6, we apply various micromechanical models to the problem of X-ray diffraction stress analysis. First, established theoretical work

from material science is rederived using the micromechanical apparatus of Chapter 3. We apply the general Singular Approximation to diffraction stress analysis of statistically isotropic cubic polycrystals, and show that this presents a consistent generalization of existing models. Furthermore, we apply the MEM to the same problem, and prove equivalence with the Singular Approximation in this case. The model is then extended towards textured materials, where Singular Approximation and MEM diverge.

In Chapter 7, we summarize the main results of this manuscript and offer concluding remarks.

Chapter 2

Mathematical tools

2.1 Introduction to tensor algebra and tensor analysis

2.1.1 Vector spaces

The purpose of this chapter is to provide the mathematical foundations for the rest of the manuscript. In the interest of precision, basic definitions are repeated here, especially insofar as they help define conventions of notation. The formulation of vector and tensor algebra is based on that described by Halmos (2017). While that text is rather general, the contents of this chapter are largely restricted to real-valued finite-dimensional tensor spaces with orthonormal bases. More general mathematical frameworks for continuum mechanics, such as those discussed by Marsden and Hughes (1994) and Krawietz (2013), will not be considered.

A *vector space* is a set which satisfies the axioms described in §2 of Halmos (2017). Vectors are written as bold-faced lower-case letters ($\boldsymbol{v}$), while vector spaces are calligraphic ($\mathcal{V}$). The most commonly reoccurring example in this work is the *real coordinate space*, a vector space defined by the set of triples of real numbers $\mathbb{R}^3$ along with the usual definitions of addition and scaling (Halmos (2017), §3, example 3). The real coordinate

space will be denoted as $\mathcal{R}$, omitting its dimension, as only three-dimensional mechanical problems will be considered in this manuscript. For ease of notation, we immediately introduce an inner product (Halmos (2017), §59). All vector and tensor spaces discussed in this manuscript are inner product spaces, and their canonical inner product is always denoted as $\square \cdot \square$. The inner product allows the definition of the *Euclidean norm*

$$\|\boldsymbol{v}\| = \sqrt{\boldsymbol{v} \cdot \boldsymbol{v}}. \tag{2.1}$$

Following Halmos (2017), §62, vectors $\boldsymbol{a}, \boldsymbol{b} \in \mathcal{V}$ are *orthogonal* if

$$\boldsymbol{a} \cdot \boldsymbol{b} = 0, \tag{2.2}$$

and a vector $\boldsymbol{a}$ is *normal* if

$$\|\boldsymbol{a}\| = 1. \tag{2.3}$$

A set of vectors $\{\boldsymbol{v}_i | i \in [1, n]\} \subset \mathcal{V}$ is called *orthonormal* if the condition

$$\boldsymbol{v}_i \cdot \boldsymbol{v}_j = \delta_{ij} \tag{2.4}$$

holds, where δ is the Kronecker delta

$$\delta_{ij} = \begin{cases} 1 & \text{if} \quad i = j, \\ 0 & \text{else.} \end{cases} \tag{2.5}$$

Based on Halmos (2017), §63, an orthonormal set of n vectors for an n-dimensional vector space spans that space. That set can therefore be used as an *orthonormal basis*. Without loss of generality, a single basis of $\mathcal{R}$ is defined to be canonical and denoted as $\{\boldsymbol{e}_i | i \in [1, 3]\}$ or $\{\boldsymbol{e}_i\}$ for short. The *components* of a vector $\boldsymbol{v}$ respective to $\{\boldsymbol{e}_i\}$ are

$$v_i = \boldsymbol{v} \cdot \boldsymbol{e}_i. \tag{2.6}$$

The canonical basis establishes a unique relationship between the 3-tuple set $\mathbb{R}^3$ and the Euclidean space $\mathcal{R}$. Similarly, for any n-dimensional Euclidean space regardless of its origin, the components of an element $\boldsymbol{v}$ respective to that space's canonical basis are denoted v_i. For components respective to non-canonical bases $\{\boldsymbol{a}_i\}$, no shorthand notation is defined, and they are written explicitly as $\boldsymbol{v} \cdot \boldsymbol{a}_i$.

The concept of vector components leads to additional options with regard to notation. Einstein's summation convention states that sums over index pairs are implicit, i.e.

$$v_i a_i := \sum_{i=1}^{n} v_i a_i, \tag{2.7}$$

whereas single indices are *free indices* which always imply a system of equations,

$$v_i = a_i \quad \forall i \in [1, n]. \tag{2.8}$$

The value of n is inferred from context; when Einstein's summation is applied to vector components, n is the dimension of the underlying vector space. With Einstein's summation convention, a vector can be succinctly written as its component decomposition

$$\boldsymbol{v} = v_i \boldsymbol{e}_i, \tag{2.9}$$

giving rise to the *mixed notation*, in which the only tensorial quantities are basis tensors. If all bases are assumed to be canonical, it is possible to omit the basis tensors for brevity, such that

$$\boldsymbol{v} \mathrel{\hat{=}} v_i, \tag{2.10}$$

where $\mathrel{\hat{=}}$ is shorthand for the assumption of canonical bases. This is the *index notation* which is used frequently in this manuscript where brevity is required.

To explicitly specify the component values of a tensor, the *matrix notation* is used, which reads

$$v_i \mathrel{\hat{=}} \begin{pmatrix} v_1 \\ v_2 \\ v_3 \end{pmatrix} \tag{2.11}$$

for assumed canonical bases and

$$\boldsymbol{v} = \begin{pmatrix} v_1 \\ v_2 \\ v_3 \end{pmatrix}_{\{\boldsymbol{e}_i\}} \tag{2.12}$$

with an explicit basis definition.

Since component notations respective two different bases must be equivalent, i.e.,

$$(\boldsymbol{v} \cdot \boldsymbol{a}_j)\boldsymbol{a}_j = (\boldsymbol{v} \cdot \boldsymbol{b}_j)\boldsymbol{b}_j, \tag{2.13}$$

basis transformations between orthonormal bases are accomplished via

$$(\boldsymbol{v} \cdot \boldsymbol{a}_i) = (\boldsymbol{a}_i \cdot \boldsymbol{b}_j)(\boldsymbol{v} \cdot \boldsymbol{b}_j) \tag{2.14}$$

with a *transformation matrix* $\underline{\underline{T}}$ for which

$$T_{ij} = \boldsymbol{a}_i \cdot \boldsymbol{b}_j. \tag{2.15}$$

On occasion, it will be necessary to use *complexified* vector spaces as described in Halmos (2017), §77. The canonical basis of the complexified equivalent of a real vector space $\mathcal{V}$ is the real space's canonical basis, and therefore real. Since fully real tensors are left unchanged by conjugation,

$$\overline{\boldsymbol{e}}_i = \boldsymbol{e}_i, \tag{2.16}$$

the complex conjugate of a general vector $\boldsymbol{v}$ is given as

$$\overline{\boldsymbol{v}} = \overline{v}_i \boldsymbol{e}_i. \tag{2.17}$$

With the complex conjugate, the canonical inner product on the complexified space can be defined as

$$\boldsymbol{a} \cdot \boldsymbol{b} = a_i \overline{b}_i. \tag{2.18}$$

For calculations in complex-valued bases, the complex conjugate follows via transformation to a real-valued basis, leading to a more complicated expression involving transformation matrices. To avoid this, real bases are preferred in this manuscript.

A set of n linearly independent vectors of $\mathcal{V}$ spans an n-dimensional *subspace* $\mathcal{W}$, written

$$\mathcal{W} \subseteq \mathcal{V}, \quad n \leq \dim \mathcal{V}. \tag{2.19}$$

A subspace is again a vector space, see Halmos (2017), §10. While the subspace inherits the definition of addition, scalar multiplication and inner product from its parent space, it does not necessarily inherit a canonical basis.

The *direct sum* $\oplus$ of two vector spaces $\mathcal{V}$ and $\mathcal{W}$ is defined as the set of ordered pairs

$$\mathcal{V} \oplus \mathcal{W} = \{(\boldsymbol{v}, \boldsymbol{w}) | \boldsymbol{v} \in \mathcal{V}, \boldsymbol{w} \in \mathcal{W}\}. \tag{2.20}$$

With the addition, scalar multiplication and inner product operations inherited from each of the composing spaces $\mathcal{V}$ and $\mathcal{W}$, the direct sum of two Euclidean spaces is again a Euclidean space, see Halmos (2017), §18. For elements of the direct sum, we use a matrix-like notation

$$\boldsymbol{a} = \begin{pmatrix} \boldsymbol{v} \\ \boldsymbol{w} \end{pmatrix}, \tag{2.21}$$

which, if canonical bases are defined for both subspaces, resolves to the index notation

$$a_i \mathrel{\hat{=}} \begin{pmatrix} v_1 \\ \vdots \\ v_n \\ w_1 \\ \vdots \\ w_m \end{pmatrix}, \tag{2.22}$$

with n and m being the respective dimensions of $\mathcal{V}$ and $\mathcal{W}$.

A set of subspaces $\{\mathcal{A}_i | i \in [1, n]\}$ is called a *complete decomposition* of a vector space $\mathcal{V}$ if

$$\mathcal{V} = \bigoplus_{i=1}^{k} \mathcal{A}_i, \tag{2.23}$$

elementary properties of which are discussed in Halmos (2017), §18 and §19.

2.1.2 Tensor spaces

A formal definition of tensor spaces generally rests on the notion of dual vector spaces, outlined for example in chapter 7 of Fischer (2003). Because we limit ourselves to Euclidean spaces, which are real and self-dual, it is possible to use a more intuitive approach. For two vectors $\boldsymbol{a} \in \mathcal{A}$ and $\boldsymbol{b} \in \mathcal{B}$ the *dyadic product* or tensor product of two vectors $\boldsymbol{a} \otimes \boldsymbol{b}$ is a rank-one linear map from $\mathcal{A}$ to $\mathcal{B}$ such that

$$(\boldsymbol{a} \otimes \boldsymbol{b})(\boldsymbol{b}) = \boldsymbol{a}(\boldsymbol{b} \cdot \boldsymbol{b}). \tag{2.24}$$

This definition implies an addition operation on dyadic products such that

$$(\boldsymbol{a}_1 \otimes \boldsymbol{b}_1 + \boldsymbol{a}_2 \otimes \boldsymbol{b}_2)(\boldsymbol{b}_1) = \boldsymbol{a}_1(\boldsymbol{b}_1 \cdot \boldsymbol{b}_1) + \boldsymbol{a}_2(\boldsymbol{b}_2 \cdot \boldsymbol{b}_2). \tag{2.25}$$

It is possible to show that the set of all sums of dyadic products of vectors from $\mathcal{A}$ and $\mathcal{B}$, denoted as $\mathcal{A} \otimes \mathcal{B}$, is itself a vector space, with dimension $\dim \mathcal{A} \dim \mathcal{B}$. A more formal definition of this space is given by Halmos (2017), §25.
By using the canonical bases of $\mathcal{A}$ and $\mathcal{B}$,

$$(\boldsymbol{a} \otimes \boldsymbol{b}) = a_i b_j \boldsymbol{e}_i \otimes \boldsymbol{e}_j, \tag{2.26}$$

all tensors in $\mathcal{A} \otimes \mathcal{B}$ can be written in a mixed notation as

$$\boldsymbol{A} = A_{ij} \boldsymbol{e}_i \otimes \boldsymbol{e}_j \tag{2.27}$$

with a component matrix $\underline{\underline{A}}$.
The canonical inner product of $\mathcal{A} \otimes \mathcal{B}$ is implied by the canonical products of $\mathcal{A}$ and $\mathcal{B}$ via

$$(\boldsymbol{e}_i \otimes \boldsymbol{e}_j) \cdot (\boldsymbol{e}_k \otimes \boldsymbol{e}_l) = \delta_{ik} \delta_{jl}. \tag{2.28}$$

With this, it becomes clear that the set of tuples

$$\{(\boldsymbol{e}_i, \boldsymbol{e}_j) | i \in [1, \dim \mathcal{A}], j \in [1, \dim \mathcal{B}]\} \tag{2.29}$$

can be used to identify the space $\mathcal{A} \otimes \mathcal{B}$ with its component matrices $\mathbb{R}^{m \times n}$. The matrix representation based on canonical bases of $\mathcal{A}$ and $\mathcal{B}$ is the canonical matrix representation, written as

$$\boldsymbol{A} \mathrel{\hat{=}} A_{ij}. \tag{2.30}$$

The equivalence to component matrices shows that the tensor space $\mathcal{A} \otimes \mathcal{B}$ is equivalent to the space of linear maps from $\mathcal{A}$ to $\mathcal{B}$. Through the inner product, $\mathcal{A} \otimes \mathcal{B}$ is also equivalent to the space of bilinear forms on the Cartesian product space $\mathcal{A} \times \mathcal{B}$.

With the equivalence between tensors and linear maps, all matrix operations known from linear algebra can be extended to tensors, as long as care is taken with the respective tensor spaces. For example, the matrix-matrix product can be written as

$$\boldsymbol{AB} = A_{ij}B_{jk}\boldsymbol{e}_i \otimes \boldsymbol{e}_k, \tag{2.31}$$

but this operation is only sensible if, for $\boldsymbol{A} \in \mathcal{A}_1 \otimes \mathcal{A}_2$ and $\boldsymbol{B} \in \mathcal{B}_1 \otimes \mathcal{B}_2$, the spaces $\mathcal{A}_2$ and $\mathcal{B}_1$ are identical. A list of matrix operations and their application to tensors is given in Appendix A.

The existence of the identity matrix implies an *identity tensor* for every vector space $\mathcal{V}$ which is defined by

$$\boldsymbol{I}(\mathcal{V})\boldsymbol{v} = \boldsymbol{v} \quad \forall \boldsymbol{v} \in \mathcal{V}, \tag{2.32}$$

with the canonical matrix components

$$\boldsymbol{I}(\mathcal{V}) \mathrel{\hat{=}} \delta_{ij}. \tag{2.33}$$

The identity tensor $\boldsymbol{I}(\mathcal{R})$ of the real Euclidean space is simply called $\boldsymbol{I}$.

As tensor spaces are themselves vector spaces, more complicated tensor spaces can be found by using, e.g., $\mathcal{A} \otimes \mathcal{B}$ in place of $\mathcal{A}$ or $\mathcal{B}$ in the above definitions. For multiple dyadic products of a space with itself, we introduce the shorthand

$$\mathcal{A}^{\otimes n} = \underbrace{\mathcal{A} \otimes \mathcal{A} \otimes \cdots \otimes \mathcal{A}}_{n \text{ times}}. \tag{2.34}$$

The dyadic product is associative, such that

$$(\mathcal{A} \otimes \mathcal{B}) \otimes \mathcal{C} = \mathcal{A} \otimes (\mathcal{B} \otimes \mathcal{C}). \tag{2.35}$$

In view of the associativity of the dyadic product, it is useful to define the *order* of a tensor space. A vector space defined via n-tuples like $\mathcal{R}$ has order 1, while the order of tensor spaces which can be decomposed into dyadic products is given as the sum of the orders of their component spaces. Tensors of order 2 are written as capital bold character $\boldsymbol{A}$, while tensors of order higher than 2 are written as blackboard-bold characters $\mathbb{A}$. Frequently occurring higher order tensor spaces in this work are

$$\mathrm{Sym} = \mathrm{sym}\left(\mathcal{R} \otimes \mathcal{R}\right), \tag{2.36}$$

$$\mathcal{C} = \mathrm{sym}\left(\mathrm{Sym} \otimes \mathrm{Sym}\right). \tag{2.37}$$

The fourth-order identity tensor on Sym is denoted as $\mathbb{I}^{\mathrm{S}}$.

Higher-order tensors are also linear maps. However, due to the associativity of the dyadic product, the definition of matrix operations on higher-order tensors is ambiguous. A fourth-order tensor $\mathbb{V} \in \mathcal{R}^{\otimes 4}$ can for example be understood as a linear map from $\mathcal{R}$ to $\mathcal{R}^{\otimes 3}$, or as one from $\mathcal{R}^{\otimes 2}$ to $\mathcal{R}^{\otimes 2}$. Consequently, we define matrix operations only for those tensor spaces for which there is a canonical dyadic decomposition into two tensor spaces. Of particular note is the tensorial Kronecker product $\times$, which we define for $\mathbb{A} \in \mathcal{A} \otimes \mathcal{A}$ and $\mathbb{B} \in \mathcal{B} \otimes \mathcal{B}$ as

$$\mathbb{A} \times \mathbb{B} = A_{ik} B_{jl} \mathbb{B}_i \otimes \tilde{\mathbb{B}}_j \otimes \mathbb{B}_k \otimes \tilde{\mathbb{B}}_l \tag{2.38}$$

where $\mathbb{B}$ and $\tilde{\mathbb{B}}$ are basis tensors of $\mathcal{A}$ and $\mathcal{B}$ respectively. A detailed explanation of properties of the tensorial Kronecker product is offered by Zheng and Spencer (1993).

2.1.3 Tensor calculus in orthonormal real bases

A function is called a *tensor function* if its arguments include one or more tensors. The partial derivative by a vector argument is the (generalized)

gradient, which can be calculated in the canonical orthonormal basis as

$$\frac{\partial f(\boldsymbol{a})}{\partial \boldsymbol{a}} = \frac{\partial f(\boldsymbol{a})}{\partial a_i} \boldsymbol{e}_i. \tag{2.39}$$

For second-order tensorial arguments, the gradient reads

$$\frac{\partial f(\boldsymbol{A})}{\partial \boldsymbol{A}} = \frac{\partial f(\boldsymbol{A})}{\partial A_{ij}} \boldsymbol{e}_i \otimes \boldsymbol{e}_j, \tag{2.40}$$

which intuitively extends to higher-order tensors. The gradient respective to an argument is always an element of the same vector space as that argument. For tensor-valued tensor functions, by convention, the gradient is defined as a right-side gradient, such that

$$\frac{\partial \boldsymbol{f}(\boldsymbol{a})}{\partial \boldsymbol{a}} = \frac{\partial f_i(\boldsymbol{a})}{\partial a_j} \boldsymbol{e}_i \otimes \boldsymbol{e}_j. \tag{2.41}$$

If one of the arguments of a tensor function is a position vector $\boldsymbol{x} \in \mathcal{R}$, the function is called a *field*. The gradient of a field f is written

$$\operatorname{grad}\left(f(\boldsymbol{x})\right) = \frac{\partial f(\boldsymbol{x})}{\partial \boldsymbol{x}}. \tag{2.42}$$

For tensor-valued fields of order at least 1, the (right-side) *divergence* is defined as

$$\operatorname{div}\left(\boldsymbol{f}(\boldsymbol{x})\right) = \operatorname{grad}\left(\boldsymbol{f}(\boldsymbol{x})\right)[\boldsymbol{I}]. \tag{2.43}$$

2.2 Tensorial harmonic bases[1]

2.2.1 The rotation group $SO(3)$

In the previous section, canonical bases were frequently mentioned, while only the canonical basis of $\mathcal{R}$ was explicitly defined. This section is intended to constructively define tensorial harmonic bases which will serve as canonical bases for various tensor spaces relevant to subsequent chapters. These bases are chosen as they allow for the depiction of higher-order tensors as vectors and matrices while efficiently taking into account both index and material symmetries of the original tensors. As such, the harmonic bases are deeply connected to properties of the rotation group $SO(3)$.

In the context of this work, an element Q of $SO(3)$ is a linear map on $\mathcal{R}$ such that for $\boldsymbol{v} \in \mathcal{R}$,

$$Q(\boldsymbol{v}) = \boldsymbol{Q}\boldsymbol{v} = Q_{ij} v_j \boldsymbol{e}_i. \tag{2.44}$$

In other words, the action of $Q \in SO(3)$ on $\mathcal{R}$ has a specific second-order tensor representation

$$\boldsymbol{Q} = Q_{ij} \boldsymbol{e}_i \otimes \boldsymbol{e}_j. \tag{2.45}$$

This representation can be used to calculate the action of $SO(3)$ on an n-th order tensor $\mathbb{V}^n \in \mathcal{R}^{\otimes n}$ via the Rayleigh product defined as

$$\begin{aligned} Q(\mathbb{V}^n) &= \boldsymbol{Q} \star \mathbb{V}^n \\ &= Q_{ai} Q_{bj} \dots Q_{ck} V_{ij\dots k} \boldsymbol{e}_a \otimes \boldsymbol{e}_b \otimes \dots \otimes \boldsymbol{e}_c. \end{aligned} \tag{2.46}$$

[1] This section is based on sections 2–5 of the publication *Tensorial harmonic bases of arbitrary order with applications in elasticity, elastoviscoplasticity and texture-based modeling* (Krause and Böhlke, 2024)

After algebraic manipulation, we find the $2n$-order tensor representation of the action of Q on the higher order tensor space,

$$\begin{aligned} Q(\mathbb{V}^n) &= \boldsymbol{Q}^{\star n}[\mathbb{V}^n] \\ &= (Q_{ai} \dots Q_{bj} \boldsymbol{e}_a \otimes \dots \boldsymbol{e}_b \otimes \boldsymbol{e}_i \otimes \dots \boldsymbol{e}_k)\,[\mathbb{V}^n], \end{aligned} \tag{2.47}$$

where we call $\boldsymbol{Q}^{\star n}$ the n-th Rayleigh power of $\boldsymbol{Q}$. The properties of the Rayleigh power were previously discussed in a continuum mechanics context by Zheng and Spencer (1993), who denote it as a Kronecker power $\langle \boldsymbol{Q} \rangle_n$. Being a linear map from $\mathcal{R}^{\otimes n}$ to $\mathcal{R}^{\otimes n}$, the action of Q implies a (right) eigenvalue problem

$$\boldsymbol{Q}^{\star n}[\mathbb{E}^n] = \lambda \mathbb{E}^n. \tag{2.48}$$

The eigentensors $\mathbb{E}^n$ of any particular $\boldsymbol{Q}^{\star n}$ depend on that rotation's axis. However, they can be grouped into certain sets of eigentensors which span subspaces of $\mathcal{R}^{\otimes n}$ which are independent of the axis chosen, forming a complete decomposition of the tensor space. Formally, we call $\mathcal{W}^n \subset \mathcal{R}^{\otimes n}$ an *invariant* subspace of $\mathcal{R}^{\otimes n}$ if

$$\boldsymbol{Q} \star \mathcal{W}^n = \mathcal{W}^n \quad \forall \boldsymbol{Q} \in SO(3), \tag{2.49}$$

where the action of $\boldsymbol{Q}$ on the entire subspace $\mathcal{W}$ is defined as

$$\boldsymbol{Q} \star \mathcal{W}^n = \{\boldsymbol{Q} \star \mathbb{W}^n | \mathbb{W}^n \in \mathcal{W}^n\}. \tag{2.50}$$

If an invariant subspace cannot be decomposed further into smaller invariant subspaces, we call it a *harmonic* subspace. The decomposition of a tensor space $\mathcal{V}^n$ into $n_{\mathcal{H}}$ harmonic subspaces

$$\mathcal{V}^n = \bigoplus_{i=1}^{n_{\mathcal{H}}(\mathcal{V}^n)} \mathcal{H}_i(\mathcal{V}^n) \tag{2.51}$$

is known in continuum mechanics as the harmonic decomposition of $\mathcal{V}^n$, cf. Forte and Vianello (1996). Harmonic subspaces of $\mathcal{R}^{\otimes n}$ are at most of order $2n+1$. In fact, $\mathcal{R}^{\otimes n}$ has exactly one harmonic subspace of dimension $2n+1$, sometimes called irreducible subspace in continuum mechanics. As it is traceless and symmetric, we will call it the *deviatoric* subspace $\mathcal{D}^n$. Other harmonic subspaces have dimension $2k+1, k<n$ and are each isomorphic to the k-th-order deviatoric subspace $\mathcal{D}^k$. We call the map from the k-th order deviatoric subspace $\mathcal{D}^k$ to an n-th order harmonic subspace $\mathcal{H}_i$ the inclusion $\mathbb{P}\left(\mathcal{H}_i, k\right)$. The harmonic decomposition can then be written as

$$\mathcal{V}^n = \bigoplus_{i=1}^{n_{\mathcal{H}}(\mathcal{V}^n)} \mathbb{P}\left(\mathcal{H}_i, k\right)[\mathcal{D}^k]. \tag{2.52}$$

By its definition as a map between specific subspaces, the tensor $\mathbb{P}\left(\mathcal{H}_i, k\right)$ has a canonical matrix interpretation as a $3^n \times (2n+1)$ matrix, for which the various matrix operations in Table A.4 are defined.

Using these concepts, we say that a basis of an n-th order tensor space is *harmonic* if its basis tensors are elements of harmonic subspaces. In the following we will calculate orthonormal harmonic bases by calculating orthonormal bases for deviatoric subspaces and finding their inclusions into higher-order spaces.

2.2.2 Harmonic bases for deviatoric tensor spaces

By the eigenvalue problem in Eq. (2.48), a basis of a deviatoric subspace can be found using deviatoric eigentensors of an arbitrarily chosen rotation Q. Since the eigentensor decomposition of Q depends on the axis of rotation, the harmonic basis convention depends on a choice of axis. We choose the Z axis $\boldsymbol{e}_3$ to ensure compatibility to a number of other common conventions in continuum mechanics, such as the ZXZ and ZYZ Euler angle conventions. This specific choice does not affect

the generality of the approach. While it is possible to calculate these eigentensors directly, for high-order tensors, it is cumbersome. Instead, one may use the fact that $SO(3)$ is a Lie group with a corresponding Lie algebra $\mathfrak{so}(3)$. Eigentensors of Q are eigentensors of $\mathfrak{q} \in \mathfrak{so}(3)$ as eigentensors are preserved by the exponential map

$$Q = \exp(\mathfrak{q}). \tag{2.53}$$

Just as the action of $SO(3)$ on higher-order tensor spaces is defined by the Rayleigh product $\star$, the action of its Lie algebra $\mathfrak{so}(3)$ is described by the infinitesimal Rayleigh product

$$\begin{aligned}\mathfrak{q}(\mathbb{V}^n) = \boldsymbol{q} \boxtimes \mathbb{V}^n = \mathfrak{q}_{ai} V_{ij\ldots k} \boldsymbol{e}_a \otimes \boldsymbol{e}_j \ldots \boldsymbol{e}_k \\ + \mathfrak{q}_{bj} V_{ij\ldots k} \boldsymbol{e}_i \otimes \boldsymbol{e}_b \ldots \boldsymbol{e}_k \\ + \ldots \\ + \mathfrak{q}_{ck} V_{ij\ldots k} \boldsymbol{e}_i \otimes \boldsymbol{e}_j \ldots \boldsymbol{e}_c.\end{aligned} \tag{2.54}$$

Analogously to the Rayleigh power of Eq. (2.47), the infinitesimal Rayleigh power is defined as

$$\begin{aligned}(\boldsymbol{q}_i^{\boxtimes n}) = \mathfrak{q}_{ai} \ldots \delta_{bj} \boldsymbol{e}_a \otimes \ldots \otimes \boldsymbol{e}_b \otimes \boldsymbol{e}_i \otimes \ldots \otimes \boldsymbol{e}_j \\ + \ldots \\ + \delta_{ai} \ldots \mathfrak{q}_{bj} \boldsymbol{e}_a \otimes \ldots \otimes \boldsymbol{e}_b \otimes \boldsymbol{e}_i \otimes \ldots \otimes \boldsymbol{e}_j.\end{aligned} \tag{2.55}$$

The following eigentensor calculation scheme is based on the angular momentum operator approach known from quantum mechanics, cf. Edmonds (1996). Using the Levi-Civita or permutation tensor $\boldsymbol{\epsilon}$ and the imaginary number i, we define angular momentum operators around the first-order axes $\boldsymbol{e}_i$ as

$$\boldsymbol{J}_i = \mathrm{i}\boldsymbol{\epsilon}[\boldsymbol{e}_i]. \tag{2.56}$$

The set of momentum operators forms a basis of the tensor representation of the action of $\mathfrak{so}(3)$ on $\mathcal{R}$. The scalar factor $\mathfrak{i}$ is an arbitrarily chosen convention in quantum mechanics; we use it for our results to be compatible to pre-existing results and implementations.

Based on the choice of $\boldsymbol{e}_3$ as fundamental axis, we are interested in the eigenvectors of $\boldsymbol{J}_3$, which can be calculated directly. However, to define bases for n-th order tensor spaces, eigentensors of the $2n$-th order momentum operator $\boldsymbol{J}_3^{\boxtimes n}$ are required, direct calculation of which is more involved, leading to a different approach. Based on the eigentensors of $\boldsymbol{J}_3$, the n-th order eigentensor associated with the eigenvalue $-n\mathfrak{i}$ is given by

$$\mathbb{E}^n(-n\mathfrak{i}) = \left(\frac{1}{\sqrt{2}}(\boldsymbol{e}_1 + \mathfrak{i}\boldsymbol{e}_2)\right)^{\otimes n}. \tag{2.57}$$

To calculate other eigentensors based on $\mathbb{E}^n(-n\mathfrak{i})$, we use the Z-axis raising operator given by Edmonds (1996) among others as

$$\boldsymbol{J}_+^n = \boldsymbol{J}_1^{\boxtimes n} + \mathfrak{i}\boldsymbol{J}_2^{\boxtimes n}. \tag{2.58}$$

This operator maps a given eigentensor $\mathbb{E}^n(w)$ of $\boldsymbol{J}_3^{\boxtimes n}$ with eigenvalue w to that with $w + \mathfrak{i}$, but introduces a scalar factor. To calculate all $2n + 1$ eigentensors, we recursively apply this operator and renormalize, resulting in

$$\mathbb{E}^n((k+1)\mathfrak{i}) = \frac{1}{\sqrt{(n-k)(n+k+1)}}\boldsymbol{J}_+^n[\mathbb{E}^n(k\mathfrak{i})]. \tag{2.59}$$

In quantum mechanics, this complexified orthonormal eigentensor basis $\{\mathbb{E}^n(-k\mathfrak{i}), \dots \mathbb{E}^n(k\mathfrak{i})\}$ is used directly. This approach is also used by Man and Du (2022) in a texture description context. We note that respective to a complexified basis, even fully real tensors may have complex components. As classical continuum mechanics deals with

fully real tensors, it is simpler to use a real basis instead. We define the n-th order real deviatoric basis $\mathbb{D}_i^n$ as

$$\mathbb{D}_{2(n-k)+1}^n = \frac{1}{\sqrt{2}} \left(\mathbb{E}^n(k\mathrm{i}) + (-1)^k \mathbb{E}^n(-k\mathrm{i}) \right), \quad k \in [1, n] \tag{2.60}$$

$$\mathbb{D}_{2(n-k)+2}^n = \frac{-\mathrm{i}}{\sqrt{2}} \left(\mathbb{E}^n(k\mathrm{i}) + (-1)^{k+1} \mathbb{E}^n(-k\mathrm{i}) \right), \quad k \in [1, n] \tag{2.61}$$

$$\mathbb{D}_{2n+1}^n = \mathbb{E}^n(0). \tag{2.62}$$

These tensors are real-valued because the eigentensors form complex conjugate pairs

$$\mathbb{E}^n(-k\mathrm{i}) = \bar{\mathbb{E}}^n(-k\mathrm{i}), \quad k \in [1, n]. \tag{2.63}$$

Furthermore, they are orthonormal because the $\mathbb{E}^n(k\mathrm{i})$ are orthonormal. Finally, they form a basis because of orthonormality and the fact that there are $2n + 1$ tensors $\mathbb{D}_i^n$ for any given n.

As the above definition is linear, there exists a transformation matrix $\underline{\underline{T}}^n$ that maps $\mathbb{E}_j^n$ to $\mathbb{D}_i^n$ via

$$\mathbb{D}_i^n = T_{ij}^n \mathbb{E}^n \left(j\mathrm{i} - n\mathrm{i} \right). \tag{2.64}$$

With this particular convention for $\mathbb{D}_i^n$,

$$\boldsymbol{D}_i^1 = \boldsymbol{e}_i. \tag{2.65}$$

These *deviatoric bases* are fully real and orthonormal and will be used as the canonical bases of deviatoric subspaces in the following. All results discussed in Section 2.1 apply. In particular, when using a deviatoric basis, it is not necessary to distinguish between primal and dual bases or co- and contravariant indices.

2.2.3 Harmonic bases for arbitrary tensor spaces

To compose arbitrary tensor spaces from deviatoric subspaces, we use the harmonic decomposition. Unlike the usual depictions of that decomposition in continuum mechanics, e.g., Boehler et al. (1994) or Forte and Vianello (1996), we construct the decomposition of higher-order tensor spaces directly from that of lower-order ones. As the fundamental units of the harmonic decomposition are the deviatoric tensor spaces, we first calculate how the dyadic product of two deviatoric tensor spaces decomposes harmonically. Fundamentally, the space decomposes harmonically into

$$\mathcal{D}^m \otimes \mathcal{D}^n = \bigoplus_{l=|m-n|}^{m+n} \mathcal{H}(\mathcal{D}^m \otimes \mathcal{D}^n, l) \tag{2.66}$$

where the harmonic subspace $\mathcal{H}(\mathcal{D}^m \otimes \mathcal{D}^n, l)$ has dimension $2l+1$ and is isomorphic to $\mathcal{D}^l$. For example,

$$\mathcal{H}(\mathcal{D}^m \otimes \mathcal{D}^n, m+n) = \mathcal{D}^{m+n}. \tag{2.67}$$

$\mathcal{H}(\mathcal{D}^m \otimes \mathcal{D}^n, 0)$, which exists only for $m = n$, is isomorphic to the scalars. Therefore, $\mathcal{H}(\mathcal{D}^m \otimes \mathcal{D}^m, 0)$ is of dimension 1 and spanned by a single basis tensor $\mathbb{E}^{2m}$. As harmonic subspaces are rotation-invariant, it follows that

$$\boldsymbol{Q} \star \mathcal{H}(\mathcal{D}^m, \mathcal{D}^m, 0) = \mathcal{H}(\mathcal{D}^m, \mathcal{D}^m, 0) \tag{2.68}$$

$$\Rightarrow \{\boldsymbol{Q} \star \alpha\mathbb{E}^{2m} | \alpha \in \mathbb{R}\} = \{\alpha\mathbb{E}^{2m} | \alpha \in \mathbb{R}\}, \tag{2.69}$$

which means that $\mathbb{E}^{2m}$ is necessarily *isotropic*.

Note that because each $\mathcal{H}(\mathcal{D}^m \otimes \mathcal{D}^n, l)$ is of different dimension, this decomposition is unique. As the harmonic subspaces $\mathcal{H}(\mathcal{D}^m \otimes \mathcal{D}^n, l)$

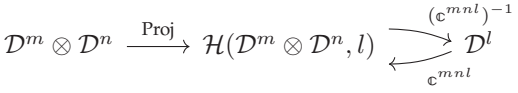

Figure 2.1: Maps between harmonic and deviatoric subspaces. Figure based on Figure 1 of Krause and Böhlke (2024).

are orthogonal to each other and their dimensions add up to mn, the decomposition is complete.

To calculate $\mathcal{H}$, consider the maps portrayed in Fig. 2.1. First, there exists a unique projection from $\mathcal{D}^m \otimes \mathcal{D}^n$ to $\mathcal{H}(\mathcal{D}^m \otimes \mathcal{D}^n, l)$ which can be given as a $2m + 2n$ order tensor of rank $2l + 1$ that has projector properties. Its pseudoinverse is the inclusion from $\mathcal{H}(\mathcal{D}^m \otimes \mathcal{D}^n, l)$ into $\mathcal{D}^m \otimes \mathcal{D}^n$. Second, the isomorphism between $\mathcal{H}(\mathcal{D}^m \otimes \mathcal{D}^n, l)$ and $\mathcal{D}^l$ is again a tensor, this one of order $m + n + l$ and rank $2l + 1$. This tensor, being an isomorphism, is bijective when considered as a map from $\mathcal{H}(\mathcal{D}^m \otimes \mathcal{D}^n, l)$. Being more interested in its inverse, we call this isomorphism $\left(\mathbb{c}^{mnl}\right)^{-1}$. By inserting

$$\mathcal{H}(\mathcal{D}^m \otimes \mathcal{D}^n, l) = \mathbb{c}^{mnl}[\mathcal{D}^l] \tag{2.70}$$

into Eq. (2.66), we retrieve

$$\mathcal{D}^m \otimes \mathcal{D}^n = \bigoplus_{l=|m-n|}^{m+n} \mathbb{c}^{mnl}[\mathcal{D}^l], \tag{2.71}$$

which is an explicit harmonic decomposition of the dyadic product of two deviatoric tensor spaces. The superscripts m, n and l which indicate tensor order are not indices and the summation convention does not apply to them.

To calculate the tensor $\mathbb{c}^{mnl}$ we borrow established calculation schemes from quantum mechanics. There, the deviatoric eigentensors $\mathbb{E}(k\mathrm{i})$ are discussed in the context of angular momentum as eigenstates of the

angular momentum operator $\boldsymbol{J}$. Correspondingly, $\mathbb{c}^{mnl}$ is discussed in the context of coupled angular momenta, and is known by its tensor components

$$(C^{mnl})^{q'}_{o'p'} = \mathbb{c}^{mnl} \cdot (\mathbb{E}^m(q'\mathfrak{i}) \otimes \mathbb{E}^n(o'\mathfrak{i}) \otimes \bar{\mathbb{E}}^l(p'\mathfrak{i})), \tag{2.72}$$

which are called Clebsch-Gordan coefficients, see, e.g., Griffiths (2019). The indices q', o' and p' start at $-m$, $-n$ and $-l$ respectively, as is common in quantum mechanics, and the complex conjugate $\bar{\boldsymbol{E}}$ is a consequence of the complexified tensor algebra involved. Edmonds (1996) gives explicit recursive calculation schemes for Clebsch-Gordan coefficients, but uses the bra-ket notation, which compares to the one above via

$$(C^{mnl})^{q'}_{o'p'} = \langle mno'p'|mnlq'\rangle. \tag{2.73}$$

The bra-ket notation emphasizes the Clebsch-Gordan coefficients being linear maps from component vectors of dimension $2l+1$ to component matrices of size $2(m+1) \times 2(n+1)$, while the notation used above emphasizes their tensorial nature. In either case, the Clebsch-Gordan coefficients, being tensor components, admit basis transformations, in particular the transformation from Eq. (2.64), which yields

$$c^{mnl}_{ijk} = \mathfrak{i}^{m+n+l} T^m_{io} T^n_{jp} \overline{T^l_{kq}} (C^{mnl})^{q'}_{o'p'}. \tag{2.74}$$

The indices without primes are defined as $o = o' + m + 1$ such that $o \in [1, 2m+1]$, and respectively for q and n and p and l. The components c^{mnl}_{ijk} are given respective to real-valued deviatoric bases, such that the Clebsch-Gordan tensor can be written

$$\mathbb{c}^{mnl} = c^{mnl}_{ijk} \mathbb{D}^m_i \otimes \mathbb{D}^n_j \otimes \mathbb{D}^l_k. \tag{2.75}$$

Because the coefficients and basis tensors in this expression are fully real, $\mathbb{c}^{mnl}$ is a fully real tensor.

Using the Clebsch-Gordan tensors, the harmonic basis for $\mathcal{D}^m \otimes \mathcal{D}^n$ has orthonormal basis tensors

$$\mathbb{H}^{m+n}_{i(l,j)} = \mathbb{c}^{mnl}[\mathbb{D}^l_j], \quad l \in [|m-n|, m+n], j \in [0, l], \tag{2.76}$$

with an appropriate enumeration convention $i(l, j)$. By convention, we sort the harmonic subspaces starting from the least-dimensional, which leads to

$$i(l,j) = j + \sum_{k=|m-n|}^{l} 2(k+1). \tag{2.77}$$

In the general case, we are interested in the harmonic decomposition of an arbitrary tensor space which is constructed as the dyadic product of two other tensor spaces $\mathcal{V}^m$ and $\mathcal{V}^n$. In the interest of building an iterative procedure, we assume that $\mathcal{V}^m$ is already decomposed into harmonic subspaces of dimension $2l+1$, of which there are $a(m, l)$. Instead of giving a formula for $a(m, l)$, we treat it as the number of inclusions $\mathbb{P}\left(\mathcal{H}^l_i, \mathcal{D}^p\right)$ which map the deviatoric space $\mathcal{D}^p$ to the various $(2l+1)$-dimensional harmonic subspaces, and give a formula for those inclusions. Then, $\mathcal{V}^m$ decomposes into

$$\mathcal{V}^m = \bigoplus_{i=1}^{n_{\mathcal{H}}(\mathcal{V}^m)} \mathbb{P}\left(\mathcal{H}^m_i, p\right)[\mathcal{D}^p], \tag{2.78}$$

and $\mathcal{V}^n$ is given as

$$\mathcal{V}^n = \bigoplus_{j=1}^{n_{\mathcal{H}}(\mathcal{V}^n)} \mathbb{P}\left(\mathcal{H}^n_j, q\right)[\mathcal{D}^q]. \tag{2.79}$$

The space $\mathcal{V}^m \otimes \mathcal{V}^n$ is given as

$$\mathcal{V}^m \otimes \mathcal{V}^n = \bigoplus_{i=1}^{n_\mathcal{H}(\mathcal{V}^m)} \bigoplus_{j=1}^{n_\mathcal{H}(\mathcal{V}^n)} \mathbb{P}\left(\mathcal{H}_i^m, p\right)[\mathcal{D}^p] \otimes \mathbb{P}\left(\mathcal{H}_j^n, q\right)[\mathcal{D}^q]. \tag{2.80}$$

Based on the canonical interpretation of the inclusions as linear maps, the (tensorial) Kronecker product $\times$ is defined for them as

$$\begin{aligned}\left(\mathbb{P}\left(\mathcal{H}_i^m, p\right) \times \mathbb{P}\left(\mathcal{H}_j^n, \mathcal{D}^p\right)\right)[\mathcal{D}^p \otimes \mathcal{D}^q] \\ = \mathbb{P}\left(\mathcal{H}_i^m, p\right)[\mathcal{D}^p] \otimes \mathbb{P}\left(\mathcal{H}_j^n, q\right)[\mathcal{D}^q].\end{aligned} \tag{2.81}$$

Using the Clebsch-Gordan tensors, we find

$$\begin{aligned}\mathbb{P}\left(\mathcal{H}_i^m, p\right)[\mathcal{D}^p] \otimes \mathbb{P}\left(\mathcal{H}_j^n, q\right)[\mathcal{D}^q] = \\ \sum_{l=|p-q|}^{p+q} \left(\mathbb{P}\left(\mathcal{H}_i^m, p\right) \times \mathbb{P}\left(\mathcal{H}_j^n, q\right)\right) \mathbb{c}^{pql}[\mathcal{D}^l].\end{aligned} \tag{2.82}$$

The sums can be rearranged with the deviatoric order l and a new index variable k such that a tensor product of arbitrary tensor spaces $\mathcal{V}^m \otimes \mathcal{V}^n$ can be harmonically decomposed into

$$\mathcal{V}^m \otimes \mathcal{V}^n = \bigoplus_{k=0}^{n_\mathcal{H}(\mathcal{V}^m \otimes \mathcal{V}^n)} \mathbb{P}\left(\mathcal{H}_k^{m+n}, l\right)[\mathcal{D}^l]. \tag{2.83}$$

The new inclusions are obtained via

$$\mathbb{P}\left(\mathcal{H}_k^{m+n}, l\right) = \left(\mathbb{P}\left(\mathcal{H}_i^m, p\right) \times \mathbb{P}\left(\mathcal{H}_j^n, q\right)\right) \mathbb{c}^{pql}, \tag{2.84}$$

where the definition of the matrix-matrix product on tensors was used between the inclusion Kronecker product and the Clebsch-Gordan tensor. The new index k enumerates all harmonic spaces in an order which is chosen by convention. We first sort subspaces by deviatoric order l,

then by p, q, i and finally j, each ascending. In all concrete examples considered in this manuscript, the number of harmonic subspaces is limited due to various index symmetries, and the enumeration of the various projectors proves quite simple.

Relative to a harmonic basis, an n-th order tensor $\mathbb{A}^n \in \mathcal{V}^n$ is depicted as

$$\mathbb{A}^n = \sum_{i=0}^{n_{\mathcal{H}}(\mathcal{V}^n)} \sum_{j=1}^{2k+1} A_{h(k,i,j)} \mathbb{P}\left(\mathcal{H}_i, k\right) [\mathbb{D}_j^k], \tag{2.85}$$

with the harmonic basis components $A_{h(k,i,j)}$ and basis tensors $\mathbb{P}\left(n, k\right)_i [\mathbb{D}_j^k]$. For any deviatoric subspace $\mathcal{H}_i$, k is the order of the corresponding deviatoric subspace, which can be calculated as

$$k = \frac{1}{2}(\dim \mathcal{H}_i - 1). \tag{2.86}$$

In the form

$$\mathbb{A}^n = \sum_{i=0}^{n_{\mathcal{H}}(\mathcal{V}^n)} \mathbb{P}\left(\mathcal{H}_i, k\right) \left[\sum_{j=1}^{2k+1} A_{h(i,j)} \mathbb{D}_j^k \right], \tag{2.87}$$

it is more clear that the harmonic components $A_{h(i,j)}$ are grouped into sets of $2k+1$ components which each belong to one harmonic subspace. Therefore, the components themselves represent a harmonic decomposition of $\mathbb{A}^n$.

The construction of inclusions from Clebsch-Gordan tensors defined above allows the calculation of a harmonic decomposition from the ground up by repeatedly applying dyadic products. By using the $\mathbb{D}^p$ basis for the deviatoric spaces $\mathcal{D}^p$, we can thus construct harmonic bases, albeit with some effort. Thankfully, in continuum mechanics, a few specific harmonic bases are most relevant, and it is usually not necessary to construct others. With that in mind, the following sections are concerned with specific bases.

2.2.4 Second-order harmonic bases

To calculate the harmonic basis equivalent of the Voigt basis, we harmonically decompose the space of second-order tensors $\mathcal{R}^{\otimes 2}$. First, we note that both the zeroth-order tensor space $\mathbb{R}$ and the first-order tensor space $\mathcal{R}$ are fully deviatoric, i.e.,

$$\mathcal{R} = \mathcal{D}^1 \text{ with } \boldsymbol{e}_i = \boldsymbol{D}_i^1. \tag{2.88}$$

The harmonic basis of $\mathcal{R}^{\otimes 2}$ fundamentally results from the definition of invariant subspaces (Eq. (2.49)). Working with this definition, the isotropic (or spherical) subspace

$$V^\circ = \frac{\mathrm{tr}(\boldsymbol{V})}{3}\boldsymbol{I} \tag{2.89}$$

is harmonic. The traceless part of $\mathcal{R}^{\otimes 2}$ remains. Since rotations only map symmetric tensors to symmetric tensors, the remaining traceless tensors can be further split into the skew-symmetric and symmetric deviatoric parts

$$\mathrm{skw}\left(\boldsymbol{V}\right) = \frac{1}{2}\left(\boldsymbol{V} - \boldsymbol{V}^\mathsf{T}\right) \text{ and} \tag{2.90}$$

$$\boldsymbol{V}' = \boldsymbol{V} - \boldsymbol{V}^\circ - \mathrm{skw}\left(\boldsymbol{V}\right). \tag{2.91}$$

We thus arrive at the harmonic decomposition of $\mathcal{R}^{\otimes 2}$, which is exactly the decomposition into spherical, deviatoric and skew-symmetric parts

$$\mathcal{R}^{\otimes 2} = \mathrm{Sph} \oplus \mathrm{Skw} \oplus \mathcal{D}^2. \tag{2.92}$$

The same result can also be reached by direct calculation. Because $\mathcal{R}$ is deviatoric,

$$\mathcal{R}^{\otimes 2} = \mathcal{R} \otimes \mathcal{R} = D^1 \otimes D^1 \tag{2.93}$$

and the projectors are given by Clebsch-Gordan tensors according to Eq. (2.71), leading to a harmonic decomposition in the form

$$\mathcal{D}^{\otimes 2} = \boldsymbol{c}^{110}[D^0] \oplus \mathbb{c}^{111}[D^1] \oplus \mathbb{c}^{112}[D^2]. \tag{2.94}$$

The relevant Clebsch-Gordan tensors can be calculated via Eq. (2.75) as

$$\boldsymbol{c}^{110} = \frac{1}{\sqrt{3}}\boldsymbol{I}, \tag{2.95}$$

$$\mathbb{c}^{111} = \frac{1}{\sqrt{2}}\boldsymbol{\epsilon}, \tag{2.96}$$

$$\mathbb{c}^{112} = \mathbb{P}'. \tag{2.97}$$

Using Eq. (2.85), a second-order tensor can therefore be depicted as

$$\boldsymbol{A} = A_{h(0,1,1)}\boldsymbol{c}^{110} + A_{h(1,1,i)}\boldsymbol{c}^{111}[\boldsymbol{e}_i] + A_{h(2,1,j)}\boldsymbol{c}^{112}[\boldsymbol{D}^2_j]. \tag{2.98}$$

To find the basis of $\mathcal{D}^2$, we apply the eigentensor calculation scheme of Section 2.2.2, finding as eigentensors

$$\boldsymbol{E}^2(0) = \frac{1}{\sqrt{6}}\left(3\boldsymbol{e}_3 \otimes \boldsymbol{e}_3 - \boldsymbol{I}\right), \tag{2.99}$$

$$\boldsymbol{E}^2(\mathrm{i}) = -\operatorname{sym}\left(\boldsymbol{e}_1 \otimes \boldsymbol{e}_3\right) + \mathrm{i}\operatorname{sym}\left(\boldsymbol{e}_2 \otimes \boldsymbol{e}_3\right), \tag{2.100}$$

$$\boldsymbol{E}^2(-\mathrm{i}) = \operatorname{sym}\left(\boldsymbol{e}_1 \otimes \boldsymbol{e}_3\right) + \mathrm{i}\operatorname{sym}\left(\boldsymbol{e}_2 \otimes \boldsymbol{e}_3\right), \tag{2.101}$$

$$\boldsymbol{E}^2(2\mathrm{i}) = \frac{1}{2}\left(\boldsymbol{e}_1 \otimes \boldsymbol{e}_1 - \boldsymbol{e}_2 \otimes \boldsymbol{e}_2\right) - \mathrm{i}\operatorname{sym}\left(\boldsymbol{e}_2 \otimes \boldsymbol{e}_1\right), \tag{2.102}$$

$$\boldsymbol{E}^2(-2\mathrm{i}) = \frac{1}{2}\left(\boldsymbol{e}_1 \otimes \boldsymbol{e}_1 - \boldsymbol{e}_2 \otimes \boldsymbol{e}_2\right) + \mathrm{i}\operatorname{sym}\left(\boldsymbol{e}_2 \otimes \boldsymbol{e}_1\right), \tag{2.103}$$

from which $\boldsymbol{D}^2_i$ can be calculated via Eq. (2.64). After combining the deviatoric bases and the inclusion tensors, the second-order harmonic

basis tensors in the Z-axis-convention read

$$\boldsymbol{H}_1^2 = \frac{1}{\sqrt{3}}\boldsymbol{I}, \tag{2.104}$$

$$\boldsymbol{H}_2^2 = \frac{1}{\sqrt{2}}\,\mathrm{skw}\,(\boldsymbol{e}_2 \otimes \boldsymbol{e}_3)\,, \tag{2.105}$$

$$\boldsymbol{H}_3^2 = \frac{1}{\sqrt{2}}\,\mathrm{skw}\,(\boldsymbol{e}_3 \otimes \boldsymbol{e}_1)\,, \tag{2.106}$$

$$\boldsymbol{H}_4^2 = \frac{1}{\sqrt{2}}\,\mathrm{skw}\,(\boldsymbol{e}_1 \otimes \boldsymbol{e}_2)\,, \tag{2.107}$$

$$\boldsymbol{H}_5^2 = \boldsymbol{D}_2^2 = \frac{1}{\sqrt{2}}(\boldsymbol{e}_1 \otimes \boldsymbol{e}_1 - \boldsymbol{e}_2 \otimes \boldsymbol{e}_2), \tag{2.108}$$

$$\boldsymbol{H}_6^2 = \boldsymbol{D}_1^2 = \sqrt{2}\,\mathrm{sym}\,(\boldsymbol{e}_1 \otimes \boldsymbol{e}_2)\,, \tag{2.109}$$

$$\boldsymbol{H}_7^2 = \boldsymbol{D}_3^2 = \sqrt{2}\,\mathrm{sym}\,(\boldsymbol{e}_1 \otimes \boldsymbol{e}_3)\,, \tag{2.110}$$

$$\boldsymbol{H}_8^2 = \boldsymbol{D}_4^2 = \sqrt{2}\,\mathrm{sym}\,(\boldsymbol{e}_2 \otimes \boldsymbol{e}_3)\,, \tag{2.111}$$

$$\boldsymbol{H}_9^2 = \boldsymbol{D}_5^2 = \frac{1}{\sqrt{6}}(3\boldsymbol{e}_3 \otimes \boldsymbol{e}_3 - \boldsymbol{I}). \tag{2.112}$$

The space of symmetric second-order tensors Sym is frequently used in this manuscript. Consequently, it is useful to define the symmetric second-order harmonic basis as that space's canonical basis by simply omitting tensors $\boldsymbol{H}_1^2 \ldots \boldsymbol{H}_3^2$, which are associated with Skw. The canonical component depiction of a symmetric second-order tensor $\boldsymbol{\varepsilon}$ then resolves to

$$\varepsilon_i = \begin{pmatrix} \frac{1}{\sqrt{3}}\,(\varepsilon_{11} + \varepsilon_{22} + \varepsilon_{33}) \\ \frac{1}{\sqrt{2}}(\varepsilon_{11} - \varepsilon_{22}) \\ \sqrt{2}\varepsilon_{12} \\ \sqrt{2}\varepsilon_{13} \\ \sqrt{2}\varepsilon_{23} \\ \frac{1}{\sqrt{6}}\,(2\varepsilon_{33} - \varepsilon_{11} - \varepsilon_{22}) \end{pmatrix}. \tag{2.113}$$

While the harmonic basis is an efficient way of depicting Sym as a vector space, it obscures its tensorial nature. To treat $\boldsymbol{\varepsilon} \in \mathrm{Sym}$ as a matrix, the

induced canonical basis of $\mathcal{R}$ must be used, which will continue to be written ε_{ij}.

When purely deviatoric tensors are considered, the resulting five-dimensional $\boldsymbol{D}^2$-basis is equivalent to the various Kocks-type bases, for example those of Lequeu (1986)

$$\underline{\varepsilon}_{\text{Lequeu}} = \begin{pmatrix} \frac{1}{\sqrt{2}}(\varepsilon_{22} - \varepsilon_{11}) \\ \sqrt{\frac{3}{2}}(\varepsilon_{11} + \varepsilon_{22}) \\ \sqrt{2}\varepsilon_{23} \\ \sqrt{2}\varepsilon_{13} \\ \sqrt{2}\varepsilon_{12} \end{pmatrix} \tag{2.114}$$

and Van Houtte (1988)

$$\underline{\varepsilon}_{\text{van Houtte}} = \begin{pmatrix} \frac{(\sqrt{3}+1)}{2}\varepsilon_{22} + \frac{(\sqrt{3}-1)}{2}\varepsilon_{33} \\ \frac{(\sqrt{3}-1)}{2}\varepsilon_{22} + \frac{(\sqrt{3}+1)}{2}\varepsilon_{33} \\ \sqrt{2}\varepsilon_{23} \\ \sqrt{2}\varepsilon_{13} \\ \sqrt{2}\varepsilon_{12} \end{pmatrix}. \tag{2.115}$$

A full discussion of those bases can be found in Mánik (2021).

The basis most commonly used in commercial software is the non-normalized basis of Voigt (1910). Also common is its normalized equivalent, generally called the Mandel basis after Mandel (1965). Conversions between the harmonic basis and the Mandel basis can be written as

$$\underline{\varepsilon} = \underline{\underline{M}}\, \underline{\varepsilon}_{\text{M}} \tag{2.116}$$

with

$$\underline{\underline{M}} = \begin{pmatrix} \frac{1}{\sqrt{3}} & \frac{1}{\sqrt{3}} & \frac{1}{\sqrt{3}} & 0 & 0 & 0 \\ \frac{1}{\sqrt{2}} & \frac{-1}{\sqrt{2}} & 0 & 0 & 0 & 0 \\ 0 & 0 & 0 & 0 & 0 & 1 \\ 0 & 0 & 0 & 0 & 1 & 0 \\ 0 & 0 & 0 & 1 & 0 & 0 \\ \frac{-1}{\sqrt{6}} & \frac{-1}{\sqrt{6}} & \frac{2}{\sqrt{6}} & 0 & 0 & 0 \end{pmatrix}. \tag{2.117}$$

For conversions from the non-normalized Voigt basis, rows 3 to 5 acquire a factor of $\sqrt{2}$ or its inverse depending on whether the strain or stress Voigt basis is used. As some commercial software uses different index conventions, the shear components in rows 3 to 5 may need to be reordered.

When working with anisotropic tensors, a recurring task is the application of rotations to arbitrary order tensors. In the $\boldsymbol{e}_i$ basis, this is done via direct application of the Rayleigh product as defined in Eq. (2.46). In the harmonic basis, it is necessary to calculate a harmonic basis representation of the Kronecker power of Eq. (2.47). In the following, an approach to parameterize harmonic rotation matrices by Euler angles is demonstrated for the example of the second-order symmetric harmonic basis. To calculate harmonic rotation matrices, we begin with deviatoric rotation matrices. The n-th order eigentensor basis $\mathbb{E}^n$ from Eq. (2.59) is defined via eigentensor decomposition of Z rotations. Therefore, Z rotations act on $\mathcal{D}^n$ as

$$\boldsymbol{Q}_{\mathrm{Z}}^{\star n}(\alpha)[\mathcal{D}^n] = \sum_{k=-n}^{n} e^{ik\alpha} \left(\mathbb{E}^n(k\mathfrak{i}) \otimes \mathbb{E}^n(k\mathfrak{i})\right)[\mathcal{D}^n]. \tag{2.118}$$

After transforming into the deviatoric basis via Eq. (2.64),

$$\sum_{k=-n}^{n} e^{-ik\alpha} \mathbb{E}_k^n \otimes \mathbb{E}_k^n = d_{\mathrm{Z}ij}^n \mathbb{D}_i^n \otimes \mathbb{D}_j^n \tag{2.119}$$

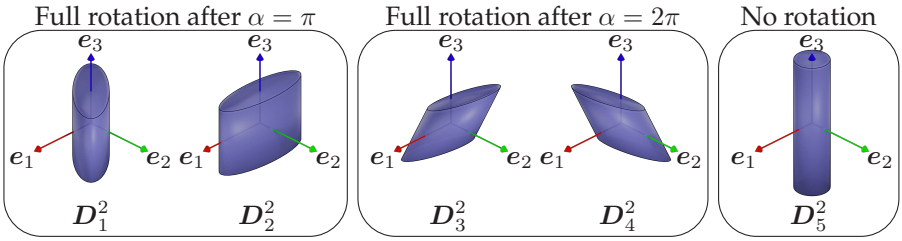

Figure 2.2: $\boldsymbol{D}^2$-transformed cylinders visualize the Z-rotation of $\mathcal{D}^2$. Figure based on Figure 3 of Krause and Böhlke (2024).

with

$$d^n_{Zij} = \begin{cases} \cos(k\alpha) & i = j = 2(n-k)+1 \\ \cos(k\alpha) & i = j = 2(n-k)+2 \\ -\sin(k\alpha) & i = 2(n-k)+2, j = 2(n-k)+1 \\ \sin(k\alpha) & i = 2(n-k)+1, j = 2(n-k)+2 \\ 1 & i = j = 2n+1 \\ 0 & \text{else.} \end{cases} \tag{2.120}$$

For $n = 1$, this is the classic rotation matrix around $\boldsymbol{e}_3$. Increasing the tensorial order from $n-1$ to n adds a 2×2 block analogous to an $n\alpha$ rotation matrix. To further clarify this point, we may consider the involved rotations. The rotation of $\mathcal{D}^1$ around the Z-axis proceeds as usual: of the three basis tensors $\mathbb{D}^1_i = \boldsymbol{e}_i$, $\boldsymbol{e}_3$ does not rotate while the other two complete a full rotation after $\alpha = 2\pi$. In Fig. 2.2, the second-order tensors are visualized as strain modes applied to a cylinder which may be imagined to rotate around $\boldsymbol{e}_3$. $\boldsymbol{D}^2_5 = \boldsymbol{e}_3 \otimes \boldsymbol{e}_3$ does not rotate. $\boldsymbol{D}^2_3$ and $\boldsymbol{D}^2_4$ complete a full rotation after $\alpha = 2\pi$, while $\boldsymbol{D}^2_1$ and $\boldsymbol{D}^2_2$, due to symmetry, are indistinguishable from their starting form after $\alpha = \pi$. In other words, $\boldsymbol{D}^2_1$ and $\boldsymbol{D}^2_2$ rotate with 2α.

For rotations around other axes, the d-matrices are different. Rotations around Y and X are calculated in quantum mechanics via Wigner-d-matrices. These are components respective to the $\mathbb{E}^n$-basis and are given by Wigner (1931) as

$$d^n_{\mathrm{Y}^*ij}(\beta) = \left((n+m')!(n-m')!(n+m)!(n-m)!\right)^{\frac{1}{2}} \sum_{s=s_{\min}}^{s_{\max}} \frac{(-1)^{m'-m+s}\left(\cos\frac{\beta}{2}\right)^{2n+m-m'-2s}\left(\sin\frac{\beta}{2}\right)^{m'-m+2s}}{(n+m-s)!s!(m'-m+s)!(n-m'-s)!} \tag{2.121}$$

and

$$d^n_{\mathrm{X}^*ij}(\beta) = \left((n+m')!(n-m')!(n+m)!(n-m)!\right)^{\frac{1}{2}} \sum_{s=s_{\min}}^{s_{\max}} \frac{(-1)^{s}\mathfrak{i}^{m-m'}\left(\cos\frac{\beta}{2}\right)^{2n+m-m'-2s}\left(\sin\frac{\beta}{2}\right)^{m'-m+2s}}{(n+m-s)!s!(m'-m+s)!(n-m'-s)!} \tag{2.122}$$

with

$$i = m' + n, \quad j = m + n, \tag{2.123}$$

and

$$s_{\min} = \max(0, m - m'), \tag{2.124}$$

$$s_{\max} = \min(n + m, n - m'). \tag{2.125}$$

The d-functions can be transformed into the $\boldsymbol{D}$-basis via T. For $\boldsymbol{D}^2$, we retrieve

$$\underline{\underline{d}}^2_{\mathrm{Z}\boldsymbol{D}^2} = \begin{pmatrix} \cos(2\alpha) & \sin(2\alpha) & 0 & 0 & 0 \\ -\sin(2\alpha) & \cos(2\alpha) & 0 & 0 & 0 \\ 0 & 0 & \cos(\alpha) & \sin(\alpha) & 0 \\ 0 & 0 & -\sin(\alpha) & \cos(\alpha) & 0 \\ 0 & 0 & 0 & 0 & 1 \end{pmatrix}, \tag{2.126}$$

$$\underline{\underline{d}}^2_{\mathrm{Y}\boldsymbol{D}^2} = \begin{pmatrix} \cos(\alpha) & 0 & 0 & -\sin(\alpha) & 0 \\ 0 & \frac{\cos(2\alpha)}{4} + \frac{3}{4} & \frac{\sin(2\alpha)}{2} & 0 & -\frac{\sqrt{3}\sin^2(\alpha)}{2} \\ 0 & -\frac{\sin(2\alpha)}{2} & \cos(2\alpha) & 0 & -\frac{\sqrt{3}\sin(2\alpha)}{2} \\ \sin(\alpha) & 0 & 0 & \cos(\alpha) & 0 \\ 0 & -\frac{\sqrt{3}\sin^2(\alpha)}{2} & \frac{\sqrt{3}\sin(2\alpha)}{2} & 0 & \frac{3\cos(2\alpha)}{4} + \frac{1}{4} \end{pmatrix}, \tag{2.127}$$

$$\underline{\underline{d}}^2_{\mathrm{X}\boldsymbol{D}^2} = \begin{pmatrix} \cos(\alpha) & 0 & -\sin(\alpha) & 0 & 0 \\ 0 & \frac{\cos^2(\alpha)}{2} + \frac{1}{2} & 0 & -\frac{\sin(2\alpha)}{2} & \frac{\sqrt{3}(1-\cos(2\alpha))}{4} \\ \sin(\alpha) & 0 & \cos(\alpha) & 0 & 0 \\ 0 & \frac{\sin(2\alpha)}{2} & 0 & \frac{\cos^2(\alpha)}{2} + \frac{3\cos(2\alpha)}{4} - \frac{1}{4} & -\frac{\sqrt{3}\sin(2\alpha)}{2} \\ 0 & \frac{\sqrt{3}(1-\cos(2\alpha))}{4} & 0 & \frac{\sqrt{3}\sin(2\alpha)}{2} & \frac{\cos^2(\alpha)}{2} + \frac{\cos(2\alpha)}{2} \end{pmatrix}, \tag{2.128}$$

from which the usual ZXZ or ZYZ Euler conventions can be assembled. The full rotation $\underline{\underline{R}}$ of Sym[2] is

$$\underline{\underline{R}} = \begin{pmatrix} \underline{\underline{d}}^0_{\mathrm{ZXZ}D^0} & 0 \\ 0 & \underline{\underline{d}}^2_{\mathrm{ZXZ}\boldsymbol{D}^2} \end{pmatrix} \text{ with } d^0_{\mathrm{ZXZ}} = 1. \tag{2.129}$$

Even for the full three-angle rotation, the block matrix structure of $\underline{\underline{R}}$ remains. This sparsity simplifies calculations particularly in a theoretical context. For example, the effect of a rotation on a cubic stiffness is evident in this form: the compression modulus of a cubic single-crystal is rotation-invariant.

2.2.5 Fourier series on $SO(3)$

Due to its relation to $SO(3)$, the harmonic basis can be used to provide a basis of (square-integrable) functions on $SO(3)$. If we restrict ourselves to square-integrable functions on $SO(3)$ which are positive

$$f : SO(3) \to \mathbb{R}_{\geq 0}, \tag{2.130}$$

and normalized

$$\int_{SO(3)} f(Q)\,\mathrm{d}V(Q) = 1, \tag{2.131}$$

the function f can be understood as a probability distribution. In particular, it can be used to model an orientation distribution function (ODF) to describe the geometrical properties of polycrystalline materials. Well-established applications include the calculation of effective stiffnesses (e.g. Böhlke and Bertram (2001)) and plasticity (e.g. Man and Huang (2001)).

We assume f to be square-integrable. By choosing a basis of the space of square-integrable functions, f can be described with a series of coefficients relative to this basis, cf. Bunge (1965). A coordinate-independent series expansion is possible by using tensorial coefficients (Adams et al., 1992). Lobos Fernández and Böhlke (2019) define these tensors as general deviatoric basis tensors $\boldsymbol{H}_{\langle n \rangle}$ equivalent to our $\mathbb{D}^n$, but do not choose a specific basis. Building on those results, Man and Du (2022) have chosen the complexified eigentensor bases which we refer to in this work as $\mathbb{E}^n$, which leads to complexified texture coefficients. We instead remain in a real tensor space by using the deviatoric bases $\mathbb{D}^n$, and write the i-th texture coefficient of order n as

$$\mathbb{V}_i^n = \int_{SO(3)} f(Q) Q(\mathbb{D}_i^n)\,\mathrm{d}V(Q). \tag{2.132}$$

The series description of f follows as

$$f(Q) = \sum_{n=0}^{\infty} \sum_{i=0}^{2n+1} (2n+1) \mathbb{V}_i^n \cdot Q(\mathbb{D}_i^n). \tag{2.133}$$

In mechanics of polycrystalline materials, a common expression is the expectation value of an orientation-dependent tensor $\boldsymbol{Q} \star \mathbb{A}_0^n$, which may be computed as an $SO(3)$ average weighted by f. Using the harmonic basis,

$$\begin{aligned} &\int_{SO(3)} f(Q) \boldsymbol{Q} \star \mathbb{A}_0^n \, \mathrm{d}V(Q) \\ &= \int_{SO(3)} f(Q) \boldsymbol{Q} \star \sum_{i=1}^{n_{\mathcal{H}}(\mathcal{V}^n)} \sum_{j=1}^{2k+1} A_{h(i,j)} \mathbb{P}\left(\mathcal{H}_i, k\right) [\mathbb{D}_j^k] \, \mathrm{d}V(Q). \end{aligned} \tag{2.134}$$

After rearranging the integral and using the isotropy of the inclusion tensors, Eq. (2.132) can be used to arrive at

$$\int_{SO(3)} f(Q) \boldsymbol{Q} \star \mathbb{A}_0^n \, \mathrm{d}V(Q) = \sum_{i=1}^{n_{\mathcal{H}}(\mathcal{V}^n)} \sum_{j=1}^{2k+1} A_{h(i,j)} \mathbb{P}\left(\mathcal{H}_i, k\right) [\mathbb{V}_j^k]. \tag{2.135}$$

We note that the harmonic basis components $A_{h(i,j)}$ are directly reflected in the calculation of these expectation values.

2.2.6 Computational effort of tensor rotations

In practice, dealing with Fourier series of $SO(3)$ functions involves large numbers of rotations of high-order tensors. We therefore investigate the computational efficiency of rotations. Given a generally anisotropic n-th order tensor $\mathbb{A}^n$, calculating $\boldsymbol{Q} \star \mathbb{A}^n$ via the definition of the Rayleigh product in Eq. (2.46) requires n multiplications of a 3×3 matrix with a $3^{\times n}$ component array. This resolves to $3^{n-1}n$ matrix-vector products

with 9 floating-point multiplications each, or $3^{n+1}n$ floating-point multiplications. If we instead use the n-th order harmonic basis, we write $\boldsymbol{Q}^{\star n}$ as a $3^n \times 3^n$ matrix. Crucially, this matrix is sparse, comprising copies of d^k_{ZXZ}-matrices up to order $k = n$, where each matrix has size $(2k+1) \times (2k+1)$. We may ignore d-matrices of order 0. The total number of floating-point multiplications resolves to

$$\sum_{k=1}^{n} a(n,k)(2k+1)^2, \tag{2.136}$$

where $a(n,k)$ is the number of $2k+1$-dimensional harmonic subspaces of order n. Because the dimensions of all harmonic subspaces must add up to the dimension of the original tensor space,

$$\sum_{k=0}^{n} a(n,k)(2k+1) = 3^n. \tag{2.137}$$

Therefore, an upper bound for the total number of floating-point multiplications is

$$\begin{aligned}\sum_{k=1}^{n} a(n,k)(2k+1)^2 &\leq \sum_{k=1}^{n} a(n,k)(2k+1)(2n+1) \\ &= (2n+1)3^n. \end{aligned} \tag{2.138}$$

Notably, these are fewer than $3^{n+1}n$ for $n > 1$. When considering total computational effort, floating point additions are roughly as expensive as floating point multiplications. While the number of floating point additions increases with matrix size and is therefore potentially higher when using the harmonic approach, the harmonic approach is still less expensive in total. When the tensor to be rotated has index symmetries, the computational expense of a harmonic rotation can be reduced further, as fewer harmonic subspaces are involved, whereas index symmetries are generally difficult to incorporate into the standard

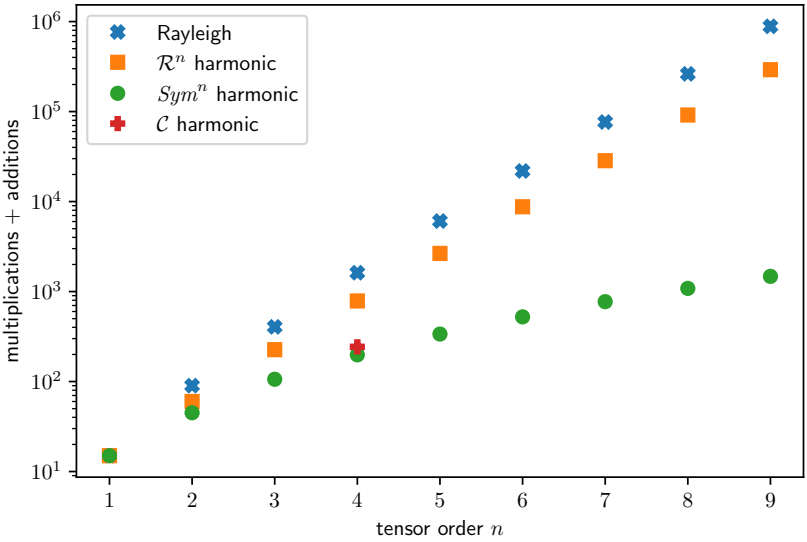

Figure 2.3: Number of additions and multiplications involved in rotations of n-th order tensors by using the tensorial Rayleigh product or using a harmonic basis for the spaces $\mathcal{R}^n$, Sym$[n]$ and $\mathcal{C}$. Figure based on Figure 4 of Krause and Böhlke (2024).

definition of the Rayleigh product. A visualization of exact values is given in Fig. 2.3. While the harmonic basis rotation is generally faster than a naive Rayleigh product, it requires more space, as n matrices of size $(2k+1) \times (2k+1)$ need to be stored as opposed to one 3×3 matrix. Non-harmonic tensorial bases generally require fully occupied $3^n \times 3^n$ rotation matrices, greatly increasing the computational cost compared to even the Rayleigh product.

If the rotations in question are always applied to a given reference state, as is common for orientations of single crystals in a polycrystal, it is also possible to implement material symmetries to reduce the computational effort further. As is well known in the texture analysis community, material symmetries reduce the number of tensorial texture coefficients involved in a texture description, cf. Lobos Fernández and Böhlke

(2019). Equivalently, one might say that material symmetries reduce the $2n+1$-dimensional deviatoric space $\mathcal{D}^n$ to a k-dimensional symmetric subspace. This subspace is however not invariant under arbitrary rotations; for example, the one-dimensional transversal isotropic subspace may change its axis of symmetry under rotations which are not aligned to that axis. Let $\mathbb{T}^n_j$ with $j = [1, k]$ denote the n-th order texture coefficient of a materially symmetric single crystal in a reference orientation. Using Eq. (2.129), the rotation tensor may be implemented as a $(2n+1) \times k$ matrix given by

$$Q_{ij} = \boldsymbol{Q}^{\star n} \cdot \left(\mathbb{D}^n_i \otimes \mathbb{T}^n_j\right) = d^n_{\mathrm{ZXZ}il} \mathbb{D}^n_l \cdot \mathbb{T}^n_j. \tag{2.139}$$

Applying Q_{ij} to orient a $\mathcal{D}^n$ tensor given in the reference orientation involves $(2n+1)k$ multiplications and $(2n+1)(k-1)$ additions.

For example, fiber orientation tensors are both fully index symmetric and transversal isotropic. In the reference orientation aligned with $\boldsymbol{e}_3$, the only transversally isotropic tensor of the n-th order deviatoric subspace is given by

$$\mathbb{T}^n_0 = \mathbb{D}^n_{2n+1}. \tag{2.140}$$

Correspondingly, rotating a transversally isotropic n-th order tensor such as a fiber material property from a reference configuration by individually rotating all third-kind orientation tensors up to n-th order requires no additions and only

$$\sum_{l=1}^{n} 2l + 1 = n^2 + 2n \tag{2.141}$$

multiplications. We summarize that rotating high-order tensors in the harmonic basis is computationally efficient compared to a naive Rayleigh product implementation in the general case, and increasingly specialized rotation implementations can be found for both index- and material symmetries, further increasing the efficiency.

Chapter 3

Introduction to continuum mechanics

3.1 Small-Strain continuum mechanics

3.1.1 Kinematics

This section gives a short derivation of the kinematics required in linear elastic continuum mechanics. A more detailed account can be found in Marsden and Hughes (1994), chapter 1.

Continuum mechanics is the study of the deformation of continuous bodies. *Continuous* means that for any two material points $\mathfrak{p}$ within the body, another point can be found which lies between them, a notion which can be formalized by treating the body as a topological manifold, see, e.g., Jänich (2013). The core element of continuum mechanics is therefore the body manifold $\mathfrak{B}$, a 3D manifold with boundary. We will restrict ourselves to cases where $\mathfrak{B}$ is simply connected and remains so during all mechanical processes we consider, meaning that there are no pores, cracks or holes. Furthermore, only those body manifolds are considered which can be *embedded* into a 3D vector space via a map

$$M : \mathfrak{B} \to \mathcal{R}, \tag{3.1}$$

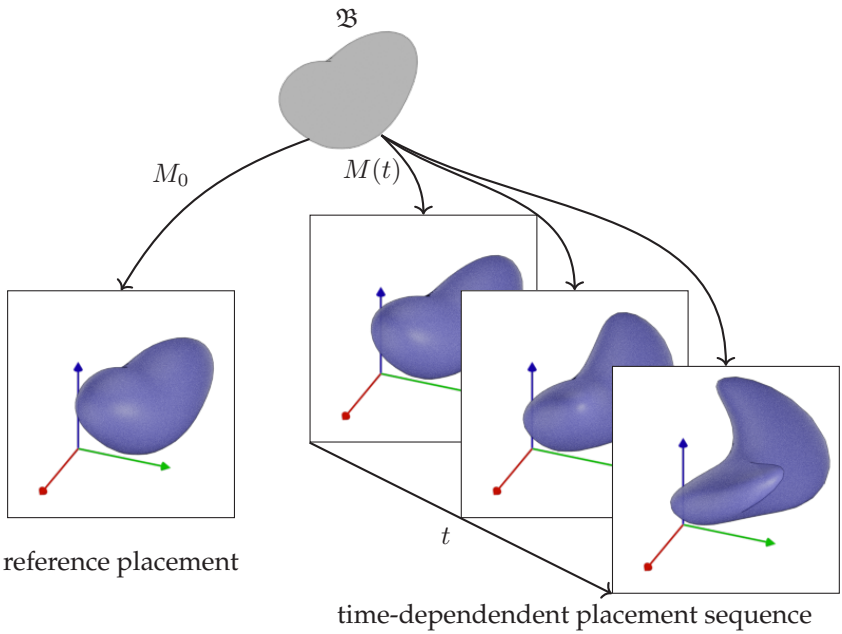

Figure 3.1: Body manifold and various placements.

which is bijective and continuous and called a *placement* in continuum mechanics. A kinematically consistent deformation of a body is described by a continuously differentiable time sequence of placements as depicted in Fig. 3.1. Physical effects of the deformation on the body are caused by changes of volume or shape, which are locally described by a metric tensor on the body manifold. This deformation tensor is the canonical metric of $\mathcal{R}$ pulled back onto the manifold, which essentially describes how the body must be locally squashed or stretched to fit into Euclidean space via the mapping. For a rigorous formalization of this notion, see Marsden and Hughes (1994), chapter 1, eq. 4.13.

Working with the body manifold directly is possible, but cumbersome, which is why a *reference placement* is generally used, see Liu (2002),

section 1.1. The usual approach is to define an undeformed placement of the body M_0 relative to which all other placements are described. The transformation of positions between the undeformed placement and the placement at time t is

$$\boldsymbol{x}(t) = M^{-1}(M_0(\boldsymbol{X}), t) =: \boldsymbol{\chi}(\boldsymbol{X}, t), \quad \boldsymbol{X} \in M_0(\mathfrak{B}). \tag{3.2}$$

Transformations of a placement which do not change the induced metric are called *rigid body transformations* and can be parameterized as

$$T(\boldsymbol{x}) = \boldsymbol{Q}\boldsymbol{x} + \boldsymbol{c}, \tag{3.3}$$

with an orthogonal tensor $\boldsymbol{Q}$ and a vector $\boldsymbol{c}$. By the assumption that effects described as material behavior are caused by changes of the induced metric, it follows that a rigid body transformation should not cause material effects, a principle which is known as *frame indifference* (Marsden and Hughes, 1994). Frame indifference is defined for time-dependent rigid body transformations which do not cause additional accelerations, with which the entire deformation history of the body is transformed. In the framework introduced here, the reference placement is not part of the deformation history and is not transformed. Formally, for any material function $f(\mathfrak{p})$ defined on $\mathfrak{B}$, frame indifference requires that

$$f\left(M^{-1}(\boldsymbol{x})\right) = f\left(M^{-1}\left(T(\boldsymbol{x})\right)\right). \tag{3.4}$$

This principle is also called *material objectivity*, compare Liu (2002), section 3.2. To fulfill Eq. (3.4), it is necessary to describe the deformation by objective terms, which, for tensorial terms in the reference placement, is equivalent to invariance under rigid body transformations. A Taylor series expansion of $\boldsymbol{\chi}$ up to first order yields

$$\boldsymbol{\chi}(\boldsymbol{X}) \approx \boldsymbol{\chi}(\boldsymbol{X}_0) + \frac{\partial \boldsymbol{\chi}}{\partial \boldsymbol{X}}(\boldsymbol{X} - \boldsymbol{X}_0), \tag{3.5}$$

of which only the second term which involves the deformation gradient

$$\boldsymbol{F} = \frac{\partial \boldsymbol{\chi}}{\partial \boldsymbol{X}}, \tag{3.6}$$

is invariant to translations. The rotation-dependent term can be factored out via the polar decomposition

$$\boldsymbol{F} = \boldsymbol{R}\boldsymbol{U}, \quad \boldsymbol{R} \in SO(3), \tag{3.7}$$

which can be used to prove that the *right Cauchy-Green tensor*

$$\boldsymbol{C} = \boldsymbol{F}^{\mathsf{T}}\boldsymbol{F} = \boldsymbol{U}^{\mathsf{T}}\boldsymbol{U} \tag{3.8}$$

is rotation-independent and therefore an objective quantity. A number of *strain* measures can be introduced, of which we use the *Green St.-Venant strain*

$$\boldsymbol{E}_{\mathrm{G}} = \frac{1}{2}(\boldsymbol{C} - \boldsymbol{I}) \tag{3.9}$$

as an example. According to Seth (1964) and Hill (1968), other objective strain measures exist, but the choice of strain measure is not relevant if the deformations are sufficiently small, i.e., $\boldsymbol{F}$ is close to $\boldsymbol{I}$. In the limit of small deformations, any strain measure tends to

$$\boldsymbol{\varepsilon} = \operatorname{sym}\left(\frac{\partial \boldsymbol{u}}{\partial \boldsymbol{X}}\right) \tag{3.10}$$

with the *displacement*

$$\boldsymbol{u} = \boldsymbol{x} - \boldsymbol{X}. \tag{3.11}$$

A strain field is *kinematically compatible* if it is integrable to a continuous displacement field.

Owing to the different placements, there are two ways to define time derivatives. *Spatial* time derivatives, which are partial derivatives with

respect to the current position $\boldsymbol{x}$, are written

$$\frac{\partial \square}{\partial t} := \left.\frac{\partial \square}{\partial t}\right|_{\boldsymbol{x}=\text{const.}}. \tag{3.12}$$

Material time derivatives, which are calculated on the body manifold itself, or, equivalently, on the reference placement, are partial derivatives with respect to $\boldsymbol{X}$ and are written

$$\dot{\square} := \left.\frac{\partial \square}{\partial t}\right|_{\boldsymbol{X}=\text{const.}}. \tag{3.13}$$

The *velocity* of a material point is

$$\boldsymbol{v} = \boldsymbol{v} = \dot{\boldsymbol{u}}. \tag{3.14}$$

3.1.2 Balance equations

Physical laws are described here from the point of view of the balance equation formalism, a modern description of which is found in Liu (2002). The balance equation formalism rests on general integral-differential relationships to which various physical assumptions are applied. Over a volume V, a volume density ψ has the total value

$$\int_V \psi \,\mathrm{d}V. \tag{3.15}$$

The change of the total value consists of the *flux* $\boldsymbol{q}$, which consists of transmitted quantities of ψ through the boundary ∂V; the *supply* s, which describes changes in ψ stemming from the interaction with other fields; and the *production* p, which consists of internally caused changes of ψ. As a formula,

$$\frac{\mathrm{d}}{\mathrm{d}t}\int_V \psi \,\mathrm{d}V = \int_V s + p \,\mathrm{d}V + \int_{\partial V} \boldsymbol{q}\cdot\boldsymbol{n}\,\mathrm{d}A, \tag{3.16}$$

where A is the infinitesimal area element of ∂V and $\boldsymbol{n}$ its normal vector. The scalar fields s and p, which are not differentiated by Liu (2002), but by others such as Papenfuß (2020), differ only in their physical meaning. Since s is caused by interaction with other fields and $\boldsymbol{q}$ by interaction with other volumes, for a volume in isolation,

$$\frac{\partial}{\partial t}\int_V \psi \,\mathrm{d}V = \int_V p \,\mathrm{d}V. \tag{3.17}$$

For an isolated volume, the left-hand side is zero for *conserved* quantities, which implies that p is generally zero for conserved quantities.

Before evaluating the balance equations for particular physical quantities, some general results can be derived. First, by the transport theorem as described by Liu (2002), section 2.1.1, the change in the volume integral can be decomposed into an internal change and the change of the volume itself, reading

$$\frac{\mathrm{d}}{\mathrm{d}t}\int_V \psi \,\mathrm{d}V = \int_V \frac{\partial}{\partial t}\psi \,\mathrm{d}V + \int_{\partial V} \psi v_\perp \,\mathrm{d}A, \tag{3.18}$$

where $v_\perp$ is the normal speed of the surface of the volume. If the volume is material, i.e.,

$$M^{-1}(V,t) = \text{const.}, \tag{3.19}$$

the normal surface speed is given by the normal component of the speed of material points,

$$v_\perp = \boldsymbol{v}\cdot\boldsymbol{n}. \tag{3.20}$$

Surface integrals can be transformed by using the divergence theorem

$$\int_{\partial V} \boldsymbol{a}\cdot\boldsymbol{n}\,\mathrm{d}A = \int_V \mathrm{div}\,(\boldsymbol{a})\;\mathrm{d}V. \tag{3.21}$$

Applying both theorems to the general balance equation for a material volume leads to

$$\int_V \frac{\partial \psi}{\partial t} \, \mathrm{d}V = \int_V s + p + \operatorname{div}(\boldsymbol{q}) - \operatorname{div}(\psi \boldsymbol{v}) \, \mathrm{d}V, \tag{3.22}$$

which, as it needs to hold for an arbitrary volume V, is equivalent to the *differential balance equation*

$$\frac{\partial \psi}{\partial t} = s + p + \operatorname{div}(\boldsymbol{q}) - \operatorname{div}(\psi \boldsymbol{v}) \,. \tag{3.23}$$

The above derivation of the differential balance equation assumes a volume consisting of *regular* points, which are those in which ψ is smooth. Along a *singular* surface, the values of ψ in the limit taken from either side are different, denoted ψ^+ and ψ^-, and their *jump* is defined as

$$[\![\psi]\!] = \psi^+ - \psi^- . \tag{3.24}$$

As shown by Liu (2002), section 2.1.1, in a singular point, the general balance equation reduces to the *jump condition*

$$[\![\psi(\boldsymbol{v} \cdot \boldsymbol{n} - u_n)]\!] + [\![\boldsymbol{q} \cdot \boldsymbol{n}]\!] = 0, \tag{3.25}$$

in which u_n is the normal velocity of the singular surface. If the singular surface moves with the material, which is the case considered in this manuscript, the first term becomes zero.

The balance equations are generally applied to conserved quantities. A rigorous approach to proving which quantities are conserved in the general case is based on postulating an action functional, which in classical mechanics is the Lagrangian, and applying the principle of frame indifference using Noether's theorems, see Hanc et al. (2004) for an introductory treatment. We instead directly postulate that mass density, energy density, momentum density and angular momentum

density are conserved quantities. In addition to these quantities, Liu (2002) considers the balance of the entropy density η, often associated with temperature, which can be generally understood as a statistical measure of the number of microscopic realizations of a given state, see Greven et al. (2014). The entropy density is not a conserved quantity, but in a closed system, it is statistically overwhelmingly likely to only increase, such that $p_\eta \geq 0$, which leads to a balance of entropy.

In the following, the balance equations required for small deformations of purely mechanical material models will be described. The mass density ρ is a conserved quantity without interaction with other fields and without a flux. Thus,

$$\frac{\partial \rho}{\partial t} = -\operatorname{div}(\rho \boldsymbol{v}), \tag{3.26}$$

or equivalently

$$\dot{\rho} = 0, \tag{3.27}$$

meaning that the mass density associated with a given material point does not change.

Singular density surfaces occur at the interface between materials with different densities. These singular surfaces move with the material by definition, and since $\boldsymbol{q} = \boldsymbol{0}$, the jump condition is always fulfilled for the balance of mass.

The linear momentum density is given by

$$\boldsymbol{p} = \rho \boldsymbol{v}. \tag{3.28}$$

According to Newton's first law, changes in linear momentum are caused by the application of a force. Thus, the supply $p_{\boldsymbol{q}}$ is given by volume force densities $\boldsymbol{b}$ resulting from other fields, such as gravity. The flux $\boldsymbol{q}_{\boldsymbol{p}}$ is related to area force densities acting on the boundary area, which can,

using Cauchy's lemma, be written as

$$\boldsymbol{t} = \boldsymbol{\sigma}\boldsymbol{n}, \tag{3.29}$$

where $\boldsymbol{\sigma}$ denotes the Cauchy stress, a second order tensor. As linear momentum is a conserved quantity, the balance of linear momentum in regular points results as

$$\frac{\partial \rho}{\partial t}\boldsymbol{v} = \boldsymbol{b} + \operatorname{div}(\boldsymbol{\sigma}) - \operatorname{div}(\rho \boldsymbol{v}). \tag{3.30}$$

Using the product rule on the left-hand side and the balance of mass,

$$\rho \ddot{\boldsymbol{x}} = \boldsymbol{b} + \operatorname{div}(\boldsymbol{\sigma}). \tag{3.31}$$

In this work, the only singular surfaces in the balance of linear momentum occur at the interface between two materials with different properties. As such, the singular surface is always material and the jump condition reads

$$[\![\boldsymbol{\sigma}\boldsymbol{n}]\!] = \boldsymbol{0}. \tag{3.32}$$

In the purely mechanical case, energy volume density follows from linear momentum density by

$$w = \frac{1}{2}\rho \boldsymbol{v} \cdot \boldsymbol{v}, \tag{3.33}$$

and after some calculation, the balance of energy follows from the balances of linear momentum and mass, and does not need to be considered separately. Similarly, due to the kinematic assumption that material points only have positions, not orientations, the balance of angular momentum can be simplified using existing balances until the only term that remains is

$$\boldsymbol{\sigma}^{\mathsf{T}} = \boldsymbol{\sigma}, \tag{3.34}$$

an algebraic condition which is fulfilled if $\boldsymbol{\sigma}$ is symmetric. A detailed derivation is given by Liu (2002), section 2.3.3. The only remaining balance equation is the balance of entropy, which will not be evaluated, as we do not consider temperature fields or systems with a large number of implicit microstates.

In the following, we will only consider the *static* case, in which the body is at rest. As a result, velocities generally vanish. The static balance of linear momentum reduces to

$$\operatorname{div}(\boldsymbol{\sigma}) + \boldsymbol{b} = \mathbf{0}. \tag{3.35}$$

3.1.3 Material laws

To formulate the balance of linear momentum as a differential equation in the displacement field, a relationship between stresses and strains must be established. On the level of atomistic mechanics, stresses are linked with strains through interatomic potentials, which are in theory determined by quantum mechanics. As continuum mechanics does not contain explicit models of interatomic interactions, the relationship between stresses and strains is considered via empirical *material models*, but many theoretical restrictions apply which constrain the possible options for models.

We consider only materials which are *hyperelastic*. As defined by, e.g., Marsden and Hughes (1994), this means that there exists an elastic potential $w(\boldsymbol{\varepsilon})$, a scalar function of Sym which determines the stress-strain relationship through

$$\boldsymbol{\sigma} = \frac{\partial w}{\partial \boldsymbol{\varepsilon}}. \tag{3.36}$$

Hyperelasticity implies that the behavior of the material does not depend on its prior history and that the stress field is conservative. The hyperelastic stress-strain relationship can be linearized via a truncated

Taylor series, leading to

$$\boldsymbol{\sigma}(\boldsymbol{\varepsilon}) \approx \frac{\partial w}{\partial \boldsymbol{\varepsilon}}(\boldsymbol{E}) + \frac{\partial^2 w}{\partial \boldsymbol{\varepsilon}^2}(\boldsymbol{E})[\boldsymbol{\varepsilon} - \boldsymbol{E}]. \tag{3.37}$$

Choosing $\boldsymbol{E}$ to be the stress-free strain of the material, also called *eigenstrain*, and designating the second strain gradient of w as the stiffness tensor $\mathbb{C}$ leads to

$$\boldsymbol{\sigma} \approx \mathbb{C}[\boldsymbol{\varepsilon} - \boldsymbol{E}]. \tag{3.38}$$

For many materials, the above relationship is exact for any strain $\boldsymbol{\varepsilon}$ which is small enough to lead to a purely elastic response. These *affine linear elastic* materials have an elastic potential of the form

$$\begin{aligned} w &= \int_{\boldsymbol{E}}^{\boldsymbol{\varepsilon}} \boldsymbol{\sigma}(\tilde{\boldsymbol{\varepsilon}}) \cdot \mathrm{d}\tilde{\boldsymbol{\varepsilon}} \\ &= \frac{1}{2}(\boldsymbol{\varepsilon} - \boldsymbol{E}) \cdot \mathbb{C}[\boldsymbol{\varepsilon} - \boldsymbol{E}]. \end{aligned} \tag{3.39}$$

Materials with a vanishing stress-free strain are *linear elastic*.

The eigenstrain and stiffness tensor are treated as material parameters which are constant over time but spatially heterogeneous in general. The eigenstrain $\boldsymbol{E}$ is a second-order symmetric tensor field which, unlike the strain field, is not necessarily the gradient of a vector field, and is therefore not always kinematically compatible. If a body with non-compatible eigenstrains were stress-free at every point, the strain field would equal the eigenstrain field, such that there is no consistent displacement field anymore. As such, for affine linear elastic materials with incompatible eigenstrains, there is no state which is entirely free of internal stresses. Physical causes of incompatible eigenstrain fields include thermal expansion, prior plastic deformations, or phase transitions, among other possibilities.

The stiffness tensor is a fourth-order tensor. Because the stiffness tensor is defined via a second gradient, due to Schwarz's theorem, it is a

symmetric linear map from Sym to Sym, i.e., an element of $\mathcal{C}$. For the elastic potential to be positive, it is also required that $\mathbb{C}$ is positive definite in the sense of

$$\boldsymbol{\varepsilon} \cdot \mathbb{C}[\boldsymbol{\varepsilon}] > 0 \quad \forall \boldsymbol{\varepsilon}, \|\boldsymbol{\varepsilon}\| > 0. \tag{3.40}$$

If $\mathbb{C}$ were only positive semi-definite, the value of $\boldsymbol{\varepsilon}$ could not be uniquely determined from a given $\boldsymbol{\sigma}$. Only materials with a positive definite $\mathbb{C}$ will be considered in the following.

Substituting the material law and the kinematic relations into the balance of linear momentum leads to the Navier-Lamé equation

$$\operatorname{div}\left(\mathbb{C}[\operatorname{sym}\left(\operatorname{grad}\left(\boldsymbol{u}\right)\right) - \boldsymbol{E}]\right) + \boldsymbol{b} = 0. \tag{3.41}$$

In the general affine-linear elastic continuum mechanics problem, the Navier-Lamé equation is evaluated on the material volume $B = M(\mathfrak{B})$ with boundary conditions on the boundary $\partial B = M(\partial\mathfrak{B})$. The boundary is disjunctively decomposed into a Dirichlet boundary ∂B_{D} and a Neumann boundary ∂B_{N} such that

$$\partial B = \partial B_{\mathrm{D}} \cup \partial B_{\mathrm{N}}. \tag{3.42}$$

The boundary conditions are defined as

$$\boldsymbol{u}(\boldsymbol{x}) = \boldsymbol{u}_{\mathrm{D}}(\boldsymbol{x}) \quad \forall \boldsymbol{x} \in \partial B_{\mathrm{D}}, \tag{3.43}$$

$$\boldsymbol{\sigma}(\boldsymbol{x})\boldsymbol{n}(\boldsymbol{x}) = \boldsymbol{t}_{\mathrm{N}}(\boldsymbol{x}) \quad \forall \boldsymbol{x} \in \partial B_{\mathrm{N}}. \tag{3.44}$$

3.1.4 Material symmetries

A spatial symmetry group is a set of spatial transformations which can be applied to tensorial quantities such as positions, stresses and strains. In the context of material symmetry, rotational symmetries $S \subseteq SO(3)$ are of particular interest. The action of a rotation on tensorial quantities

is, as in the case $S = SO(3)$, calculated via the Rayleigh product of Eq. (2.46). A hyperelastic material is S-symmetric if its elastic potential w is invariant to S,

$$w(\boldsymbol{\varepsilon}) = w(\boldsymbol{Q} \star \boldsymbol{\varepsilon}) \quad \forall \boldsymbol{Q} \in S. \tag{3.45}$$

For affine linear elastic materials, this is equivalent to symmetry of both material properties,

$$\boldsymbol{Q} \star \mathbb{C} = \mathbb{C}, \quad \boldsymbol{Q} \star \boldsymbol{E} = \boldsymbol{E}, \quad \forall \boldsymbol{Q} \in S. \tag{3.46}$$

Because symmetries of tensors are conserved under addition and scalar multiplication, symmetric tensors form subspaces. The projector to the n-th order symmetric subspace associated with a finite symmetry group S is given by

$$\mathbb{P}_S^{2n} = \frac{1}{n(S)} \sum_{i=1}^{n(S)} \boldsymbol{Q}_i^{\times n}, \tag{3.47}$$

while the equivalent relation for an infinite symmetry group is given by

$$\mathbb{P}_S^{2n} = \int_S \boldsymbol{Q}_i^{\times n} \, \mathrm{d}V(S). \tag{3.48}$$

With the symmetric projector, S-symmetry of an n-th order tensor $\mathbb{V}^n$ can be reduced to the algebraic condition

$$\mathbb{P}_S^{2n}[\mathbb{V}^n] = \mathbb{V}^n. \tag{3.49}$$

For linear elastic materials, the necessary and sufficient conditions for material symmetry are given by

$$\mathbb{P}_S^8[\mathbb{C}] = \mathbb{C}, \quad \mathbb{P}_S^4[\boldsymbol{E}] = \boldsymbol{E}. \tag{3.50}$$

Crystal system	I	C	orth	H	trig	tetr	mono
Symmetry group	SO(3)	$\mathcal{O}$	D_2	$O(2)$	D_3	D_4	Z_2

Table 3.1: Symmetry group equivalence classes according to Forte and Vianello (1996) associated with crystal systems.

Restricting the symmetry requirement to tensors of up to fourth order causes many potential symmetry groups to be equivalent. As shown by Forte and Vianello (1996), aside from full anisotropy, seven equivalence classes of symmetry groups need to be considered. In the following, these equivalence classes will be named after the crystal systems which they describe, as listed in Table 3.1. For the purpose of this discussion, the set of crystal systems will include isotropy even though there is no isotropic regular lattice. The harmonic basis depiction of symmetric stiffnesses shown below are based on Krause and Böhlke (2024).

Isotropic materials are invariant under all rotations. The stiffness is given by

$$\mathbb{C}^{\mathrm{I}} = 3K\mathbb{P}^{\circ} + 2G\mathbb{P}' \tag{3.51}$$

with the compression modulus K and the shear modulus G. In the second-order symmetric harmonic basis, the isotropic stiffness is given by

$$\underline{\underline{C}}^{\mathrm{I}} = \begin{pmatrix} 3K & 0 & 0 & 0 & 0 & 0 \\ 0 & 2G & 0 & 0 & 0 & 0 \\ 0 & 0 & 2G & 0 & 0 & 0 \\ 0 & 0 & 0 & 2G & 0 & 0 \\ 0 & 0 & 0 & 0 & 2G & 0 \\ 0 & 0 & 0 & 0 & 0 & 2G \end{pmatrix} \tag{3.52}$$

$$= \operatorname{diag}(3K, 2G, 2G, 2G, 2G, 2G)\,, \tag{3.53}$$

where diag $(\square)$ is a shorthand description of a diagonal matrix by its diagonal entries.

For cubic materials, an explicit projector decomposition is given by

$$\mathbb{C}^{\mathrm{C}} = \lambda_1^{\mathrm{C}}\mathbb{P}_1^{\mathrm{C}} + \lambda_2^{\mathrm{C}}\mathbb{P}_2^{\mathrm{C}} + \lambda_3^{\mathrm{C}}\mathbb{P}_3^{\mathrm{C}}. \tag{3.54}$$

The cubic projectors of a cubic crystal which is aligned with the harmonic basis axis $\boldsymbol{e}_3$ are given by

$$\underline{\underline{P}}_1^{\mathrm{C}} = \mathrm{diag}\,(1,0,0,0,0,0)\,, \tag{3.55}$$

$$\underline{\underline{P}}_2^{\mathrm{C}} = \mathrm{diag}\,(0,1,0,0,0,1)\,, \tag{3.56}$$

$$\underline{\underline{P}}_3^{\mathrm{C}} = \mathrm{diag}\,(0,0,1,1,1,0)\,. \tag{3.57}$$

For transversal-isotropic or hexagonal stiffness tensors whose symmetry axis is aligned with $\boldsymbol{e}_3$,

$$\underline{\underline{C}}^{\mathrm{H}} = \begin{pmatrix} C_{11}^{\mathrm{H}} & 0 & 0 & 0 & 0 & C_{16}^{\mathrm{H}} \\ 0 & C_{22}^{\mathrm{H}} & 0 & 0 & 0 & 0 \\ 0 & 0 & C_{22}^{\mathrm{H}} & 0 & 0 & 0 \\ 0 & 0 & 0 & 2C_{2323} & 0 & 0 \\ 0 & 0 & 0 & 0 & 2C_{2323} & 0 \\ C_{16}^{\mathrm{H}} & 0 & 0 & 0 & 0 & C_{66}^{\mathrm{H}} \end{pmatrix}. \tag{3.58}$$

with

$$C_{11}^{\mathrm{H}} = \frac{1}{3}\left(2C_{1111} + 2C_{1122} + 4C_{1133} + C_{3333}\right), \tag{3.59}$$

$$C_{22}^{\mathrm{H}} = C_{1111} - C_{1122} \tag{3.60}$$

$$C_{66}^{\mathrm{H}} = \frac{\sqrt{2}}{3}\left(-C_{1111} - C_{1122} + C_{1133} + C_{3333}\right), \tag{3.61}$$

$$C_{16}^{\mathrm{H}} = \frac{1}{3}\left(C_{1111} + C_{1122} - 4C_{1133} + 2C_{3333}\right). \tag{3.62}$$

The tetragonal stiffness reads

$$\underline{\underline{C}}^{\text{tetr}} = \begin{pmatrix} C_{11}^{\text{H}} & 0 & 0 & 0 & 0 & C_{16}^{\text{H}} \\ 0 & C_{22}^{\text{H}} & 0 & 0 & 0 & 0 \\ 0 & 0 & 2C_{1212} & 0 & 0 & 0 \\ 0 & 0 & 0 & 2C_{2323} & 0 & 0 \\ 0 & 0 & 0 & 0 & 2C_{2323} & 0 \\ C_{16}^{\text{H}} & 0 & 0 & 0 & 0 & C_{66}^{\text{H}} \end{pmatrix} \tag{3.63}$$

and the trigonal stiffness

$$\underline{\underline{C}}^{\text{trig}} = \begin{pmatrix} C_{11}^{\text{H}} & 0 & 0 & 0 & 0 & C_{16}^{\text{H}} \\ 0 & C_{22}^{\text{H}} & 0 & 0 & 2C_{1123} & 0 \\ 0 & 0 & C_{22}^{\text{H}} & 2C_{1123} & 0 & 0 \\ 0 & 0 & 2C_{1123} & 2C_{2323} & 0 & 0 \\ 0 & 2C_{1123} & 0 & 0 & 2C_{2323} & 0 \\ C_{16}^{\text{H}} & 0 & 0 & 0 & 0 & C_{66}^{\text{H}} \end{pmatrix}. \tag{3.64}$$

We write the orthotropic stiffness as

$$\underline{\underline{C}}^{\text{orth}} = \begin{pmatrix} C_{11}^{\text{orth}} & C_{12}^{\text{orth}} & 0 & 0 & 0 & C_{16}^{\text{orth}} \\ C_{12}^{\text{orth}} & C_{22}^{\text{orth}} & 0 & 0 & 0 & C_{26}^{\text{orth}} \\ 0 & 0 & 2C_{1212} & 0 & 0 & 0 \\ 0 & 0 & 0 & 2C_{1313} & 0 & 0 \\ 0 & 0 & 0 & 0 & 2C_{2323} & 0 \\ C_{16}^{\text{orth}} & C_{26}^{\text{orth}} & 0 & 0 & 0 & C_{66}^{\text{orth}} \end{pmatrix}, \tag{3.65}$$

with the abbreviations

$$C_{11}^{\text{orth}} = \frac{1}{3}(C_{1111} + C_{2222} + C_{3333}) + \frac{2}{3}(C_{1122} + 2C_{1133} + 2C_{2233}), \tag{3.66}$$

$$C_{12}^{\text{orth}} = \frac{1}{\sqrt{6}}\left(C_{1111} + C_{1133} - C_{2222} - C_{2233}\right), \tag{3.67}$$

$$C_{22}^{\text{orth}} = \frac{C_{1111}}{2} - C_{1122} + \frac{C_{2222}}{2} \tag{3.68}$$

$$C_{16}^{\text{orth}} = \frac{1}{3\sqrt{2}}(2C_{3333} - C_{1111} - C_{2222} - 2C_{1122} + C_{1133} + C_{2233}), \tag{3.69}$$

$$C_{26}^{\text{orth}} = \frac{1}{2\sqrt{3}}\left(-C_{1111} + 2C_{1133} + C_{2222} - 2C_{2233}\right), \tag{3.70}$$

$$C_{66}^{\text{orth}} = \frac{1}{6}(C_{1111} + C_{2222} + 4C_{3333}) + \frac{1}{6}\left(\frac{C_{1122}}{3} - 4C_{1133} - 4C_{2233}\right). \tag{3.71}$$

Finally, the monoclinic symmetry is given by

$$\underline{\underline{C}}^{\text{mono}} = \begin{pmatrix} C_{11}^{\text{orth}} & C_{22}^{\text{orth}} & 0 & 0 & C_{15}^{\text{mono}} & C_{16}^{\text{orth}} \\ C_{12}^{\text{orth}} & C_{22}^{\text{orth}} & 0 & 0 & C_{15}^{\text{mono}} & C_{26}^{\text{orth}} \\ 0 & 0 & 2C_{1212} & 2C_{1312} & 0 & 0 \\ 0 & 0 & 2C_{1312} & 2C_{1313} & 0 & 0 \\ C_{15}^{\text{mono}} & C_{25}^{\text{mono}} & 0 & 0 & 2C_{2323} & C_{56}^{\text{mono}} \\ C_{16}^{\text{orth}} & C_{26}^{\text{orth}} & 0 & 0 & C_{56}^{\text{mono}} & C_{66}^{\text{orth}} \end{pmatrix}, \tag{3.72}$$

S	I, C	H, trig, tetr	orth	mono
$\underline{E}$	$\begin{pmatrix} E_1 \\ 0 \\ 0 \\ 0 \\ 0 \\ 0 \end{pmatrix}$	$\begin{pmatrix} E_1 \\ 0 \\ 0 \\ 0 \\ 0 \\ E_6 \end{pmatrix}$	$\begin{pmatrix} E_1 \\ E_2 \\ 0 \\ 0 \\ 0 \\ E_6 \end{pmatrix}$	$\begin{pmatrix} E_1 \\ E_2 \\ E_3 \\ 0 \\ 0 \\ E_6 \end{pmatrix}$

Table 3.2: Symmetric eigenstrain tensors in the aligned harmonic basis.

with

$$C_{15}^{\text{mono}} = \frac{\sqrt{6}\,(C_{1123} + C_{2223} + C_{3323})}{3}, \tag{3.73}$$

$$C_{15}^{\text{mono}} = C_{1123} - C_{2223} \tag{3.74}$$

$$C_{56}^{\text{mono}} = \frac{\sqrt{3}\,(-C_{1123} - C_{2223} + 2C_{3323})}{3}. \tag{3.75}$$

A detailed explanation of the advantages of the harmonic basis depiction of symmetric stiffness tensors compared with the more common Mandel basis depiction can be found in Krause and Böhlke (2024).

For an affine linear elastic material to be symmetric, the eigenstrain must also be symmetric. The harmonic basis depictions of symmetric eigenstrain tensors are given in Table 3.2. The monoclinic eigenstrain, like any symmetric second-order tensor, can be diagonalized such that only three non-zero values remain. However, while the monoclinic eigenstrain might appear orthotropic when diagonalized, it is still described by four independent material parameters, as the eigenvector decomposition calculated during diagonalization depends on the fourth material parameter. Therefore, we depict the harmonic basis form with four explicit parameters, the orientation of which is defined independently of the concrete material parameters by aligning $\boldsymbol{e}_3$ with the monoclinic symmetry axis.

3.2 Mean-Field methods

3.2.1 Stochastic microstructure description

Stochastic micromechanics is the study of materials with random heterogeneous structure significantly smaller than the part scale. A heterogeneous material with affine linear properties is fully described by the fields of material properties $\mathbb{C}(\boldsymbol{x}), \boldsymbol{E}(\boldsymbol{x})$. To achieve maximally general results, the geometry of the microstructure is described separately from the material properties. For composite materials, which are composed of a finite number of component materials, the chemical composition and material structure are piecewise constant, with each of the finite component materials comprising a *phase*. Following Torquato (2002), spatial fields of phase distribution are defined via *indicator functions*

$$I_\alpha(\boldsymbol{x}) = \begin{cases} 1 & \text{if phase } \alpha \text{ is at } \boldsymbol{x}, \\ 0 & \text{else.} \end{cases} \tag{3.76}$$

By definition, the indicator function is *idempotent*

$$I_\alpha(\boldsymbol{x})^n = I_\alpha(\boldsymbol{x}) \quad \forall n > 0. \tag{3.77}$$

If the microstructure is fully described by N indicator functions, this set of indicator functions is *complete*

$$\sum_{\alpha}^{N} I_\alpha(\boldsymbol{x}) = 1, \tag{3.78}$$

and because each material point belongs to only one phase, the indicator functions must be *biorthogonal*

$$I_\alpha(\boldsymbol{x}) I_\beta(\boldsymbol{x}) = 0 \quad \alpha \neq \beta. \tag{3.79}$$

In the definition above, the index α indicates a phase, not a set of material properties. While the stiffness field is constant for a given phase in most common applications, eigenstrain fields caused by prior plastic deformations are not. An extended definition of a phase could allow the modeling of continuous fields using $\alpha \in \mathbb{R}$. In all applications discussed here, we limit ourselves to thermally caused eigenstrain fields with homogeneous temperature fields, such that a phase always has constant material properties.

In the case of anisotropic component materials, in addition to the indicator functions, it is also necessary to specify the field of material orientations $\boldsymbol{Q}(\boldsymbol{x})$. Following Etingof and Adams (1993), we introduce the orientation indicator function $I_{\boldsymbol{Q}}(\boldsymbol{x})$. Because the number of possible values of $\boldsymbol{Q} \in SO(3)$ is infinite, the completeness condition is written

$$\int_{SO(3)} I_{\boldsymbol{Q}}(\boldsymbol{x}) \, \mathrm{d}V(\boldsymbol{Q}) = 1. \tag{3.80}$$

In the following, the distinction between different phases and different orientation is not relevant, as both lead to heterogeneous local material properties. To describe the microstructure geometrically without considering specific material properties, we introduce the combined phase-orientation indicator function

$$I(\alpha, \boldsymbol{Q}, \boldsymbol{x}) = I_\alpha(\boldsymbol{x}) I_{\boldsymbol{Q}}(\boldsymbol{x}). \tag{3.81}$$

The combined indicator function describes only one specific microstructure. In practice, microstructures result from production processes which are not perfectly controlled on the microscopic level, and a stochastic description is necessary. To this end, each specific microstructure is considered to be a *realization* from a stochastic *ensemble*. With the realizations indexed by ω, the expectation value over the ensemble of any value F_ω

is defined by

$$\langle F_\omega \rangle = \frac{1}{N} \sum_{\omega=1}^{N} F_\omega. \tag{3.82}$$

For a stochastic description of the microstructure, the moments of the indicator function are of particular interest, which are introduced as *correlation functions*. The one-point correlation function is written

$$S^1(\alpha, \boldsymbol{Q}, \boldsymbol{x}) = \langle I(\alpha, \boldsymbol{Q}, \boldsymbol{x}) \rangle, \tag{3.83}$$

and the two-point correlation function is

$$S^2(\alpha_1, \boldsymbol{Q}_1, \boldsymbol{x}_1, \alpha_2, \boldsymbol{Q}_2, \boldsymbol{x}_2) = \langle I(\alpha_1, \boldsymbol{Q}_1, \boldsymbol{x}_1) I(\alpha_2, \boldsymbol{Q}_2, \boldsymbol{x}_2) \rangle. \tag{3.84}$$

The n-th order correlation function has n sets of parameters, which is for brevity written as

$$S^n(\alpha_i, \boldsymbol{Q}_i, \boldsymbol{x}_i) = \left\langle \prod_{i=1}^{n} I(\alpha_i, \boldsymbol{Q}_i, \boldsymbol{x}_i) \right\rangle. \tag{3.85}$$

The correlation functions can be understood as probability densities which specify the infinitesimal probability that at points $\boldsymbol{x}_i$, the phase α_i is present in the exact orientation $\boldsymbol{Q}_i$, as discussed by Torquato (2002), Section 2.2.1.

The ensemble is *statistically invariant* under a spatial transformation T if

$$S^n(\alpha_i, \boldsymbol{Q}_i, \boldsymbol{x}_i) = S^n(\alpha_i, T(\boldsymbol{Q}_i), T(\boldsymbol{x}_i)) \quad \forall n, \forall \alpha_i. \tag{3.86}$$

An ensemble which is statistically invariant under translation is called *statistically homogeneous*, and as described by, e.g., Torquato (2002), it follows that

$$S^1(\alpha, \boldsymbol{Q}, \boldsymbol{x}) = S^1(\alpha, \boldsymbol{Q}) = v_\alpha f_\alpha(\boldsymbol{Q}) \tag{3.87}$$

with the phase volume fraction v_α and the phase orientation distribution function (ODF) $f_\alpha(\boldsymbol{Q})$. Given statistical homogeneity, the n-point correlation function depends only on relative positions, not absolute positions, such that

$$S^n(\alpha_i, \boldsymbol{Q}_i, \boldsymbol{x}_i) = S^n(\alpha_i, \boldsymbol{Q}_i, \boldsymbol{x}_i - \boldsymbol{x}_1), \tag{3.88}$$

which reduces the parameter set by $\boldsymbol{x}_1$.

Rotational symmetry of a statistically homogeneous ensemble under the action of a rotational symmetry group $S \subseteq SO(3)$ is called *statistical S-symmetry*. The condition Eq. (3.86) applies, with T written as

$$T(\boldsymbol{Q}) = \boldsymbol{R}\boldsymbol{Q}, \qquad T(\boldsymbol{x}) = \boldsymbol{R} \star \boldsymbol{x}. \tag{3.89}$$

Of particular interest is the case of $S = SO(3)$, *statistical isotropy*, for which the one-point probability distribution simplifies to

$$S^1(\alpha, \boldsymbol{Q}, \boldsymbol{x}) = v_\alpha. \tag{3.90}$$

In discussions of polycrystalline microstructures, partial symmetries are often introduced. A *crystallographic symmetry* applies only to the orientations, i.e.,

$$S^n(\alpha_i, \boldsymbol{Q}_i, \boldsymbol{x}_i - \boldsymbol{x}_1) = S^n(\alpha_i, \boldsymbol{R}\boldsymbol{Q}_i, \boldsymbol{x}_i - \boldsymbol{x}_1) \quad \forall \boldsymbol{R} \in S, \tag{3.91}$$

while a *morphological symmetry* applies only to the spatial distribution of phases, i.e.,

$$S^n(\alpha_i, \boldsymbol{Q}_i, \boldsymbol{x}_i - \boldsymbol{x}_1) = S^n(\alpha_i, \boldsymbol{Q}_i, \boldsymbol{R} \star (\boldsymbol{x}_i - \boldsymbol{x}_1)) \quad \forall \boldsymbol{R} \in S. \tag{3.92}$$

As defined above, crystallographic and morphological symmetries together imply statistical symmetry, but the converse is not true. A weaker form of crystallographic symmetry is sometimes defined using the ODF,

and reads

$$f(\boldsymbol{Q}) = f(\boldsymbol{RQ}) \quad \forall \boldsymbol{R} \in S. \tag{3.93}$$

Using results from Section 2.2.5, a symmetric ODF can be described by using a symmetric set of deviatoric basis tensors, leading to a reduced set of texture tensors. Note that the ODF-based definition of crystallographic symmetry is not sufficient to imply statistical symmetry, as n-point correlations of orientations are not sufficiently constrained by a one-point constraint.

The final symmetry that needs to be distinguished is *material symmetry*. In the above discussion of statistical properties, it was generally assumed that the materials are fully anisotropic. If the material itself is symmetrical as described in Section 3.1.4, a full description of the material orientation is not necessary, and crystallographic symmetry can be assumed.

In statistical mechanics, *ergodicity* is the notion that a single realization can be sufficient to describe the entire ensemble. For micromechanics, following Torquato (2002), Section 2.2.1, ergodicity is expressed in the limit of infinitely large realizations and an infinite ensemble by the condition that

$$S^n(\alpha_i, \boldsymbol{Q}_i, \boldsymbol{x}_i) = \lim_{V\to\infty} \frac{1}{V} \int_V \prod_{i=1}^{n} I(\alpha_i, \boldsymbol{Q}_i, \boldsymbol{x}_i)\, \mathrm{d}V \quad \forall n, \forall \alpha_i. \tag{3.94}$$

If this condition holds, all ensemble averages can be computed as volume averages over an infinite volume. The infinite volume is then considered *representative* of the ensemble. Ergodicity is often assumed for ease of calculation even when it is not strictly necessary. Following the approach of Kreher and Pompe (1989), we will attempt to avoid the assumption of ergodicity wherever possible.

3.2.2 The stochastic boundary-value problem

The stated goal of micromechanics is to model the behavior of material bodies with stochastically distributed material properties. An example from an industrial application would be a part which, due to uncontrolled factors in its production process, has a random microstructure. As a material body, such a part is governed by the Navier-Lamé equation Eq. (3.41), which holds for every regular material point of every realization. We neglect body forces, leading to

$$\operatorname{div}\left(\mathbb{C}[\operatorname{sym}\left(\operatorname{grad}\left(\boldsymbol{u}\right)\right) - \boldsymbol{E}]\right) = \boldsymbol{0} \tag{3.95}$$

with random fields $\mathbb{C}$ and $\boldsymbol{u}$. In the industrial application example, the boundary conditions remain deterministic, such that

$$\boldsymbol{u}_{\mathrm{D}}(\boldsymbol{x}) = \langle \boldsymbol{u}_{\mathrm{D}} \rangle(\boldsymbol{x}), \tag{3.96}$$

$$\boldsymbol{t}_{\mathrm{N}}(\boldsymbol{x}) = \langle \boldsymbol{t}_{\mathrm{N}} \rangle(\boldsymbol{x}). \tag{3.97}$$

We assume that the microstructure is statistically homogeneous. However, the boundary conditions are statistically heterogeneous. As a result, the ensemble of displacement fields $\boldsymbol{u}(\boldsymbol{x})$ which can be calculated by solving the Navier-Lamé equation for every realization is not generally speaking statistically homogeneous. The same is true for $\boldsymbol{\sigma}$ and $\boldsymbol{\varepsilon}$. Following Kreher and Pompe (1989), we restrict ourselves to boundary conditions leading to statistically homogeneous internal fields

$$\langle \boldsymbol{\sigma}(\boldsymbol{x}) \rangle = \bar{\boldsymbol{\sigma}}, \tag{3.98}$$

$$\langle \boldsymbol{\varepsilon}(\boldsymbol{x}) \rangle = \bar{\boldsymbol{\varepsilon}}, \tag{3.99}$$

with the *effective stress* $\bar{\boldsymbol{\sigma}}$ and *effective strain* $\bar{\boldsymbol{\varepsilon}}$. To describe the overall behavior of the microstructure, it is sufficient to establish a relationship between effective stresses and strains. Such a theory is called a mean-

field theory. Possible motivations for the underlying assumption that the internal fields are statistically homogeneous include statistically homogeneous boundary conditions or an ergodic hypothesis. In general, the assumption of statistically homogeneous internal fields is less restrictive than ergodicity.

Following the approach outlined by Kreher and Pompe (1989), section 2.4.3, we separate the influences of eigenstrains and external loads by superposition. If external loads are zero, $\bar{\boldsymbol{\sigma}}$ vanishes. However, internal random strain and stress fields are still present, caused by the kinematic incompatibility of the eigenstrains. The fields for this specific state are the *residual fields* $\boldsymbol{\sigma}_{\mathrm{R}}$ and $\boldsymbol{\varepsilon}_{\mathrm{R}}$. As the influence of the eigenstrain is entirely contained within the residual fields, the influence of external loads can be described with a linear elastic material law. For the linear elastic fields $\boldsymbol{\sigma}_{\mathrm{L}}$ and $\boldsymbol{\varepsilon}_{\mathrm{L}}$,

$$\boldsymbol{\sigma}_{\mathrm{L}} = \mathbb{C}[\boldsymbol{\varepsilon}_{\mathrm{L}}]. \tag{3.100}$$

As the ensuing Lamé equation is a linear partial differential equation, and the influence of the boundary conditions is described by the effective stress or strain, respectively, there must be a linear relationship between the linear elastic random fields and the linear elastic effective fields. This relationship was first formalized by Hill (1963) using the strain concentration tensor

$$\boldsymbol{\varepsilon}_{\mathrm{L}} = \mathbb{A}(\boldsymbol{x})[\bar{\boldsymbol{\varepsilon}}_{\mathrm{L}}]. \tag{3.101}$$

By taking the expectation value of Hooke's law, we find

$$\bar{\boldsymbol{\sigma}}_{\mathrm{L}} = \langle \mathbb{C}\mathbb{A}(\boldsymbol{x}) \rangle [\bar{\boldsymbol{\varepsilon}}_{\mathrm{L}}], \tag{3.102}$$

and define

$$\bar{\mathbb{C}} = \langle \mathbb{C}\mathbb{A}(\boldsymbol{x}) \rangle \tag{3.103}$$

as the effective stiffness.

The effective residual strain is the strain which applies to the entire body when there are no external loads, and is thus considered the *effective eigenstrain*. Therefore,

$$\bar{\boldsymbol{\varepsilon}}_{\mathrm{R}} = \bar{\boldsymbol{E}}, \tag{3.104}$$

such that the effective affine Hooke's law

$$\bar{\boldsymbol{\sigma}}_{\mathrm{R}} = \bar{\mathbb{C}}[\bar{\boldsymbol{\varepsilon}}_{\mathrm{R}} - \bar{\boldsymbol{E}}] = \boldsymbol{0} \tag{3.105}$$

is consistent with the prior definition of vanishing external loads. Because the residual stress problem is not linear, but affine linear, the concentration relation includes the second order concentration tensor

$$\boldsymbol{a} = \boldsymbol{\varepsilon}_{\mathrm{R}} - \mathbb{A}[\bar{\boldsymbol{E}}]. \tag{3.106}$$

If the second-order concentration tensor is known, the effective eigenstrain can be calculated via

$$\bar{\boldsymbol{E}} = \bar{\mathbb{C}}^{-1}[\langle \mathbb{C}[\boldsymbol{a} - \boldsymbol{E}] \rangle]. \tag{3.107}$$

By superposition, the total strain field is given by

$$\boldsymbol{\varepsilon} = \boldsymbol{\varepsilon}_{\mathrm{L}} + \boldsymbol{\varepsilon}_{\mathrm{R}}, \tag{3.108}$$

$$\bar{\boldsymbol{\varepsilon}} = \bar{\boldsymbol{\varepsilon}}_{\mathrm{L}} + \bar{\boldsymbol{E}}, \tag{3.109}$$

and the total strain field depends on the effective strain via

$$\boldsymbol{\varepsilon}(\boldsymbol{x}) = \mathbb{A}(\boldsymbol{x})[\bar{\boldsymbol{\varepsilon}}] + \boldsymbol{a}(\boldsymbol{x}). \tag{3.110}$$

As shown by Kreher and Pompe (1989), section 2.5.2, statistical homogeneity and deterministic boundary conditions are sufficient to prove

the Hill-Mandel condition

$$\langle \bar{\boldsymbol{\sigma}} \cdot \bar{\varepsilon} \rangle = \bar{\boldsymbol{\sigma}} \cdot \bar{\varepsilon}, \tag{3.111}$$

which holds for any divergence-free $\boldsymbol{\sigma}$ and kinematically compatible ε, even if they are not related by any material law.
Via the Hill-Mandel condition, the effective elastic energy simplifies to

$$\begin{aligned} \bar{w}(\boldsymbol{\varepsilon}_{\mathrm{L}}) &= \frac{1}{2}\langle \boldsymbol{\varepsilon}_{\mathrm{L}} \cdot \mathbb{C}[\boldsymbol{\varepsilon}_{\mathrm{L}}] \rangle \\ &= \frac{1}{2}\bar{\boldsymbol{\varepsilon}}_{\mathrm{L}} \cdot \bar{\mathbb{C}}[\bar{\boldsymbol{\varepsilon}}_{\mathrm{L}}] \\ &= \frac{1}{2}(\bar{\varepsilon} - \bar{\boldsymbol{E}}) \cdot \bar{\mathbb{C}}[\bar{\varepsilon} - \bar{\boldsymbol{E}}]. \end{aligned} \tag{3.112}$$

After some manipulation involving the Hill-Mandel condition, Kreher and Pompe (1989) in section 2.5.4 give the total energy as

$$\bar{w} = \frac{1}{2}(\bar{\varepsilon} - \bar{\boldsymbol{E}}) \cdot \bar{\mathbb{C}}[\bar{\varepsilon} - \bar{\boldsymbol{E}}] + \bar{w}_{\mathrm{R}} \tag{3.113}$$

with the effective residual strain energy

$$\bar{w}_{\mathrm{R}} = -\frac{1}{2}\langle \boldsymbol{\sigma}_{\mathrm{R}} \cdot \boldsymbol{E} \rangle. \tag{3.114}$$

In the general case, the effective quantities $\bar{\mathbb{C}}$, $\bar{\boldsymbol{E}}$ and $\bar{w}_{\mathrm{R}}$ are independent of each other and require for their calculation the full strain field, or equivalently, the concentration tensors. Even if the microstructure ensemble were fully known, calculating the fields would require solving the Navier-Lamé equation for every realization, which is impractical for large ensembles. Thus, models for working with simplifying assumptions and incomplete information are needed. All models discussed in the following require known phase properties $\mathbb{C}_\alpha$ and $\boldsymbol{E}_\alpha$. Besides the phase properties,

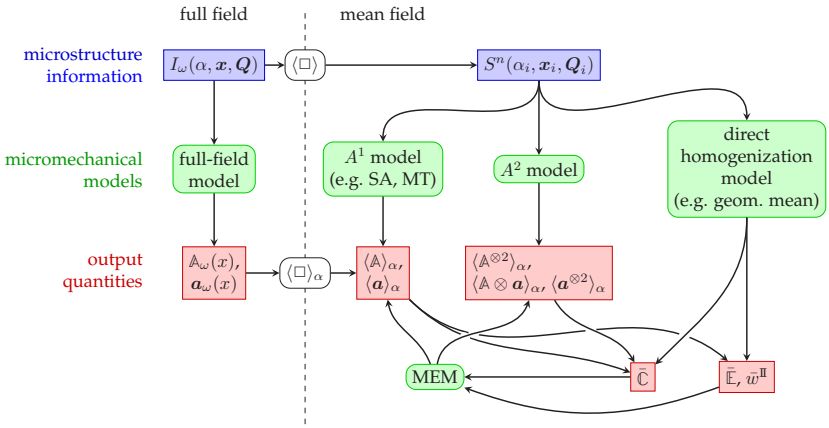

Figure 3.2: Classification of micromechanical models by required microstructure information and output quantities.

- *full-field simulations* use the entire indicator function $I(\alpha, \boldsymbol{Q}, \boldsymbol{x})$ of one realization to calculate the strain field for that realization;
- *direct homogenization approaches* use a limited set of correlation functions, generally S^1, to approximate effective quantities $\bar{\mathbb{C}}$, $\bar{\boldsymbol{E}}$ and $\bar{w}$ via ad-hoc relationships;
- A^1 *models* use those correlation functions to approximate the phase-wise mean of concentration tensors $\langle\mathbb{A}\rangle_\alpha$ and $\langle\boldsymbol{a}\rangle_\alpha$; and
- A^2 *models* use those correlation functions to approximate the phase-wise second moments of concentration tensors $\langle\mathbb{A}\otimes\mathbb{A}\rangle_\alpha$, $\langle\mathbb{A}\otimes\boldsymbol{a}\rangle_\alpha$ and $\langle\boldsymbol{a}\otimes\boldsymbol{a}\rangle_\alpha$.

Using equations (3.103), (3.107), and (3.114), every A^1 model implies a homogenization approach. Using the Hill-Mandel condition, A^2 models imply a homogenization approach for $\bar{\mathbb{C}}$, but not $\bar{\boldsymbol{\varepsilon}}$ and $\bar{w}^{\text{II}}$. Full-field models describe the behavior of the microstructure in arbitrary detail, and can thus be used to calculate the results of all other models. These re-

lations are illustrated in Fig. 3.2. The Maximum-Entropy Method (MEM), included in this figure for completeness, is explained in Chapter 5.

3.2.3 General results for simple material systems

The above results were derived for general linear thermoelastic materials with arbitrary many phases. For simple material systems, specific results are available. For linear elastic stress and strain fields, the equations Eq. (3.99) and Eq. (3.98) can be written

$$\langle \mathbb{A} \rangle = \mathbb{I}, \tag{3.115}$$

$$\langle \mathbb{C}\mathbb{A} \rangle = \bar{\mathbb{C}}. \tag{3.116}$$

Two-phase composites are heterogeneous material systems with two piecewise constants values for $\mathbb{C}$ and $\boldsymbol{E}$, a common example of which are composites consisting of two isotropic phases. For such materials, Eq. (3.115) and (3.116) form an equation system in the phase mean concentration tensors $\langle \mathbb{A} \rangle_1$ and $\langle \mathbb{A} \rangle_2$, which solves to

$$\langle \mathbb{A} \rangle_1 = \frac{1}{v_1} (\mathbb{C}_1 - \mathbb{C}_2)^{-1} (\bar{\mathbb{C}} - \mathbb{C}_2) \tag{3.117}$$

with indices reversed for phase 2. Thus, the linear elastic fields are uniquely determined by the value of $\bar{\mathbb{C}}$. For materials with eigenstrains, as shown by Levin (1967),

$$\langle \boldsymbol{a} \rangle_1 = \frac{1}{v_1} (\mathbb{C}_2 - \mathbb{C}_1)^{-1} [\bar{\mathbb{C}}[\bar{\boldsymbol{E}}] - \mathbb{C}_2[\langle \boldsymbol{E} \rangle]] + \boldsymbol{E}_1, \tag{3.118}$$

with indices reversed for phase 2. Consequently, for two-phase systems, the effective properties uniquely imply an A^1 model even in the affine linear elastic case. As shown by Rosen and Hashin (1970), the effective stiffness alone is sufficient, as it can be used to calculate effective

eigenstrains and the effective residual strain energy with the formulas

$$\bar{\boldsymbol{E}} = \langle \boldsymbol{E} \rangle + (\langle \mathbb{C}^{-1} \rangle - \bar{\mathbb{C}}^{-1})(\mathbb{C}_1^{-1} - \mathbb{C}_2^{-1})^{-1}[\boldsymbol{E}_2 - \boldsymbol{E}_1], \tag{3.119}$$

$$\begin{aligned} \bar{w}_{\mathrm{R}} &= \frac{1}{2}(\boldsymbol{E}_2 - \boldsymbol{E}_1)(\mathbb{C}_1^{-1} - \mathbb{C}_2^{-1})^{-1}[\bar{\boldsymbol{E}} - \langle \boldsymbol{E} \rangle] \\ &= \frac{1}{2}(\boldsymbol{E}_2 - \boldsymbol{E}_1)(\mathbb{C}_1^{-1} - \mathbb{C}_2^{-1})^{-1}(\langle \mathbb{C}^{-1} \rangle - \bar{\mathbb{C}}^{-1})(\mathbb{C}_1^{-1} - \mathbb{C}_2^{-1})^{-1}[\boldsymbol{E}_2 - \boldsymbol{E}_1]. \end{aligned} \tag{3.120}$$

For statistically isotropic single-phase cubic polycrystals, the local stiffness is given by

$$\mathbb{C}(\boldsymbol{Q}) = \boldsymbol{Q} \star \mathbb{C}^{\mathrm{C}}, \tag{3.121}$$

where the stiffness $\mathbb{C}^{\mathrm{C}}$ has cubic symmetry with symmetry axes aligned to the canonical coordinate system. Due to statistical isotropy for multi-point correlation functions, the grain shape and the grain orientation are isotropically correlated. When considering the statistical neighborhood of all points $\boldsymbol{x}$ with a given orientation $\boldsymbol{Q}$, the stiffness $\mathbb{C}(\boldsymbol{x})$ is the only source of anisotropy, since the neighborhood is isotropically correlated and therefore, in the statistical mean, resembles a spherical inclusion. Due to this symmetry, the expectation value of concentration tensors for those points is

$$\langle \mathbb{A} \rangle_{\boldsymbol{Q}} = \boldsymbol{Q} \star \mathbb{A}^{\mathrm{C}}, \tag{3.122}$$

where $\mathbb{A}^{\mathrm{C}}$ has the same symmetry as $\mathbb{C}^{\mathrm{C}}$. In the harmonic basis described in Section 2.2.4,

$$\underline{\underline{A}}^{\mathrm{C}} = \mathrm{diag}\,(\lambda_1, \lambda_2, \lambda_3, \lambda_3, \lambda_3, \lambda_2)\,. \tag{3.123}$$

By applying results from Section 2.2.5, the expected value of rotated concentration tensors becomes

$$\langle \mathbb{A} \rangle = \lambda_1^{\mathrm{A}} \mathbb{P}^{\circ} + \frac{2\lambda_2^{\mathrm{A}} + 3\lambda_3^{\mathrm{A}}}{5} \mathbb{P}'. \tag{3.124}$$

As with two-phase materials, Eq. (3.115) and Eq. (3.116) can be solved as an equation system, yielding

$$\lambda_1^{\mathrm{A}} = 1 \tag{3.125}$$

$$\lambda_2^{\mathrm{A}} = \frac{-5\lambda_3^{\mathrm{C}} + 10\bar{G}}{2\lambda_2^{\mathrm{C}} - 2\lambda_3^{\mathrm{C}}}, \tag{3.126}$$

$$\lambda_3^{\mathrm{A}} = \frac{5\lambda_2^{\mathrm{C}} - 10\bar{G}}{3\lambda_2^{\mathrm{C}} - 3\lambda_3^{\mathrm{C}}}. \tag{3.127}$$

By Eq. (3.125), the phase-wise means of spherical stresses and strains are homogeneous in a statistically isotropic cubic polycrystal; spherical loads form a *mean homogeneous mode*. A homogeneous phase-wise mean of the strain localization tensor does not prohibit strain fluctuations within a given phase. Unlike the two-phase case, we do not consider solutions for cubic materials with eigenstrains, since cubic eigenstrains are spherical and therefore homogeneous for a single-phase polycrystals.

3.2.4 Approximations for the effective stiffness

In the following, selected homogenization approaches will be discussed for the case of linear elastic materials. Direct homogenization approaches rely on ad-hoc relationships between phase properties and effective properties, such as the *geometric mean*

$$\bar{\mathbb{C}}_{\mathrm{geom}} = \exp(\langle \ln(\mathbb{C}) \rangle). \tag{3.128}$$

According to Matthies and Humbert (1995), the geometric mean is a reasonably good approximation for single-phase polycrystals. However,

such recommendations for direct homogenization approaches are necessarily grounded in experimental data, which is difficult to generalize to novel material systems. Therefore, the following homogenization approaches will be based on A^1 models which can be motivated using microstructural assumptions.

Following Kreher and Pompe (1989), we focus on A^1 models which are based on the work of Eshelby (1957). The Eshelby solution is an analytical full-field model of a specific ensemble, in which each realization consists of an infinite matrix (phase 1) with a single ellipsoidal inclusion (phase 2). The ellipsoidal inclusion is aligned with the canonical coordinate system and its three half-axes have respective length a_i. We define an ellipsoidal shape tensor

$$\boldsymbol{A} \hat{=} \begin{pmatrix} \frac{1}{a_1} & & \\ & \frac{1}{a_2} & \\ & & \frac{1}{a_3} \end{pmatrix}. \tag{3.129}$$

With a strain $\boldsymbol{\varepsilon}_1$ applying at an infinite distance, the strain in the inclusion is given by

$$\langle \boldsymbol{\varepsilon} \rangle_2 = \mathbb{L}\mathbb{P}_1^{-1}[\boldsymbol{\varepsilon}_1], \tag{3.130}$$

$$\mathbb{L} = (\mathbb{P}_1^{-1} + \mathbb{C}_2 - \mathbb{C}_1)^{-1}. \tag{3.131}$$

Hill's polarization tensor $\mathbb{P}_\alpha$ for a matrix stiffness $\mathbb{C}_\alpha$ is given by Willis (1977) as

$$\mathbb{P}_\alpha = \frac{1}{4\pi \det(\boldsymbol{A})} \iint_{\partial S} \mathbb{H}(\mathbb{C}_\alpha, \boldsymbol{n})(\boldsymbol{n} \cdot (\boldsymbol{A}^{-\mathsf{T}} \boldsymbol{A}^{-1} \boldsymbol{n}))^{-3/2} \, \mathrm{d}S, \tag{3.132}$$

with

$$\mathbb{H} = \mathbb{I}^{\mathrm{S}}((\boldsymbol{n} \otimes \boldsymbol{n}) \times \boldsymbol{K}_1^{-1})\mathbb{I}^{\mathrm{S}}. \tag{3.133}$$

The acoustic tensor $\boldsymbol{K}_1$ is given by

$$\boldsymbol{K}_1 = \mathbb{I} \times (\boldsymbol{n} \otimes \boldsymbol{n})[\mathbb{C}_1]. \tag{3.134}$$

If the stiffness $\mathbb{C}_1$ is isotropic with Lamé constants λ and μ, the inverse of the acoustic tensor can be calculated directly as

$$\boldsymbol{K}_1^{-1} = -\frac{\lambda_1 + \mu_1}{\mu_1(\lambda_1 + 2\mu_1)} \boldsymbol{n} \otimes \boldsymbol{n} + \frac{1}{\mu_1} \boldsymbol{I}. \tag{3.135}$$

If the ellipsoid is a sphere,

$$\mathbb{P}_1 = \frac{1}{4\pi} \iint_{\partial S} \mathbb{H}(\mathbb{C}_1, \boldsymbol{n}) \, \mathrm{d}S. \tag{3.136}$$

and following Willis (1977), Hill's polarization tensor for an isotropic $\mathbb{C}_1$ and spherical inclusions becomes

$$\mathbb{P}_1 = \frac{1}{3(\lambda_0 + 2\mu_0)} \mathbb{P}^{\circ} + \frac{3\lambda_0 + 8\mu_0}{15\mu_0(\lambda_0 + 2\mu_0)} \mathbb{P}'. \tag{3.137}$$

The strain field in the inclusion is spatially homogeneous, and the matrix tends, as its size goes to infinity, to spatial homogeneity with a mean strain value $\boldsymbol{\varepsilon}_0$. Therefore, the full-field Eshelby solution can be described by reducing it to an A^1-model.

Because the Eshelby solution has a vanishing inclusion volume fraction, it is ill-suited as a direct approximation of real microstructures. Mori and Tanaka (1973) bypassed this issue by requiring that the infinite distance strain $\boldsymbol{\varepsilon}_0$ is equal to the matrix mean strain $\langle \boldsymbol{\varepsilon} \rangle_1$, which they compute from the inclusion mean strain and Eq. (3.99). For two-phase materials with homogeneous orientations, this approach yields

$$\langle \mathbb{A} \rangle_1 = \mathbb{P}_1 (v_2 \mathbb{L} + v_1 \mathbb{P}_1)^{-1} \tag{3.138}$$

$$\langle \mathbb{A} \rangle_2 = (\mathbb{L} - \mathbb{P}_1)(v_2 \mathbb{L} + v_1 \mathbb{P}_1)^{-1} \tag{3.139}$$

and a corresponding effective stiffness

$$\bar{\mathbb{C}} = \mathbb{C}_2 + v_1(\mathbb{C}_1 - \mathbb{C}_2)\mathbb{P}_1(v_2\mathbb{L} + v_1\mathbb{P}_1)^{-1}. \tag{3.140}$$

The Mori-Tanaka approach assumes that one phase morphologically forms a connected matrix, while the other consists of non-connected ellipsoidal inclusions. A more general approach to modeling phase interaction is given by the Singular Approximation first formulated by Fokin (1972). Fokin's original approach relies on the assumption that the Green's function of the Navier-Lamé equation can be approximated by its singular part. This is, roughly speaking, similar to the assumption that each material point is not influenced by its direct surroundings, only by the overall continuum-mechanical problem. In Eshelby's solution, this is true for material points in the inclusion, as the inclusion strain field is spatially constant. Therefore, we motivate the Singular Approximation by replacing our actual microstructure to be modeled with an ensemble of Eshelby problems where each of the phases of the material is represented as an inclusion. The matrix material is treated as an unknown reference material $\mathbb{C}_0$. The material phases and orientations are present among inclusions in proportion to the one-point statistic of the microstructure to be modeled, such that the one-point statistic over the inclusions, disregarding the reference material, matches the one-point statistic of the original microstructure. The ellipsoidal shape is constant over the ensemble and chosen to match the two-point statistic of the original microstructure. Finally, the expectation value of the infinite-distance strain $\boldsymbol{\varepsilon}_0$ is equal for all phases, i.e.

$$\langle \boldsymbol{\varepsilon}_0 \rangle_{\alpha,\boldsymbol{Q}} = \langle \boldsymbol{\varepsilon}_0 \rangle. \tag{3.141}$$

The expectation value of the strain in a given phase results from Eq. (3.130) as

$$\langle \boldsymbol{\varepsilon} \rangle_{\alpha,\boldsymbol{Q}} = \mathbb{L}_{\alpha,\boldsymbol{Q}}\mathbb{P}_0^{-1}[\langle \boldsymbol{\varepsilon}_0 \rangle]. \tag{3.142}$$

By enforcing Eq. (3.99), $\boldsymbol{\varepsilon}_0$ can be eliminated, leading to

$$\langle \boldsymbol{\varepsilon} \rangle_{\alpha,\boldsymbol{Q}} = \mathbb{L}_{\alpha,\boldsymbol{Q}} \langle \mathbb{L} \rangle^{-1} [\bar{\boldsymbol{\varepsilon}}]. \tag{3.143}$$

Notably, this result was also derived by Willis (1977) in the context of the Hashin-Shtrikman bounds by assuming that the two-point statistic of the microstructure is ellipsoidal. Walpole (1966) writes the effective stiffness in the form

$$\bar{\mathbb{C}} = \langle \mathbb{L} \rangle^{-1} + \mathbb{C}_0 - \mathbb{P}_0^{-1}. \tag{3.144}$$

The Singular Approximation has a free parameter, the reference stiffness $\mathbb{C}_0$. In the limit $\mathbb{C}_0 \to \mathbb{0}$, the Singular Approximation tends to the Reuss stiffness

$$\mathbb{C}_- = \langle \mathbb{C}^{-1} \rangle^{-1} \tag{3.145}$$

which was originally derived by Reuss (1929) using the assumption of constant stress fields. The limit $\mathbb{C}_0^{-1} \to \mathbb{0}$ leads to the Voigt stiffness

$$\mathbb{C}_+ = \langle \mathbb{C} \rangle, \tag{3.146}$$

originally derived by Voigt (1889) using the assumption of constant strain fields. As the reference stiffness is assumed to be positive definite, and the same holds for its inverse, the Voigt and Reuss approximations are based on bounds of the reference stiffness. It can be shown that they form bounds on the effective stiffness in the sense that $\mathbb{C}_+ - \bar{\mathbb{C}}$ and $\bar{\mathbb{C}} - \mathbb{C}_-$ are positive definite. Notably, these bounds are independent of $\mathbb{P}_0$, and therefore only incorporate the single-point correlation function S^1.

Tighter bounds can be obtained by requiring that the reference stiffness, which serves as a replacement for the rest of the microstructure, lies between the phase stiffnesses, again in the sense of positive definiteness. As described by Nadeau and Ferrari (2001), this is equivalent to the

application of zeroth order bounds to the reference stiffness. To calculate the isotropic zeroth order upper bound of a single anisotropic phase, we define

$$\lambda_{\max}(\gamma) = \max(\mathrm{eig}(\mathbb{C}_\alpha - \gamma\mathbb{P}^\circ)), \qquad \gamma_{\min} = \min_\gamma(\gamma + 6\lambda_{\max}(\gamma)), \tag{3.147}$$

where $\mathrm{eig}(\mathbb{A})$ denotes the set of eigenvalues of a major symmetric fourth-order tensor $\mathbb{A}$, leading to

$$2G_{0\alpha}^+ = \lambda_{\max}(\gamma_{\min}), \quad 3K_{0\alpha}^+ = \gamma_{\min} + 2G_{0\alpha}^+. \tag{3.148}$$

For composites, the maximum or minimum of the above single-phase bounds defines the composite bound

$$G_0^+ = \max(G_{0\alpha}), \quad K_0^+ = \max(K_{0\alpha}^+). \tag{3.149}$$

Following Lobos and Böhlke (2016), the lower bound $\mathbb{C}_0^-$ is given by the upper bound of the compliance $\mathbb{C}^{-1}$. With the zeroth order bounds as the reference stiffness in the Singular Approximation, the Hashin-Shtrikman bounds are recovered, as described by Willis (1977). Unlike the Voigt and Reuss bounds, which apply regardless of microstructure, the Hashin-Shtrikman bounds only serve as bounds for ensembles with an ellipsoidal two-point statistic.

In the self-consistent approximation due to Kröner (1977), the reference stiffness equals the effective stiffness. In the general case, this yields a nonlinear tensorial equation system given by

$$\bar{\mathbb{C}} = \langle\mathbb{L}\rangle^{-1} + \mathbb{C}_0 - \mathbb{P}_0^{-1} \tag{3.150}$$

$$\mathbb{L} = (\mathbb{C} - \bar{\mathbb{C}} + \mathbb{P}_0^{-1}) \tag{3.151}$$

with $\mathbb{P}_0$ as in Eq. (3.132), but with $\bar{\mathbb{C}}$ as a reference stiffness. Since $\bar{\mathbb{C}}$ is generally anisotropic, $\mathbb{P}_0$ must be calculated numerically to evaluate the right-hand side, as done by, e.g., Brenner et al. (2004) or Behnken (1992).

Chapter 4

Second moments of local stresses and strains[1]

4.1 Introduction

In this chapter, the exact second-order statistical moments of local fields for particulate composites with isotropic phases are derived in the complete tensor form. The effective strain energy density is evaluated considering the Singular Approximation, the Mori-Tanaka method and the upper and lower Hashin-Shtrikman bounds. Explicit formulas are given for each of these cases. The analytical results are compared with full-field simulations for a random sphere assemblage. The differences of the methods are discussed for both the effective stiffness and the local field statistics.

The chapter is organized as follows. In Section 4.2, a short proof of the formula to calculate exact second-order moments is given. In Section 4.3, analytical formulas are derived for the Singular Approximation, the Hashin-Shtrikman bounds and the Mori-Tanaka method. In Section 4.4, the analytical methods are compared with FEM full-field simulations of microstructures with random arrangements of spherical inclusions. In Section 4.5, the results are summarized.

[1] This chapter is based on the publication *Exact second moments of strain for composites with isotropic phases* (Krause et al., 2023).

4.2 General Second Moments Formula

A short derivation of the analytical approach for determining the phase-wise second-order moments of stress and strain due to Bobeth and Diener (1987) shall be given here. Beginning with the effective strain energy density

$$\bar{w} = \frac{1}{2}\langle \boldsymbol{\varepsilon} \cdot \mathbb{C}[\boldsymbol{\varepsilon}] \rangle, \tag{4.1}$$

we vary the local stiffness $\mathbb{C}$ while the effective strain is kept constant. In effect, this is equivalent to considering a different composite under the same load by changing the phases' properties, but not the geometry of the microstructure itself. Such a change causes a variation of the local strain. The formal definition of the total variation of the effective energy is given by

$$\delta\bar{w} = \frac{1}{2}\left|\frac{\partial}{\partial\gamma}\langle(\boldsymbol{\varepsilon}+\gamma\delta\boldsymbol{\varepsilon})\cdot(\mathbb{C}+\gamma\delta\mathbb{C})[\boldsymbol{\varepsilon}+\gamma\delta\boldsymbol{\varepsilon}]\rangle\right|_{\gamma=0}. \tag{4.2}$$

When the variation in the stiffness is restricted to any single phase (denominated here as 1) the energy of the other phases changes only through changes in the strain field, which can be written as

$$\begin{aligned} 2\delta\bar{w} = {} & \frac{\partial}{\partial\gamma}\langle(\boldsymbol{\varepsilon}+\gamma\delta\boldsymbol{\varepsilon})\cdot\mathbb{C}[\boldsymbol{\varepsilon}+\gamma\delta\boldsymbol{\varepsilon}]\rangle\Big|_{\gamma=0} \\ & + c_1\,\frac{\partial}{\partial\gamma}\langle(\boldsymbol{\varepsilon}+\gamma\delta\boldsymbol{\varepsilon})\cdot(\gamma\delta\mathbb{C}_1)[\boldsymbol{\varepsilon}+\gamma\delta\boldsymbol{\varepsilon}]\rangle_1\Big|_{\gamma=0}. \end{aligned} \tag{4.3}$$

Both terms may be rearranged as follows, where $\mathbb{E}$ stands for either fourth-order tensor:

$$\begin{aligned}&\frac{\partial}{\partial\gamma}\left(\langle(\boldsymbol{\varepsilon}+\gamma\delta\boldsymbol{\varepsilon})\cdot\mathbb{E}[\boldsymbol{\varepsilon}+\gamma\delta\boldsymbol{\varepsilon}]\rangle\right)\Big|_{\gamma=0}\\&=\underbrace{\frac{\partial}{\partial\gamma}\langle\boldsymbol{\varepsilon}\cdot\mathbb{E}[\boldsymbol{\varepsilon}]\rangle\Big|_{\gamma=0}}_{\text{(I)}}+\underbrace{\frac{\partial}{\partial\gamma}\left(2\gamma\langle\delta\boldsymbol{\varepsilon}\cdot\mathbb{E}[\boldsymbol{\varepsilon}]\rangle\right)\Big|_{\gamma=0}}_{\text{(II)}}+\underbrace{\frac{\partial}{\partial\gamma}\left(\gamma^2\langle\delta\boldsymbol{\varepsilon}\cdot\mathbb{E}[\delta\boldsymbol{\varepsilon}]\rangle\right)\Big|_{\gamma=0}}_{\text{(III)}}.\end{aligned}\tag{4.4}$$

Term (I) disappears for $\mathbb{E}=\mathbb{C}$. Term (III) disappears after differentiation as $\gamma=0$, as does Term (II) if $\mathbb{E}=\gamma\delta\mathbb{C}$. If $\mathbb{E}=\mathbb{C}$, $\mathbb{E}[\boldsymbol{\varepsilon}]$ is the stress and $\delta\boldsymbol{\varepsilon}$ is kinematically compatible, such that Term (II) is subject to the Hill-Mandel condition

$$\langle\delta\boldsymbol{\varepsilon}\cdot\mathbb{E}[\boldsymbol{\varepsilon}]\rangle=\langle\delta\boldsymbol{\varepsilon}\rangle\cdot\langle\mathbb{E}[\boldsymbol{\varepsilon}]\rangle.\tag{4.5}$$

As a variation of the local stiffness does not vary the effective strain, $\langle\delta\boldsymbol{\varepsilon}\rangle=\mathbf{0}$, and term (II) vanishes again, leaving only term (I) for $\mathbb{E}=\gamma\delta\mathbb{C}$. From the laws of variational calculus, it follows that

$$\frac{2}{c_1}\frac{\partial\bar{w}}{\partial\mathbb{C}_1}\cdot\delta\mathbb{C}_1=\langle\boldsymbol{\varepsilon}\otimes\boldsymbol{\varepsilon}\rangle_1\cdot\delta\mathbb{C}_1\qquad\forall\delta\mathbb{C}_1.\tag{4.6}$$

The derivative on the left-hand side must be understood as a derivative over the full (anisotropic) space of major, left and right symmetric fourth-order tensors, regardless of the symmetries of $\mathbb{C}_1$. Therefore, the method is constrained by the homogenization method employed to calculate $\bar{w}$, which may be an analytical approximation that does not support materials with arbitrarily anisotropic phases. In that case, only specific isotropic projections of the second moment may be calculated. Such a

special case appears, e.g., in Castañeda and Suquet (1997):

$$\mathbb{P}^{\circ} \cdot \langle \boldsymbol{\varepsilon} \otimes \boldsymbol{\varepsilon} \rangle_1 = \frac{2}{3c_1} \frac{\partial \bar{w}}{\partial K_1}, \qquad \mathbb{P}' \cdot \langle \boldsymbol{\varepsilon} \otimes \boldsymbol{\varepsilon} \rangle_1 = \frac{1}{c_1} \frac{\partial \bar{w}}{\partial G_1}. \tag{4.7}$$

Even in statistically isotropic composites with isotropic phases, if the effective strain is not an isotropic second-order tensor (i.e. spherical), there is no symmetry argument that the second moment should be isotropic. Hence, these simple derivatives by K_1 and G_1 are generally not sufficient to describe the second moments. In the following, a derivative by all components of $\mathbb{C}_1$ is used to calculate the full second moment.

By using the relation between the effective energy and the effective strain and stiffness, Eq. (4.6) may also take the form

$$\langle \boldsymbol{\varepsilon} \otimes \boldsymbol{\varepsilon} \rangle_1 = \frac{1}{c_1} \left(\frac{\partial \bar{\mathbb{C}}}{\partial \mathbb{C}_1} \right)^{\mathsf{T}} [\bar{\boldsymbol{\varepsilon}} \otimes \bar{\boldsymbol{\varepsilon}}]. \tag{4.8}$$

As discussed in Section 2.1.2, matrix operation are defined for arbitrary-order tensors via their canonical interpretation as linear maps, such that in this context, T is the eighth-order main transposition swapping the first four with the last four indices.

For the affine linear elastic case, similar results have been derived by Kreher (1990) and Buryachenko and Kreher (1995). Second moment expressions based on affine linear elastic homogenization theories differ from the linear elastic ones by also taking into account stiffness derivatives of the effective eigenstrain $\bar{\boldsymbol{E}}$ and the effective residual strain energy density $\bar{w}^{\mathrm{II}}$. The exact form of these derivatives is beyond the scope of this manuscript.

4.3 Second Moments in Eshelby's Problem

4.3.1 Derivative of Hill's Polarization Tensor

In the following, second moments of Eshelby-based approaches as described in Section 3.2.4 will be calculated. Only composites with spherical inclusion morphologies and an isotropic reference stiffness $\mathbb{C}_0$ will be considered. To calculate the gradient by the full anisotropic stiffness as described in Section 4.2, the assumption of isotropic $\mathbb{C}_0$ will only be used after any derivatives by the stiffness are already performed.

Determining the second moments of Eshelby-based approaches requires calculating the derivative $\partial\mathbb{P}_0/\partial\mathbb{C}_0$ of Hill's polarization tensor by the reference stiffness. Bounded integrals commute with bounded derivatives, such that

$$\frac{\partial\mathbb{P}_0}{\partial\mathbb{C}_0} = \frac{1}{4\pi}\frac{\partial}{\partial\mathbb{C}_0}\int_{\partial S}\mathbb{H}\,\mathrm{d}S = \frac{1}{4\pi}\int_{\partial S}\frac{\partial\mathbb{H}}{\partial\mathbb{C}_0}\,\mathrm{d}S. \tag{4.9}$$

As $\mathbb{H}$ can be calculated explicitly, we retrieve

$$\frac{\partial\mathbb{H}}{\partial\mathbb{C}_0} = \mathbb{I}^{\mathrm{S}\times 2}\frac{\partial(\boldsymbol{n}\otimes\boldsymbol{n})\times\boldsymbol{K}^{-1}}{\partial\mathbb{C}_0}, \tag{4.10}$$

$$\begin{aligned}\frac{\partial\boldsymbol{K}^{-1}}{\partial\mathbb{C}_0} &= -(\boldsymbol{K}^{-1})^{\times 2}\frac{\partial\boldsymbol{K}}{\partial\mathbb{C}_0}\\ &= -(\boldsymbol{K}^{-1})^{\times 2}\times(\boldsymbol{n}\otimes\boldsymbol{n}).\end{aligned} \tag{4.11}$$

The integration can then be performed explicitly as well, resulting in the rather lengthy expression

$$\frac{\partial \mathbb{P}_0}{\partial \mathbb{C}_0} = -\frac{1}{4\pi}\mathbb{I}^{\mathrm{S}\times 2}\left[\left(\frac{\lambda_0+\mu_0}{\mu_0(\lambda_0+2\mu_0)}\right)^2 \int_{\partial S} \boldsymbol{n}^{\otimes 8}\,\mathrm{d}S \right. \\ - \frac{\lambda_0+\mu_0}{2\mu_0^2(\lambda_0+2\mu_0)}\int_{\partial S} \boldsymbol{I}\times\boldsymbol{n}^{\otimes 6} + \boldsymbol{n}^{\otimes 6}\times\boldsymbol{I}\,\mathrm{d}S \\ \left. + \frac{1}{4\mu_0^2}\int_{\partial S}\boldsymbol{I}\times\boldsymbol{n}^{\otimes 4}\times\boldsymbol{I}\,\mathrm{d}S\right]. \quad (4.12)$$

As unwieldy as the above equation seems, the involved integrals simply impose isotropic symmetry on $2n$-fold tensor products

$$\int_{\partial S} \boldsymbol{n}^{\otimes 2n}\,\mathrm{d}S = 4\pi \mathrm{Iso}(\boldsymbol{e}_1^{\otimes \mathrm{2n}}). \quad (4.13)$$

Finding the isotropic projection of an index-symmetric tensor is equivalent to index-symmetrizing a corresponding isotropic tensor, as long as both tensors project onto the same index-symmetric isotropic tensor. In this case, calculation of the integral over $\boldsymbol{n}^{\otimes 2n}$ is equivalent to full index symmetrization of $\boldsymbol{I}^{\otimes n}$. The general tensor symmetrization formula given by Spencer (1970) can be used in a simplified form in this case because of the minor symmetries already present. Instead of calculating the sum over all index permutations of the tensor, we sum only those index permutations which are not trivialized by existing symmetries and denote those as Perm. With the double factorial $n!! = n(n-2)(n-4)...$,

$$\int_{\partial S} \boldsymbol{n}^{\otimes 2n}\,\mathrm{d}S = \frac{4\pi}{(2n+1)!!}\mathrm{Perm}(\boldsymbol{I}^{\otimes \mathrm{n}}). \quad (4.14)$$

As examples, symbolic forms are given for orders 2 and 4

$$\int_{\partial S} \boldsymbol{n}^{\otimes 2}\,\mathrm{d}S = \frac{4\pi}{3}\boldsymbol{I}, \qquad \int_{\partial S} \boldsymbol{n}^{\otimes 4}\,\mathrm{d}S = \frac{4\pi}{15}(3\mathbb{P}^{\circ} + 2\mathbb{I}^{\mathrm{S}}). \quad (4.15)$$

Due to the large number of possible index combinations for higher orders, symbolic forms for orders greater than four are not given here.

4.3.2 Second Moments Implied by the Mori-Tanaka Approach

Differentiating the Mori-Tanaka effective stiffness given in Eq. (3.140) by the matrix stiffness yields

$$\frac{\partial \bar{\mathbb{C}}}{\partial \mathbb{C}_\mathrm{M}} = \mathbb{I}^\mathrm{S}_{\langle 8 \rangle} - c_\mathrm{F} \left(\left((\mathbb{C}_\mathrm{F} - \mathbb{C}_\mathrm{M})^{-1} + c_\mathrm{M} \mathbb{P}_0 \right)^{-1} \right)^{-\times 2} \left(\left((\mathbb{C}_\mathrm{F} - \mathbb{C}_\mathrm{M})^{-1} \right)^{\times 2} + c_\mathrm{M} \frac{\partial \mathbb{P}_0}{\partial \mathbb{C}_\mathrm{M}} \right). \quad (4.16)$$

When differentiating by the inclusion stiffness, $\partial \mathbb{P}_0 / \partial \mathbb{C}_\mathrm{F}$ vanishes, such that

$$\frac{\partial \bar{\mathbb{C}}}{\partial \mathbb{C}_\mathrm{F}} = c_\mathrm{F} \left((\mathbb{I}^S + c_\mathrm{M} \mathbb{P}_0 (\mathbb{C}_\mathrm{F} - \mathbb{C}_\mathrm{M}))^{-1} \right)^{\times 2} = c_\mathrm{F} \langle \mathbb{A}_\mathrm{MT} \rangle_\mathrm{F}^{\times 2}. \quad (4.17)$$

Therefore, the inclusion covariance vanishes and the strain fields in the inclusion are homogeneous, as implied by the direct use of Eshelby's solution.

4.3.3 Second Moments Implied by the Singular Approximation

Deriving the general Singular Approximation stiffness of Eq. (3.144) by the phase stiffness yields

$$\frac{\partial \bar{\mathbb{C}}}{\partial \mathbb{C}_\alpha} = \frac{\partial \langle \mathbb{L} \rangle^{-1}}{\partial \mathbb{C}_\alpha} + \frac{\partial \mathbb{C}_0}{\partial \mathbb{C}_\alpha} - \frac{\partial \mathbb{P}_0^{-1}}{\partial \mathbb{C}_0} \frac{\partial \mathbb{C}_0}{\partial \mathbb{C}_\alpha}, \quad (4.18)$$

with the $\mathbb{L}$-term

$$\frac{\partial \langle \mathbb{L} \rangle^{-1}}{\partial \mathbb{C}_\alpha} = \langle \mathbb{L} \rangle^{-\times 2} \frac{\partial}{\partial \mathbb{C}_\alpha} \left(\sum_{\beta=1}^{N} c_\beta (\mathbb{C}_\beta - \mathbb{C}_0 + \mathbb{P}_0^{-1})^{-1} \right). \tag{4.19}$$

The derivative of the phasewise mean $\mathbb{L}_\beta = (\mathbb{C}_\beta - \mathbb{C}_0 + \mathbb{P}_0^{-1})^{-1}$ is

$$\frac{\partial c_\beta \mathbb{L}_\beta}{\partial \mathbb{C}_\alpha} = c_\beta \mathbb{L}_\beta^{\times 2} \left(\delta_{\alpha\beta} \mathbb{I}^{\mathrm{S}}_{\langle 8 \rangle} - \frac{\partial \mathbb{C}_0}{\partial \mathbb{C}_\alpha} + \frac{\partial \mathbb{P}_0^{-1}}{\partial \mathbb{C}_\alpha} \right). \tag{4.20}$$

Finally, the derivative of $\mathbb{P}_0^{-1}$ is

$$\frac{\partial \mathbb{P}_0^{-1}}{\partial \mathbb{C}_\alpha} = (\mathbb{P}_0^{-1})^{\square 2} \frac{\partial \mathbb{P}_0}{\partial \mathbb{C}_0} \frac{\partial \mathbb{C}_0}{\partial \mathbb{C}_\alpha}. \tag{4.21}$$

Notably, even though the Singular Approximation can be motivated by Eshelby's solution, as described in Section 3.2.4, neither phase has constant strains in the most general case. Because the standard deviation of the phase strains is linearly related to the standard deviation of the infinite distance strain $\boldsymbol{\varepsilon}_0$, this implies that the infinite distance strains in the Eshelby-based replacement ensemble are not constant within a single phase.

As a simple example for applying the above formulas, we model a microstructure which consists of inclusions F within a matrix M. Consequently, $\mathbb{C}_0$ is chosen as the matrix material, and the derivatives follow as

$$\frac{\partial \mathbb{C}_0}{\partial \mathbb{C}_\mathrm{M}} = \mathbb{I}^{\mathrm{S}}_{\langle 8 \rangle}, \qquad \frac{\partial \mathbb{C}_0}{\partial \mathbb{C}_\mathrm{F}} = \mathbb{0}. \tag{4.22}$$

While the terms for the second moment of the matrix are not appreciably simplified in this case, the second moment of the inclusion is compatible with Eshelby's result that the inclusion fluctuation vanishes, leading to a

vanishing covariance tensor

$$\langle \boldsymbol{\varepsilon} \otimes \boldsymbol{\varepsilon} \rangle_{\mathrm{F}} = \langle \boldsymbol{\varepsilon} \rangle_{\mathrm{F}} \otimes \langle \boldsymbol{\varepsilon} \rangle_{\mathrm{F}} \tag{4.23}$$

This can be proven using

$$\frac{\partial \mathbb{P}_0}{\partial \mathbb{C}_{\mathrm{F}}} = \mathbb{0}, \tag{4.24}$$

which leads to

$$\frac{\partial \langle \mathbb{L} \rangle^{-1}}{\partial \mathbb{C}_{\mathrm{F}}} = c_{\mathrm{F}} \langle \mathbb{L} \rangle^{-\times 2} \mathbb{L}_{\mathrm{F}}^{\times 2} \mathbb{I}^{\mathrm{S}}_{\langle 8 \rangle} = c_{\mathrm{F}} (\langle \mathbb{L} \rangle^{-1} \mathbb{L}_{\mathrm{F}})^{\times 2}. \tag{4.25}$$

With the strain localization tensor $\mathbb{A} = \mathbb{L} \langle \mathbb{L} \rangle^{-1}$, we find

$$\frac{\partial \bar{\mathbb{C}}}{\partial \mathbb{C}_{\mathrm{F}}} = c_{\mathrm{F}} (\langle \mathbb{A} \rangle_{\mathrm{F}}^{\mathsf{T}})^{\times 2}. \tag{4.26}$$

The second moment follows as outlined in Section 4.2

$$\langle \boldsymbol{\varepsilon} \otimes \boldsymbol{\varepsilon} \rangle_{\mathrm{F}} = \frac{1}{c_{\mathrm{F}}} \left(\frac{\partial \bar{\mathbb{C}}}{\partial \mathbb{C}_{\mathrm{F}}} \right)^{\mathsf{T}} [\bar{\boldsymbol{\varepsilon}} \otimes \bar{\boldsymbol{\varepsilon}}] = \langle \mathbb{A} \rangle_{\mathrm{F}} [\bar{\boldsymbol{\varepsilon}}] \otimes \langle \mathbb{A} \rangle_{\mathrm{F}} [\bar{\boldsymbol{\varepsilon}}] = \langle \boldsymbol{\varepsilon} \rangle_{\mathrm{F}} \otimes \langle \boldsymbol{\varepsilon} \rangle_{\mathrm{F}}. \tag{4.27}$$

4.3.4 Second Moments Implied by the Hashin-Shtrikman Bounds

The Hashin-Shtrikman bounds are recovered from the Singular Approximation by setting $\mathbb{C}_0 = \mathbb{C}_0^{+,-}$ as defined in Section 3.2.4 via the eigenvalue decompositions of the phase stiffnesses $\mathbb{C}$. Since all eigenvalues are positive in the vicinity of $\gamma = \gamma_{\min}$, the corresponding value of $\lambda_{\max}$ is the spectral radius $r(\mathbb{C} - \gamma \mathbb{P}^{\circ})$. The spectral radius is not differentiable for arguments with multiple maximum eigenvalues, see e.g. Cohen (1978). As a result, $\mathbb{C}_0$ is not differentiable for isotropic phases. Worse,

$\gamma + 6\lambda_{\max}(\gamma)$ is not differentiable in the critical point regardless of the material symmetry, making it quite difficult to find an explicit formula for the minimum. However, a necessary condition is that calculating the effective energy with the covariances resulting from these derivatives gives the same result as using the effective stiffness and effective strains. Such a result may be found by assuming that

$$3\frac{\partial K_{0\alpha}}{\partial \mathbb{C}_\alpha} = \mathbb{P}^\circ, \qquad 2\frac{\partial G_{0\alpha}}{\partial \mathbb{C}_\alpha} = \frac{1}{5}\mathbb{P}'. \tag{4.28}$$

For the lower bound, we derive, with $\partial \mathbb{S}_0/\partial \mathbb{S}$ analogous to the above derivatives,

$$\frac{\partial \mathbb{C}_0}{\partial \mathbb{C}} = (\mathbb{C}_0 \times \mathbb{C}_0)\frac{\partial \mathbb{S}_0}{\partial \mathbb{S}}(\mathbb{S} \times \mathbb{S}). \tag{4.29}$$

In many industrial applications, the composite consists of a weak phase which is reinforced by a stronger phase. In such microstructures, $\mathbb{C}_0$ does not depend on the weaker phase if the upper bound is being considered. Consequently, the weaker phase experiences no fluctuation. For the lower bound, the stronger phase experiences no fluctuation.

4.3.5 Second Moments in Terms of Effective Stiffnesses

For the general Singular Approximation for anisotropic materials, we write

$$\begin{aligned}\langle \boldsymbol{\varepsilon} \otimes \boldsymbol{\varepsilon} \rangle_\alpha =& \langle \boldsymbol{\varepsilon} \rangle_\alpha^{\otimes 2} \\ &+ \frac{1}{c_\alpha}\left(\frac{\partial \mathbb{C}_0}{\partial \mathbb{C}_\alpha}\right)^{\mathsf{T}}\left(\frac{\partial \mathbb{P}_0^{-1}}{\partial \mathbb{C}_0} - \mathbb{I}^{\mathrm{S}}_{\langle 8\rangle}\right)^{\mathsf{T}}\left[-\bar{\boldsymbol{\varepsilon}}^{\otimes 2} + \sum_{\beta=1} c_\beta \langle \boldsymbol{\varepsilon} \rangle_\beta^{\otimes 2}\right].\end{aligned} \tag{4.30}$$

In the following, the more concise formula for the covariance of strains $\mathbb{K}_\alpha = \langle \boldsymbol{\varepsilon} \otimes \boldsymbol{\varepsilon} \rangle_\alpha - \langle \boldsymbol{\varepsilon} \rangle_\alpha \otimes \langle \boldsymbol{\varepsilon} \rangle_\alpha$ will be given. For the above case,

$$\mathbb{K}_\alpha = \frac{1}{c_\alpha} \left(\frac{\partial \mathbb{C}_0}{\partial \mathbb{C}_\alpha} \right)^\mathsf{T} \left(\frac{\partial \mathbb{P}_0^{-1}}{\partial \mathbb{C}_0} - \mathbb{I}^\mathrm{S}_{\langle 8 \rangle} \right)^\mathsf{T} \left[-\bar{\boldsymbol{\varepsilon}} \otimes \bar{\boldsymbol{\varepsilon}} + \sum_{\beta=1} c_\beta \langle \boldsymbol{\varepsilon} \rangle_\beta \otimes \langle \boldsymbol{\varepsilon} \rangle_\beta \right]. \tag{4.31}$$

The simple Singular Approximation with an inclusion (F) and a matrix phase (M) yields

$$\mathbb{K}_\mathrm{F} = \mathbb{0} \tag{4.32}$$

$$\mathbb{K}_\mathrm{M} = \frac{1}{c_\mathrm{M}} \left(\left(\frac{\partial \mathbb{P}_0^{-1}}{\partial \mathbb{C}_0} - \mathbb{I}^\mathrm{S}_{\langle 8 \rangle} \right)^\mathsf{T} \left[-\bar{\boldsymbol{\varepsilon}} \otimes \bar{\boldsymbol{\varepsilon}} + \sum_{\beta=1} c_\beta \langle \boldsymbol{\varepsilon} \rangle_\beta \otimes \langle \boldsymbol{\varepsilon} \rangle_\beta \right] \right). \tag{4.33}$$

With γ_K denoting the phase with extremal K_0 and γ_G for G_0, the Hashin-Shtrikman bounds for isotropic phases yield

$$\begin{aligned} \mathbb{K}_\alpha = & \frac{\delta_{\alpha\gamma_K}}{c_\alpha} \left(\left(\frac{\partial \mathbb{P}_0^{-1}}{\partial \mathbb{C}_0} [\mathbb{P}^\circ] - \mathbb{P}^\circ \right) \cdot \left(-\bar{\boldsymbol{\varepsilon}} \otimes \bar{\boldsymbol{\varepsilon}} + \sum_{\beta=1} c_\beta \langle \boldsymbol{\varepsilon} \rangle_\beta \otimes \langle \boldsymbol{\varepsilon} \rangle_\beta \right) \right) \mathbb{P}^\circ \\ & + \frac{\delta_{\alpha\gamma_G}}{5c_\alpha} \left(\left(\frac{\partial \mathbb{P}_0^{-1}}{\partial \mathbb{C}_0} [\mathbb{P}'] - \mathbb{P}' \right) \cdot \left(-\bar{\boldsymbol{\varepsilon}} \otimes \bar{\boldsymbol{\varepsilon}} + \sum_{\beta=1} c_\beta \langle \boldsymbol{\varepsilon} \rangle_\beta \otimes \langle \boldsymbol{\varepsilon} \rangle_\beta \right) \right) \mathbb{P}'. \end{aligned} \tag{4.34}$$

The effective stiffness of the Hashin-Shtrikman lower bound coincides with the simple Singular Approximation when $\mathbb{C}_\mathrm{M} = \mathbb{C}_0$, such as for fiber-reinforced polymers. The second moments given by the two approaches may still differ. For the Mori-Tanaka approach, the results have been found numerically to be identical to the simple Singular Approximation. An analytical proof remains to be found to our knowledge.

Section 4.3.2 yields the outwardly different form

$$\begin{aligned}\langle \boldsymbol{\varepsilon} \otimes \boldsymbol{\varepsilon} \rangle_{\mathrm{F}} =& \langle \boldsymbol{\varepsilon} \rangle_{\mathrm{F}} \otimes \langle \boldsymbol{\varepsilon} \rangle_{\mathrm{F}}, \\ \langle \boldsymbol{\varepsilon} \otimes \boldsymbol{\varepsilon} \rangle_{\mathrm{M}} =& \frac{1}{c_{\mathrm{M}}} \left(\bar{\boldsymbol{\varepsilon}}^{\otimes 2} - c_{\mathrm{F}} \langle \boldsymbol{\varepsilon} \rangle_{\mathrm{F}}^{\otimes 2} - c_{\mathrm{F}} \left(\frac{\partial \mathbb{P}_0}{\partial \mathbb{C}_0} \right)^{\mathsf{T}} \left[(\mathbb{C}_{\mathrm{F}} - \mathbb{C}_{\mathrm{M}}) [\langle \boldsymbol{\varepsilon} \rangle_{\mathrm{F}}]^{\otimes 2} \right] \right).\end{aligned} \tag{4.35}$$

From the full tensorial second moment expression, the more commonly used scalar second moments of $\|\boldsymbol{\varepsilon}^{\circ}\|$ and $\|\boldsymbol{\varepsilon}'\|$, the latter of which is in isotropic phases directly related to the second moment of the von Mises equivalent stress, can be recovered by a scalar product with the isotropic projectors $\mathbb{P}^{\circ}$ and $\mathbb{P}'$, respectively. In the matrix-inclusion case, for example, the expressions read

$$\langle \|\boldsymbol{\varepsilon}^{\circ}\|^2 \rangle_{\mathrm{F}} = \langle \boldsymbol{\varepsilon}^{\circ} \rangle_{\mathrm{F}} \cdot \langle \boldsymbol{\varepsilon}^{\circ} \rangle_{\mathrm{F}}, \quad \langle \|\boldsymbol{\varepsilon}^{\circ}\|^2 \rangle_{\mathrm{M}} = \langle \boldsymbol{\varepsilon}^{\circ} \rangle_{\mathrm{M}} \cdot \langle \boldsymbol{\varepsilon}^{\circ} \rangle_{\mathrm{M}} + \mathbb{K}_{\mathrm{M}} \cdot \mathbb{P}^{\circ}, \tag{4.36}$$

and

$$\langle \|\boldsymbol{\varepsilon}'\|^2 \rangle_{\mathrm{F}} = \langle \boldsymbol{\varepsilon}' \rangle_{\mathrm{F}} \cdot \langle \boldsymbol{\varepsilon}' \rangle_{\mathrm{F}}, \quad \langle \|\boldsymbol{\varepsilon}'\|^2 \rangle_{\mathrm{M}} = \langle \boldsymbol{\varepsilon}' \rangle_{\mathrm{M}} \cdot \langle \boldsymbol{\varepsilon}' \rangle_{\mathrm{M}} + \mathbb{K}_{\mathrm{M}} \cdot \mathbb{P}'. \tag{4.37}$$

In contrast to the second moments shown here, the first moment $\langle \|\boldsymbol{\varepsilon}'\| \rangle_{\mathrm{M}}$ is in general inaccessible to mean-field methods if the fluctuations are non-zero, because the norm is nonlinear in the components of $\boldsymbol{\varepsilon}'$.

4.4 Comparison with Full-Field Simulations

To validate the theoretical results, we use full-field simulation results. The methodology for generating these results, including resolution and representativity studies, is described in Krause et al. (2023)[2].

[2] The full-field simulations were carried out by Dr. Tarkes Dora Pallicity during his time at the Institute of Engineering Mechanics, ITM and are therefore not part of this thesis.

As an example material, we consider a glass-reinforced polymer, due to its relatively high elastic contrast. The matrix material models an elastic unsaturated polyester-polyurethane hybrid (UPPH), as described e.g. by Trauth et al. (2021). Instead of fibers, spherical glass inclusions are considered. The material properties of the matrix and the particles are given in Table 4.1.

Material	E in GPa	ν
Matrix	3.4	0.385
Inclusion	73	0.22

Table 4.1: Material properties of UPPH matrix and glass spherical particles (Kehrer, 2019). Table based on Table 1 of Krause et al. (2023).

For the analytical comparison, four results in particular are considered: the Singular Approximation with a distinct matrix (SA), the Hashin-Shtrikman lower bound (HS), and the Mori-Tanaka approach (MT). In the isotropic case, these analytical methods yield the same effective stiffness, but not necessarily the same covariance.

Method	$\bar{K}$ in GPa	$\bar{G}$ in GPa
SA, HSLB, MT	6.7105	2.0346
FEM	6.7400	2.1145

Table 4.2: Effective stiffness comparison

Instead of the strain covariances, we will describe the stress covariances given by $\mathbb{K}_\sigma = \mathbb{C}\mathbb{K}_\varepsilon\mathbb{C}$. For a uniaxial effective stress of $1\,\mathrm{MPa}$, the matrix

covariances result, in units of MPa^2, as

$$\mathbb{K}_{\mathrm{SA,MT}} \hat{=} \begin{pmatrix} 0.0946 & 0.0 & 0.0 & 0.0 & 0.0 & 0.0393 \\ 0.0 & 0.0123 & 0.0 & 0.0 & 0.0 & 0.0 \\ 0.0 & 0.0 & 0.0123 & 0.0 & 0.0 & 0.0 \\ 0.0 & 0.0 & 0.0 & 0.0178 & 0.0 & 0.0 \\ 0.0 & 0.0 & 0.0 & 0.0 & 0.0178 & 0.0 \\ 0.0393 & 0.0 & 0.0 & 0.0 & 0.0 & 0.0308 \end{pmatrix}, \tag{4.38}$$

$$\mathbb{K}_{\mathrm{HS}} \hat{=} \begin{pmatrix} 0.0947 & 0.0 & 0.0 & 0.0 & 0.0 & 0.0 \\ 0.0 & 0.0182 & 0.0 & 0.0 & 0.0 & 0.0 \\ 0.0 & 0.0 & 0.0182 & 0.0 & 0.0 & 0.0 \\ 0.0 & 0.0 & 0.0 & 0.0182 & 0.0 & 0.0 \\ 0.0 & 0.0 & 0.0 & 0.0 & 0.0182 & 0.0 \\ 0.0 & 0.0 & 0.0 & 0.0 & 0.0 & 0.0182 \end{pmatrix}, \tag{4.39}$$

$$\mathbb{K}_{\mathrm{FEM}} \hat{=} \begin{pmatrix} 0.1259 & 0.0008 & -0.0013 & 0.0047 & -0.0016 & 0.0430 \\ 0.0008 & 0.0128 & -0.0008 & -0.0004 & 0.0015 & 0.0002 \\ -0.0013 & -0.0008 & 0.0115 & 0.0009 & -0.0005 & 0.0003 \\ 0.0047 & -0.0004 & 0.0009 & 0.0161 & -0.0003 & 0.0024 \\ -0.0016 & 0.0015 & -0.0005 & -0.0003 & 0.0168 & -0.0006 \\ 0.0430 & 0.0002 & 0.0003 & 0.0024 & -0.0006 & 0.0287 \end{pmatrix}. \tag{4.40}$$

In the harmonic basis representations of the covariance tensors, it can be seen directly that the Hashin-Shtrikman is isotropic, while the other analytical solution is transversal-isotropic. As the microstructure is isotropic and the loading transversal-isotropic, the FEM should yield a transversal-isotropic result as well. Any deviation from the transversal-isotropic symmetry must be considered a numerical error, which is either due to the 20-sphere microstructure not being perfectly representative of an isotropic composite or due to numerical imprecision of the FEM discretization, i.e, resolution errors. The asymmetry serves as a lower bound of the total error, which comes out to

$$\|\mathbb{K}_{\mathrm{FEM}} - \mathrm{tiso}(\mathbb{K}_{\mathrm{FEM}})\| = 0.0087\,\mathrm{MPa}^2 \tag{4.41}$$

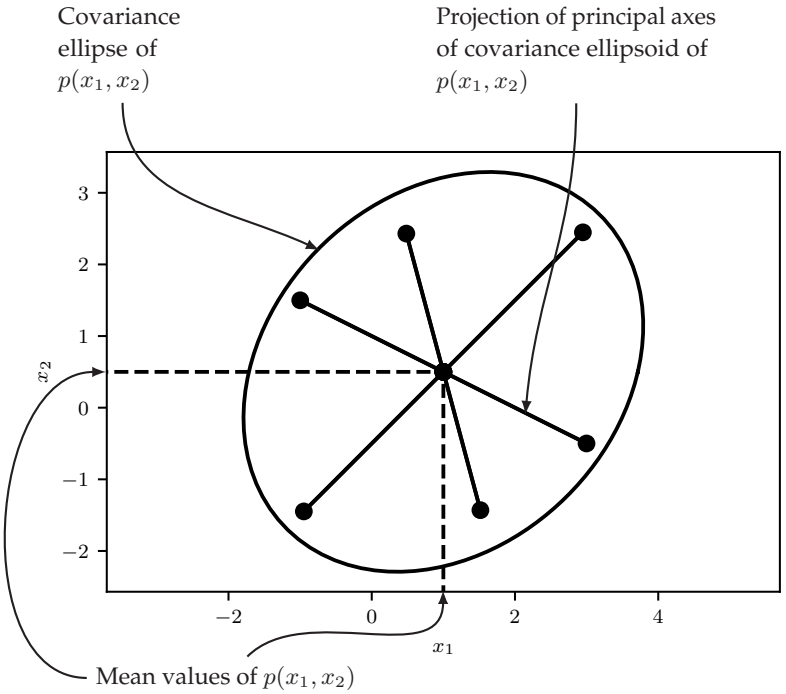

Figure 4.1: Annotated example covariance ellipse of a marginal distribution $p(x_1, x_2)$ of a full distribution $p(\boldsymbol{x})$, showing the information conveyed in this diagram type.

or about $5\,\%$ in relative terms.

To visually compare the various covariance results, we use covariance ellipse diagrams similar to those used in Krause and Böhlke (2020). Unlike that earlier work, in which the $\boldsymbol{e}_i$-basis was used to depict stresses and strains, we will use the second-order symmetric harmonic basis, which is particularly useful for transversal-isotropic covariances. In Fig. 4.1, an example of this kind of diagram is illustrated for a probability distribution $p(\boldsymbol{x})$ of a three-dimensional variable $\boldsymbol{x}$. In the shown projection, only two components x_1 and x_2 are explicitly visible. The center of the ellipse is the expectation value of $\boldsymbol{x}$. For a multivariate

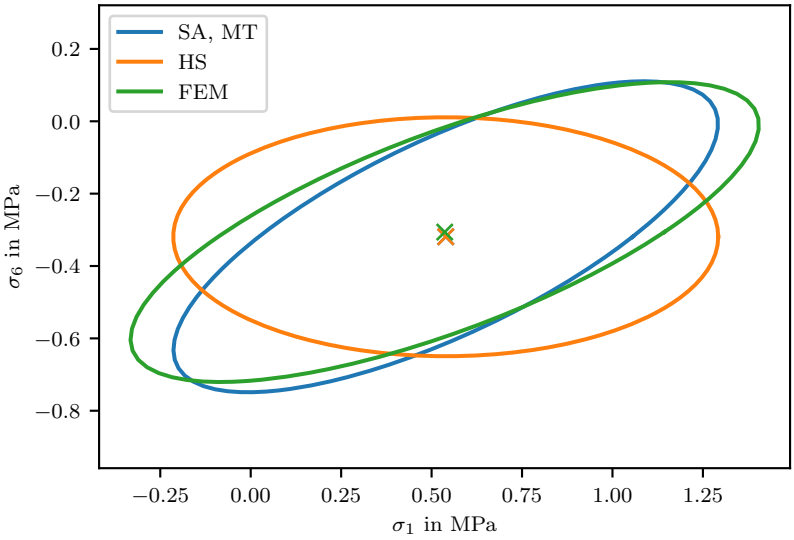

Figure 4.2: Covariance ellipse of the marginal distribution $p(\sigma_1, \sigma_6)$.

normal distribution $p(\boldsymbol{x})$, the shown ellipse is scaled so that it contains $95\,\%$ of all random points.

The σ_1-σ_6 ellipse shown in Fig. 4.2 shows the spherical stresses σ_1 and the load-aligned deviatoric stresses σ_6. For transversal-isotropic results, these correlate, showing a tilt of the FEM covariance ellipse that the Hashin-Shtrikman approach cannot reproduce, but the SA approach does.

Another significant difference between methods can be seen in Fig. 4.3, which shows the σ_3-σ_4 covariance, i.e., the σ_{12} and σ_{13} shear components. For the isotropic Hashin-Shtrikman covariances, these have the same covariance, while the transversal-isotropic covariances show the same slight slight difference between those two directions for both the numerical and the analytical solution. The numerical solution also shows a slight tilt, which is on the order of the numerical error. For perfectly

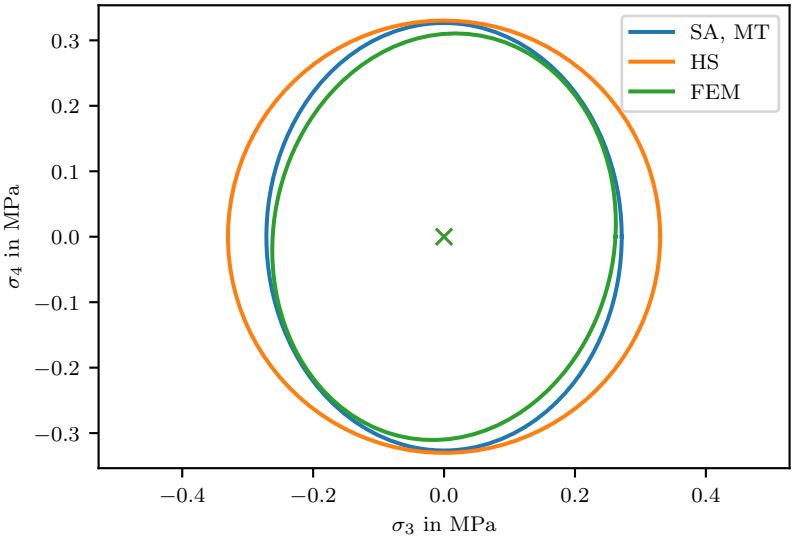

Figure 4.3: Covariance ellipse of the marginal distribution $p(\sigma_3, \sigma_4)$.

transversal-isotropic covariances, the σ_1-σ_6 and σ_3-σ_4 diagrams, taken together, show all independent components.

The FEM solution, unlike the analytical solutions, also yields a nonzero inclusion covariance, which is

$$\mathbb{K}_{\mathrm{FEM,incl}} \hat{=} \begin{pmatrix} 0.0433 & 0.0052 & -0.0026 & -0.0015 & -0.0035 & 0.0261 \\ 0.0052 & 0.0301 & -0.0054 & -0.005 & 0.0025 & 0.0015 \\ -0.0026 & -0.0054 & 0.025 & -0.002 & -0.0001 & -0.0006 \\ -0.0015 & -0.005 & -0.002 & 0.0339 & -0.0029 & 0.0009 \\ -0.0035 & 0.0025 & -0.0001 & -0.0029 & 0.032 & -0.0039 \\ 0.0261 & 0.0015 & -0.0006 & 0.0009 & -0.0039 & 0.0474 \end{pmatrix}. \tag{4.42}$$

The numerical error is higher than in the matrix at

$$\|\mathbb{K}_{\text{FEM, incl}} - \operatorname{tiso}(\mathbb{K}_{\text{FEM, incl}})\| = 0.017\,\text{MPa}^2, \tag{4.43}$$

suggesting that the inclusions are less representative of a statistically transversal-isotropic ensemble than the matrix is. Nonetheless, there is a transversal-isotropic part which significantly exceeds the anisotropic error part at

$$\|\operatorname{tiso}(\mathbb{K}_{\text{FEM, incl}})\| = 0.096\,\text{MPa}^2. \tag{4.44}$$

With transversal-isotropic covariances exceeding the error by a factor of 5, the results from the 20 sphere FEM model suggest that the stresses in the inclusions are slightly heterogeneous, which is not what the Mori-Tanaka and simple SA models predict.

4.5 Conclusions

Explicit formulas for the second moments resulting from the Mori-Tanaka approach, the Singular Approximation and the Hashin-Shtrikman bounds were derived. For the case of spherical inclusions and an isotropic matrix or reference stiffness, the results are fully analytical.

The second moments of Mori-Tanaka and a simple Singular Approximation approach are equivalent in the case of isotropic phases and spherical inclusions. By contrast, the Hashin-Shtrikman approach which yields the same effective stiffness results in different, isotropic covariances. All three approaches result in vanishing inclusion covariances, which is consistent with Eshelby's result of homogeneous inclusion stresses and strains.

A comparison with numerical solutions of a random sphere assemblage (RSA) microstructure showed that the Singular Approximation and Mori-Tanaka approach yielded good results for the second moment of matrix strain. As the Hashin-Shtrikman covariance is isotropic, it is

not well-suited for predicting the behavior under deviatoric loading. Furthermore, moments higher than the second are not accessible by the analytical method portrayed here and may significantly change the local material behavior. In the considered case of glass fiber reinforced polymer with a fiber volume fraction of $25\,\%$, the impact of higher moments seems not too large to use analytical methods.

In conclusion, this chapter uses the link between the effective energy density of a heterogeneous material and the statistics of its strain field to calculate full tensorial covariances of stress and strain fields based on various established homogenization methods. When considering nonlinear effects such as failure, knowing the covariance allows for a more accurate material description than merely considering the mean. As the expressions derived in this paper are fully analytical, they are usable in situations where computational resources are scarce, such as in micromechanically motivated material models intended for macroscale FEM simulations.

Chapter 5

The micromechanical Maximum Entropy Method

5.1 Introduction to Maximum Entropy Methods

5.1.1 Basics of discrete probability theory

The following is an introduction to basic notions of probability theory which mostly serves to define terms and notation. A more complete and rigorous definition can be found in an introductory textbook on probability theory, such as Henze (1997).

Probability is the mathematical description of the likelihood of outcomes of events. In this text, the probabilistic events under consideration are possible values of a random variable X. The variable may take any value from a finite sample space $\{X_i\}$, $i \in [1, N]$, also called *ensemble*. Any outcome is associated with a probability

$$P \in [0, 1] \tag{5.1}$$

such that

$$\sum_{i=1}^{N} P(X_i) = 1. \tag{5.2}$$

The probability of an outcome within a subset A of the sample space occurring is given by the sum

$$P(A) = \sum_{X_i \in A} P(X_i), A \subseteq \{X_i\}. \tag{5.3}$$

Equations (5.1)–(5.3) constitute the axioms of probability theory introduced by Kolmogoroff (1933). While they are sufficiently precise to define probability from a mathematical point of view, they do not provide an intuitive meaning of probability, which hinges on what one considers *random*. As a simple example, we consider a face-down deck of cards, from which one card is drawn as a probabilistic event. The outcome may be any of the cards in the deck, which are for simplicity numbered $[1, N]$. If the deck is properly shuffled, the outcome is by intuition considered random. However, in the mechanically deterministic perspective on physics, the deck is not random at all. Rather, its order is determined by the motions of the shuffler. The randomness of the situation arises not because it is truly nondeterministic, but because the motions of the shuffler, and therefore the order of the deck, are not precisely known. Unknown information can therefore be modeled as random information. Insofar as it is necessary to decide on an interpretation of probability, this suggests a Bayesian perspective on probability. In this Bayesian perspective, probabilities are estimates of likelihood based on known information, which are observer-dependent insofar as not all observers of a random event know the same information. This seeming subjectivity is not an issue for practical calculation as long as the observer state is clearly specified.

5.1.2 Information entropy

In the previous section, probability was linked to unknown information. A quantifiable approach to this correspondence was found by Shannon (1948), who defined the information content of a probabilistic ensemble as the information-theoretic entropy

$$S = -\sum_{i=1}^{N} P(X_i) \ln P(X_i). \tag{5.4}$$

Intuitively, S quantifies the amount of information gained from sampling an ensemble. We return to the example of the deck of cards. If the deck's state is entirely known, there is one state X_1 with probability 1, and $S = 0$. Drawing from a deck which is entirely known yields no information; consequently, any such state has entropy $S = 0$. A deterministic model is sufficient.

Of more interest to this work is the state with maximal entropy. In case of the deck of cards, maximizing entropy yields an ensemble with a uniform probability distribution, i.e., for which each state of the deck of cards has the same probability. As the maximally entropic state maximizes random information, it is well-suited for an observer that has no prior deterministic information. A detailed discussion of this concept is found in Jaynes (1968).

It can be argued that the simplistic model of a shuffled deck of cards, in the maximum entropy formulation, already contains a number of additional assumptions. For an artificially complicated example, suppose the dealer shuffling the deck of cards has a bias. Then, the actual probability diverges from the maximally entropic state, such that entropy maximization is only sensible under the additional assumption that there is no bias. However, if the bias is possible, but not actually known, i.e., the bias is an unknown unknown, it can be modeled simply as part of the random process of shuffling the deck. From the observer's

point of view, if there may or may not be some kind of unspecified bias, the optimal prior probability is again that which is maximally entropic. The discussion of unknown biases corresponds roughly to the distinction between aleatory (physically random) and epistemic (model-based) uncertainties in uncertainty quantification as described by Der Kiureghian and Ditlevsen (2009). As the perspective of this work is based on the assumption of probability quantifying unknown information, all probabilities discussed in this work are treated as purely aleatory.

5.1.3 Continuous probability densities

Formally, when the system under consideration can be described by a state vector $\boldsymbol{v} \in \mathcal{V}$,

$$p : \mathcal{V} \to \mathbb{R} \tag{5.5}$$

is a *probability density function* (PDF) if it satisfies

$$p(\boldsymbol{v}) \geq 0 \quad \forall \boldsymbol{v}, \tag{5.6}$$

$$\int_{\mathcal{V}} p(\boldsymbol{v}) \, \mathrm{d}V(\boldsymbol{v}) = 1. \tag{5.7}$$

The value of the PDF is not a probability, but a probability density. The integral of the PDF over a subset of $\mathcal{V}$ describes the probability that the value of the random variable falls within that subset. Correspondingly, despite their name, PDFs are not limited to functions, but may more generally be distributions, if the corresponding integrals exist. Of particular note is the Dirac delta distribution $\delta(\boldsymbol{v})$, for which

$$\delta(\boldsymbol{v}) = 0 \quad \forall \boldsymbol{v} \neq \boldsymbol{0}, \tag{5.8}$$

$$\int_{\mathcal{V}} \delta(\boldsymbol{v}) \, \mathrm{d}V(\boldsymbol{v}) = 1. \tag{5.9}$$

A distribution consisting only of weighted Dirac deltas behaves like a discrete distribution, which makes it possible to consider discrete random variables in the framework of continuous probabilities. For a more rigorous definition of the same correspondence, we refer to introductory textbooks on measure theory, e.g., Henze (1997).

5.1.4 Maximum entropy in the continuous case

Following Jaynes (1963), the continuous extension of Shannon's information entropy is defined as the entropy functional

$$S = -\int_{\mathcal{V}} p(\boldsymbol{v}) \ln\left(\frac{p(\boldsymbol{v})}{p_0}\right) \mathrm{d}V(\boldsymbol{v}). \tag{5.10}$$

The normalizing factor p_0 is described by Jaynes (1963) as a density measure of $\mathcal{V}$ which arises as the limit of discrete probability measures is taken, which we presume to be constant. If the above integral is not defined for a given PDF p and domain $\mathcal{V}$, neither is the information entropy.

As discussed in Section 5.1.2, maximizing information entropy yields the most sensible prior probability in the absence of further information. The maximization problem can be formally stated as

$$\max_p S \quad \text{subject to} \quad F_\beta(p) = 0, \tag{5.11}$$

where $F_\beta(p)$ are optimization constraints in the form of functionals. By specifying these optimization constraints, information that is available about the problem can be integrated into the entropy maximization.

5.1.5 Applicability of the continuous Maximum Entropy Method

A maximum entropy probability density is generally an approximation. The difference between the maximum entropy solution and the real solution is the result of whatever information about the system remained unknown. Consequently, the MEM is not expected to perform well if the system under consideration is constrained in some manner that is not implemented into the entropy maximization, i.e., has hidden structure. In the example of the deck of cards, the MEM does not perform well if the dealer is cheating and the observer is not aware of it.

A more fundamental restriction of the MEM goes back to Bertrand (1889). According to Bertrand's paradox, the optimal prior probability depends on the choice of random variables with which to parametrize the probabilistic problem. A simple example is a probabilistic ensemble of cubes of random size. If the side length of the cubes is considered as the random variable, the MEM yields a different result than if the volume of the cubes is considered as the random variable, at least if p_0 is presumed to be constant in both cases. In this simplistic example, the conclusion seems obvious, but Bertrand's original paradox is slightly more subtle, involving the distribution of chords on a circle. Jaynes (1973) attempted to solve Bertrand's paradox by deriving the probability distribution from fundamental invariants of the problem. However, as Drory (2015) showed, this invariance-based approach suffers from fundamentally the same problem. Thus, the MEM is fundamentally dependent on the choice of variables, and a MEM result that is not a good model of reality may simply suffer from a poor choice of variables.

If the integral in Eq. (5.10) does not converge, the MEM is ill-defined. A simple example is given by the unconstrained maximum entropy problem on $\mathbb{R}$. By analogy with the finite discrete case, the expected result is a constant PDF. However, on an infinite domain, there is no

constant such that the integral converges. Correspondingly, the MEM cannot be applied to this seemingly simple problem.

Despite the above arguments, the MEM is particularly well-suited for the class of problems considered in this work. For problems with quadratic constraints, i.e., constraints of the form

$$F(p) = \int_{\mathcal{V}} (\boldsymbol{v} - \boldsymbol{b}) \cdot \boldsymbol{A}[\boldsymbol{v} - \boldsymbol{b}] \, \mathrm{d}V(\boldsymbol{v}), \tag{5.12}$$

where $\boldsymbol{A} \in \mathcal{V} \otimes \mathcal{V}$ is positive-definite, the MEM is not only well-defined, but analytically solvable.

5.2 The Single-Point micromechanical Maximum Entropy Method

5.2.1 Single-Point statistical micromechanics

The following section discusses the Maximum Entropy Method first described by Kreher and Pompe (1989), chapter 7.2. This one-point Maximum Entropy Method is a method to estimate the probability distribution of the material properties and local fields in a single material point without considering correlations with other points. The MEM assumes an affine linear elastic material as described in Section 3.1.3. Kreher's original approach involves additively splitting the random strain field $\boldsymbol{\varepsilon}$ into residual strains $\boldsymbol{\varepsilon}_{\mathrm{R}}$ and strains caused by an applied external load $\boldsymbol{\varepsilon}_{\mathrm{L}}$, in the same manner as Section 3.2.2. However, the same results can be obtained without this split, simplifying the derivation. Thus, the probability distribution to be investigated is the joint probability distribution $p(\boldsymbol{\varepsilon}, \mathbb{C}, \boldsymbol{E})$. From this distribution, the linear and residual fields can be recovered by the superposition principle.

The micromechanical maximum entropy problem is constrained by known information. First, the joint probability distribution p must be compatible with the known one-point probability distribution of material properties p_1^{C}, which yields the marginalization condition

$$p_1^{\mathrm{C}}(\mathbb{C}, \boldsymbol{E}) = \int_{\mathrm{Sym}} p(\boldsymbol{\varepsilon}, \mathbb{C}, \boldsymbol{E}) \, \mathrm{d}V(\boldsymbol{\varepsilon}). \tag{5.13}$$

To be physically consistent, the local strain field must fulfill the balance of momentum and be kinematically compatible. In the one-point setting, a direct formulation based on partial differential equations is not possible. Instead, the Hill-Mandel condition (Eq. (3.111)), which holds only if $\boldsymbol{\sigma}$ is divergence-free and $\boldsymbol{\varepsilon}$ is compatible, is presumed to hold. With the Hill-Mandel condition, classical homogenization can be applied to yield a macroscopic effective problem with homogeneous fields $\bar{\boldsymbol{\sigma}}$ and $\bar{\boldsymbol{\varepsilon}}$, which are each given by expectation values, reading

$$\bar{\boldsymbol{\sigma}} = \langle \mathbb{C}[\boldsymbol{\varepsilon} - \boldsymbol{E}] \rangle, \tag{5.14}$$

$$\bar{\boldsymbol{\varepsilon}} = \langle \boldsymbol{\varepsilon} \rangle, \tag{5.15}$$

In the context of the MEM, the definition of the effective fields imposes constraints on the first statistical moments or mean values of the strain field. The Hill-Mandel condition

$$\langle \boldsymbol{\varepsilon} \cdot \mathbb{C}[\boldsymbol{\varepsilon}] \rangle = \bar{\boldsymbol{\varepsilon}} \cdot \bar{\mathbb{C}}[\bar{\boldsymbol{\varepsilon}}], \tag{5.16}$$

imposes a constraint on the second statistical moments of the strain field. As described in Section 3.2.2, the effective eigenstrain energy is independent of $\bar{\mathbb{C}}$ and $\bar{\boldsymbol{E}}$ and therefore yields the additional constraint

$$\bar{w}_{\mathrm{R}} = -\frac{1}{2} \langle \boldsymbol{\sigma}^{\mathrm{R}} \cdot \boldsymbol{E} \rangle, \tag{5.17}$$

which can be formulated without splitting the fields as

$$\bar{w}_{\mathrm{R}} = \frac{1}{2}\left(\bar{\boldsymbol{E}} \cdot \bar{\mathbb{C}}[\bar{\boldsymbol{\varepsilon}} - \bar{\boldsymbol{E}}] - \langle \boldsymbol{E} \cdot \mathbb{C}[\boldsymbol{\varepsilon} - \boldsymbol{E}]\rangle\right). \tag{5.18}$$

5.2.2 General solution

The one-point micromechanical entropy functional is

$$S = -\int_{\mathcal{V}} p(\boldsymbol{v}) \ln\left(\frac{p(\boldsymbol{v})}{p_0}\right) \mathrm{d}V(\boldsymbol{v}), \tag{5.19}$$

where for brevity, we introduce

$$\mathcal{V} = \mathrm{Sym} \oplus \mathcal{C} \oplus \mathrm{Sym} \tag{5.20}$$

such that $\boldsymbol{v} \in \mathcal{V}$ is a 33-dimensional vector defined as the concatenation

$$\boldsymbol{v} = \begin{pmatrix} \boldsymbol{\varepsilon} \\ \mathbb{C} \\ \boldsymbol{E} \end{pmatrix}. \tag{5.21}$$

Equations (5.16) and (5.18) result in the scalar constraints 1 and 2, which each take the form

$$\langle f_i(\boldsymbol{v})\rangle = 0, \quad i \in \{1, 2\}. \tag{5.22}$$

Equations (5.14) and (5.15) result in the second-order symmetric tensorial constraints 3 and 4, which each take the form

$$\langle \boldsymbol{F}_i(\boldsymbol{v})\rangle = \boldsymbol{0}, \quad i \in \{3, 4\}. \tag{5.23}$$

To incorporate constraints into the maximum entropy problem of Eq. (5.19), the method of Lagrange multipliers is used, which leads

to the modified functional

$$S^* = S + \sum_{i=1}^{2} \lambda_i \langle f_i(\boldsymbol{v}) \rangle + \sum_{i=3}^{4} \boldsymbol{\lambda}_i \cdot \langle \boldsymbol{F}_i(\boldsymbol{v}) \rangle. \tag{5.24}$$

The final constraint to be implemented is the marginalization constraint. As discussed in Krause and Böhlke (2020), the marginalization constraint is an arbitrary function of $\mathbb{C}$ and $\boldsymbol{E}$, and therefore an element of an infinite-dimensional vector space. As with the finite-dimensional constraints, the Lagrange multiplier must be from the same space as the corresponding constraint and is therefore also a function $\lambda^{\mathrm{C}}(\mathbb{C}, \boldsymbol{E})$. The scalar product is then given by the usual scalar product on square-integrable function spaces, leading to

$$\begin{aligned} &\lambda^{\mathrm{C}} \cdot \left(\int_{\mathrm{Sym}} p(\boldsymbol{v}) \, \mathrm{d}V(\boldsymbol{\varepsilon}) - p_1^{\mathrm{C}} \right) = \\ &\int_{\mathcal{C}} \left(\int_{\mathrm{Sym}} \left(\lambda_C(\mathbb{C}, \boldsymbol{E}) \int_{\mathrm{Sym}} \left(p(\boldsymbol{v}) - p_1^{\mathrm{C}}(\mathbb{C}, \boldsymbol{E}) \, \mathrm{d}V(\boldsymbol{\varepsilon}) \right) \mathrm{d}V(\boldsymbol{E}) \right) \mathrm{d}V(\mathbb{C}) \right). \end{aligned} \tag{5.25}$$

Because each of the constraints involves an integral over $\mathcal{V}$, they can all be pulled into the same integral together, leading to

$$\begin{aligned} S^* = \int_{\mathcal{V}} p(\boldsymbol{v}) \left(-\ln \left(\frac{p(\boldsymbol{v})}{p_0} \right) + \sum_{i=1}^{2} f_i(\boldsymbol{v}) + \sum_{i=3}^{4} \boldsymbol{F}_i(\boldsymbol{v}) + \lambda^{\mathrm{C}}(\mathbb{C}, \boldsymbol{E}) \right) \\ + \lambda^{\mathrm{C}}(\mathbb{C}, \boldsymbol{E}) p_1^{\mathrm{C}}(\mathbb{C}, \boldsymbol{E}) \, \mathrm{d}V(\boldsymbol{v}). \end{aligned} \tag{5.26}$$

A necessary condition for maximal entropy is the stationarity condition

$$\frac{\delta S^*}{\delta p} = 0, \tag{5.27}$$

which is fulfilled if the partial derivative of the integrand by p is 0, leading to

$$\ln\left(\frac{p(\boldsymbol{v})}{p_0}\right) = p_0 + \sum_{i=1}^{2} f_i(\boldsymbol{v}) + \sum_{i=3}^{4} \boldsymbol{F}_i(\boldsymbol{v}) + \lambda^{\mathrm{C}}(\mathbb{C}, \boldsymbol{E}). \tag{5.28}$$

This necessary condition for maximal entropy is also sufficient, as proven by Jaynes (1963). After some rearrangement, the probability distribution resulting from the micromechanical MEM reads

$$p(\boldsymbol{v}) = m(\mathbb{C}, \boldsymbol{E}) \exp\left(g(\boldsymbol{v})\right), \tag{5.29}$$

where m is a function which is entirely specified by the marginalization constraint in Eq. (5.13), while g is a quadratic function of $\boldsymbol{\varepsilon}$. In the most general case, $g(\boldsymbol{v})$ can be written as

$$g(\boldsymbol{v}) = -\frac{1}{2}\left(\boldsymbol{\varepsilon} - \boldsymbol{\gamma}(\mathbb{C}, \boldsymbol{E})\right) \cdot \frac{1}{k}\mathbb{C}\left[\boldsymbol{\varepsilon} - \boldsymbol{\gamma}(\mathbb{C}, \boldsymbol{E})\right]. \tag{5.30}$$

The scalar covariance constant k is related to the Lagrange multiplier of the Hill-Mandel condition constraint. The function $\boldsymbol{\gamma}$ is given by

$$\boldsymbol{\gamma} = \mathbb{C}^{-1}[\boldsymbol{\mu}_\varepsilon] + \boldsymbol{\mu}_\sigma + r\boldsymbol{E}, \tag{5.31}$$

with constants $\boldsymbol{\mu}$ and r defined by the remaining Lagrange multipliers. As $g(\boldsymbol{v})$ is a quadratic form, the conditional probability density $p(\boldsymbol{\varepsilon}|\mathbb{C}, \boldsymbol{E})$ for any fixed $\mathbb{C}$ and $\boldsymbol{E}$ is a multivariate normal probability density. For such a distribution, the conditional expectation values of the strains are

$$\langle \boldsymbol{\varepsilon}|\mathbb{C}, \boldsymbol{E}\rangle = \boldsymbol{\gamma}(\mathbb{C}, \boldsymbol{E}). \tag{5.32}$$

The conditional second moment is given by

$$\langle \boldsymbol{\varepsilon}|\mathbb{C}, \boldsymbol{E}\rangle = \boldsymbol{\gamma}(\mathbb{C}, \boldsymbol{E}) \otimes \boldsymbol{\gamma}(\mathbb{C}, \boldsymbol{E}) + k\mathbb{C}^{-1}. \tag{5.33}$$

Using these formulas, constraints 1–4 can be evaluated to yield two scalar and two second-order tensorial equations containing the constants $\boldsymbol{\mu}$, r, and k. When evaluating the constraints, various expectation values of terms in $\mathbb{C}$ and $\boldsymbol{E}$ arise. These have mechanical meaning as the first-order bounds of the stiffness,

$$\mathbb{C}_+ = \langle \mathbb{C} \rangle, \tag{5.34}$$

$$\mathbb{C}_- = \langle \mathbb{C}^{-1} \rangle^{-1}, \tag{5.35}$$

the effective eigenstrains associated with the first-order bounds,

$$\boldsymbol{E}_+ = \langle \boldsymbol{E} \rangle, \tag{5.36}$$

$$\boldsymbol{E}_- = \mathbb{C}_+^{-1}[\langle \mathbb{C}[\boldsymbol{E}] \rangle], \tag{5.37}$$

and an estimate of the eigenstrain energy,

$$w_0 = \langle \boldsymbol{E} \cdot \mathbb{C}[\boldsymbol{E}] \rangle - \boldsymbol{E}_- \cdot \mathbb{C}_+[\boldsymbol{E}_-] - (\boldsymbol{E}_- - \boldsymbol{E}_+) \cdot \left(\mathbb{C}_-^{-1} - \mathbb{C}_+^{-1}\right)^{-1} [\boldsymbol{E}_- - \boldsymbol{E}_+]. \tag{5.38}$$

The inverse $\left(\mathbb{C}_-^{-1} - \mathbb{C}_+^{-1}\right)^{-1}$ appearing in the eigenstrain energy estimate is ill-defined if the material is homogeneous for specific deformation modes. For example, given a material consisting of isotropic phases with different shear moduli but equal compression moduli K, the spherical deformation mode is homogeneous due to

$$\mathbb{C}_+^{-1} \cdot \mathbb{P}^\circ = \frac{1}{3K} = \mathbb{C}_-^{-1} \cdot \mathbb{P}^\circ. \tag{5.39}$$

When there are homogeneous deformation modes, the compliance difference $\mathbb{C}_-^{-1} - \mathbb{C}_+^{-1}$ becomes singular, as does the stiffness difference $\mathbb{C}_+ - \mathbb{C}_-$. This singular tensor then has a non-zero kernel $\mathcal{K}$ which is a subspace of Sym such that

$$(\mathbb{C}_+ - \mathbb{C}_-)[\boldsymbol{V}] = \boldsymbol{0} \Rightarrow \boldsymbol{V} \in \mathcal{K}. \tag{5.40}$$

The largest subspace on which inversion is possible is the complement of the kernel $\mathrm{Sym}/\mathcal{K}$. In this work, left- and right-symmetric fourth-order tensors are preferentially depicted as 6×6 matrices in the symmetric second-order harmonic basis defined in Section 2.2. The inversion on the largest possible subspace for these matrices can be calculated via the Moore-Penrose pseudoinverse, denoted as $\square^+$. The projectors for kernel and complement are given by

$$\mathbb{P}_{\mathrm{Sym}/\mathcal{K}} = (\mathbb{C}_+ - \mathbb{C}_-)^+(\mathbb{C}_+ - \mathbb{C}_-)\mathbb{P}_{\mathcal{K}} = \mathbb{I}^{\mathrm{S}} - \mathbb{P}_{\mathrm{Sym}/\mathcal{K}}. \tag{5.41}$$

Returning to Eq. (5.38), partial homogeneity causes both the singularity of the stiffness difference and a partial equality of $\boldsymbol{E}_-$ and $\boldsymbol{E}_+$ such that

$$\mathbb{P}_{\mathcal{K}}[\boldsymbol{E}_- - \boldsymbol{E}_+] = \boldsymbol{0}. \tag{5.42}$$

Therefore, Eq. (5.38) is well-defined in the partially homogeneous limit as

$$w_0 = \langle \boldsymbol{E} \cdot \mathbb{C}[\boldsymbol{E}] \rangle - \boldsymbol{E}_- \cdot \mathbb{C}_+[\boldsymbol{E}_-] - (\boldsymbol{E}_- - \boldsymbol{E}_+) \cdot \left(\mathbb{C}_-^{-1} - \mathbb{C}_+^{-1}\right)^+ [\boldsymbol{E}_- - \boldsymbol{E}_+]. \tag{5.43}$$

This slightly more general form of the MEM using the Moore-Penrose pseudoinverse is correct for partially homogeneous cases, unlike the form given in Krause and Böhlke (2020).

After calculating the constant Lagrange multipliers using constraints 1–4, $m(\mathbb{C}, \boldsymbol{E})$ results from the marginalization constraints as

$$m(\mathbb{C}, \boldsymbol{E}) = \frac{p_1^{\mathrm{C}}(\mathbb{C}, \boldsymbol{E})}{n(\mathbb{C})}, \tag{5.44}$$

where $n(\mathbb{C})$ normalizes the multivariate normal distribution $\exp\left(g(\boldsymbol{v})\right)$ and has the value

$$n(\mathbb{C}) = \sqrt{(2\pi)^6 k \det(\mathbb{C}^{-1})}. \tag{5.45}$$

The full MEM solution for the general case is given in Appendix B.2. The remaining sections of Appendix B contain formulas for special which are defined in the following.

5.2.3 Selected special cases

Discrete Phases. In most applications, the microstructure is composed of a finite number of phases with stiffness tensors which are homogeneous in a given phase. Additionally, eigenstrain fields which are due to internal material processes such as thermal expansion are often homogeneous in a phase. Those that are due to external heterogeneous fields, such as process-induced plastic deformations, are generally heterogeneous even within a phase. For anisotropic phases, both stiffness tensors and homogeneous eigenstrain fields also depend on the orientation $\boldsymbol{Q}$ of the material. Overall, with phase stiffnesses $\mathbb{C}_\alpha$ and phase-constant eigenstrains $\boldsymbol{E}_\alpha$, each given in the reference orientation, the one-point probability distribution of material properties reads

$$p_1^{\mathrm{C}}(\mathbb{C}, \boldsymbol{E}) = \sum_{\alpha=1}^{N} v_\alpha f_\alpha(\boldsymbol{Q}) \delta(\mathbb{C} - \boldsymbol{Q} \star \mathbb{C}_\alpha) \delta(\boldsymbol{E} - \boldsymbol{Q} \star \boldsymbol{E}_\alpha), \tag{5.46}$$

where v_α are the volume fractions and $f_\alpha(\boldsymbol{Q})$ is the ODF of the phase. From the mathematical point of view, as the Dirac delta distribution is not square integrable, the dot product used with the Lagrange multiplier λ^{C} is not well-defined. However, setting $m(\mathbb{C}_\alpha, \boldsymbol{E}_\alpha) = v_\alpha / n(\mathbb{C}_\alpha)$ yields the correct MEM solution nonetheless. A detailed form of this MEM solution is given in Appendix B, with further special cases for heterogeneous eigenstrains, single-phase polycrystals and the purely linear elastic case.

Materials with exact phase-wise expectation values. As described in Section 3.2, for some materials, the Hill-Mandel condition together with an effective stiffness $\bar{\mathbb{C}}$ implies the exact expectation values of the strain

localization tensor for each local stiffness. As a result, by specifying only $\bar{\mathbb{C}}$, exact values of $\bar{\boldsymbol{E}}$ and $\bar{w}_{\mathrm{R}}$ can be calculated. Examples include statistically isotropic cubic polycrystals and two-phase materials. As the Hill-Mandel condition is a constraint of the MEM, the MEM yields the analytically known localization in those cases. For these cases, it is sensible to use the analytically known values of $\bar{\boldsymbol{E}}$ and $\bar{w}_{\mathrm{R}}$ as MEM inputs to avoid inconsistent results.

5.2.4 Notes on applicability

As described in Section 5.1.5, maximum entropy methods can be expected to perform well in contexts where the prescribed constraints capture all known information about the problem. In the case of the micromechanical MEM, the Hill-Mandel constraints are sufficient if the microstructure is particularly random. The MEM is not expected to yield accurate results for microstructures with a high degree of internal order, such as microstructures reinforced with aligned fibers. Beyond that general observation, two fundamental theoretical issues limit the applicability of the method.

First, the MEM does not respect the linearity of affine linear elasticity. The localization problem of affine linear elasticity can be written as

$$\boldsymbol{\varepsilon}(\boldsymbol{x}) = \mathbb{A}(\boldsymbol{x})[\bar{\boldsymbol{\varepsilon}}] + \boldsymbol{a}(\boldsymbol{x}), \tag{5.47}$$

where the strain localization tensor $\mathbb{A}$ models strain fluctuations due to heterogeneities of the local stiffness $\mathbb{C}$, whereas $\boldsymbol{a}$ is due to heterogeneities of eigenstrains $\boldsymbol{E}$. In the general MEM solution, r^{L} is linear in $\bar{\boldsymbol{\varepsilon}}$, which makes it part of $\mathbb{A}$; however, the term $r^{\mathrm{L}}\boldsymbol{E}$ also depends on $\boldsymbol{E}$. In classical micromechanical models, $\mathbb{A}$ does not depend on $\boldsymbol{E}$. As the relationship of the effective eigenstrain to the phase eigenstrains contains information about the microstructure, this dependency is not entirely unexpected in the MEM. However, varying $\boldsymbol{E}$ while keeping the

microstructure constant should not lead to a variation of $\mathbb{A}$. For example, when multiplying $\boldsymbol{E}$ by a constant scalar factor, $\bar{\boldsymbol{E}}$ is multiplied by the same, and $\mathbb{A}$ remains constant. For many other such variations, the single-point MEM solution does not fulfill this condition.

Second, the MEM estimates second moments from a given homogenization method. However, these second moments conflict with the exact second moments as calculated in Chapter 4. As multiple different homogenization methods with different second moments may yield the same effective stiffness for particular phase properties, such as the Hashin-Shtrikman and Mori-Tanaka approaches, the MEM cannot be expected to approximate the correct second moment, since only the value of the effective stiffness for one set of phase properties is used as input. In practice, this means that any given homogenization method is likely to be inconsistent with a corresponding MEM approximation.

Both of these shortcomings of the MEM are a fundamental consequence of the constraints and might be compensated by a more refined theory. In practice, while the MEM is not perfectly consistent with micromechanical theory as stated, it may still be a more accurate estimate of local stress and strain distributions than classical mean field approximations.

5.3 Numerical full-field validation of the Single-Point MEM[1]

5.3.1 Computational setup

As a comparison to the MEM results, we perform full-field simulations using solvers based on the fast Fourier transform (FFT). The method-

[1] This section is based on section 4 of the publication *Maximum-Entropy Based Estimates of Stress and Strain in Thermoelastic Random Heterogeneous Materials* (Krause and Böhlke, 2020)

ology is based on the approach of Moulinec and Suquet (1998). The conjugate gradient method proposed by Zeman et al. (2010) is used as it is particularly suited for linear problems. By relying upon the staggered grid discretization (Schneider et al., 2016), so-called *ringing artifacts* or *Gibbs' oscillations* which might impact the statistics of the results are minimized. All calculations were carried out in Python 3 using the FFTW library (Frigo and Johnson, 2005). Further details on the FFT-based solver used can be found in (Wicht et al., 2020a) and Wicht et al. (2020b). The microstructures used for the full-field simulations are generated as cubes with a resolution of 256 voxels on each side.

5.3.2 Isotropic Al-Al_2O_3

In this section, we investigate the metal matrix composite Al-Al_2O_3as an example composite with two clearly distinguished phases and a medium phase contrast. Aluminum and ceramic are modeled as discrete isotropic elastic phases with parameters according to Table 5.1.

Material	E in GPa	ν	α in $10^{-6}\,\mathrm{K}^{-1}$
Al	70	0.35	23.7
Al_2O_3	380	0.22	6.6

Table 5.1: Material parameters for the Al-Al_2O_3 composite according to Agrawal and Sun (2003). Table based on Table 2 of Krause and Böhlke (2020).

As shown in the formulas of Appendix B, in the case of only two phases, strains caused by effective stresses and strains caused by eigenstrains are independent of each other. First, we neglect thermal eigenstrains and apply an effective mean stress of $\bar{\boldsymbol{\sigma}}^{\mathrm{I}} = 100\,\mathrm{MPa}\,\boldsymbol{e}_3 \otimes \boldsymbol{e}_3$ to the composite. The value and direction of this loading are chosen arbitrarily, yet are representative for all unidirectional stresses because of the MEM's linearity and the isotropy of the material.

For the FFT simulations, we use three different microstructures with an Al_2O_3 volume fraction of $30\,\%$ each, as shown in Fig. 5.1. In the center is a polycrystal microstructure generated via Voronoi tessellation. 8000 grains are each randomly chosen to contain either of the two phases, yielding a co-continuous structure. The two other microstructures are matrix-inclusion structures with Al as the matrix, on the left with 300 spherical inclusions of equal radius and on the right with cylindrical inclusions with a ratio of length to diameter of 10, in the following referred to as fibers.

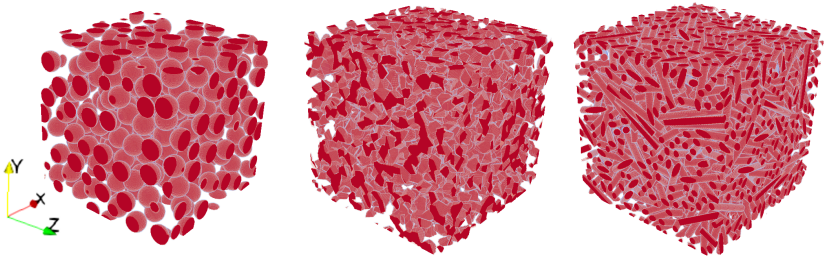

Figure 5.1: Al_2O_3 phase of microstructures used for the FFT reference solutions. From left to right: spherical inclusions, two-phase polycrystal, fiber inclusions. Figure based on Figure 2 of Krause and Böhlke (2020).

In Table 5.2, the results of numerical homogenization of all three microstructures are shown. The effective stiffness is projected to an isotropic value using

$$\bar{\mathbb{C}}_{\mathrm{iso}} = (\bar{\mathbb{C}} \cdot \mathbb{P}_1)\mathbb{P}_1 + \frac{1}{5}(\bar{\mathbb{C}} \cdot \mathbb{P}_2)\mathbb{P}_2. \tag{5.48}$$

The numerically computed effective shear moduli are within $5\,\%$ of each other, with slightly smaller variations among the compression moduli. In this approach, the anisotropic parts of the stiffness are neglected,

which is quantified by the anisotropic error

$$e_{\text{aniso}} = \frac{\left\|\bar{\mathbb{C}}_{\text{iso}} - \bar{\mathbb{C}}\right\|}{\left\|\bar{\mathbb{C}}\right\|}. \tag{5.49}$$

As the considered microstructures would be isotropic if they were arbitrarily large and arbitrarily finely resolved, the anisotropic error is a lower bound on the total error of the full-field approach. Defining the error based on the stiffness alone is somewhat arbitrary. An alternative definition of the anisotropic error using the compliance tensor yields qualitatively similar results.

	Polycrystal	Spherical Inclusions	Fiber Inclusions
$\bar{K}$ in GPa	101.7	103.8	103.6
$\bar{G}$ in GPa	42.2	44.4	43.7
e_{aniso}	$0.298\,\%$	$0.554\,\%$	$0.621\,\%$

Table 5.2: Numerical effective stiffnesses and anisotropic error for three different Al-Al_2O_3 microstructures shown in Fig. 5.1. Table based on Table 3 of Krause and Böhlke (2020).

The distributions of phase stresses along the $\boldsymbol{e}_3 \otimes \boldsymbol{e}_3$-direction for the two phases according to the MEM are shown in Fig. 5.2. Two Gaussian distributions with means as given by the exact analytical solution for two phases can be seen. Statistical moments with orders exceeding two vanish. As the microstructures yield similar effective stiffnesses, the MEM results are also similar. For comparison, the distributions according to the FFT simulations along with one MEM result are shown in Fig. 5.3. For the polycrystal and the fiber inclusions, higher statistical moments apparently do not vanish. In the case of the polycrystal and the fiber inclusions, the variance is high compared to the MEM. The variance of the spherical inclusions is comparatively low.

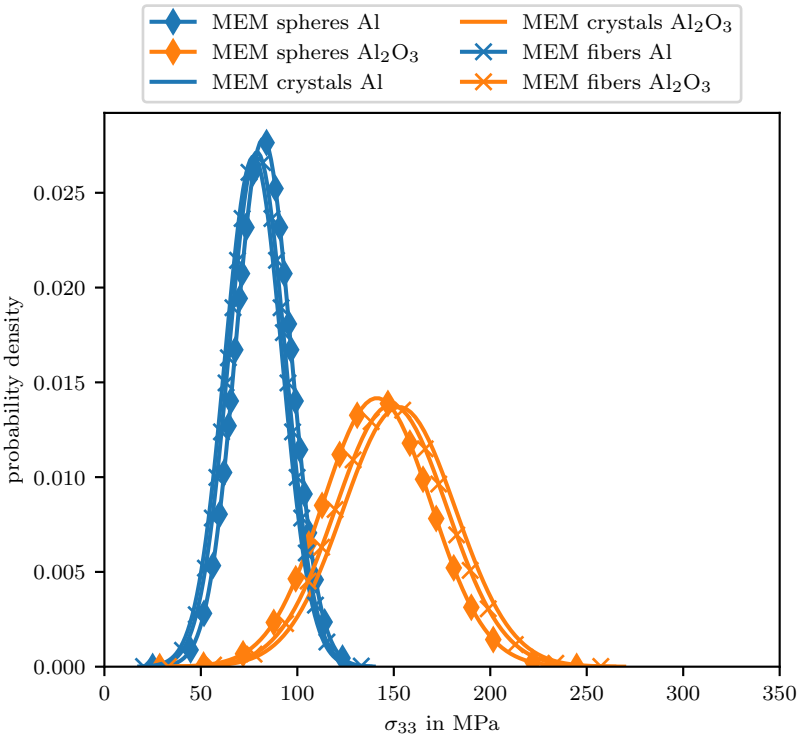

Figure 5.2: Phase-wise MEM σ_{33} distributions for Al-Al_2O_3 under $\bar{\sigma}_{33}$-load for three different microstructures. Figure based on Figure 3 of Krause and Böhlke (2020).

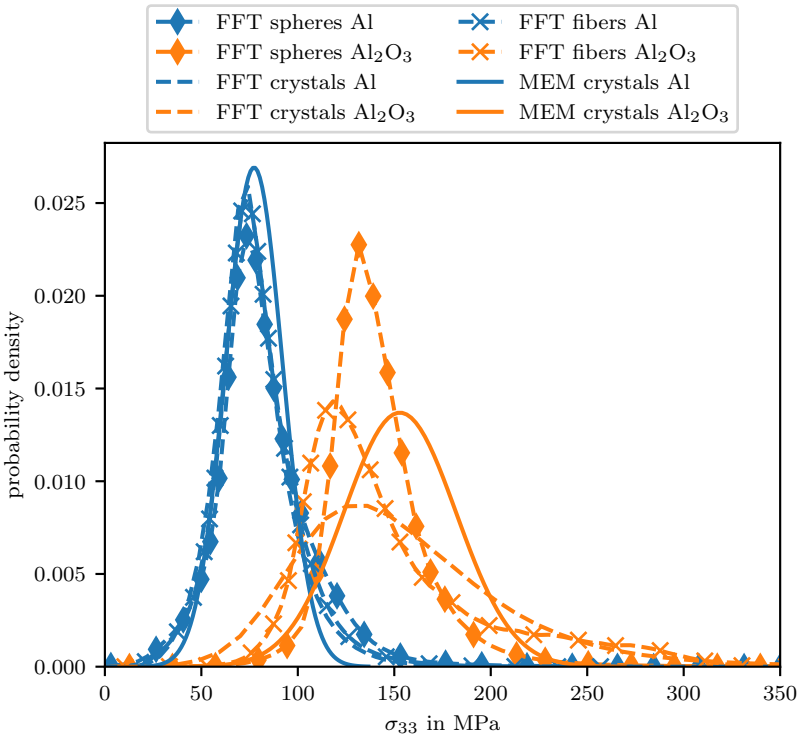

Figure 5.3: Phase-wise MEM σ_{33} distributions for Al-Al_2O_3 under $\bar{\sigma}_{33}$-load for polycrystal microstructure; comparison with polycrystal, sphere and fiber inclusion FFT simulation. Figure based of Figure 4 on Krause and Böhlke (2020).

The previous diagrams show the marginalized distribution of only one component of the stress. To show covariances between different tensor components, we use covariance ellipses as defined in Section 4.4. As the covariances are expected to be transversal-isotropic due to the symmetries of the microstructure, the material, and the loading, the σ_1-σ_6 and σ_3-σ_4 diagrams are sufficient to depict all components of the full covariance.

In the σ_1-σ_6 diagram shown in Fig. 5.4, all full-field covariances are transversal-isotropic and approximately proportional to each other. For the MEM, phase covariances are proportional to phase stiffnesses, which enforces isotropy. As a result, the covariance between σ_1 and σ_6 components cannot be reproduced by the MEM. Additionally, the σ_6 covariance is significantly smaller than in the full-field results.

The σ_3-σ_4 diagram is shown in Fig. 5.5. In these shear components, the full-field covariances are again approximately proportional. The MEM covariances, however, are not only isotropic, but also significantly larger than in the full-field results. This effect is due to isotropy of the covariance. As σ_6 and σ_3 covariances need to be equal, the MEM cannot reproduce the significant differences between these components shown in the full-field solution. In summary, the MEM has the same shortcomings as the Hashin-Shtrikman solution of Section 4.4.

In the Al-Al_2O_3 composite, differing thermal expansion coefficients cause spherical eigenstrains of $0.355\,\%$ and $0.099\,\%$, respectively, at a process temperature of $\Delta\theta = 150\,°\mathrm{C}$ (Agrawal and Sun, 2003). The resulting one-dimensional distributions are shown in Fig. 5.6. The MEM solution shows marked differences to each of the FFT solutions. In particular, higher statistical moments are not negligible in the FFT solutions and the variances of the MEM solution are considerably larger.

The $\sigma_1 - \sigma_6$ covariance ellipse is shown in Fig. 5.7. As the purely thermal load case is isotropic, this diagram is sufficient to characterize the covariances. Unlike the linear-elastic case, the three microstructures

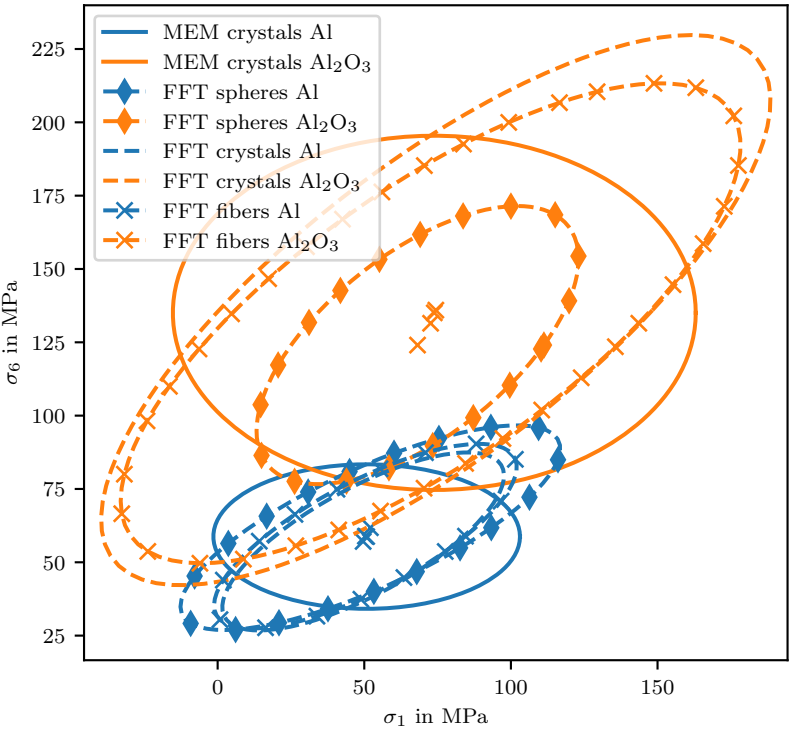

Figure 5.4: Phase-wise MEM covariance ellipses of σ_1 and σ_6 for Al-Al_2O_3 under $\bar{\sigma}_{33}$-load; comparison with polycrystal, sphere and fiber inclusion FFT simulation.

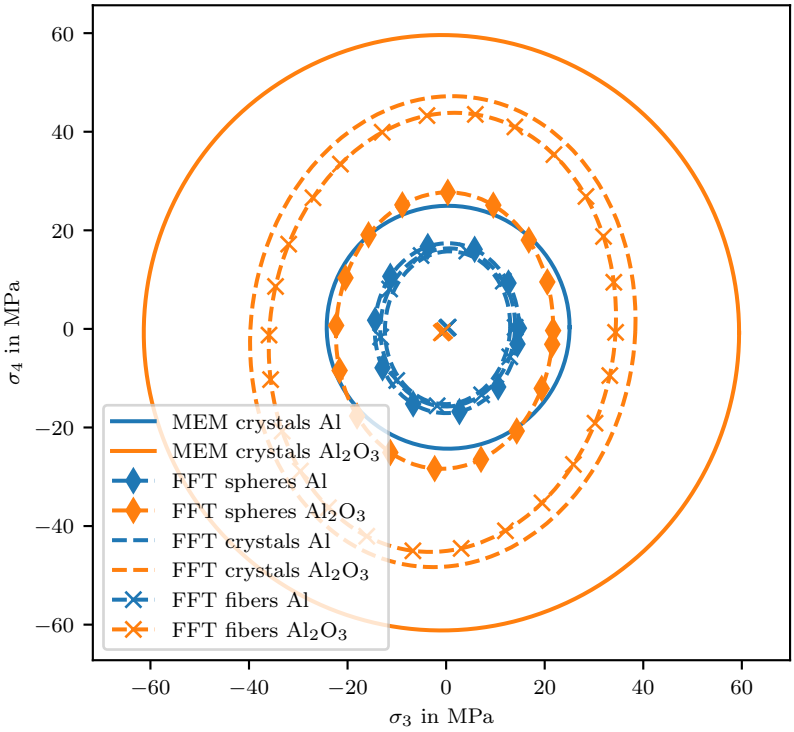

Figure 5.5: Phase-wise MEM covariance ellipses of σ_3 and σ_4 for Al-Al_2O_3 under $\bar{\sigma}_{33}$-load; comparison with polycrystal, sphere and fiber inclusion FFT simulation.

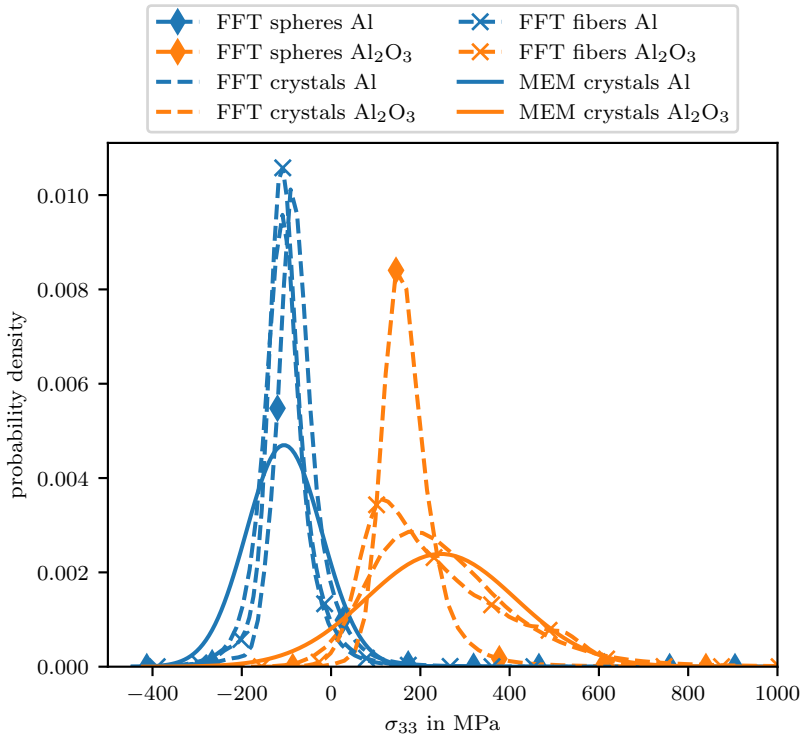

Figure 5.6: Phase-wise MEM σ_{33} distributions for Al-Al_2O_3 under thermal strain. Figure based of Figure 8 of Krause and Böhlke (2020).

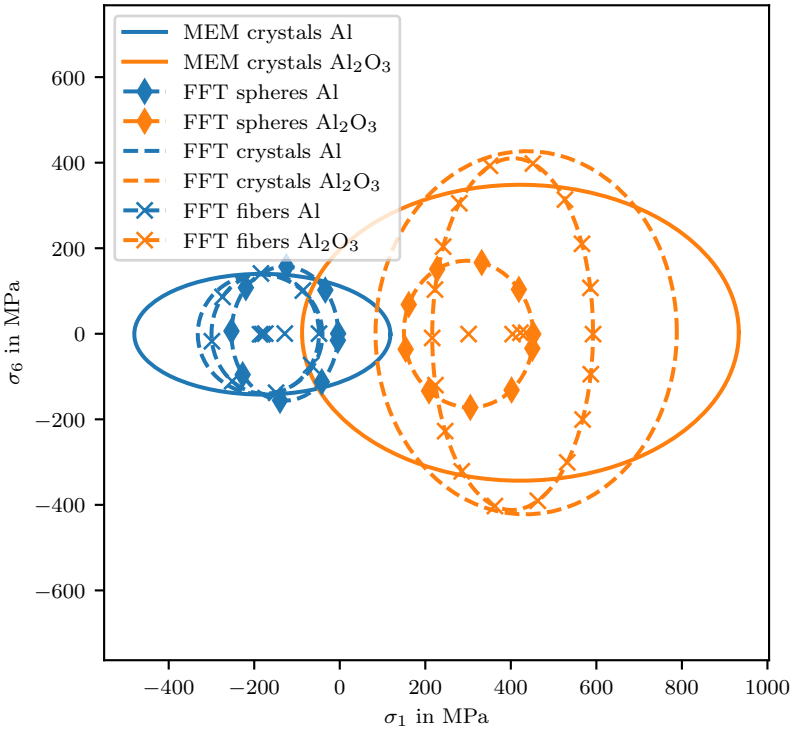

Figure 5.7: Phase-wise MEM covariance ellipses of σ_1 and σ_6 for Al-Al_2O_3 under thermal load; comparison with polycrystal, sphere and fiber inclusion FFT simulation.

have markedly different thermal stress distributions, particularly in the inclusions. In the σ_6 component, the MEM approximates crystal and fiber thermal stresses well. However, in the σ_1 component, the MEM overestimates even the stresses in the aluminum matrix by a factor of two. This is again due to the MEM covariance being proportional to the phase stiffness. This restriction imposes not only an isotropic symmetry, but also a specific ratio between spherical and deviatoric parts of the covariance. Particularly in the calculation of thermal stresses, details of the microstructure appear to significantly influence this ratio, which the MEM cannot reproduce. With this ratio fixed for the MEM, it tends to neglect the spherical component while approximating the deviatoric component well. This is due to $\sigma_{2\ldots6}$ being equal, which effectively makes the deviatoric component five times as significant as the spherical component.

5.3.3 Uniform globally isotropic polycrystal

As an example for polycrystals, we consider a cubic polycrystal with a uniform ODF, yielding an isotropic effective behavior. The polycrystal is composed of copper single crystals of different orientation. Copper has been chosen for its significant degree of anisotropy. Its elastic constants are given as $C_{1111} = 170.2\,\mathrm{GPa}$, $C_{1122} = 114.9\,\mathrm{GPa}$, and $C_{1212} = 61.0\,\mathrm{GPa}$ by Simmons and Wang (1971), which are the components of the stiffness tensor in the crystal lattice coordinate system. As in the previous example, a unidirectional stress of $\bar{\sigma}_{11} = 100\,\mathrm{MPa}$ is applied to the material.

An FFT simulation is used as a reference. The microstructure is generated via Voronoi tessellation, with $8000\,\mathrm{c}$rystals distributed over a cube $256\,\mathrm{v}$oxels wide in each direction. The orientations were sampled from a uniform distribution, yielding a numerical effective stiffness which is only slightly anisotropic. The relative anisotropic error e_{aniso} is below $0.05\,\%$. The numerical stiffness is used as input of the MEM to

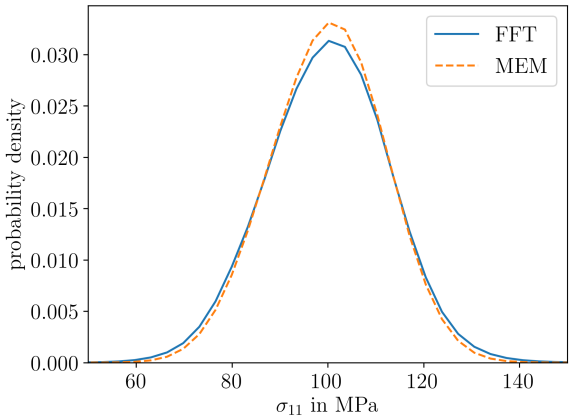

Figure 5.8: Probability distribution of σ_{11} for isotropic polycrystalline copper, calculated with MEM and FFT. Figure based of Figure 13 of Krause and Böhlke (2020).

ensure comparability between the methods. However, while the FFT result is calculated with 8000 grain orientations drawn from a uniform distribution, the MEM results can be calculated using the uniform distribution itself.

In Fig. 5.8 depicts the distribution of σ_{11} for both methods. For the FFT, the diagram was compiled from the available full-field information, while in the case of the MEM, we used Monte Carlo integration to calculate this marginalized distribution. The overall variance of the distribution is on the order of $10\,\mathrm{MPa}$ in both cases, which is not negligible, yet both methods yield quite similar distributions.

Fig. 5.9 shows the σ_1-σ_6 diagram for a single crystal of an arbitrarily chosen orientation. The coordinate system is rotated to coincide with the crystal axes. Therefore, the effective stress shown is also rotated. The shown MEM mean and covariance is calculated for the set of all crystal grains of the given orientation in an infinitely large ensemble, while the FFT mean and covariance represent only one grain. For the MEM stress mean, the mean homogeneity of the spherical mode discussed in

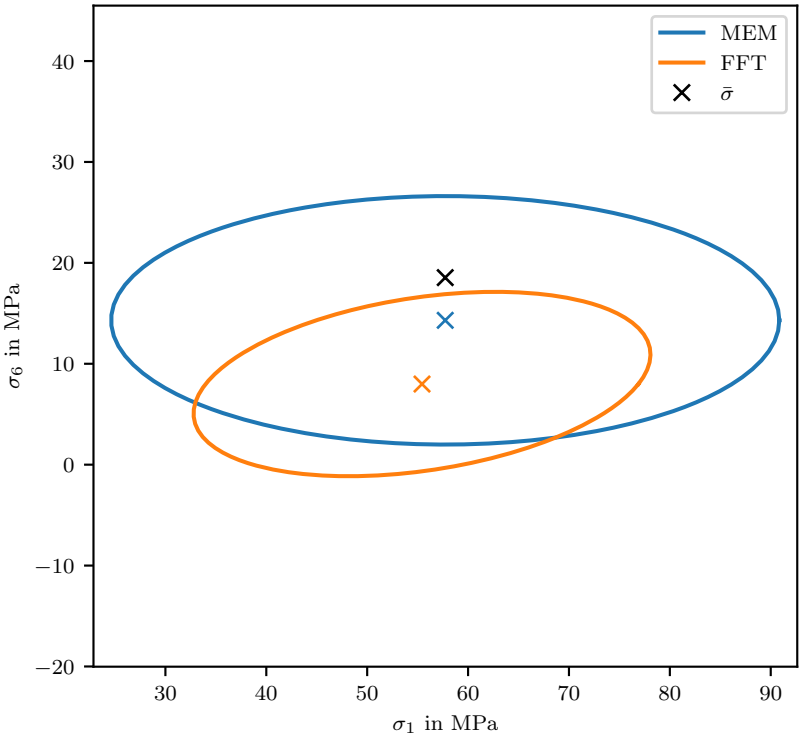

Figure 5.9: Mean stress $\bar{\sigma}$ and covariance ellipses for polycrystalline copper according to the MEM solution for all grains aligned with the coordinate axes and according to an FFT full-field solution for one grain aligned with the coordinate axes.

Section 3.2.3 leads to

$$\langle \sigma_1 \rangle_{\boldsymbol{Q}} = \bar{\sigma}_1. \tag{5.50}$$

This relation does not hold for an average over only a single grain, due to the influence of the specific grain neighborhood. Similarly, the FFT covariance is generally smaller than the MEM covariance, as a less diverse set of grain-boundary interactions is represented. These *neighborhood effects* can be averaged out by considering similarly oriented grains over a large ensemble of microstructures. A large ensemble study by Gehrig et al. (2022) found that when neighborhood effects are averaged out, the full-field covariances and the MEM covariances are similar to within $5\,\%$ even for strongly anisotropic cubic materials such as plutonium.

5.4 The Singular Approximation Maximum Entropy Method

The micromechanical MEM as described in the previous section does not take microstructural morphology information into account directly. While the effective stiffness, taken as an input parameter, does contain partial information on the microstructure morphology, it does not contain enough information to allow the reliable prediction of strain statistics of matrix-inclusion morphologies, particularly highly ordered ones, such as those in which all inclusions have the same shape. For such microstructures, the Eshelby solution can be incorporated into the MEM constraints to refine the solution.

The approach described by Kreher and Pompe (1989) begins by using the MEM to solve the infinite-point statistical problem instead of the single-point statistical problem. The solution can be formally stated using infinite-point correlation functions and the Green's function formalism, but cannot be directly evaluated in practice. To find an approximate

solution, Kreher and Pompe assume that only the region directly around a material point correlates with that point, which makes it possible to replace all further regions by random fields, which are treated statistically. The region around the material point is modeled via the Eshelby problem, which reduces the infinite-point problem to a single-point problem because the inclusion in the Eshelby problem is homogeneous, as described in Section 3.2.4. From that point onward, the solution path is identical to the single-point MEM: by maximizing entropy with constraints based on the Hill-Mandel condition, an analytical solution is retrieved. Unlike the single-point MEM, this infinite-point Eshelby MEM is parameterized by a reference stiffness $\mathbb{C}_0$, and yields the effective properties alongside the local strain statistics. We note that both these effective properties and the phase-wise means of the strain are identical to those given by the Singular Approximation, and thus call Kreher's infinite-point Eshelby MEM the Singular Approximation MEM, or SA MEM for short.

In Kreher and Pompe (1989), the SA MEM is derived directly as a solution of Eshelby's problem, which requires lengthy functional analysis. We instead attempt a formal derivation based on the Singular Approximation as discussed in Section 3.2.4. Based on the fundamental assumption of the Singular Approximation that each material point is influenced only by the microstructure as a whole, not its immediate neighborhood, the microstructure is statistically equivalent to an ensemble of Eshelby problems with equal one- and two-point correlation functions to the original microstructure. Here we assume that the two-point correlation function of the original microstructure is elliptical, such that each Eshelby problem has the same ellipsoidal shape tensor $\boldsymbol{A}$. The inclusion strain of each Eshelby problem is given by

$$\boldsymbol{\varepsilon} = (\mathbb{P}_0^{-1} + \mathbb{C} - \mathbb{C}_0)^{-1}\mathbb{P}_0^{-1}[\boldsymbol{\varepsilon}_0]. \tag{5.51}$$

This relationship is deterministic, from which it follows that the problem of determining the strain statistics can be reduced to determining the statistics of $\boldsymbol{\varepsilon}_0$. In theory, this can be accomplished by maximizing the entropy with the same constraints on $\boldsymbol{\varepsilon}$ as the single-point MEM. In that case, with the same constraints, the results would also be the same.

If, as an additional constraint, we assume $\langle \boldsymbol{\varepsilon}_0 \rangle_\alpha = \text{const.}$, the A^1 model implied by the Singular Approximation results. This is no surprise because the constraints of this MEM model are precisely the assumptions behind the Singular Approximation. As discussed in Section 5.2.3 for the single-point MEM, if only one A^1 model is compatible with given constraints, the MEM yields that A^1 model. With no further constraints on the second moments of $\boldsymbol{\varepsilon}_0$, the second moments are given as in the single-point MEM. Note that it would also be possible to apply additional constraints to the MEM which are based on the exact elastic second moments of the Singular Approximation calculated in Chapter 4. In that case, the MEM yields multivariate normal distributions with the exact statistical moments given by the Singular Approximation. The utility of the MEM then lies in extending the elastic second moments to the affine linear elastic case. Additionally, like other MEM approaches, this approach directly gives the result that higher moments are zero.

Kreher and Pompe (1989) instead determine the statistics of $\boldsymbol{\varepsilon}_0$ by using a maximum entropy approach. Instead of directly assuming that the phase-wise mean $\langle \boldsymbol{\varepsilon}_0 \rangle_\alpha$ is constant, Kreher and Pompe treat each Eshelby problem in the ensemble as an inclusion in a larger microstructure. The inclusions each have stiffness $\mathbb{C}_0$ and ellipsoid shape $\boldsymbol{A}$. By assuming that each inclusion experiences random surroundings approximated by $\mathbb{C}_0$, each inclusion, together with its surroundings, can be modeled by an Eshelby problem with homogeneous stiffness and a random eigenstrain for each inclusion $\boldsymbol{E}_0$, from which $\boldsymbol{\varepsilon}_0$ results as a residual strain. The Eshelby solution of each problem is

$$\boldsymbol{\varepsilon}_0 = \mathbb{P}_0 \mathbb{C}_0 [\boldsymbol{E}_0]. \tag{5.52}$$

For this homogeneous stiffness residual strain problem, the usual effective quantities can be defined, leading to

$$\langle \boldsymbol{\varepsilon}_0 \rangle = \bar{\boldsymbol{\varepsilon}}_0, \tag{5.53}$$

$$\langle \boldsymbol{\sigma} \rangle = \mathbf{0}, \tag{5.54}$$

$$\frac{1}{2}\langle (\boldsymbol{\varepsilon}_0 - \boldsymbol{E}_0) \cdot \mathbb{C}_0 [\boldsymbol{\varepsilon}_0 - \boldsymbol{E}_0] \rangle = \bar{w}^{\mathrm{II}}. \tag{5.55}$$

Applying the Eshelby solution and the Hill-Mandel condition leads to

$$\langle \boldsymbol{\varepsilon}_0 \rangle = \langle \boldsymbol{E}_0 \rangle, \tag{5.56}$$

$$\langle \boldsymbol{\varepsilon}_0 \otimes \boldsymbol{\varepsilon}_0 \rangle \cdot \mathbb{P}_0^{-1} = 2\bar{w}^{\mathrm{II}} + \langle \boldsymbol{E}_0 \otimes \boldsymbol{E}_0 \rangle \cdot \mathbb{C}_0. \tag{5.57}$$

These equations form constraints for a maximum entropy problem for $p(\boldsymbol{\varepsilon}_0, \boldsymbol{E}_0)$, where $\boldsymbol{E}_0$ is assumed to be known. The solution is a multivariate normal distribution of $\boldsymbol{\varepsilon}_0$ with mean $\langle \boldsymbol{E}_0 \rangle$ and covariance

$$\mathbb{K}_0 = k_0 \mathbb{P}_0. \tag{5.58}$$

Since $\boldsymbol{E}_0$ is not actually known, the constants $\langle \boldsymbol{E}_0 \rangle$ and k_0 remain to be calculated. This is done by transforming the $\boldsymbol{\varepsilon}_0$-statistic via Eq. (5.51) to an $\boldsymbol{\varepsilon}$-statistic and evaluating the MEM constraints (5.14)–(5.16) and (5.18). The resulting probability distribution is

$$p_1(\boldsymbol{\varepsilon}, \mathbb{C}, \boldsymbol{E}) = \frac{p_1^{\mathrm{C}}(\mathbb{C}, \boldsymbol{E})}{\sqrt{(2\pi)^6 \det(\mathbb{K})}} \exp\left(-\frac{1}{2} (\boldsymbol{\varepsilon} - \boldsymbol{\gamma}) \cdot \mathbb{K}^{-1} [\boldsymbol{\varepsilon} - \boldsymbol{\gamma}] \right). \tag{5.59}$$

The mean strains $\boldsymbol{\gamma}$ are exactly those given by the Singular Approximation, i.e.,

$$\boldsymbol{\gamma} = \mathbb{L} \langle \mathbb{L} \rangle^{-1} [\bar{\boldsymbol{\varepsilon}} - \langle \mathbb{L}\mathbb{C}[\boldsymbol{E}] \rangle] + \mathbb{L}\mathbb{C}[\boldsymbol{E}]. \tag{5.60}$$

The covariance $\mathbb{K}$ is given by

$$\mathbb{K} = k\mathbb{L}(\mathbb{C})\mathbb{P}_0^{-1}\mathbb{L}(\mathbb{C}) \tag{5.61}$$

with $\mathbb{L}$ defined as in Section 3.2. According to Kreher and Pompe (1989), the scalar factor k follows after lengthy calculation as

$$\begin{aligned} k = \frac{1}{t_q}(\bar{\boldsymbol{\varepsilon}}_{\mathrm{L}} \cdot (\bar{\mathbb{C}} - \frac{1}{4}\langle\mathbb{L}\rangle^{-1}\mathbb{C}_{\mathrm{Q}}\langle\mathbb{L}\rangle^{-1})[\bar{\boldsymbol{\varepsilon}}_{\mathrm{L}}] \\ + \langle \boldsymbol{E} \cdot \mathbb{C}\mathbb{L}(\mathbb{P}_0^{-1} - \mathbb{C}_0)\mathbb{L}\mathbb{C}[\boldsymbol{E}]\rangle \\ - \frac{1}{4}\bar{\boldsymbol{E}} \cdot (\mathbb{P}_0^{-1} - \mathbb{C}_0)\mathbb{C}_{\mathrm{Q}}^{-1}(\mathbb{P}_0^{-1} - \mathbb{C}_0)[\bar{\boldsymbol{E}}] - \frac{1}{2}\bar{\boldsymbol{E}}(\mathbb{P}_0^{-1} - \mathbb{C}_0)[\boldsymbol{\varepsilon}_{\mathrm{D}} - \boldsymbol{\varepsilon}_{\mathrm{Q}}] \\ + \frac{1}{2}\bar{\boldsymbol{\varepsilon}}_{\mathrm{L}} \cdot \mathbb{L}^{-1}\mathbb{C}_{\mathrm{Q}}^{-1}(\mathbb{C}_{\mathrm{Q}}[\boldsymbol{\varepsilon}_{\mathrm{Q}}] - (\mathbb{P}_0^{-1} - \mathbb{C}_0)[\boldsymbol{E}])) \end{aligned} \tag{5.62}$$

with the abbreviations

$$\mathbb{C}_{\mathrm{Q}} = \frac{1}{4}\langle\mathbb{L}\mathbb{C}\mathbb{L}\rangle^{-1}, \tag{5.63}$$

$$\boldsymbol{\varepsilon}_{\mathrm{Q}} = 4\langle\mathbb{L}(\mathbb{P}_0^{-1} - \mathbb{C}_0)\mathbb{L}\mathbb{C}[\boldsymbol{E}]\rangle, \tag{5.64}$$

$$\boldsymbol{\varepsilon}_{\mathrm{D}} = 2\langle\mathbb{L}\mathbb{C}\boldsymbol{E}\rangle, \tag{5.65}$$

$$t_{\mathrm{Q}} = \frac{1}{4}\mathbb{P}_0^{-1} \cdot \mathbb{C}_{\mathrm{Q}}^{-1}. \tag{5.66}$$

Like any MEM approach, the SA MEM is an approximation. The core assumption of the SA MEM is that the transformed Singular Approximation problem is maximally entropic, while the single-point MEM assumes that the single-point micromechanical problem is maximally entropic. While the incorporation of microstructural information via $\mathbb{P}_0$ leads Kreher and Pompe (1989) to call the SA MEM an "improved solution for strong heterogeneity", which MEM approach is more accurate depends on the microstructure and material system under consideration.

5.5 Comparison of different MEM approaches

In the following, three different MEM approaches are compared using a concrete example. In comparing the Singular Approximation MEM with the single-point MEM, we use a material for which both approaches are well-suited, i.e., a polycrystal. Because the orientation average of the strain concentration tensor of an isotropic cubic polycrystal is exactly determined by the effective stiffness, we use a statistically isotropic titanium polycrystal as an example, which is locally hexagonally symmetric. This study follows the same example material as Krause and Böhlke (2022), but all calculations have been redone. With the stiffness parameters given by Dryburgh et al. (2022), the single crystal stiffness is

$$\mathbb{C}^{\mathrm{H}} \mathrel{\hat{=}} \begin{pmatrix} 313.67 & 0.0 & 0.0 & 0.0 & 0.0 & -5.42 \\ 0.0 & 70.5 & 0.0 & 0.0 & 0.0 & 0.0 \\ 0.0 & 0.0 & 70.5 & 0.0 & 0.0 & 0.0 \\ 0.0 & 0.0 & 0.0 & 94.0 & 0.0 & 0.0 \\ 0.0 & 0.0 & 0.0 & 0.0 & 94.0 & 0.0 \\ -5.42 & 0.0 & 0.0 & 0.0 & 0.0 & 111.83 \end{pmatrix} \mathrm{GPa}. \tag{5.67}$$

The thermal expansion as measured by Pawar and Deshpande (1968) is

$$\boldsymbol{\alpha} \mathrel{\hat{=}} \begin{pmatrix} 1.42 \cdot 10^{-5} \\ 0.0 \\ 0.0 \\ 0.0 \\ 0.0 \\ -3.18 \cdot 10^{-6} \end{pmatrix} 1/\mathrm{K}. \tag{5.68}$$

We assume that titanium, as it cools from the molten state, begins to accumulate residual stresses as it reaches the stress relaxation temperature, which is $480\,^{\circ}\mathrm{C}$ according to Donachie (2000). This leads to an

eigenstrain at room temperature of

$$\boldsymbol{E} \mathrel{\hat{=}} \begin{pmatrix} -0.653 \\ 0.0 \\ 0.0 \\ 0.0 \\ 0.0 \\ 0.146 \end{pmatrix} \%. \tag{5.69}$$

As in Section 5.3, a full-field solution is used as a reference. The microstructure is a Laguerre tessellation with $20\,000$ crystal grains discretized using 256^3 voxels, generated using the approach of Kuhn et al. (2020). The large number of crystal grains is chosen to yield a representative overall probability distribution. Neither crystallographic nor morphological texture are present, leading to a statistically isotropic polycrystal. The local strain fields are calculated using the staggered grid discretization (Schneider et al., 2016) and a solver based on the conjugated gradient method as described by Wicht et al. (2020a). Numerical homogenization yields an effective stiffness of

$$\bar{\mathbb{C}} \mathrel{\hat{=}} \begin{pmatrix} 313.53 & 0.01 & 0.01 & -0.01 & 0.0 & 0.0 \\ 0.01 & 86.81 & 0.0 & 0.02 & -0.01 & 0.02 \\ 0.01 & 0.0 & 86.81 & -0.02 & 0.0 & 0.02 \\ -0.01 & 0.02 & -0.02 & 86.81 & -0.03 & 0.01 \\ 0.0 & -0.01 & 0.0 & -0.03 & 86.84 & 0.0 \\ 0.0 & 0.02 & 0.02 & 0.01 & 0.0 & 86.82 \end{pmatrix} \mathrm{GPa}. \tag{5.70}$$

The anisotropic error is on the order of tens of MPa, which suggests that the microstructure is highly representative of a statistically isotropic ensemble. The numerically homogenized effective thermal strain is

similarly isotropic with a value of

$$\bar{\boldsymbol{E}} \mathrel{\hat{=}} \begin{pmatrix} -0.654 \\ 0.0 \\ 0.0 \\ 0.0 \\ 0.0 \\ 0.0 \end{pmatrix} \%. \tag{5.71}$$

Because the SA MEM necessarily requires a Singular Approximation model, we choose to use such a model for all MEM calculations. Similarly to the full-field solution, $20\,000$ grains of randomly chosen orientations are used to represent the statistically isotropic ensemble. With a reference stiffness of

$$\mathbb{C}_0 = \mathbb{C}_+, \tag{5.72}$$

the effective stiffness is given by

$$\bar{\mathbb{C}} \mathrel{\hat{=}} \begin{pmatrix} 313.53 & -0.01 & 0.01 & -0.01 & 0.02 & 0.0 \\ -0.01 & 86.82 & 0.03 & 0.03 & 0.07 & -0.04 \\ 0.01 & 0.03 & 86.81 & -0.06 & 0.03 & 0.03 \\ -0.01 & 0.03 & -0.06 & 86.87 & -0.04 & 0.01 \\ 0.02 & 0.07 & 0.03 & -0.04 & 86.79 & -0.05 \\ 0.0 & -0.04 & 0.03 & 0.01 & -0.05 & 86.83 \end{pmatrix} \text{GPa}, \tag{5.73}$$

and the effective eigenstrain is

$$\bar{\boldsymbol{E}} \mathrel{\hat{=}} \begin{pmatrix} -0.655 \\ 0.0 \\ 0.0 \\ 0.0 \\ -0.001 \\ 0.0 \end{pmatrix} \tag{5.74}$$

The anisotropic error is slightly higher than when using the FFT-based numerical homogenization. The actual values, however, are extremely similar, with the total difference between effective stiffnesses resolving to only

$$\|\bar{\mathbb{C}}_{\mathrm{FFT}} - \bar{\mathbb{C}}_{\mathrm{SA}}\| = 0.20\,\mathrm{GPa}. \tag{5.75}$$

It follows that $\mathbb{C}_+$ is a sufficiently accurate choice for $\mathbb{C}_0$.

We use three different MEM approaches which differ in how much of the SA model they incorporate. The first is a single-point MEM approach using the effective quantities given by the SA. The second is a SA MEM approach which uses the reference stiffness of Eq. (5.72), thus exactly reproducing the strain concentration tensors. Finally, the third approach also incorporates the orientation-dependent elastic covariances $\mathbb{K}_{\boldsymbol{Q}}$ calculated in Chapter 4 into the MEM solution. This is done by applying the additional constraint

$$\langle \boldsymbol{\varepsilon}_{\mathrm{L}} \otimes \boldsymbol{\varepsilon}_{\mathrm{L}} \rangle_{\boldsymbol{Q}} = \langle \boldsymbol{\varepsilon}_{\mathrm{L}} \rangle_{\boldsymbol{Q}} \otimes \langle \boldsymbol{\varepsilon}_{\mathrm{L}} \rangle_{\boldsymbol{Q}} + \mathbb{K}_{\boldsymbol{Q}} \quad \forall \boldsymbol{Q} \in SO(3). \tag{5.76}$$

As this constraint is a function of $\boldsymbol{Q}$ which, after integration, resolves to the elastic Hill condition constraint, it is not in conflict with any of the constraints of the SA MEM, but merely serves as a refinement of the existing theory. After maximizing the entropy and determining the Lagrange multipliers in the usual manner, the resulting formulas contain the prescribed elastic covariances, with all other parts of the SA MEM solution unchanged. In the following, this MEM approach is called the *exact covariance MEM*.

As the numerical homogenization does not provide a sufficiently large ensemble to eliminate neighborhood effects, we do not attempt to compare the stress distributions in individual crystals, and restrict ourselves to the overall stress distributions. For the MEM solutions, this requires

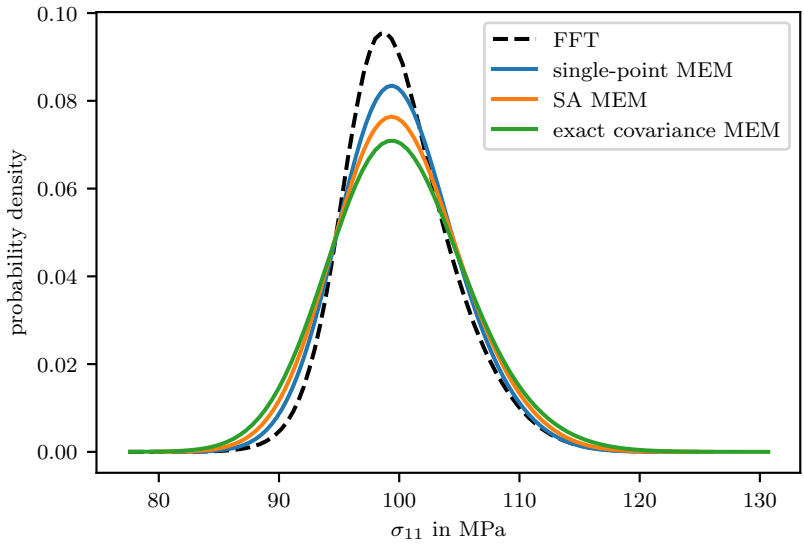

Figure 5.10: $p(\sigma_{11})$ in polycrystalline titanium for various MEM models and a full-field solution assuming linear elasticity with no eigenstrains.

the calculation of

$$p(\boldsymbol{\sigma}) = \int_{SO(3)} p(\boldsymbol{\sigma}, \boldsymbol{Q}) \, \mathrm{d}V(\boldsymbol{Q}), \tag{5.77}$$

which is accomplished by numerical integration. While there are numerous $SO(3)$ integration schemes known in the literature, in the interest of consistency with the analytical and numerical homogenization schemes, we choose $N = 20\,000$ random orientations and calculate

$$p(\boldsymbol{\sigma}) = \frac{1}{N} \sum_{\alpha}^{N} p(\boldsymbol{\sigma}, \boldsymbol{Q}_\alpha). \tag{5.78}$$

Fig. 5.10 shows the overall probability distribution of the stress in loading direction for a purely linear elastic case, i.e., with $\boldsymbol{E} = \boldsymbol{0}$. The FFT

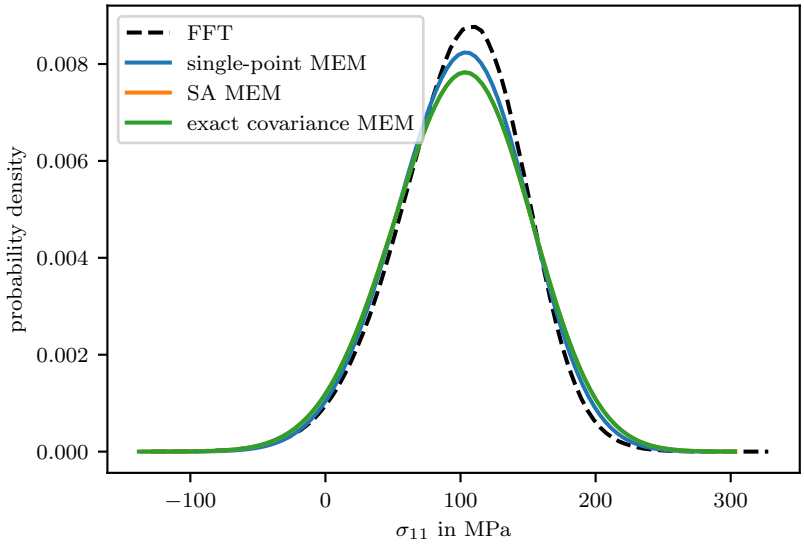

Figure 5.11: $p(\sigma_{11})$ in polycrystalline titanium for various MEM models and a full-field solution assuming linear elasticity with thermal eigenstrains.

distribution looks similar to a normal distribution, but has a slight skew. All MEM models show good overall agreement in reproducing the means and covariances, but do not fully capture the slight deviations from a normal distribution the FFT distribution suggests. Among the MEM models, the single-point MEM is closest to the full-field statistic. The SA MEM is slightly further away, and "correcting" the SA MEM by using the exact covariances results in an estimate that is even further from the full-field solution.

When thermal strains are taken into account, these tendencies remain. Fig. 5.11 again shows the probability density of the σ_{11} component. With thermal eigenstrains taken into account, the covariances are significantly larger. Again, the FFT distribution is slightly non-normal, with a skew that is now pointing in the other direction. Unlike the linear elastic

case, SA MEM and exact covariance MEM almost exactly coincide, as the covariance corrections only apply to the comparatively less relevant linear elastic part. Again, of the MEM variants considered here, the single-point MEM most closely matches the full-field stress statistics.

In conclusion, the MEM provides accurate approximations for overall stress distributions of polycrystalline titanium. Despite its simplicity, the single-point MEM is more accurate than the SA MEM and exact covariance MEM in the specific case considered here. Unlike the full-field calculation used as a reference, the MEM calculation is fully analytical except for the numerical evaluation of the integral for calculating the overall distribution. Even taking the numerical integration into account, the MEM is numerically less expensive than the full-field calculations by orders of magnitude.

Chapter 6

X-Ray diffraction (XRD) stress analysis

6.1 Introduction to XRD stress analysis[1]

6.1.1 The $\sin^2(\psi)$ technique

The following section summarizes stress analysis based on diffraction measurements using the $\sin^2(\psi)$ technique as described by Noyan and Cohen (1987). Fig. 6.1 shows a simplified geometry of the experimental setup. A monochromatic X-ray originating from the source interacts with the sample at the origin point of the sample coordinate system $\boldsymbol{e}_i$. Due to diffraction of the X-ray beam at the crystal lattice, diffraction cones form. Typically, the diffracted signal can be recorded by cuts through the diffraction cones in specific orientations by means of appropriately positioned detectors. With respect to the sample coordinate system $\boldsymbol{e}_i$, the scattering vector $\boldsymbol{n}$ is given by

$$\boldsymbol{n}(\varphi, \psi) = \cos(\varphi)\sin(\psi)\boldsymbol{e}_1 + \sin(\varphi)\sin(\psi)\boldsymbol{e}_2 + \cos(\psi)\boldsymbol{e}_3. \tag{6.1}$$

[1] This chapter is based on section 2 of the publication *Determination of diffraction elastic constants using the Maximum Entropy Method* (Krause et al., 2024).

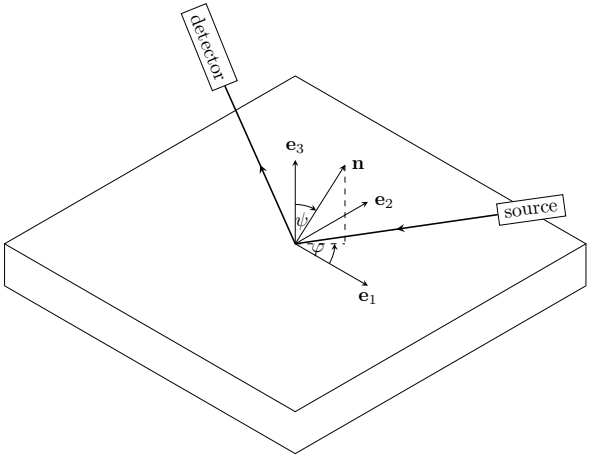

Figure 6.1: Simplified geometry of the experimental setup for diffraction-based stress analysis. Figure based on Figure 1 of Krause et al. (2024).

The phenomenon of diffraction of X-rays at a crystal lattice is explained by Bragg's law as depicted in Fig. 6.2. For a given lattice plane described by the lattice plane normal $\boldsymbol{n}$, diffraction occurs if the angle between lattice plane and incident beam θ, the wavelength λ and the lattice plane distance D satisfy

$$n\lambda = 2D\sin(\theta), \quad n \in \mathbb{N}. \tag{6.2}$$

The samples considered in this work are polycrystalline, such that multiple randomly oriented grains (crystallites) are irradiated by the beam, and fine-grained, such that there is always a sufficient number of crystallites in diffraction position. In this work, crystallites are presumed to have approximately perfect lattices without twinning, plastic strain gradients or other heterogeneities, such that the lattice orientation is constant in a single crystallite. The crystallite orientation can be described by a second-order orientation tensor $\boldsymbol{Q} \in SO(3)$. In the cubic case,

$$\boldsymbol{g}_i = \boldsymbol{Q}\boldsymbol{e}_i \tag{6.3}$$

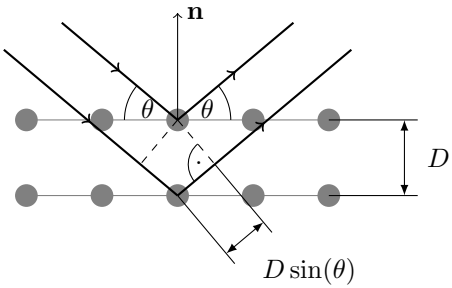

Figure 6.2: Bragg diffraction. Figure based on Figure 2 of Krause et al. (2024).

yields the normalized lattice basis vectors, which form an orthonormal coordinate system.

In Fig. 6.2, diffraction is shown schematically for a simplified example lattice in a 2D projection. Depending on the crystal structure, diffraction can occur on various differently oriented lattice planes. For a given lattice plane specified by Miller indices (hkl), the scattering vector is given in the normalized crystal coordinate system $\boldsymbol{g}_i$ as

$$\boldsymbol{n}((hkl), \boldsymbol{Q}) = \frac{h\boldsymbol{g}_1 + k\boldsymbol{g}_2 + l\boldsymbol{g}_3}{\sqrt{h^2 + k^2 + l^2}}. \tag{6.4}$$

As it is not possible to crystallographically distinguish the (hkl) plane with geometrically symmetric planes such as the (klh) plane, a more precise definition of $\boldsymbol{n}$ is based on the set of all geometrically symmetric lattice planes $\{hkl\}$, called the family of lattice planes of type hkl, which in the cubic case is given by all permutations of the indices hkl with any combination of signs.

In both Fig. 6.1 and Fig. 6.2, the scattering vector $\boldsymbol{n}$ is the same. This correspondence defines the set g of crystal orientations for which diffraction can be experimentally observed under given angles,

$$g(\{hkl\}, \varphi, \psi) = \{\boldsymbol{Q} \in SO(3) : \boldsymbol{n}(\{hkl\}, \boldsymbol{Q}) = \boldsymbol{n}(\varphi, \psi)\}. \tag{6.5}$$

In Fig. 6.2, diffraction is illustrated with a crystallite of one orientation. The set g includes all rotations of that orientation around $\boldsymbol{n}$. Therefore, g as a set is invariant with respect to arbitrary rotations around $\boldsymbol{n}$, i.e.,

$$g = \boldsymbol{R}(\boldsymbol{n}, \alpha) \star g = \{\boldsymbol{R}(\boldsymbol{n}, \alpha)\boldsymbol{Q} : \boldsymbol{Q} \in g\} \quad \forall \alpha \in [0, 2\pi]. \tag{6.6}$$

A direct calculation of g is possible by choosing one diffracting orientation $\boldsymbol{Q}_0$ and rotating around $\boldsymbol{n}$. A possible choice for $\boldsymbol{Q}_0$ can be calculated by first finding a rotation which maps the lattice normal vector in the reference configuration

$$\boldsymbol{n}((hkl), \mathbf{1}) = \frac{h\boldsymbol{e}_1 + k\boldsymbol{e}_2 + l\boldsymbol{e}_3}{\sqrt{h^2 + k^2 + l^2}} \tag{6.7}$$

to $\boldsymbol{e}_3$, and then multiplying with a rotation that maps $\boldsymbol{e}_3$ to the scattering vector $\boldsymbol{n}(\varphi, \psi)$. Using Euler angles, $\boldsymbol{Q}_0$ can be written

$$\boldsymbol{Q}_0 = \boldsymbol{R}(\varphi_1, \phi, \varphi_2), \tag{6.8}$$

$$\varphi_1 = \varphi \tag{6.9}$$

$$\phi = \psi - \arccos(l) \tag{6.10}$$

$$\varphi_2 = \begin{cases} -\arcsin\left(\frac{k}{\sqrt{1-l^2}}\right) & |l| \neq 1 \\ 0 & |l| = 1 \end{cases} \tag{6.11}$$

in the ZYZ convention, i.e., with intrinsic rotations around those three axes, as shown for φ and ψ in Fig. 6.1. Every permutation in $\{hkl\}$ yields a different $\boldsymbol{Q}_0$. The set g can then be written as

$$g(\{hkl\}, \varphi, \psi) = \{\boldsymbol{R}(\boldsymbol{n}, \theta)\boldsymbol{Q}_0((hkl), \varphi, \psi) : \theta \in [0, 2\pi)\,, (hkl) \in \{hkl\}\}. \tag{6.12}$$

The use of the diffraction relation to analyze stresses is based on the lattice plane distance D implied by Eq. ((6.2)). Residual stresses within

the material cause elastic strains such that the stress-free lattice plane distance D_0 is compressed or elongated to the lattice plane distance D. As elastic strains are small in metals, small-deformation strains can be assumed, the lattice plane normal of which is given by

$$\frac{D - D_0}{D_0} = \boldsymbol{\varepsilon} \cdot (\boldsymbol{n} \otimes \boldsymbol{n}). \tag{6.13}$$

The relationship between these purely elastic strains and the corresponding residual stresses is given by Hooke's Law

$$\boldsymbol{\sigma} = \mathbb{C}[\boldsymbol{\varepsilon}]. \tag{6.14}$$

These stresses, strains and stiffnesses are in the following called local or microscale quantities. The local stiffness tensor $\mathbb{C}$ is specified by the stiffness reference tensor $\mathbb{C}_0$ of the crystallite aligned to $\boldsymbol{e}_i$, which is rotated by the local crystal orientation to yield

$$\mathbb{C} = \boldsymbol{Q} \star \mathbb{C}_0. \tag{6.15}$$

In experimental applications, various assumptions made in the previous section do not hold exactly. For example, the beam is not perfectly monochromatic, but exhibits a wavelength distribution, and the crystallite does not have an ideal lattice, i.e., it contains lattice imperfections. As a result, measurements of the diffraction angle θ include statistical noise from various sources. When using the $\sin^2(\psi)$ technique, the statistically scattered θ values are integrated over to retrieve one single angle. Due to this averaging process, only $\langle D \rangle_g$, the statistical mean of the lattice plane distance over g, can be calculated from measurements. Taking this statistical mean over the stress-strain relationship leads to

$$\frac{\langle D \rangle_g - D_0}{D_0} = \langle \boldsymbol{\varepsilon} \rangle_g \cdot (\boldsymbol{n} \otimes \boldsymbol{n}) = (\boldsymbol{n} \otimes \boldsymbol{n}) \cdot \langle \mathbb{C}^{-1}[\boldsymbol{\sigma}] \rangle_g. \tag{6.16}$$

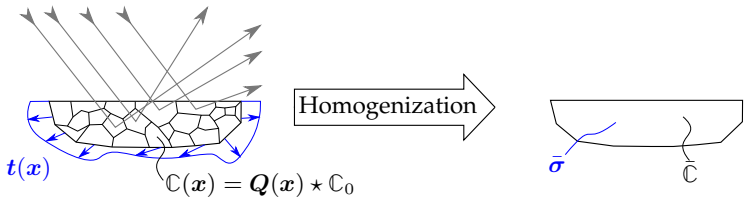

Figure 6.3: Schematic of the irradiated crystallites versus a homogenized replacement problem. Figure based on Figure 3 of Krause et al. (2024).

Establishing a relation between $\langle \mathbb{C}^{-1}[\boldsymbol{\sigma}] \rangle_g$ and a macroscopically observable stress quantity requires various micromechanical assumptions. As depicted in Fig. 6.3, the beam irradiates multiple crystallites at once, generally many more than shown in this schematic drawing. At the edge of the irradiated material volume, generally, heterogeneous boundary conditions apply which depend on crystallites which are not irradiated. Problems of this kind are micromechanically simplified by defining a replacement problem with a homogeneous material $\bar{\mathbb{C}}$ and homogeneous loads as sketched in Fig. 6.3. The necessary condition for equivalence between the heterogeneous and homogeneous problems is the Hill-Mandel condition discussed in Section 3.2.2. Absent specific boundary conditions, the Hill-Mandel condition holds in the limit of an infinitely large sample, which in this case is given if an infinite number of very small grains is irradiated by the beam. In the X-ray diffraction setting, the Hill-Mandel condition is therefore an approximation that is improved as the number of grains under consideration increases. More accurate results are expected for finer-grained materials.

As discussed in Section 3.2.2, the relationship between effective strains and local strains can be formalized using the strain concentration tensor $\mathbb{A}(\boldsymbol{x})$. In the following, only the mean strain of all grains of a given orientation is needed, and the corresponding mean of $\mathbb{A}$ is a function of $\boldsymbol{Q}$ instead of $\boldsymbol{x}$.

Averaging Hooke's Law on the microscale leads to

$$\bar{\boldsymbol{\sigma}} = \langle \mathbb{C}\mathbb{A} \rangle [\bar{\boldsymbol{\varepsilon}}], \tag{6.17}$$

thus leading to an explicit expression for the effective stiffness,

$$\bar{\mathbb{C}} = \langle \mathbb{C}\mathbb{A} \rangle. \tag{6.18}$$

Combining the concentration tensor with Eq. ((6.16)) yields the fundamental XRD stress analysis equation

$$\begin{aligned} \frac{\langle D \rangle_g - D_0}{D_0} =& (\boldsymbol{n} \otimes \boldsymbol{n}) \cdot \langle \mathbb{A} \rangle_g [\bar{\boldsymbol{\varepsilon}}] \\ =& (\boldsymbol{n} \otimes \boldsymbol{n}) \cdot \langle \mathbb{A} \rangle_g \bar{\mathbb{C}}^{-1} [\bar{\boldsymbol{\sigma}}] \\ =& \bar{\mathbb{C}}^{-1} \langle \mathbb{A}^{\mathsf{T}_{\mathrm{H}}} \rangle_g [\boldsymbol{n} \otimes \boldsymbol{n}] \cdot \bar{\boldsymbol{\sigma}}. \end{aligned} \tag{6.19}$$

Following Behnken and Hauk (1991), the second order tensor

$$\boldsymbol{F}(\varphi, \psi, hkl) = \bar{\mathbb{C}}^{-1} \langle \mathbb{A}^{\mathsf{T}_{\mathrm{H}}} \rangle_g [\boldsymbol{n} \otimes \boldsymbol{n}] \tag{6.20}$$

is called a stress factor. In the general form of Eq. ((6.19)), the XRD equation is applicable to arbitrary crystal symmetries and textures. Its accuracy depends on finding an accurate estimate for the strain concentration $\mathbb{A}(\boldsymbol{Q})$.

6.2 XRD for statistically isotropic polycrystals[2]

6.2.1 Simplified XRD problem for cubic polycrystals without texture

In the following, we assume that the polycrystals under consideration are statistically isotropic as defined in Section 3.2.1. Following Behnken and Hauk (1991), the stress factor for a statistically isotropic polycrystal is

$$\boldsymbol{F}(\varphi,\psi,hkl) = s_1(hkl)\boldsymbol{I} + \frac{1}{2}s_2(hkl)\boldsymbol{n}(\varphi,\psi)\otimes\boldsymbol{n}(\varphi,\psi), \tag{6.21}$$

where s_1 and $½s_2$ are called diffraction elastic constants (DECs).

As the material has a cubic symmetry, the results shown in Section 3.2.3 apply. The average of the strain concentration tensor over all grains of a single orientation $\mathbb{A}(\boldsymbol{Q})$ can then be directly determined from the effective shear modulus $\bar{G}$. After some calculation, the DECs are given in terms of the effective shear modulus as

$$s_1 = \frac{-5\lambda_1^{\mathrm{C}}\left(2\Gamma\lambda_2^{\mathrm{C}} + 3\Gamma\lambda_3^{\mathrm{C}} - 10\Gamma\bar{G} - \lambda_3^{\mathrm{C}} + 2\bar{G}\right) + 4\bar{G}\left(\lambda_2^{\mathrm{C}} - \lambda_3^{\mathrm{C}}\right)}{12\lambda_1^{\mathrm{C}}\bar{G}\left(\lambda_2^{\mathrm{C}} - \lambda_3^{\mathrm{C}}\right)}, \tag{6.22}$$

$$\frac{s_2}{2} = \frac{5\left(2\Gamma\lambda_2^{\mathrm{C}} + 3\Gamma\lambda_3^{\mathrm{C}} - 10\Gamma\bar{G} - \lambda_3^{\mathrm{C}} + 2\bar{G}\right)}{4\bar{G}\left(\lambda_2^{\mathrm{C}} - \lambda_3^{\mathrm{C}}\right)} \tag{6.23}$$

where the *lattice plane orientation parameter* 3Γ contains the influence of the lattice plane consideration, reading

$$3\Gamma = 3\frac{h^2k^2 + h^2l^2 + k^2l^2}{\left(h^2+k^2+l^2\right)^2}. \tag{6.24}$$

[2] This chapter is based on sections 3–6 of the publication *Determination of diffraction elastic constants using the Maximum Entropy Method* (Krause et al., 2024).

Depending on the experimental conditions, pure plane stress conditions can sometimes be assumed in $\sin^2(\psi)$ analysis, particularly if the effective penetration depth of the X-rays is in the range of a few micrometers. In that case, Eq. (6.19) takes the form

$$\begin{aligned}&\langle\boldsymbol{\varepsilon}\rangle_g \cdot (\boldsymbol{n}\otimes\boldsymbol{n}) = \\ &\frac{s_2}{2}(\bar{\sigma}_{11}\cos^2(\varphi) + \bar{\sigma}_{12}\sin(2\varphi) + \bar{\sigma}_{22}\sin^2(\varphi))\sin^2(\psi) + s_1(\bar{\sigma}_{11}+\bar{\sigma}_{22}),\end{aligned} \tag{6.25}$$

such that $\langle\boldsymbol{\varepsilon}\rangle_g$ is linear with respect to $\sin^2(\psi)$. This linearity may be lost if any of the above assumptions are violated, e.g., if stress gradients, texture, or shear stresses $\bar{\sigma}_{13}$ or $\bar{\sigma}_{23}$ are present (Noyan and Cohen, 1987).

6.2.2 Singular Approximation DECs

This section discusses the Voigt, Reuss, Hashin-Shtrikman and self-consistent (also known as Eshelby-Kröner) models of local strain fields in a polycrystal by characterizing them as special cases of the Singular Approximation described in Section 3.2.4. As we only consider statistically isotropic polycrystals, we restrict ourselves to an isotropic reference stiffness $\mathbb{C}_0$ and mean spherical inclusion shapes. In this particular case, the Singular Approximation shear modulus is given by

$$\bar{G}^{\mathrm{S}} = \frac{16G_0^2\lambda_2^{\mathrm{C}} + 24G_0^2\lambda_3^{\mathrm{C}} + 18G_0K_0\lambda_2^{\mathrm{C}} + 27G_0K_0\lambda_3^{\mathrm{C}} + 30G_0\lambda_2^{\mathrm{C}}\lambda_3^{\mathrm{C}} + 15K_0\lambda_2^{\mathrm{C}}\lambda_3^{\mathrm{C}}}{2\left(40G_0^2 + 45G_0K_0 + 18G_0\lambda_2^{\mathrm{C}} + 12G_0\lambda_3^{\mathrm{C}} + 9K_0\lambda_2^{\mathrm{C}} + 6K_0\lambda_3^{\mathrm{C}}\right)}. \tag{6.26}$$

For the sake of brevity, we do not rederive the DECs by using the strain concentration tensor implied by Eq. (3.143). Instead, Eq. (6.26) can be used together with Eq. (6.22) and Eq. (6.23) to calculate DECs. Theoretically, as the choice of G_0 and K_0 uniquely specifies $\bar{G}$, either parameterization yields the same result. If $\bar{G}$ is already known, e.g., from experimental measurements, using the Singular Approximation

framework is not necessary. We introduce the Singular Approximation because various possible choices of G_0 and K_0 can be motivated on theoretical grounds to yield established micromechanical models, and because the Singular Approximation is amenable to a possible future generalization for textured polycrystals, unlike the direct method using $\bar{G}$.

As an example, we consider statistically isotropic pure copper with single crystal elastic constants

$$C_{1111} = 170.2\,\mathrm{GPa}, \quad C_{1122} = 114.9\,\mathrm{GPa}, \quad C_{1212} = 61.0\,\mathrm{GPa}, \tag{6.27}$$

taken from Simmons and Wang (1971). The microstructure is not specified, leading to an unknown effective shear stiffness. The resulting DECs are depicted in Fig. 6.4. This diagram shows a monotonic relationship between the effective shear stiffness and the DECs which depends on the considered lattice plane. The range of effective shear moduli spans all values that can be realized by the Singular Approximation if $\mathbb{C}_0$ is positive semidefinite and isotropic.

We now discuss the specific models depicted as dashed lines in Fig. 6.4. Using the direct assumption of homogeneous strains, the isotropic DECs for the Voigt estimate follow simply as

$$s_1^+ = \frac{1}{3\lambda_1^{\mathbb{C}}} - \frac{5}{3(2\lambda_2^{\mathbb{C}} + 3\lambda_3^{\mathbb{C}})}, \tag{6.28}$$

$$\frac{s_2^+}{2} = \frac{5}{2\lambda_2^{\mathbb{C}} + 3\lambda_3^{\mathbb{C}}}. \tag{6.29}$$

For the Reuss estimate,

$$s_1^- = \left(\Gamma - \frac{1}{3}\right)\left(\frac{1}{\lambda_3^{\mathbb{C}}} - \frac{1}{\lambda_2^{\mathbb{C}}}\right), \tag{6.30}$$

$$\frac{s_2}{2}^- = \frac{3\Gamma}{\lambda_3^{\mathbb{C}}} - \frac{1}{\lambda_2^{\mathbb{C}}}\left(3\Gamma - 1\right). \tag{6.31}$$

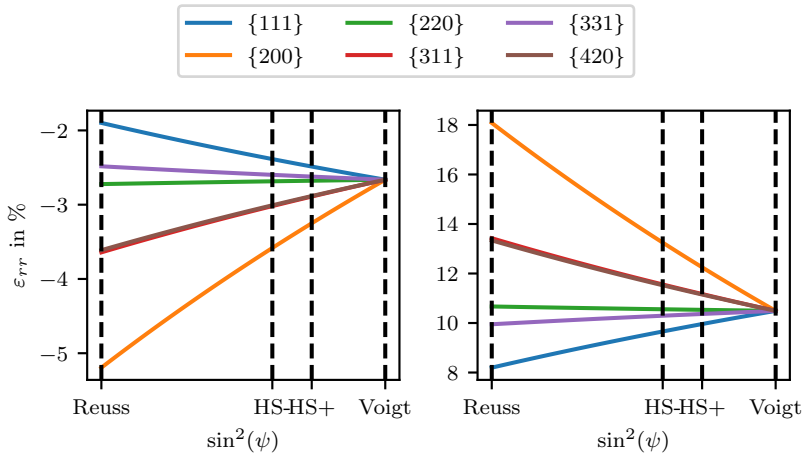

Figure 6.4: s_1 (left) and ½s_2 (right) depending on $\bar{G}$ for statistically isotropic copper. Figure based on Figure 4 of Krause et al. (2024).

The Voigt and Reuss estimates represent strict bounds for the effective strain energy density as discussed in Section 3.2.4. Similarly, the corresponding Voigt and Reuss DECs form bounds on the possible values of the DECs, as shall be discussed in the following. In the specific case of statistically isotropic cubic polycrystals, the bounds on the effective shear modulus are

$$G_+ \geq \bar{G} \geq G_-. \tag{6.32}$$

Because both s_1 and ½s_2 are monotonic in $\bar{G}$, these bounds then also hold for s_1 and ½s_2. Any experimentally measured values of the DECs which violate these bounds contradict underlying micromechanical assumptions. The Voigt and Reuss estimates are first-order bounds depending only on the crystallographic texture and the material properties, meaning that they hold for arbitrarily asymmetric grain shapes. If they are clearly violated beyond measurement error, possible explana-

tions include material imperfections of the polycrystal such as pores or material heterogeneities.

The Reuss DECs depend on 3Γ and match the values of the Voigt elastic constants at

$$3\Gamma = \frac{3\lambda_3^{\mathrm{C}}}{2\lambda_2^{\mathrm{C}} + 3\lambda_3^{\mathrm{C}}}, \tag{6.33}$$

such that for higher 3Γ, the upper and lower bounds swap places. Because Voigt and Reuss values are strict bounds, all methods for calculating DECs, including experimental results, are required to coincide at this specific value of 3Γ.

Following the approach described in Section 3.2.4, the upper Hashin-Shtrikman bound for a cubic polycrystal is calculated by choosing an isotropic $\mathbb{C}_0$ with

$$3K_0 = \lambda_1^{\mathrm{C}}, \tag{6.34}$$

$$2G_0 = \max(\lambda_2^{\mathrm{C}}, \lambda_3^{\mathrm{C}}), \tag{6.35}$$

and the lower HS bounds by choosing

$$3K_0 = \lambda_1^{\mathrm{C}}, \tag{6.36}$$

$$2G_0 = \min(\lambda_2^{\mathrm{C}}, \lambda_3^{\mathrm{C}}). \tag{6.37}$$

The formula for the lower HS bound with $\lambda_2^{\mathrm{C}} < \lambda_3^{\mathrm{C}}$ corresponds to the upper HS bound with $\lambda_2^{\mathrm{C}} > \lambda_3^{\mathrm{C}}$. Either case results in the effective shear modulus

$$\bar{G}^{\mathrm{HS}}(G_0 = \lambda_2^{\mathrm{C}}) = \frac{\lambda_2 \left(3\lambda_1\lambda_2 + 7\lambda_1\lambda_3 + 8\lambda_2^2 + 27\lambda_2\lambda_3\right)}{2\left(9\lambda_1\lambda_2 + \lambda_1\lambda_3 + 29\lambda_2^2 + 6\lambda_2\lambda_3\right)}. \tag{6.38}$$

The corresponding other bound reads

$$\bar{G}^{\mathrm{HS}}(G_0 = \lambda_3^{\mathrm{C}}) = \frac{\lambda_3 \left(11\lambda_1\lambda_2 + 9\lambda_1\lambda_3 + 46\lambda_2\lambda_3 + 24\lambda_3^2\right)}{2\left(3\lambda_1\lambda_2 + 17\lambda_1\lambda_3 + 18\lambda_2\lambda_3 + 52\lambda_3^2\right)}. \tag{6.39}$$

DECs can be recovered using Eq. (6.22) and Eq. (6.23).

Similarly to the Voigt-Reuss bounds, if the HS shear modulus bounds the effective shear modulus, the HS DECs are bounds on DECs as well. Compared to the Voigt-Reuss bounds, the additional assumption needed is that the two-point statistic of the grain orientation distribution has spherical symmetry, which is a statistical assumption that can be fulfilled even when any given grain has a non-spherical shape.

The self-consistent approximation (sometimes called the Eshelby-Kröner approximation in materials science after Eshelby (1957) and Kröner (1958)) is recovered from the Singular Approximation by setting $\mathbb{C}_0 = \bar{\mathbb{C}}$. As $\bar{\mathbb{C}}$ depends on $\mathbb{C}_0$ according to Eq. (3.144), a nonlinear equation results. For statistically isotropic cubic polycrystals, the compression modulus is

$$3K_0 = 3\bar{K} = \lambda_1^{\mathrm{C}}. \tag{6.40}$$

With $\bar{G}$ from Eq. (6.26), the self-consistent approach results in the cubic equation

$$16\bar{G}^3 + \left(18\lambda_1^{\mathrm{C}} + 4\lambda_2^{\mathrm{C}}\right)\bar{G}^2 + \left(-3\lambda_1^{\mathrm{C}}\lambda_3^{\mathrm{C}} - 6\lambda_2^{\mathrm{C}}\lambda_3^{\mathrm{C}}\right)\bar{G} - 3\lambda_1^{\mathrm{C}}\lambda_2^{\mathrm{C}}\lambda_3^{\mathrm{C}} = 0 \tag{6.41}$$

noted by Willis (1981) among others. According to Descartes' rule of signs, this equation has exactly one positive solution. From that $\bar{G}$, DECs can be calculated via Eq. (6.22) and Eq. (6.23).

Again, a mean spherical grain shape has been assumed for this calculation. In cases with significant morphological texture, i.e., rolled sheet metal, a mean ellipsoidal grain shape can be incorporated into the self-consistent approximation via a different choice of $\mathbb{P}_0$, which significantly complicates the calculations.

6.2.3 Application of the MEM to XRD stress analysis

In the following, the single-point MEM described in Section 5.2 is applied to an isotropic uniform polycrystal with cubic stiffness eigenvalues $\lambda_1^C, \lambda_2^C, \lambda_3^C$. Because the compression modulus is homogeneous, the Moore-Penrose pseudoinverse degenerates to an inversion on the space of deviatoric second order tensors, and the MEM formulas given in Appendix B.3.2 result. The resulting strain concentration tensor is

$$\begin{aligned}\mathbb{A}(\boldsymbol{Q}) =& \boldsymbol{Q} \star \mathbb{A}_0,\\ \mathbb{A}_0 =& \mathbb{I}^{\mathrm{S}} + \frac{G_+ - \bar{G}}{G_+ - G_-} \sum_{\alpha=2}^{3} \frac{2G_- - \lambda_\alpha^{\mathrm{C}}}{\lambda_\alpha^{\mathrm{C}}} \mathbb{P}_\alpha^{\mathrm{C}}.\end{aligned}$$

The MEM results are exactly the same as the formulas derived in Section 6.2.1. Since the optimization constraints of the MEM are the assumptions the theoretical derivation in Section 3.2.3 relies on, such as the Hill-Mandel condition, this is not surprising. However, unlike the theoretical approach, the MEM assumes statistical isotropy only for the ODF and the overall effective stiffness, without explicitly assuming non-correlatedness between morphological and crystallographic textures. It appears that this assumption of non-correlatedness is also maximally entropic.

6.2.4 Influence of elastic heterogeneity on diffraction measurements

In polycrystalline microstructures, the interaction of differently-oriented grains leads to heterogeneous stress and strain fields even if eigenstrains are not considered. As shown by Gehrig et al. (2022), the strain covariances given by the MEM are an accurate approximation for statistically isotropic cubic polycrystals. Using the MEM covariance given in Appendix B.3.2, the component of the covariance in the lattice plane normal

direction is given by

$$K_n = \mathbb{K} \cdot \boldsymbol{n}(\varphi, \psi)^{\otimes 4} \tag{6.42}$$

$$= k \left(\frac{2}{3\lambda_2^{\mathrm{C}}}(1 - 3\Gamma) + \frac{1}{\lambda_3^{\mathrm{C}}}\Gamma \right). \tag{6.43}$$

As an example, for pure copper with single crystal elastic constants as given in Eq. (6.27), K_n is maximal for $3\Gamma = 0$. In that case, the standard deviation of the lattice plane normal strain is

$$\sqrt{K_n^{\mathrm{Cu}}(3\Gamma = 0)} \approx 0.080 \|\bar{\boldsymbol{\varepsilon}}'\|. \tag{6.44}$$

Assuming that there are no other sources of fluctuations in the lattice normal distance D, its deviation results as

$$\sqrt{\langle D^2 \rangle - \langle D \rangle^2} = 0.080 \|\bar{\boldsymbol{\varepsilon}}'\| D_0. \tag{6.45}$$

Since $\bar{\boldsymbol{\varepsilon}}$ is generally on the order of 10^{-4}, the effect of the elastic heterogeneity is negligible compared to other sources of measurement fluctuations in experimental practice.

6.2.5 Numerical setup for full-field simulations

To validate the theoretical result, full-field microstructure simulations are used which are based on the FFT approach described in Section 5.3.1. To generate polycrystal microstructures, the algorithms described by Kuhn et al. (2022) are used. The resulting microstructures are Laguerre tessellations with grain orientations which realize a prescribed texture state with particular accuracy.

The FFT-based solver used requires periodic boundary conditions. Therefore, any simulations approximate the behavior of bulk material, not surface material. While, in the following section, an effective plane stress $\bar{\boldsymbol{\sigma}}$ is prescribed, the local stresses $\boldsymbol{\sigma}$ are not planar in every material

point, as they would be at a free surface. The theoretical models used to compute DECs share the same limitation. As these models are well-established, we assume in the following that the difference between plane-stress bulk behavior and surface behavior can be neglected in practice.

Before quantifying other numerical sources of error, we discuss the evaluation of numerical $\sin^2(\psi)$ experiments. From the local strain fields provided by full-field simulations, $\boldsymbol{\varepsilon} \cdot (\boldsymbol{n} \otimes \boldsymbol{n})$ can be calculated directly. DECs can then be calculated by linear regression on simulated D-vs-$\sin^2(\psi)$ curves. The main difficulty of the process lies in the evaluation of averages over the set g, because only a finite number of discrete grain orientations are present, such that for almost all angles, there are no grains exactly fulfilling the underlying condition in Eq. (6.5),

$$\boldsymbol{n}(\varphi, \psi) = \boldsymbol{n}(\{hkl\}, \boldsymbol{Q}). \tag{6.46}$$

In experimental practice, this condition can be violated because small misalignments do not prohibit diffraction. A full physical consideration of the underlying effects is difficult. We calculate diffraction misalignment as the distance between $\boldsymbol{Q}$ and $g(\{hkl\}, \varphi, \psi)$,

$$d = \min_{\alpha} \min_{(hkl) \in \{hkl\}} \|\boldsymbol{R}(\boldsymbol{n}, \alpha) \boldsymbol{Q}_0((hkl), \varphi, \psi) - \boldsymbol{Q}\|, \tag{6.47}$$

where the SO(3) distance by Larochelle et al. (2006) is used. Following Huynh (2009), the Frobenius norm in the above expression can be replaced by the 2-norm, and after some manipulation, the misalignment equals

$$d = \min_{(hkl) \in \{hkl\}} \|\boldsymbol{n}(\varphi, \psi) - \boldsymbol{n}((hkl), \boldsymbol{Q})\|. \tag{6.48}$$

As a simple approximation, all crystallites with misalignment below a threshold value $d_{\max}$ are considered to be involved in diffraction. The higher $d_{\max}$ is chosen, the smoother and flatter simulated D-vs-$\sin^2(\psi)$

curves appear, with the maximal value $d_{\max} = 2$ containing all grains regardless of orientation, which results in a constant curve. Very low threshold values eventually prohibit a measurement, as no crystallites can be found which are aligned correctly. For the following results, $d_{\max} = 0.05$ has been chosen as a compromise.

There are three sources of numerical error which will be discussed separately in the following. The first is discretization error, which depends on the fineness of the resolution, i.e., the number of voxels used for the microstructure. The second is representativeness error, which is present if the artificially generated microstructure is not representative of the theoretical infinite microstructure underlying it, such as the generated microstructure not being perfectly statistically isotropic. The third is the solver error, which is the precision to which the Lippmann-Schwinger equation is numerically solved. This value can be set to be smaller than the other errors by orders of magnitude and will not be considered.

The generated microstructures consist of $10\,000$ grains, which corresponds to experimental conditions with particularly fine-grained samples. As the overall polycrystal is assumed to be texture-free and therefore statistically isotropic, an observed effective anisotropy would be a sign of a nonrepresentative generated microstructure volume element. The anisotropy is therefore a lower bound estimate of the total error on results for effective quantities. After numerically calculating the effective stiffness $\bar{\mathbb{C}}$, the total effective anisotropy can be quantified as the difference to the isotropic projection $\bar{\mathbb{C}}^{\mathrm{I}}$ of the effective stiffness, yielding the anisotropic error

$$e_{\text{aniso}} = \frac{\|\bar{\mathbb{C}} - \bar{\mathbb{C}}^{\mathrm{I}}\|}{\|\bar{\mathbb{C}}\|}. \tag{6.49}$$

For an ensemble of ten microstructures of $10\,000$ grains each, the anisotropic error was found to be at a mean $0.17\,\%$ with standard deviation of $0.04\,\%$. As this error was found to be constant for resolutions

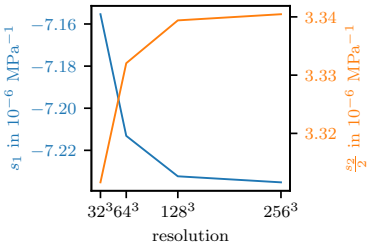

Figure 6.5: DECs for the {400} plane based on different resolutions of the same copper microstructure. Figure based on Figure 5 of Krause et al. (2024).

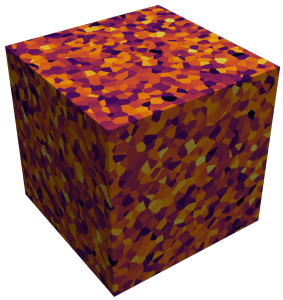

Figure 6.6: Microstructure used for full-field simulations at a resolution of 256^3. Figure based on Figure 6 of Krause et al. (2024).

ranging from 32^3 to 256^3 voxels, it is considered to be a representativeness error arising from the finite number of grains. Whether the degree of isotropy reached for calculation of effective stiffnesses is also sufficient of diffraction simulations will be discussed using concrete examples in subsequent sections.

The influence of the resolution on the determination of DECs was determined via a resolution study. To this end, a single microstructure of $10\,000$ grains was discretized with resolutions ranging from 32 voxels per side to 256 voxels per side. This corresponds to roughly 3 voxels per grain at the lower end to 1677 voxels per grain at the higher end. Between the lowest and highest resolution considered, the effective shear modulus differs on the order of $10\,\mathrm{MPa}$ or roughly $0.02\,\%$. However, the effect of low resolutions on DECs is significantly higher. In Fig. 6.5, simulated DECs for the {400} plane of pure copper are plotted for various resolutions of the same microstructure. From the highest to the lowest value, relative differences of roughly $1\,\%$ are observed. As both DECs show a clear pattern of convergence, the high-resolution microstructures with 256 voxels per side depicted in Fig. 6.6 are used for all simulations shown in the following.

6.2.6 DECs of fine-grained steel

To validate the various methods of DEC calculation, we use experimentally determined DEC values[3]. The material under consideration is the body centered cubic phase of the fine-grained ferritic construction steel S355MC. The experimental approach used is described in Krause et al. (2024).

In Fig. 6.7, the five resulting $\sin^2(\psi)$ plots at $\varphi = 0$ are shown along with linear regression plots of the same. The intersection of all five linear regressions yields the lattice plane distance of the strain-independent direction $D^* = 1.170\,15\,\text{Å}$, which is assumed to equal D_0. In Fig. 6.8, the intercepts and slopes of the linear regression plots from Fig. 6.7 are plotted against the applied load stress. A linear regression for these intercepts and slopes yields DEC values of

$$s_1 = -1.36 \times 10^{-6}\,\text{MPa}^{-1}, \tag{6.50}$$

$$\frac{s_2}{2} = 5.655 \times 10^{-6}\,\text{MPa}^{-1}. \tag{6.51}$$

The deviation of measurement points from the linear regression implies standard deviations of the DEC values of

$$\text{std}(s_1) = 1.173 \times 10^{-7}\,\text{MPa}^{-1}, \tag{6.52}$$

$$\text{std}\left(\frac{s_2}{2}\right) = 1.632 \times 10^{-8}\,\text{MPa}^{-1}. \tag{6.53}$$

These standard deviations do not include potential errors due to texture, stress gradients or other violations of the core assumptions.

In Fig. 6.9, experimental, numerical and theoretical values for the DECs of the ferritic steel S355MC are plotted against the lattice plane parameter

[3] The experimental data were provided by Michael Zürn and Dr. Jens Gibmeier from the Institute of Applied Materials, KIT. The measurement methodology is therefore not part of this thesis.

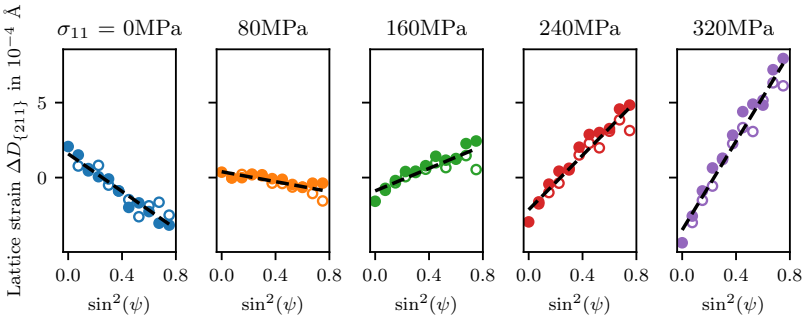

Figure 6.7: $\sin^2(\psi)$ plots of uniaxially loaded S355MC samples in the {211} lattice plane at $\varphi = 0$. Filled circles for $\psi \leq \pi/2$, hollow circles for $\psi \geq \pi/2$. Lines fitted using linear regression. Figure based on Figure 7 of Krause et al. (2024).

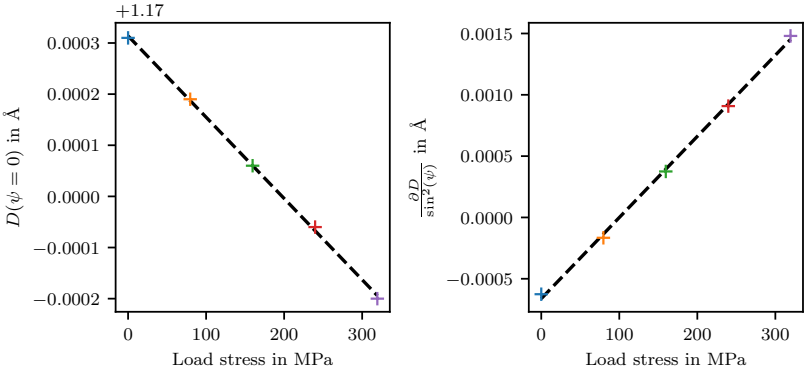

Figure 6.8: Axis intercepts (left) and slopes (right) of D-vs-$\sin^2(\psi)$ curves shown in Fig. 6.7. From the slope of both plots the diffraction elastic constants s_1 and ½s_2 can be derived. Figure based on Figure 8 of Krause et al. (2024).

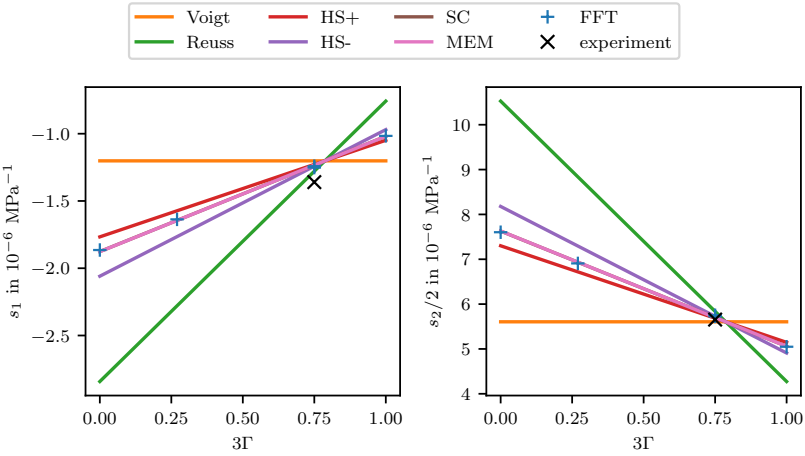

Figure 6.9: s_1 (left) and $½s_2$ (right) plotted against the lattice plane parameter 3Γ for the ferritic steel S355MC. Figure based on Figure 9 of Krause et al. (2024).

3Γ. Single crystal elastic constants for S355MC of

$$C_{1111} = 230\,\text{GPa}, \quad C_{1122} = 135\,\text{GPa}, \quad C_{1212} = 117\,\text{GPa}, \tag{6.54}$$

were taken from Landolt-Börnstein (Every and McCurdy, 1992). As discussed in Section 6.2.2, the Voigt and Reuss approaches form relatively wide bounds on the theoretically possible values of the DECs, while the Hashin-Shtrikman bounds are considerably tighter. The self-consistent method falls between the Hashin-Shtrikman bounds.

For the values of the MEM shown in the diagram, an effective shear modulus of $\bar{G} = 82.15\,\text{GPa}$ is used which was calculated via numerical homogenization using the same methodology as the full-field simulations. As the effective shear modulus given by the self-consistent method yields the same value to within four significant digits, the MEM and the self-consistent method are indistinguishable in the diagram.

From simulated D-vs-$\sin^2(\psi)$ curves, slopes and intercepts were obtained via linear regression for each of the {200}, {310}, {211}, and {222} lattice planes. Since in the simulated setting the stress is known exactly, simulated DECs can be calculated directly from those slopes and intercepts. The simulated DECs are very close to the theoretical results obtained via the MEM and self-consistent method. However, unlike theoretical predictions, they do not lie exactly on a straight line. This slight deviation could be explained by the slight anisotropy present in the $10\,000$ grain volume element. While the effect of nonrepresentativity of the volume element on effective elastic constants was found to be on the order of $0.1\,\%$, simulated DECs could be more sensitive to nonrepresentative anisotropy, just as simulated DECs are more sensitive to numerical errors due to low resolutions. Regardless, the deviation of the simulated DECs from a theoretical straight line is small compared to the deviations between different methods.

The experimental results violate theoretical bounds. The experimentally determined value of s_1 lies outside the Voigt-Reuss bounds by roughly $0.1 \times 10^{-6}\,\mathrm{MPa}^{-1}$, which amounts to roughly the difference spanned by the Voigt-Reuss bounds for the same value of 3Γ. While $\frac{1}{2}s_2$ respects the Voigt-Reuss bounds, it violates the Hashin-Shtrikman bounds. There are a number of possible explanations for these deviations between experiment and theory, such as unsuitable literature data for single crystal constants or experimental uncertainty. As the measured $\sin^2(\psi)$ plots do not form perfect lines, the violation of the Voigt bound could also be explained by complexities of the material which are not captured by the theory, such as slight crystallographic texture, residual stress gradients within the X-ray penetration depth, or even material heterogeneities. Regardless of the cause of the violation of the theoretical bounds, it should be noted that theoretically determined DECs are only accurate for stress analysis insofar as the theory can be applied.

When using the DECs for stress analysis, Fig. 6.9 shows that the absolute difference between various DEC calculation methods strongly depends on the lattice plane considered. For the $\{200\}$ plane, the $\frac{1}{2}s_2$-value of the Reuss bound is more than twice that of the Voigt bound, while for the $\{211\}$ plane, the differences are considerably smaller. Correspondingly, an observed violation of the Voigt and Reuss bounds in the $\{211\}$ plane is small in terms of the value of the deviation in DECs, and thus has only a small influence on the accuracy of a subsequent stress analysis. In the following section, the influence of deviations in DECs on the stress analysis is quantified for an example which is more sensitive to such inaccuracies.

6.2.7 Stress analysis of pure copper

As an example in which stress analysis is particularly sensitive with regard to the DECs, we conduct a stress analysis of pure copper for the $\{400\}$ plane. In Fig. 6.10, predicted lattice normal strains are plotted against $\sin^2(\psi)$ for a known stress state of $\sigma_{11} = 100\,\mathrm{MPa}$ and $\sigma_{22} = 100\,\mathrm{MPa}$. The results are similar to those obtained in the previous section, in that the numerical results respect the Hashin-Shtrikman bounds and are in good agreement with the MEM and the self-consistent method. The numerical results show a very slight stochastic deviation from a perfect line, which is again presumed to be due to the finite simulated volume being slightly nonrepresentative of a statistically isotropic microstructure.

While Fig. 6.10 illustrates theoretical approaches to predict lattice normal strains, XRD stress analysis requires a solution of the inverse problem, i.e., recovering the effective stress from experimentally determined lattice plane distance values. To avoid sources of error induced by experimental uncertainties, numerical simulations are used as a source of distance values in this section. The approach is based on a commonly used experimental technique, see, e.g., Dölle and Hauk (1976). Simulated

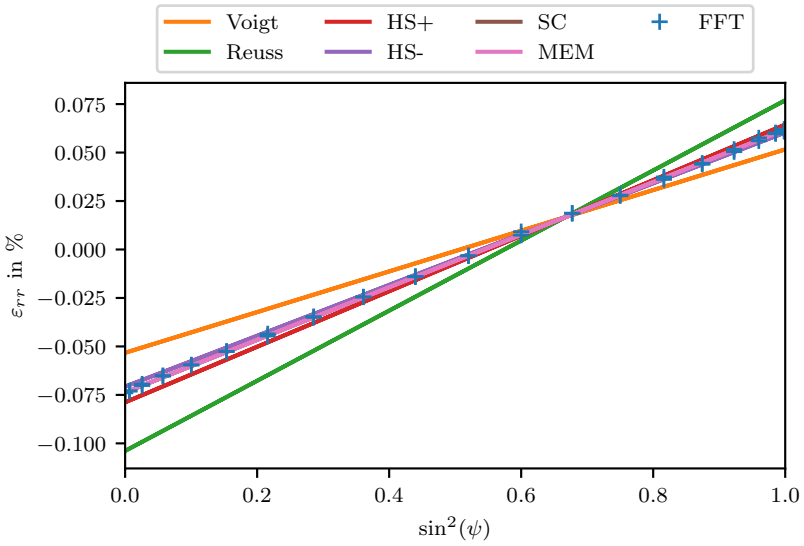

Figure 6.10: Predicted $\sin^2(\psi)$ results for uniform copper with $\varphi = 0$ for the {400} lattice plane. Figure based on Figure 10 of Krause et al. (2024).

diffraction experiments in the {400} lattice plane are performed at three azimuth angles $\varphi \in \{0, \pi/4, \pi/2\}$. The slope of the $\sin^2(\psi)$-plots equals

$$\frac{\partial \boldsymbol{\varepsilon} \cdot (\boldsymbol{n} \otimes \boldsymbol{n})}{\partial \sin^2(\psi)} = \frac{s_2}{2}(\bar{\sigma}_{11}\cos^2(\varphi) + \bar{\sigma}_{12}\sin(2\varphi) + \bar{\sigma}_{22}\sin^2(\varphi)). \tag{6.55}$$

Simulated measurements of the slope for three azimuth angles φ are sufficient to determine the three components of a planar effective stress for any given $½s_2$.

For simulated diffraction measurements, the effective stress $\boldsymbol{\sigma}_{\mathrm{FFT}}$ applied in the simulation is the reference to which analysis results must be compared. The stress $\boldsymbol{\sigma}$ resulting from the above calculation therefore

has a total relative error of

$$e_\sigma = \frac{\|\boldsymbol{\sigma} - \boldsymbol{\sigma}_{\mathrm{FFT}}\|}{\|\boldsymbol{\sigma}_{\mathrm{FFT}}\|}. \tag{6.56}$$

In Table 6.1, results for analytically calculated DEC are shown. For measurements for the $\{400\}$ lattice plane, XRD stress analysis is highly sensitive to the choice of analytical approximation. In the case of the Voigt approximation, a relative error of $6.4\,\%$ in the effective shear modulus is associated with a stress analysis error of $31.4\,\%$. An accurate estimate of the effective shear modulus is associated with a low stress analysis error. As in all other examples shown in this paper, the self-consistent method is very close to the simulated effective stiffness. The MEM, using the exact simulated effective shear modulus, yields only slightly improved results. As the difference between MEM and self-consistent results is smaller than the numerical error, these results cannot be used to draw conclusions on which method is better-suited for the material and microstructure considered. In general, if the self-consistent method and an experimentally or numerically determined shear modulus diverge significantly, a MEM approach based on a known shear modulus can be expected to yield a more accurate stress analysis than the self-consistent method.

	FFT	Reuss	HS-	MEM	SC	HS+	Voigt
$\bar{G}$ (GPa)	44.8	41.15	44.13	44.8	44.8	45.19	47.66
σ_{11} (MPa)	100	75.36	95.15	100.5	100.51	103.96	129.9
σ_{22} (MPa)	100	77.04	97.26	102.73	102.74	106.26	132.79
σ_{12} (MPa)	0	-1.36	-1.72	-1.82	-1.82	-1.88	-2.35
e_σ (%)	0	23.83	4.12	2.35	2.35	5.4	31.42

Table 6.1: Effective shear modulus and stress measurements according to various methods. Table based on Table 1 of Krause et al. (2024).

6.3 XRD for polycrystals with texture

6.3.1 Analytical stress factors in terms of texture coefficients

In the following, the results of the previous chapter are extended to polycrystals with texture. We again assume spherical mean grain shapes. For cold-formed samples such as rolled metal sheets, an elongation of the grains along sample-fixed directions can theoretically be implemented by considering non-spherical ellipsoids in the calculation of $\mathbb{P}_0$, using Eq. (3.132). However, in preliminary numerical investigations on our part, the effect of such morphological textures has tended to be negligible, which is why we restrict ourselves to crystallographic texture only.

Using a general formulation of the Singular Approximation, the effective stiffness is given by Eq. (3.144) and the strain concentration tensor is given by Eq. (3.143). The stress factors are

$$\boldsymbol{F}_{\mathrm{SA}} = \bar{\mathbb{C}}_{\mathrm{SA}} \langle \mathbb{L} \rangle^{-1} \langle \mathbb{L} \rangle_g [\boldsymbol{n} \otimes \boldsymbol{n}], \tag{6.57}$$

Depending on the model assumptions used, the reference stiffness $\mathbb{C}_0$ can be isotropic or anisotropic. If $\mathbb{C}_0$ is anisotropic, the calculation of $\mathbb{P}_0$, $\langle \mathbb{L} \rangle$ and $\langle \mathbb{L} \rangle_g$ each involve integrals which can to our knowledge only be solved numerically. Even if $\mathbb{C}_0$ is isotropic, the effective stiffness reflects the anisotropy of the texture through the expectation values $\langle \mathbb{L} \rangle$. In this particular case, a closed form solution of the integrals in terms of texture coefficients can be derived, as will be shown in the following.

The specific models under consideration are the Voigt, Reuss and self-consistent model. The Voigt stiffness is calculated as a straightforward $SO(3)$-average of the stiffness weighted with the ODF, while the Reuss stiffness is calculated analogously using the compliances. For the cubic case, the only non-vanishing texture coefficient up to fourth order has

the value

$$\mathbb{V}_{\mathrm{C}}^4 = \langle \mathbb{Q} \star \mathbb{D}_{\mathrm{C}}^4 \rangle \tag{6.58}$$

with

$$\mathbb{D}_{\mathrm{C}}^4 = \frac{\sqrt{15}}{6}\mathbb{D}_1^4 + \frac{\sqrt{21}}{6}\mathbb{D}_9^4. \tag{6.59}$$

The Voigt stiffness resolves to

$$\mathbb{C}_+ = \lambda_1^{\mathrm{C}}\mathbb{P}^\circ + \frac{2\lambda_2^{\mathrm{C}} + 3\lambda_3^{\mathrm{C}}}{5}\mathbb{P}' + \sqrt{\frac{6}{5}}(\lambda_2^{\mathrm{C}} + \lambda_3^{\mathrm{C}})\mathbb{V}_{\mathrm{C}}^4, \tag{6.60}$$

and the strain concentration tensor is, as in the isotropic case,

$$\mathbb{A}_+ = \mathbb{I}^{\mathrm{S}}. \tag{6.61}$$

Analogously, the Reuss compliance is

$$\mathbb{C}_-^{-1} = \frac{1}{\lambda_1^{\mathrm{C}}}\mathbb{P}^\circ + \left(\frac{2}{5\lambda_2^{\mathrm{C}}} + \frac{2}{5\lambda_3^{\mathrm{C}}}\right)\mathbb{P}' + \sqrt{\frac{6}{5}}\left(\frac{1}{\lambda_2^{\mathrm{C}}} - \frac{1}{\lambda_3^{\mathrm{C}}}\right)\mathbb{V}_{\mathrm{C}}^4 \tag{6.62}$$

with a strain concentration tensor of

$$\mathbb{A}_- = (\boldsymbol{Q} \star (\mathbb{C}^{\mathrm{C}})^{-1})\mathbb{C}_-. \tag{6.63}$$

The self-consistent model is significantly more difficult to compute. After taking the self-consistent effective stiffness $\mathbb{C}_{\mathrm{SC}}$ as the reference stiffness, Eq. (3.144) becomes the nonlinear fourth-order tensorial equation

$$\mathbb{C}_{\mathrm{SC}} = \langle \mathbb{L} \rangle^{-1} + \mathbb{C}_{\mathrm{SC}} - \mathbb{P}(\mathbb{C}_{\mathrm{SC}})^{-1}. \tag{6.64}$$

In the cubic case, the effective compression moduli of the Voigt and Reuss bounds are equal regardless of texture. As the Voigt and Reuss

bounds are bounds on the effective energy, any energetically consistent effective stiffness is necessarily of the block matrix form

$$\bar{\mathbb{C}} \mathrel{\hat{=}} \begin{pmatrix} \bar{K} & 0 \\ 0 & \bar{\mathbb{C}}' \end{pmatrix}, \tag{6.65}$$

where $\bar{\mathbb{C}}'$ is an element of the subspace $\mathrm{sym}\left(\mathcal{D}^2 \otimes \mathcal{D}^2\right)$, which is fifteen-dimensional. For the self-consistent model, this means that the number of equation systems to be solved can be reduced to 15. With the anisotropic tensor $\mathbb{C}_{\mathrm{SC}}$ as a reference stiffness, the calculation of $\mathbb{P}$ still involves numerical integration over S_2, for which we use the quadrature scheme of Lebedev and Laikov (1999). For the average over $\mathbb{L}$, we generally make use of a finite set of orientation samples of the texture. In our experience, a fixed-point scheme based directly on Eq. (6.64) reading

$$\mathbb{C}_{\mathrm{SC}}^{n+1} = \langle \mathbb{L}^n \rangle^{-1} + \bar{\mathbb{C}}^n - \mathbb{P}(\bar{\mathbb{C}})^{-1} \tag{6.66}$$

with the single crystal stiffness $\mathbb{C}^{\mathrm{C}}$ as a start value tends to converge quickly. Once the effective stiffness is calculated, the strain concentration tensors can be calculated directly using Eq. (3.143).

With the strain localization tensor determined, the stress factors are computed via averaging over g. In the following, we derive an explicit form for g-averages of fourth-order rotated tensors, i.e., terms of the form $\langle \boldsymbol{Q} \star \mathbb{T} \rangle_g$, which is useful particularly for models with isotropic $\mathbb{P}_0$. Following Behnken and Hauk (1991), the g-average of $\boldsymbol{Q} \star \mathbb{T}$ for an ODF with texture is

$$\langle \boldsymbol{Q} \star \mathbb{T} \rangle_g = \frac{\int_g f(\boldsymbol{Q}) \boldsymbol{Q} \star \mathbb{T} \, \mathrm{d}V(\boldsymbol{Q})}{\int_g f(\boldsymbol{Q}) \, \mathrm{d}V(\boldsymbol{Q})}. \tag{6.67}$$

From an experimental point of view, the term in the denominator describes the brightness of a diffracted beam for a given diffraction orientation compared to the texture-free case, which appears in this expression as a normalization factor. This intensity factor is measured in pole figures

to quantify the texture of a material. It depends on texture coefficients up to arbitrary order, as can be seen by using the texture coefficient series of $f(\boldsymbol{Q})$ (Eq. (2.133)) and the explicit form of g (Eq. (6.5)) to write

$$\begin{aligned}\int_g f(\boldsymbol{Q})\,\mathrm{d}V(\boldsymbol{Q}) &= \int_0^{2\pi} \sum_{n=0}^{\infty} \sum_{i=1}^{2n+1} \frac{1}{2n+1} \mathbb{V}_i^n \cdot (\boldsymbol{R}(\boldsymbol{n},\theta)\boldsymbol{Q}_0) \star \mathbb{D}_i^n \,\mathrm{d}\theta \\ &= \sum_{n=0}^{\infty} \sum_{i=1}^{2n+1} \frac{1}{2n+1} \mathbb{V}_i^n \cdot \int_0^{2\pi} \boldsymbol{R}(\boldsymbol{n},\theta)^{\star n} \,\mathrm{d}\theta[\boldsymbol{Q}_0 \star \mathbb{D}_i^n],\end{aligned} \tag{6.68}$$

where $\boldsymbol{R}(\boldsymbol{n},\theta)$ is a rotation by θ around $\boldsymbol{n}$. $\boldsymbol{Q}_0$ is defined as in Eq. (6.8) as the rotation from the normed reference orientation (hkl)-vector to $\boldsymbol{e}_3$, chained with the rotation from $\boldsymbol{e}_3$ to $\boldsymbol{n}(\varphi,\psi)$. In terms of Euler angles, this decomposition reads

$$\boldsymbol{Q}_0 = \boldsymbol{Q}_{\boldsymbol{n}} \boldsymbol{Q}_{hkl} \tag{6.69}$$

$$= \boldsymbol{R}(\varphi,\psi,0)\boldsymbol{R}\left(0, -\arccos(l), -\arcsin\left(\frac{k}{\sqrt{1-l^2}}\right)\right), \tag{6.70}$$

where for $(hkl) = (001)$, the third angle becomes 0.

The inner integral over θ is the projector onto the space of n-th order tensors which are transversally isotropic around the axis $\boldsymbol{n}$. For $\boldsymbol{n} = \boldsymbol{e}_3$, $\mathbb{D}_{2n+1}^n$ is the only deviatoric tensor of that symmetry. We define deviatoric basis tensors respective to $\boldsymbol{n}$ as the defining axis, not $\boldsymbol{e}_3$, which arise from the usual basis tensors via

$$\mathbb{D}_i^n(\boldsymbol{n}) = \boldsymbol{Q}_{\boldsymbol{n}} \star \mathbb{D}_i^n. \tag{6.71}$$

With this definition, applying the projector simplifies to

$$\int_0^{2\pi} \boldsymbol{R}(\boldsymbol{n},\theta)^{\star n} \,\mathrm{d}\theta[\mathbb{D}_i^n] = \mathbb{D}_{2n+1}^n(\boldsymbol{n}) \left(\mathbb{D}_{2n+1}^n(\boldsymbol{n}) \cdot \mathbb{D}_i^n\right). \tag{6.72}$$

Every integral term in Eq. (6.68) can be replaced in this manner, leading to

$$\int_g f(\boldsymbol{Q})\,\mathrm{d}V(\boldsymbol{Q}) = \sum_{n=0}^{\infty}\sum_{i=1}^{2n+1}\frac{1}{2n+1}\left(\mathbb{V}_i^n\cdot\boldsymbol{Q}_{\boldsymbol{n}}\star\mathbb{D}_{2n+1}^n\right)\left(\mathbb{D}_{2n+1}^n\cdot\boldsymbol{Q}_{hkl}\star\mathbb{D}_i^n\right), \quad (6.73)$$

in which the influence of the angles φ, ψ and the influence of the (cubic) lattice plane indices decompose into two separate scalar terms. When assuming cubic lattice symmetry, the texture coefficients and deviatoric reference tensors can also be simplified using cubic symmetry, greatly reducing the number of terms. The convergence of this infinite sum follows from the convergence of the Fourier series decomposition of the ODF as discussed by Guidi et al. (1992). This means that convergence is slow for sharp textures. For perfectly sharp textures, such as the single-orientation texture characterized by a Dirac distribution, the Fourier series does not converge.

We turn to the calculation of the tensorial average, which we begin by decomposing the tensor to be rotated using the harmonic basis, thus reducing the calculation to the case of g-averages of deviatoric tensors $\langle\boldsymbol{Q}\star\mathbb{D}_i^m\rangle_g$. We find

$$\int_g \boldsymbol{Q}\star\mathbb{D}_i^m(\boldsymbol{Q})\,\mathrm{d}V(\boldsymbol{Q}) = \sum_{n=0}^{\infty}\sum_{j=1}^{2n+1}\frac{1}{2n+1}\left(\int_0^{2\pi}\boldsymbol{R}(\boldsymbol{n},\theta)^{\star(m+n)}\,\mathrm{d}\theta[\boldsymbol{Q}_0\star\left(\mathbb{D}_i^m\otimes\mathbb{D}_j^n\right)]\right)[\mathbb{V}_j^n]. \quad (6.74)$$

The integral over θ is the projector on to the space of transversal-isotropic $m+n$ order tensors, which then acts on a dyadic product of deviatoric

tensors. Using the Clebsch-Gordan formalism for $\mathcal{D}^m \otimes \mathcal{D}^n$ leads to

$$\int_0^{2\pi} \boldsymbol{R}(\boldsymbol{n},\theta)^{\star(n+m)}\,\mathrm{d}\theta[\boldsymbol{Q}_0 \star \left(\mathbb{D}_i^m \otimes \mathbb{D}_j^n\right)] = \left(\sum_{o=|m-n|}^{m+n} (\mathbb{c}^{mno} \times \mathbb{c}^{mno})[\mathbb{D}_{2o+1}^o(\boldsymbol{n}) \otimes \mathbb{D}_{2o+1}^o(\boldsymbol{n})]\right)[\boldsymbol{Q}_0 \star \left(\mathbb{D}_i^m \otimes \mathbb{D}_j^n\right)]. \tag{6.75}$$

In evaluating measurements obtained using the $\sin^2(\psi)$ technique, stress factors generally need to be calculated for many different $\boldsymbol{n}(\varphi,\psi)$, while only one lattice plane family is generally considered. Thus, we factor out the rotation $\boldsymbol{Q_n}$ as much as possible. The result is

$$\int_g \boldsymbol{Q} \star \mathbb{D}_i^m(\boldsymbol{Q})\,\mathrm{d}V(\boldsymbol{Q}) = \boldsymbol{Q_n} \star \sum_{n=0}^{\infty}\sum_{j=1}^{2n+1} \frac{1}{2n+1} \left(\sum_{o=|m-n|}^{m+n} \left(\left(\mathbb{D}_i^m \otimes \mathbb{D}_j^n\right) \cdot \mathbb{c}^{mno}[\boldsymbol{Q}_{hkl} \star \mathbb{D}_{2o+1}^o]\right) \mathbb{c}^{mno}[\mathbb{D}_{2o+1}^o]\right)[\boldsymbol{Q_n}^{-1} \star \mathbb{V}_j^n], \tag{6.76}$$

such that the sum over o involving Clebsch-Gordan decomposition need only be calculated once for any particular combination of reference tensor $\mathbb{D}_i^m$ and lattice plane. For $m = 0$, Eq. (6.76) simplifies to Eq. (6.73), as would be expected. In this sense, Eq. (6.76) can be understood as a tensorial generalization of the intensity factor.

When calculating the Voigt stress factors with $\mathbb{A} = \mathbb{I}^{\mathrm{S}}$, the result is simply

$$\boldsymbol{F}_+(\{hkl\},\boldsymbol{n}) = \mathbb{C}_+^{-1}[\boldsymbol{n} \otimes \boldsymbol{n}]. \tag{6.77}$$

These stress factors are independent of the lattice plane family and only depend on texture tensors up to fourth order through the influence of $\mathbb{C}_+$, as discussed by Brakman (1987).

For the Reuss stress factors, a full calculation involving Eq. (6.76) is necessary. We write

$$\boldsymbol{F}_{-}(hkl,\boldsymbol{n}) = \langle \boldsymbol{Q} \star (\mathbb{C}^{\mathrm{C}})^{-1} \rangle_g [\boldsymbol{n} \otimes \boldsymbol{n}], \tag{6.78}$$

and find that the Reuss stress factor is influenced by texture coefficients up to arbitrary order.

For the self-consistent stress factors

$$\boldsymbol{F}_{\mathrm{SC}} = \bar{\mathbb{C}}_{\mathrm{SC}} \langle \mathbb{L} \rangle^{-1} \langle \mathbb{L} \rangle_g [\boldsymbol{n} \otimes \boldsymbol{n}], \tag{6.79}$$

no direct form in terms of texture coefficients is available. Due to the complex dependence of $\mathbb{L}$ on $\boldsymbol{Q}$, numerical integration is necessary.

Extending the MEM towards the textured case is quickly accomplished by using the Voigt and Reuss results. For linear elastic polycrystals, the linear elastic MEM strain mean in a given crystal is

$$\boldsymbol{\varepsilon}_{\mathrm{MEM}} = (\boldsymbol{Q} \star \mathbb{C}^{-1}\mathbb{C}_{-} - \mathbb{I}^{\mathrm{S}})(\mathbb{C}_{+} - \mathbb{C}_{-})^{-1}(\mathbb{C}_{+} - \bar{\mathbb{C}})[\bar{\boldsymbol{\varepsilon}}] + \bar{\boldsymbol{\varepsilon}}, \tag{6.80}$$

which can be rewritten in terms of Voigt and Reuss strain concentration tensors as

$$\mathbb{A}_{\mathrm{MEM}} = (\mathbb{A}_{-}(\boldsymbol{Q}) - \mathbb{A}_{+})(\mathbb{C}_{+} - \mathbb{C}_{-})^{+}(\mathbb{C}_{+} - \bar{\mathbb{C}}) + \mathbb{A}_{+}. \tag{6.81}$$

Applying this strain concentration tensor to stress factor calculations results in

$$\boldsymbol{F}_{\mathrm{MEM}} = (\bar{\mathbb{C}}^{-1}\mathbb{C}_{+} - \mathbb{I}^{\mathrm{S}})(\mathbb{C}_{+} - \mathbb{C}_{-})^{+}[\mathbb{C}_{-}[\boldsymbol{F}_{-}] - \mathbb{C}_{+}[\boldsymbol{F}_{+}]] + \bar{\mathbb{C}}^{-1}\mathbb{C}_{+}[\boldsymbol{F}_{+}]. \tag{6.82}$$

This relationship is general and applies regardless of the crystal symmetry, sample symmetry, crystallographic or morphological texture involved.

6.3.2 Simulated diffraction measurements of cold-rolled copper

In the following, cold-rolled copper is discussed as an example of a sharply textured state. The material parameters used are those given by Chang and Himmel (1966), which read

$$C_{1111} = 170.0\,\mathrm{GPa}, \tag{6.83}$$

$$C_{1122} = 122.5\,\mathrm{GPa}, \tag{6.84}$$

$$C_{1212} = 75.8\,\mathrm{GPa}. \tag{6.85}$$

As we are particularly interested in the sharp textures which form after large deformations, we consider textures formed by a rolling process which reduces the initial thickness to $5\,\%$. This texture is used as an input for both simulations and analytical approaches, which means that its accuracy as a model of a realistic rolling process is not critical. Nonetheless, we briefly summarize the approach. We neglect friction and approximate rolling as a volume-preserving plane strain deformation process. We further neglect grain interactions and use the Taylor-Lin assumption that the deformations are homogeneous throughout the process (Taylor, 1938; Lin, 1957). The initial set of 10.000 crystallite orientations corresponds to samples of an isotropic ODF. The deformation process of each crystallite orientations is modeled using a rate-dependent large-strain crystal elastoplasticity model. The resulting crystallite orientation samples after rolling are depicted as a (100) pole figure in Fig. 6.11.

We apply the methods discussed in Section 6.2.5 to the textured material. First, a centroidal Laguerre tessellation approach is used to generate a polycrystalline microstructure with 10.000 grains to which the simulated orientations are assigned randomly. Local strain fields are then calculated numerically via an FFT-based full-field simulation. Finally,

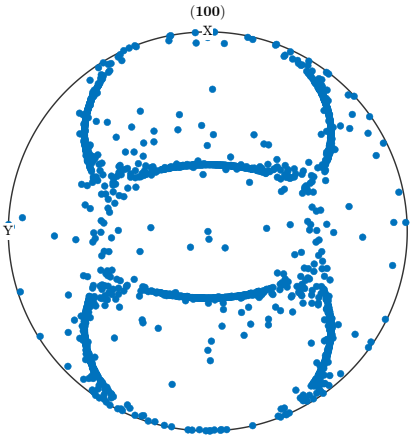

Figure 6.11: Simulated rolled copper pole figure for the (100) plane. X denotes the rolling direction, Y the direction in which no deformation occurred.

diffraction measurements are simulated using the procedure described in Section 6.2.5 with a misalignment threshold of $d = 0.1$.

In taking the texture as described by a set of discrete orientations as the ground truth, texture-coefficient-based representations become approximations. Even in the infinite limit, the Fourier series of texture coefficients does not converge for a set of discrete orientations, which is a sum of Dirac deltas. Therefore, we restrict our initial validation of the micromechanical methods to an approach which uses the discrete orientations directly. Ensemble averages resolve to

$$\langle \boldsymbol{A}(\boldsymbol{Q}) \rangle = \frac{1}{N} \sum_{\alpha=1}^{N} \boldsymbol{A}(\boldsymbol{Q}_\alpha), \tag{6.86}$$

and the Voigt, Reuss and self-consistent approximations for the strain concentration tensors follow as described in Section 6.3.1. To simulate diffraction experiments using these strain fields, we use the same pro-

cedure as for the full-field strain fields, with the same misalignment threshold of $d = 0.1$.

Simulated diffraction measurements are shown in Fig. 6.12. The $\{311\}$ family of lattice planes was chosen instead of the $\{400\}$ planes used earlier because measurements in the $\{400\}$ planes do not exhibit nonlinearity due to texture. In the $\{311\}$ planes, the nonlinearity is very strongly pronounced. Despite this, the results known from non-textured materials hold true. The self-consistent method once again yields an extremely accurate approximation, while the Voigt and Reuss approximations appear to form bounds on the simulated curves. In addition to the stress factor curves, the intensities are depicted as the percentage of irradiated grains per orientation. Due to the sharpness of the texture, only selected sections of the $\sin^2(\psi)$-interval are irradiated at all. The full-field measurements for all other values of ψ must be considered unreliable. We note that the self-consistent method closely approximates the full-field results even in those sections. As the number of irradiated crystals in these sections is very low, the individual rotations of the crystals which are accounted for have a major influence on the results. It seems likely that any approximation method which does not use the exact same orientations as the full-field result would not be this accurate.

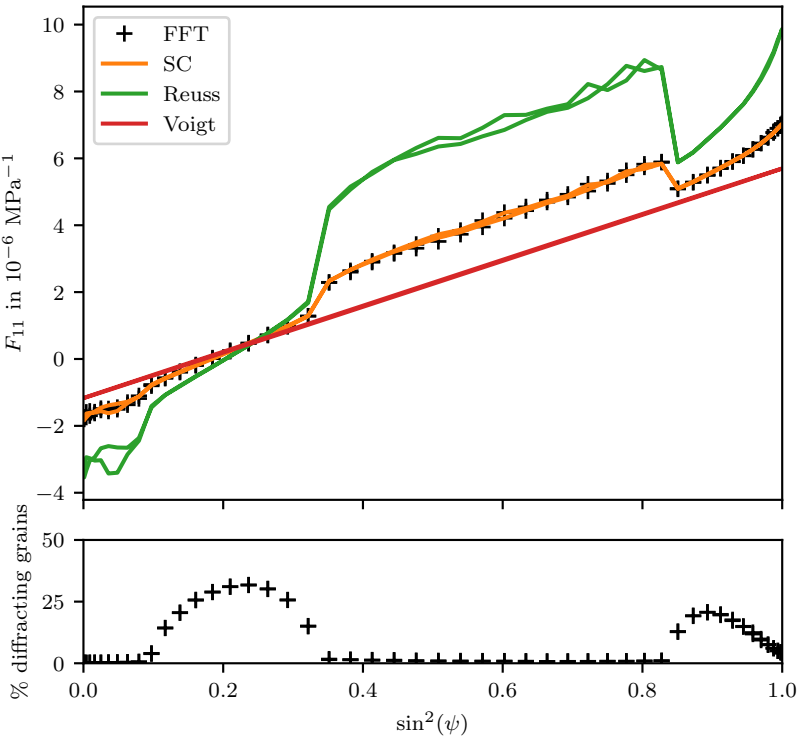

Figure 6.12: Simulated diffraction measurement for rolled copper in the {311}-plane at $\varphi = 0$ with misalignment threshold $d = 0.1$.

Using the same approach, two MEM approaches are evaluated. One uses the self-consistent effective stiffness, while the other uses the stiffness from the simulation. Fig. 6.13 shows the deviations of each method from the numerical results. The methods are each within $1 \times 10^{-7}\,\mathrm{MPa}^{-1}$ of the numerical values, an order of magnitude smaller than the deviation between the Reuss and Voigt methods. In the regions of high intensity, where the full-field simulation is particularly reliable, the deviations are significantly smaller. While the self-consistent approach and a MEM approach using the self-consistent effective stiffness are not exactly the same, as they were in the texture-free case, the differences are extremely small and can be neglected in practice. As in the texture-free case, if the effective stiffness of the sample coincides with the self-consistent stiffness, the MEM can be used with the self-consistent stiffness to yield a more simple calculation method. In cases where the self-consistent method is not a good approximation, the MEM can be parameterized using any other sample stiffness to yield more accurate results.

The previous comparisons used not only the exact same set of finite grains, but also the same misalignment threshold. Insofar as d is a regularization parameter for a texture composed of finite grains, it should be noted that simulations of the diffraction intensity do not converge as d tends to zero. Insofar as d is a parameter modeling the physical effect of diffraction despite slight misalignments, it should be noted that its true value cannot be determined in the simulated context discussed here. A strong dependence of the stress analysis procedure on this parameter is thus undesirable. Fig. 6.14 shows simulated diffraction results with $d = 0.05$. Particularly near $\sin^2(\psi) = 1$, the results are different from the previous measurement. However, those ψ-intervals which show high intensity for either value of d remain similar.

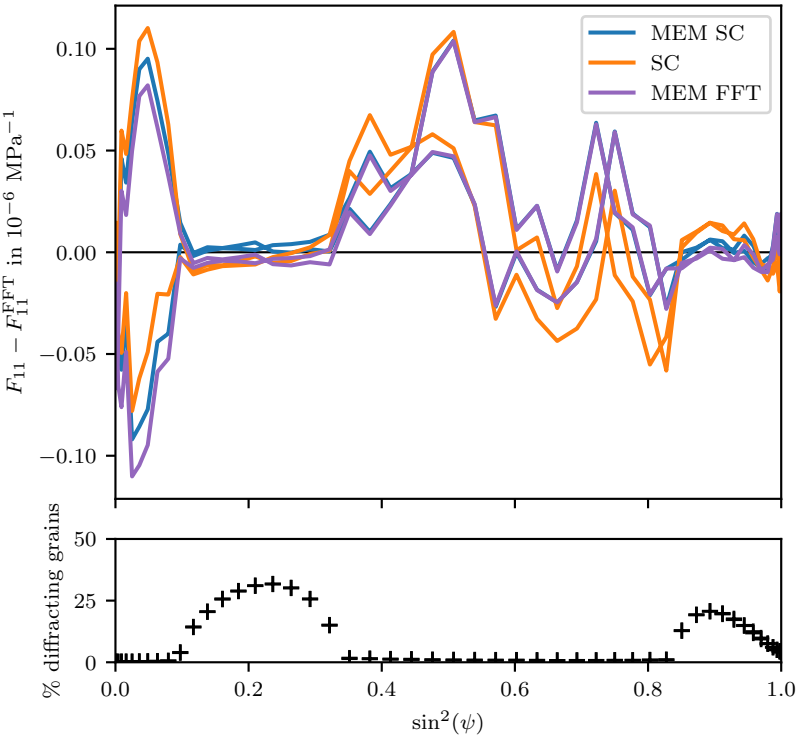

Figure 6.13: Deviation of MEM and SC approaches from full-field values.

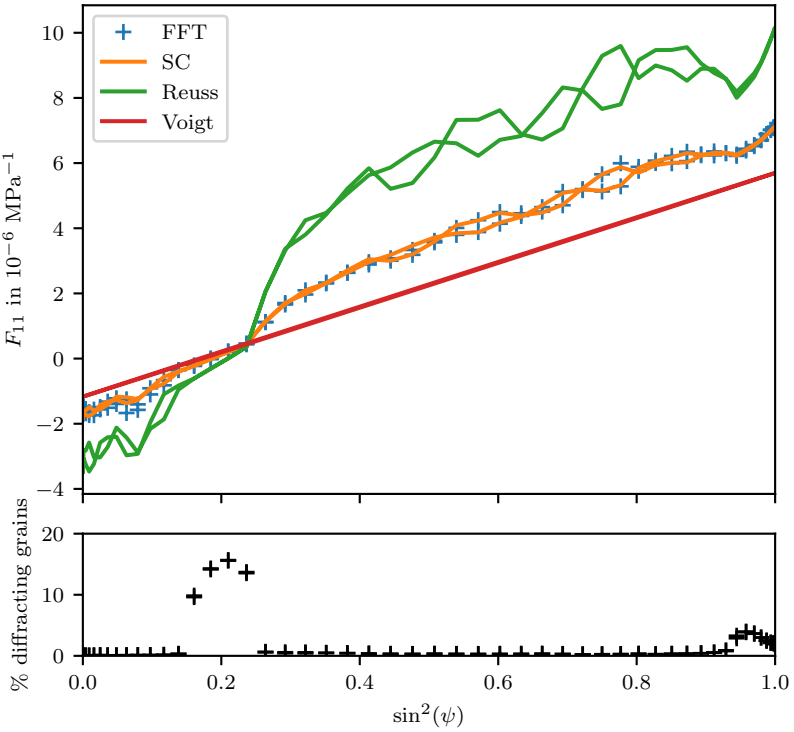

Figure 6.14: Simulated diffraction measurement for rolled copper in the {311}-plane at $\varphi = 0$ with misalignment threshold $d = 0.05$.

6.3.3 Stress analysis using truncated texture coefficient series

Stress analysis using diffraction measurement is performed by indirectly measuring $\langle \boldsymbol{\varepsilon} \cdot (\boldsymbol{n} \otimes \boldsymbol{n}) \rangle_g$ at values ψ_i, $i \in [1, N]$ and solving the overdetermined equation system

$$(\langle \boldsymbol{\varepsilon} \cdot (\boldsymbol{n} \otimes \boldsymbol{n}) \rangle_g)_i = \boldsymbol{F}(\varphi, \psi_i, \{hkl\}) \cdot \bar{\boldsymbol{\sigma}} \tag{6.87}$$

to obtain $\bar{\boldsymbol{\sigma}}$, where the stress factor $\boldsymbol{F}$ is known from prior measurements or analytical calculations. The method used in the previous section to calculate $\boldsymbol{F}$ relies on knowing the exact set of discrete orientations as well as d. With this in mind, we attempt stress analysis using a truncated texture coefficient series. As previously discussed, the Fourier series of the rolled copper texture as represented by discrete samples does not converge. Even if an infinite-sample-size rolling simulation were shown to converge to a particular continuous copper texture, this texture is likely sharp enough that extremely high orders of texture coefficient tensors would be required to adequately represent the texture. Therefore, the main question of this section is whether texture-coefficient-based stress analysis can be accurate even with a relatively low maximum order of texture coefficients.

Fig. 6.15 shows a self-consistent approximation of F_{11} with texture coefficients of up to tenth order for rolled copper, along with simulated diffraction measurements using $d = 0.05$. There are two marked differences between theory and simulation. First, the intensity values of the texture coefficient approximations can be negative. As the intensity value represents a probability density, the first impulse is to reject this result as mathematically inconsistent. However, when homogenizing polycrystals, the Voigt and Reuss stiffnesses only depend on the ODF up to the fourth order texture coefficient, and can therefore be accurately calculated using a truncated Fourier series up to fourth order, despite

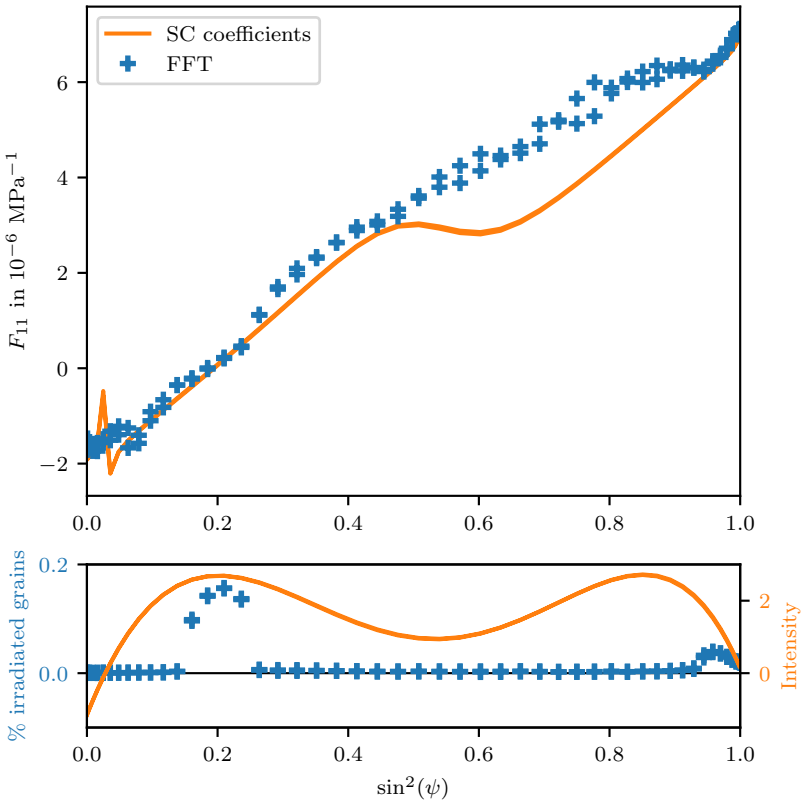

Figure 6.15: Self-consistent F_{11}-approximation using texture coefficients up to order 10 and simulated diffraction measurements with misalignment threshold $d = 0.05$, both for the $\{311\}$ plane of rolled copper $\phi = 0$.

the negative values involved. Similarly, in stress analysis, where the objective is the calculation of the effective stress, this seeming mathematical inconsistency is not necessarily a problem. The second fundamental difference between theory and simulation occurs wherever the intensity crosses zero. As the stress factor is normed by the intensity, singularities result. Besides these two fundamental differences, there are general differences in the calculated stress factors which occur mostly in those places where the simulation intensity is near zero. These could be caused by the uncertainties involved in calculating stress factors from a small number of irradiated crystals.

A straightforward approach to stress analysis would involve a least-square-error solution of the over-determined equation system Eq. (6.87). In matrix-vector form using an N-dimensional basis for the measured values and the second-order harmonic basis for $\bar{\boldsymbol{\sigma}}$, the equation system becomes

$$\underline{\varepsilon}^{nn} = \underline{\underline{F}}\,\underline{\bar{\sigma}}, \tag{6.88}$$

where $\underline{\underline{F}}$ is an $N \times 6$ matrix. The least-square approximation is given by

$$\underline{\bar{\sigma}} = (\underline{\underline{F}}^{\mathsf{T}}\,\underline{\underline{F}})^{-1}\underline{\underline{F}}^{\mathsf{T}}\underline{\varepsilon}^{nn}. \tag{6.89}$$

For a well-conditioned inner matrix $\underline{\underline{F}}^{\mathsf{T}}\,\underline{\underline{F}}$ it is necessary to obtain multiples in different values of the angle φ, of which we use $\varphi \in \{0°, 45°, 90°\}$. There is a low degree of confidence of measurements for angles corresponding to few irradiated crystals. This can be incorporated by using a weighted least-square-errors approach,

$$\underline{\bar{\sigma}} = (\underline{\underline{F}}^{\mathsf{T}}\,\underline{\underline{W}}\,\underline{\underline{F}})^{-1}\underline{\underline{F}}^{\mathsf{T}}\,\underline{\underline{W}}\,\underline{\varepsilon}^{nn}. \tag{6.90}$$

As a weight matrix, we use the measured intensity, leading to a diagonal matrix

$$\underline{\underline{W}} = \operatorname{diag}\left(n(\varphi, \underline{\psi}, d)\right), \tag{6.91}$$

	σ_1	σ_2	σ_3	σ_4	σ_5	σ_6	e_σ (%)
FFT	57.7	70.7	0.0	0.0	0.0	-40.8	0.0
least-square	84.1	71.4	-8.8	0.4	0.2	-46.9	28.4
weighted	62.3	71.4	-2.1	0.1	-0.2	-43.3	5.6
no singularities	65.8	72.2	-2.9	-0.0	0.1	-42.8	8.9

Table 6.2: Stress analysis results of rolled copper using a normal least-square fit, an intensity-weighted least-square fit, and an intensity-weighted least-square fit with singularities removed. All stresses in MPa.

where n is the number of grains within the misalignment threshold $d = 0.05$.

As a further refinement, we propose to remove the analytical singularities from the stress analysis entirely by setting the weight matrix to zero wherever the absolute value of the truncated intensity series is below some threshold. In terms of texture coefficients up to order 10, this resolves to

$$\sum_{n=0}^{10} \sum_{i=1}^{2n+1} \frac{1}{2n+1} \left(\mathbb{V}_i^n \cdot \boldsymbol{Q}_{\boldsymbol{n}} \star \mathbb{D}_{2n+1}^n \right) \left(\mathbb{D}_{2n+1}^n \cdot \boldsymbol{Q}_{hkl} \star \mathbb{D}_i^n \right) < t, \qquad (6.92)$$

where we choose $t = 0.15$.

Stress analysis using these three different least-square approaches leads to the results shown in Table 6.2. Improving the quality of the fit by disregarding low-intensity regions corresponds to a more accurate stress assessment by value. Initially, it appears that the removal of analytical singularities did not lead to a refinement of the results. This is possibly due to the fact that for the values of φ and ψ used in this analysis, the singularities have only a limited negative effect as the grid of ψ points does not coincide with particularly high singular values; or alternatively, the effect of including the singularity yields a more accurate result by chance. In Fig. 6.16, the analytical models of the measured strains using the fitted $\bar{\boldsymbol{\sigma}}$ values are shown, with the intensity weighting shown as reduced transparency of the curves. It appears that a strong nonlinearity

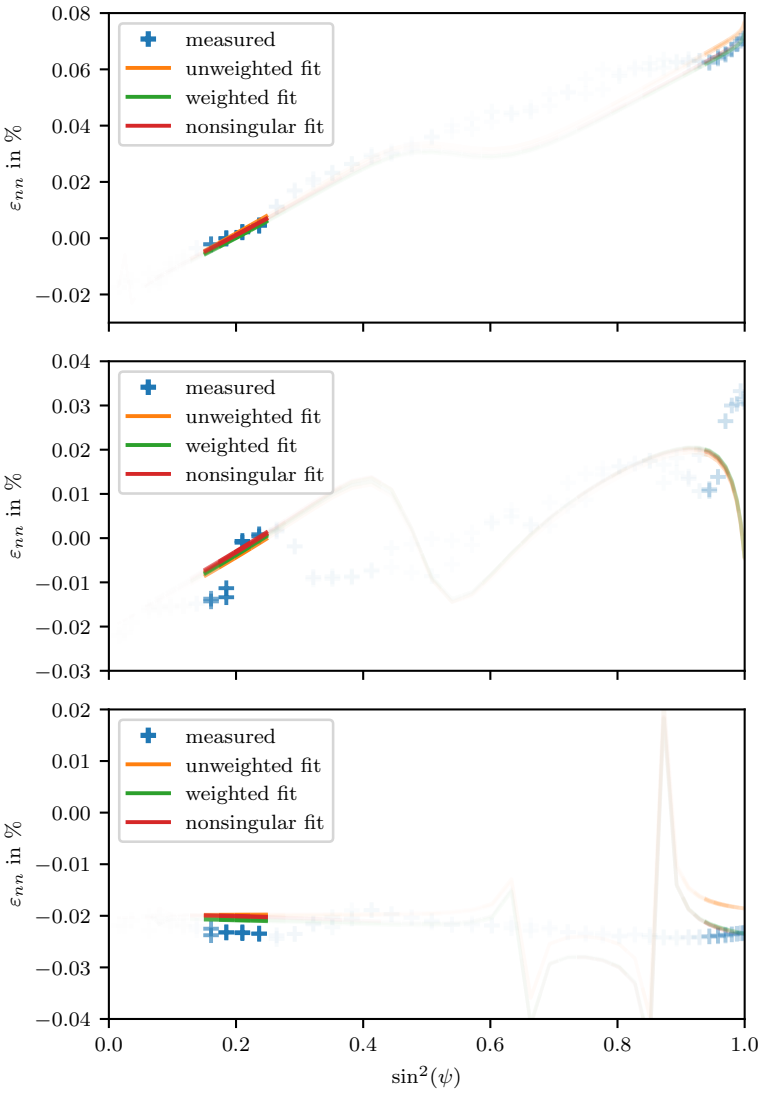

Figure 6.16: Self-consistent diffraction curves with tensor coefficients up to order 10 and simulated diffraction measurements calculated with $d = 0.05$. The self-consistent curves are fitted using unweighted, weighted and weighted-with-singularities-removed least-square methods. From top to bottom: $\varphi = 0°$, $\varphi = 45°$, $\varphi = 90°$.

in the $\varphi = 45°$ around $\sin^2(\psi) = 0.2$ is not present in the analytical model, which might explain a significant part of the remaining $8.9\,\%$ error.

To further investigate the singularity removal heuristic, we performed similar analyses on textures obtained throughout the rolling process. The results are shown in Fig. 6.17. For textures associated with thickness reductions of $86\,\%$ and $90\,\%$, a singularity coincides with critical measurement values. Correspondingly, there are pronounced singularity effects which the singularity removal heuristic mitigates. With singularities removed, the inaccuracy of the stress analysis is monotonous in the sharpness of the texture. It appears that for rolling textures, using texture coefficients up to tenth order results in single-digit percent errors in stress analysis. Because this analysis was performed on one particular rolling process for one particular material, further quantitative studies are necessary to substantiate these results. However, a texture-coefficient-based approach to stress analysis appears promising.

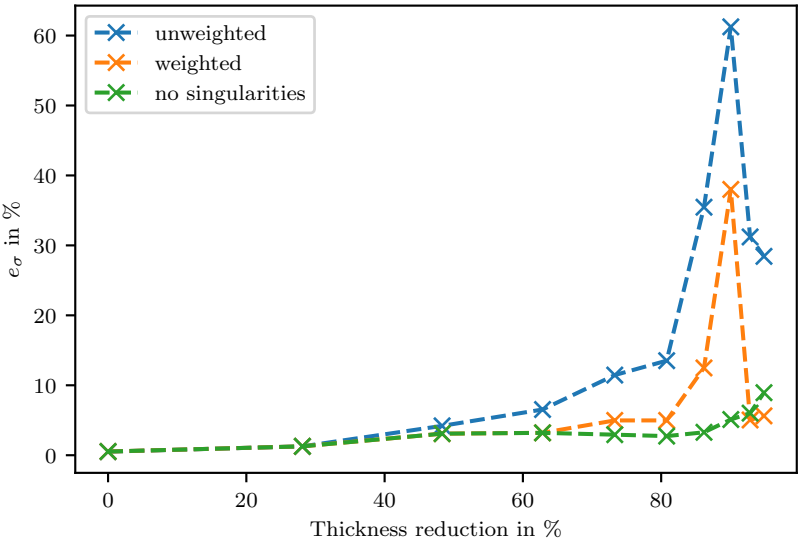

Figure 6.17: Stress measurement error e_σ for textures caused by increasingly large deformations.

Chapter 7

Summary and conclusions

7.1 Summary

In this thesis, we investigated local stresses and strains for random heterogeneous materials in general and polycrystals in particular. The core goal of the thesis was the application of the Maximum Entropy Method (MEM) to the micromechanical localization problem. Both analytical micromechanics approximations and full-field simulations were used for comparison with different versions of the MEM. After selecting the most appropriate MEM version for the use-case of approximating polycrystal stress and strain statistics, the MEM was applied to the problem of calculating diffraction elastic constants for use in X-ray diffraction stress analysis. In the following, the contributions of this thesis are summarized.

In Section 2.2, we introduced a convention for defining tensorial bases which is based on results from group representation theory of the rotation group $SO(3)$. These harmonic bases were found to yield particularly sparse representations for tensors with partial rotational symmetries, such as many tensorial material properties, which has implications both for presenting a less redundant picture of material symmetry and for numerical efficiency in calculations. Furthermore, we used the harmonic bases to find sparse forms of rotation matrices of higher order tensors,

which we found to be particularly useful for calculations involving tensorial Fourier decompositions of functions on $SO(3)$.

Chapter 4 discussed explicit analytical formulas for calculating second statistical moments of stress and strain statistics using results from classical homogenization theory. We applied an established approach based on a partial derivative of the effective strain energy to the Singular Approximation, which we characterized as a general framework uniting many Eshelby-based homogenization theories. As the core result, generally applicable formulas were derived for a simple matrix-inclusion Singular Approximation as well as the Hashin-Shtrikman and Mori-Tanaka approximation. In comparing the results, we found that multiple theories which yield the same effective stiffness may still differ in their predictions of second statistical moments. In particular, the Hashin-Shtrikman bounds yielded covariances which are independent of the direction of the applied strain, which is not compatible with results from full-field simulations.

With these foundations laid, Chapter 5 discussed the MEM. After a short introduction of the general information-theoretic maximum entropy approach, we rederived the single-point micromechanical MEM. In comparison with full-field simulations, we found that the main deviation between full-field statistics and the single-point MEM is due to MEM covariances being independent of the direction of the applied strain. In addition, matrix-inclusion morphologies were found to have pronounced higher moments, which neither the MEM nor classical approaches can currently predict. Despite both of these limitations, for polycrystals, the statistics given by the MEM were found to be highly similar to numerically expensive full-field results. To resolve the MEM covariance being independent of the applied strain direction, we used a different MEM approach which incorporates the Eshelby problem, for which we found a novel derivation which establishes its connection to the Singular Approximation. Furthermore, we found an entirely novel

MEM approach by incorporating the analytical formulas for calculating second moments directly. In comparing these refined approaches to the single-point MEM using the example of polycrystalline titanium, we found that the single-point MEM, despite its theoretical shortcomings, yielded the most accurate approximation, if only by a small margin.

An application for the MEM was discussed in Chapter 6. As optical diffraction in polycrystals depends on local deformations of the crystal lattice, statistics of local stresses and strains are critical to the use of diffraction techniques to analyze residual stresses. Using the MEM, we introduced a novel method to calculate diffraction elastic constants, which has the advantage of incorporating partial information on grain interactions based on macroscopically measurable effective stiffness values. For the statistically isotropic case, we showed equivalence between the MEM diffraction elastic constants and Singular-Approximation-based results, both of which showed good agreement with full-field simulations and experimentally measured values. For textured polycrystals, methods for the calculation of diffraction elastic constants based on tensorial texture coefficients were derived, which can be carried out in a numerically efficient manner using harmonic bases. In the textured case, the MEM was found to diverge from classical Eshelby-based approaches, yielding novel results for diffraction elastic constants which are particularly straightforward to calculate.

7.2 Conclusions

The so-called mean-field methods of classical micromechanics contain statistical information beyond mere statistical means of the phase-wise stress and strain distributions. Information on second statistical moments is implicit in the effective elastic energy, which means that even theories which are not based on approximations for phase-wise statistical means, such as the geometric mean, always provide second statistical

moments. For cases where these analytically available moments are difficult to compute or otherwise unavailable, such as materials with non-compatible eigenstrains, the MEM provides a straightforward approximation of the stress and strain distributions which is quite accurate for polycrystals in particular. This means that any situation in which local stress or strain distributions of linear elastic materials need to be approximated, there is no particular reason to restrict this approximation to phase means only.

Among the many micromechanical approximation methods, the particular advantage of the MEM is its adaptability. In its simplest form, the MEM eschews ad-hoc microstructural assumptions, and can instead be adapted to measurable macroscopic stiffness parameters. Beyond this, we found that the MEM's core assumption that the probability distribution of strains assumes maximal entropy can also be adapted by choosing the Singular Approximation reference strain field as the field which reaches maximum entropy. We therefore conclude that, while for many materials, suitable approximation methods for estimating local elastic strains already exist, further refinement is likely to be possible.

Appendix A

Notation and Frequently Used Symbols

A.1 Symbols

Symbol	Name
$\mathcal{C}$	Space of positive definite main-, left-, and rightsymmetric fourth-order tensors
$\mathcal{D}^n$	Deviatoric space of n-th order
$\mathcal{R}$	3D Euclidean space
S	Symmetry group
S_n	n-sphere
$SO(3)$	Group of rotations of $\mathcal{R}$
Sym	Space of symmetric second-order tensors

Table A.1: Symbols for sets and spaces.

Symbol	Set	Name
$\boldsymbol{a}$	Sym	Inelastic strain localization tensor
$\mathbb{A}$	$\text{Sym}^{\otimes 2}$	Strain concentration tensor
$\boldsymbol{b}$	$\mathcal{R}$	Applied volume force density
$\mathbb{c}^{mno}$	$\mathcal{D}^m \otimes \mathcal{D}^n \otimes \mathcal{D}^o$	Clebsch-Gordan coefficients
$\mathbb{C}$	$\mathcal{C}$	Elastic stiffness tensor

Symbol	Set	Name
$\mathbb{D}_i^n$	$\mathcal{D}^n$	Deviatoric basis tensors of n-th order
$\boldsymbol{e}$	$\mathcal{R}$	Basis tensor of the default orthonormal basis
$\boldsymbol{E}$	Sym	Eigenstrain
$\boldsymbol{E}_{\mathrm{G}}$	Sym	Green St.-Venant strain
$\mathbb{E}_i^n$	$\mathcal{R}^{\otimes n}$	Eigentensors of n-th order
G	$\mathbb{R}_{\geq 0}$	Shear modulus
$\boldsymbol{I}$	$\mathcal{R}^{\otimes 2}$	Second order identity tensor
$\mathbb{I}$	$\mathcal{R}^{\otimes 4}$	Fourth order identity tensor
K	$\mathbb{R}_{\geq 0}$	Compression modulus
$\mathbb{K}$	$\mathcal{C}$	Covariance tensor
$\mathbb{L}$	$\mathrm{Sym}^{\otimes 2}$	Singular approximation fluctuation tensor
$\square_{\mathrm{L}}$		Fields caused by external loads
m	$\mathbb{R}_{\geq 0}$	Mass
$\boldsymbol{n}$	$\mathcal{R}$	Normal vector
$\mathbb{P}$	$\mathcal{C}$	Hill's polarization tensor
$\mathbb{P}\left(\mathcal{H}_i, k\right)$	$\mathcal{H}_i \otimes \mathcal{D}^k$	Harmonic inclusion tensors of $\mathcal{D}^k$ into $\mathcal{H}_i$
$\boldsymbol{Q}$	$Orth^+$	Rotation tensor
$\square_{\mathrm{R}}$		Residual fields
$\boldsymbol{t}$	$\mathcal{R}$	Stress vector
$\boldsymbol{u}$	$\mathcal{R}$	Displacement
V	$\mathbb{R}_{\geq 0}$	Volume
$\boldsymbol{v}$	$\mathcal{R}$	Velocity
$\mathbb{V}^n$	$\mathcal{D}^n$	Texture coefficient of order n
w	$\mathbb{R}_{\geq 0}$	Elastic energy
$\boldsymbol{x}$	$\mathcal{R}$	Position vector
$\boldsymbol{\varepsilon}$	Sym	Small deformation strain

Symbol	Set	Name
$\boldsymbol{\sigma}$	Sym	Cauchy stress

Table A.2: Symbols for variables and fields.

A.2 Operations

Symbol	Name
$\square + \square$	Addition
$\square - \square$	Subtraction
$a\square$	Scalar multiplication, with a scalar a
$\square \otimes \square$	Dyadic product
$\square^{\otimes n}$	nth dyadic power, with an integer n
$\begin{pmatrix} \square \\ \square \end{pmatrix}$	Concatenation
$\square \cdot \square$	Inner product
$\lVert \square \rVert$	Norm

Table A.3: Operations defined on vectors.

Symbol	Name
$\det(\square)$	Determinant
$\square\square$	Matrix-matrix or matrix-vector product
$\square^n$	nth matrix power, with an integer n
$\square \times \square$	Kronecker product
$\mathrm{tr}(\square)$	Trace
$\square^{-1}$	Inverse
$\square^{\mathsf{T}}$	Transposition
$\square^{+}$	Moore-Penrose pseudoinverse
$\exp(\square)$	Matrix exponential

Symbol	Name
$\ln(\square)$	Matrix logarithm
$\sqrt{\square}$	Matrix square root

Table A.4: Matrix operations defined on tensors via their canonical representation as linear maps.

Symbol	Name
$\square \star \square$	Rayleigh product
$\square \times \square$	(Tensorial) Kronecker product
$\square^{\times n}$	nth Kronecker power, with an integer n
$\square \boxtimes \square$	Infinitesimal Rayleigh product
$\square^{\boxtimes n}$	nth infinitesimal Rayleigh power, with an integer n
$\square[\square]$	Application of a tensor as a map

Table A.5: Higher order tensor operations.

Symbol	Name
$\square \otimes \square$	Dyadic product between tensor spaces
$\square \oplus \square$	Direct product of tensor spaces
$\boldsymbol{R} \star \square$	Rotation of a tensor space with an orthogonal second-order tensor $\boldsymbol{R}$
$\mathbb{A}[\square]$	Transformation of a tensor space via a tensor $\mathbb{A}$
$\mathrm{sym}(\square)$	Index symmetrization

Table A.6: Operations on tensor spaces.

Appendix B

MEM Formulas

B.1 General abbreviations

In the following, MEM formulas for various specific material cases are collected. For ease of notation, the field L caused by external loads and the residual field R are not distinguished.

The abbreviations defined in Section 5.2.2 are repeated here for convenience.

$$w_0 = \langle \boldsymbol{E} \cdot \mathbb{C}[\boldsymbol{E}] \rangle - \boldsymbol{E}_- \cdot \mathbb{C}_+[\boldsymbol{E}_-] - (\boldsymbol{E}_- - \boldsymbol{E}_+) \cdot (\mathbb{C}_-^{-1} - \mathbb{C}_+^{-1})^+ [\boldsymbol{E}_- - \boldsymbol{E}_+], \tag{B.1}$$

$$\mathbb{C}_+ = \langle \mathbb{C} \rangle, \qquad \mathbb{C}_- = \langle \mathbb{C}^{-1} \rangle^{-1}, \tag{B.2}$$

$$\boldsymbol{E}_+ = \langle \boldsymbol{E} \rangle, \qquad \boldsymbol{E}_- = \langle \mathbb{C} \rangle^{-1} [\langle \mathbb{C}[\boldsymbol{E}] \rangle]. \tag{B.3}$$

The following solutions are all formulated in terms of strains. The corresponding stress means and covariances can be obtained through transformation via Hooke's Law, yielding

$$\boldsymbol{\gamma}_\sigma = \mathbb{C}[\boldsymbol{\gamma} - \boldsymbol{E}], \tag{B.4}$$

$$\mathbb{K}_\sigma = \mathbb{C}\mathbb{K}\mathbb{C}. \tag{B.5}$$

B.2 MEM for arbitrary heterogeneous materials

B.2.1 General MEM with heterogeneous eigenstrains

In the general affine-elastic case, the MEM solution uses as constraints the macroscopic properties the effective stiffness $\bar{\mathbb{C}}$, the effective eigenstrain $\bar{\boldsymbol{E}}$ and the effective residual strain energy $\bar{w}_{\mathrm{R}}$. No assumptions are made for the one-point statistic of local properties $p_1^{\mathrm{C}}(\mathbb{C}, \boldsymbol{E})$, in particularly not the common assumption that there are only a finite number of discrete phases. The abbreviation $p_1(\boldsymbol{v})$ is used for $p_1(\boldsymbol{\varepsilon}, \mathbb{C}, \boldsymbol{E})$.

$$
\begin{aligned}
p_1(\boldsymbol{v}) &= \frac{p_1^{\mathrm{C}}(\mathbb{C}, \boldsymbol{E})}{\sqrt{(2\pi)^6 \det(\mathbb{K})}} \exp\left(-\frac{1}{2}(\boldsymbol{\varepsilon}-\boldsymbol{\gamma}) \cdot \mathbb{K}^{-1}[\boldsymbol{\varepsilon}-\boldsymbol{\gamma}]\right) \\
\mathbb{K} &= k\mathbb{C}^{-1} \\
\boldsymbol{\gamma} &= \mathbb{C}^{-1}[\boldsymbol{\mu}_\varepsilon] + \boldsymbol{\mu}_\sigma + r\boldsymbol{E} \\
\boldsymbol{\mu}_\varepsilon &= \mathbb{C}_-(\mathbb{C}_+ - \mathbb{C}_-)^+[(\mathbb{C}_+ - \bar{\mathbb{C}})[\bar{\boldsymbol{\varepsilon}}] + \mathbb{C}_+[(r^2-1)\boldsymbol{E}_- - r\boldsymbol{E}_+] \\
&\quad + \bar{\mathbb{C}}[\bar{\boldsymbol{E}}]] \\
\boldsymbol{\mu}_\sigma &= -\mathbb{C}_-^{-1}[\boldsymbol{\mu}_\varepsilon] + \bar{\boldsymbol{\varepsilon}} - r\boldsymbol{E}_+ \\
r &= \frac{1}{w_0}\big((\bar{\boldsymbol{\varepsilon}} - \bar{\boldsymbol{E}}) \cdot \bar{\mathbb{C}}[\bar{\boldsymbol{E}}] - \boldsymbol{E}_- \cdot \mathbb{C}_+[\bar{\boldsymbol{\varepsilon}}] - 2\bar{w}_{\mathrm{R}} + \langle \boldsymbol{E} \cdot \mathbb{C}[\boldsymbol{E}] \rangle \\
&\quad -(\mathbb{C}_-[\boldsymbol{E}_+] - \mathbb{C}_+[\boldsymbol{E}_-]) \cdot (\mathbb{C}_+ - \mathbb{C}_-)^+ \left[(\mathbb{C}_+ - \bar{\mathbb{C}})[\bar{\boldsymbol{\varepsilon}}]\right. \\
&\quad \left. + \bar{\mathbb{C}}[\bar{\boldsymbol{E}}] - \mathbb{C}_+[\boldsymbol{E}_-]\right]\big) \\
k &= \frac{1}{6}\big(\bar{\boldsymbol{\varepsilon}} \cdot \bar{\mathbb{C}}[\bar{\boldsymbol{\varepsilon}}] - \bar{\boldsymbol{E}} \cdot \bar{\mathbb{C}}[\bar{\boldsymbol{E}}] - 2\bar{w}_{\mathrm{R}} + (1-r^2)\langle \boldsymbol{E} \cdot \mathbb{C}[\boldsymbol{E}] \rangle \\
&\quad -\boldsymbol{\mu}_\varepsilon \cdot (\mathbb{C}_-^{-1}[\boldsymbol{\mu}_\varepsilon] + 2\boldsymbol{\mu}_\sigma + 2r\boldsymbol{E}_+) \\
&\quad -\boldsymbol{\mu}_\sigma \cdot (\mathbb{C}_+[\boldsymbol{\mu}_\sigma + 2r\boldsymbol{E}_-])\big)
\end{aligned}
$$

B.2.2 General MEM with homogeneous eigenstrains

If eigenstrains are homogeneous, the resulting residual strain fields are also homogeneous. The MEM solution of Appendix B.2.1 can be simplified to a linear elastic form, requiring only the effective stiffness as an input parameter.

$$
\begin{aligned}
p_1(\boldsymbol{\varepsilon}, \mathbb{C}) =& \frac{p_1^{\mathrm{C}}(\mathbb{C})}{\sqrt{(2\pi)^6 \det(\mathbb{K})}} \exp\left(-\frac{1}{2}(\boldsymbol{\varepsilon} - \boldsymbol{\gamma}) \cdot \mathbb{K}^{-1}[\boldsymbol{\varepsilon} - \boldsymbol{\gamma}]\right) \\
\mathbb{K} =& k\mathbb{C}^{-1} \\
\boldsymbol{\gamma} =& \mathbb{C}^{-1}[\boldsymbol{\mu}_\varepsilon] + \boldsymbol{\mu}_\sigma \\
\boldsymbol{\mu}_\varepsilon =& \mathbb{C}_-(\mathbb{C}_+ - \mathbb{C}_-)^+(\mathbb{C}_+ - \bar{\mathbb{C}})[\bar{\boldsymbol{\varepsilon}}] \\
\boldsymbol{\mu}_\sigma =& -(\mathbb{C}_+ - \mathbb{C}_-)^+(\mathbb{C}_+ - \bar{\mathbb{C}})[\bar{\boldsymbol{\varepsilon}}] + \bar{\boldsymbol{\varepsilon}} \\
k =& \frac{1}{6}\bar{\boldsymbol{\varepsilon}} \cdot (\mathbb{C}_+ - \bar{\mathbb{C}})(\mathbb{C}_+ - \mathbb{C}_-)^+(\bar{\mathbb{C}} - \mathbb{C}_-)[\bar{\boldsymbol{\varepsilon}}]
\end{aligned}
$$

B.3 MEM for single-phase polycrystals

B.3.1 Locally cubic polycrystal MEM with crystallographic texture, no eigenstrains

For single-phase polycrystals, the stiffness statistic is directly described by the ODF, such that

$$p(\boldsymbol{Q} \star \mathbb{C}^{\mathrm{C}}) = f(\boldsymbol{Q}). \tag{B.6}$$

The determinant of $\mathbb{K}$ is orientation-invariant and can be stated using the eigenvalues of $\mathbb{C}^{\mathrm{C}}$ denoted as $\lambda_i^{\mathrm{C}}, i \in \{1,2,3\}$.

$$\begin{aligned}
p_1(\boldsymbol{\varepsilon}, \boldsymbol{Q}) =& f(\boldsymbol{Q}) \sqrt{\frac{\lambda_1^{\mathrm{C}} (\lambda_2^{\mathrm{C}})^2 (\lambda_3^{\mathrm{C}})^3}{(2\pi k)^6}} \exp\left(-\frac{1}{2} (\boldsymbol{\varepsilon} - \boldsymbol{\gamma}) \cdot \mathbb{K}^{-1} [\boldsymbol{\varepsilon} - \boldsymbol{\gamma}] \right) \\
\mathbb{K} =& k \boldsymbol{Q} \star (\mathbb{C}^{\mathrm{C}})^{-1} \\
\boldsymbol{\gamma} =& \mathbb{C}^{-1} [\boldsymbol{\mu}_\varepsilon] + \boldsymbol{\mu}_\sigma \\
\boldsymbol{\mu}_\varepsilon =& \mathbb{C}_- (\mathbb{C}_+ - \mathbb{C}_-)^+ (\mathbb{C}_+ - \bar{\mathbb{C}}) [\bar{\boldsymbol{\varepsilon}}] \\
\boldsymbol{\mu}_\sigma =& (\mathbb{C}_+ - \mathbb{C}_-)^+ (\mathbb{C}_+ - \bar{\mathbb{C}}) [\bar{\boldsymbol{\varepsilon}}] + \bar{\boldsymbol{\varepsilon}} \\
k =& \frac{1}{6} \bar{\boldsymbol{\varepsilon}} \cdot (\mathbb{C}_+ - \bar{\mathbb{C}}) (\mathbb{C}_+ - \mathbb{C}_-)^+ (\bar{\mathbb{C}} - \mathbb{C}_-) [\bar{\boldsymbol{\varepsilon}}]
\end{aligned}$$

B.3.2 Locally cubic polycrystal MEM with statistical isotropy, no eigenstrains

In the case of statistical isotropy, the formulas of Appendix B.3.1 can be simplified further. Because the compression modulus is homogeneous, the formulas depend not on the full macroscopic stiffness tensors, but only the macroscopic shear moduli G_-, G_+ and $\bar{G}$.

$$
\begin{aligned}
p_1(\boldsymbol{\varepsilon}, \boldsymbol{Q}) =& \sqrt{\frac{\lambda_1 \lambda_2^2 \lambda_3^3}{(2\pi k)^6}} \exp\left(-\frac{1}{2}(\boldsymbol{\varepsilon} - \boldsymbol{\gamma}) \cdot \mathbb{K}^{-1}[\boldsymbol{\varepsilon} - \boldsymbol{\gamma}]\right) \\
\mathbb{K} =& k(\mathbb{C}^{\mathrm{C}})^{-1} \\
\boldsymbol{\gamma} =& \mathbb{C}^{-1}[\boldsymbol{\mu}_\varepsilon] + \boldsymbol{\mu}_\sigma \\
\boldsymbol{\mu}_\varepsilon =& 2G_- \frac{G_+ - \bar{G}}{G_+ - G_-} \bar{\boldsymbol{\varepsilon}}' \\
\boldsymbol{\mu}_\sigma =& \frac{G_+ - \bar{G}}{G_+ - G_-} \bar{\boldsymbol{\varepsilon}}' + \bar{\boldsymbol{\varepsilon}} \\
k =& \frac{1}{3}\left(\frac{(G_+ - \bar{G})(\bar{G} - G_-)}{G_+ - G_-}\right) \|\bar{\boldsymbol{\varepsilon}}'\|^2
\end{aligned}
$$

B.4 MEM for locally isotropic composites

B.4.1 MEM for multiphase locally isotropic composites with phasewise constant eigenstrains

For phases which are locally isotropic, orientation statistics are irrelevant, such that the composite consists of discrete phases $\alpha \in [1, N]$ with phasewise constant properties $\mathbb{C}_\alpha$ and $\boldsymbol{E}_\alpha$ and phase volume fractions v_α. The strain probability density in phase α is denoted as $p_1(\boldsymbol{\varepsilon}, \alpha)$.

$$
\begin{aligned}
p_1(\boldsymbol{\varepsilon}, \alpha) &= \frac{v_\alpha}{\sqrt{(2\pi)^6 \det(\mathbb{K}_\alpha)}} \exp\left(-\frac{1}{2}(\boldsymbol{\varepsilon} - \boldsymbol{\gamma}_\alpha) \cdot \mathbb{K}_\alpha^{-1}[\boldsymbol{\varepsilon} - \boldsymbol{\gamma}_\alpha]\right) \\
\mathbb{K}_\alpha &= k\mathbb{C}_\alpha^{-1} \\
\boldsymbol{\gamma}_\alpha &= \mathbb{C}_\alpha^{-1}[\boldsymbol{\mu}_\varepsilon] + \boldsymbol{\mu}_\sigma + r\boldsymbol{E}_\alpha \\
\boldsymbol{\mu}_\varepsilon &= \mathbb{C}_-(\mathbb{C}_+ - \mathbb{C}_-)^+[(\mathbb{C}_+ - \bar{\mathbb{C}})[\bar{\boldsymbol{\varepsilon}}] + \mathbb{C}_+[(r-1)\boldsymbol{E}_- - r\boldsymbol{E}_+] \\
&\quad + \bar{\mathbb{C}}[\bar{\boldsymbol{E}}]] \\
\boldsymbol{\mu}_\sigma &= -\mathbb{C}_-^{-1}[\boldsymbol{\mu}_\varepsilon] + \bar{\boldsymbol{\varepsilon}} - r\boldsymbol{E}_+ \\
r &= \frac{1}{w_0}\left((\bar{\boldsymbol{\varepsilon}} - \bar{\boldsymbol{E}}) \cdot \bar{\mathbb{C}}[\bar{\boldsymbol{E}}] - \boldsymbol{E}_- \cdot \mathbb{C}_+[\bar{\boldsymbol{\varepsilon}}] - 2\bar{w}_\mathrm{R} + \langle \boldsymbol{E} \cdot \mathbb{C}[\boldsymbol{E}] \rangle \right. \\
&\quad -(\mathbb{C}_-[\boldsymbol{E}_+] - \mathbb{C}_+[\boldsymbol{E}_-]) \cdot (\mathbb{C}_+ - \mathbb{C}_-)^+ \left[(\mathbb{C}_+ - \bar{\mathbb{C}})[\bar{\boldsymbol{\varepsilon}}]\right. \\
&\quad \left.\left. + \bar{\mathbb{C}}[\bar{\boldsymbol{E}}] - \mathbb{C}_+[\boldsymbol{E}_-]\right]\right) \\
k &= \frac{1}{6}\left(\bar{\boldsymbol{\varepsilon}} \cdot \bar{\mathbb{C}}[\bar{\boldsymbol{\varepsilon}}] - \bar{\boldsymbol{E}} \cdot \bar{\mathbb{C}}[\bar{\boldsymbol{E}}] - 2\bar{w}_\mathrm{R} + (1 - r^2)\langle \boldsymbol{E} \cdot \mathbb{C}[\boldsymbol{E}] \rangle \right. \\
&\quad -\boldsymbol{\mu}_\varepsilon \cdot (\mathbb{C}_-^{-1}[\boldsymbol{\mu}_\varepsilon] + 2\boldsymbol{\mu}_\sigma + 2r\boldsymbol{E}_+) \\
&\quad \left. -\boldsymbol{\mu}_\sigma \cdot (\mathbb{C}_+[\boldsymbol{\mu}_\sigma + 2r\boldsymbol{E}_-])\right)
\end{aligned}
$$

In case only two phases are present, Eq. (3.119) and (3.120) can be used to calculate the inelastic effective properties, and the phasewise mean strains are those given by Eq. (3.117) and (3.118).

Bibliography

Adams, B., Boehler, J., Guidi, M., Onat, E., 1992. Group theory and representation of microstructure and mechanical behavior of polycrystals. Journal of the Mechanics and Physics of Solids 40 (4), 723–737.

Agrawal, P., Sun, C. T., 2003. Fracture in metal-ceramic composites. Composites Science and Technology 64, 1167 – 1178.

Badulescu, C., Lahellec, N., Suquet, P., 2015. Field statistics in linear viscoelastic composites and polycrystals. European Journal of Mechanics A/Solids 49, 329–344.

Barral, M., Lebrun, J. L., Sprauel, J. M., Maeder, G., Jul. 1987. X-ray macrostress determination on textured material; use of the ODF for calculating the X-ray compliances. Metallurgical Transactions A 18 (7), 1229–1238.

Behnken, H., Jan. 1992. Berechnung und Ermittlung der röntgenographischen Elastizitätskonstanten sowie der Mikro- und Makro-Spannungen heterogener und texturierter Werkstoffe. Dissertation, RWTH Aachen.

Behnken, H., Hauk, V., 1991. Berechnung der röntgenographischen Spannungsfaktoren texturierter Werkstoffe–Vergleich mit experimentellen Ergebnissen/Calculation of X-ray stress factors of textured materials–comparison with experimental results. International Journal of Materials Research 82 (2), 151–158.

Bensoussan, A., Lions, J. L., Papanicolaou, G., 1978. Asymptotic Analysis for Periodic Structures. Vol. 5. Noth-Halland Pub. Co., Amsterdam.

Beran, M., 1965. Statistical Continuum Theories. Transactions of The Society of Rheology 9 (1), 339–355.

Bertrand, J., 1889. Calcul des Probabilités. Gauthier-Villars, Paris.

Bobeth, M., Diener, G., 1987. Static elastic and thermoelastic field fluctuations in multiphase composites. Journal of the Mechanics and Physics of Solids 35 (2), 137–149.

Boehler, J.-P., Kirillov Jr, A. A., Onat, E. T., 1994. On the polynomial invariants of the elasticity tensor. Journal of Elasticity 34 (2), 97–110.

Bollenrath, F., Hauk, V., Müller, E. H., 1967. Zur Berechnung der vielkristallinen Elastizitätskonstanten aus den Werten der Einkristalle. International Journal of Materials Research 58 (1), 76–82.

Brakman, C. M., Jan. 1987. The Voigt model case. Philosophical Magazine A 55 (1), 39–58.

Brenner, R., Castelnau, O., Badea, L., 2004. Mechanical field fluctuations in polycrystals estimated by homogenization techniques. Proceedings of the Royal Society A: Mathematical, Physical and Engineering Sciences 460 (2052), 3589–3612.

Bunge, H.-J., 1965. Zur Darstellung allgemeiner Texturen. International Journal of Materials Research 56 (12), 872–874.

Buryachenko, V. A., Kreher, W. S., 1995. Internal residual stresses in heterogeneous solids—A statistical theory for particulate composites. Journal of the Mechanics and Physics of Solids 43 (7), 1105–1125.

Böhlke, T., Bertram, A., 2001. The evolution of Hooke's law due to texture development in FCC polycrystals. International Journal of Solids and Structures 38 (52), 9437–9459.

Castañeda, P. P., Suquet, P., 1997. Nonlinear Composites. In: Advances in Applied Mechanics. Vol. 34. Academic Press, Cambridge, pp. 171–302.

Chang, Y. A., Himmel, L., Aug. 1966. Temperature Dependence of the Elastic Constants of Cu, Ag, and Au above Room Temperature. Journal of Applied Physics 37 (9), 3567–3572.

Chernatynskiy, A., Phillpot, S. R., LeSar, R., 2013. Uncertainty quantification in multiscale simulation of materials: a prospective. Annual Review of Materials Research 43 (1), 157–182.

Cohen, J. E., 1978. Derivatives of the spectral radius as a function of non-negative matrix elements. Mathematical Proceedings of the Cambridge Philosophical Society 83 (2), 183–190.

Das, S., Castañeda, P. P., 2021. Field statistics in linearized elastic and viscous composites and polycrystals. International Journal of Solids and Structures 224, 111030.

Der Kiureghian, A., Ditlevsen, O., 2009. Aleatory or epistemic? Does it matter? Structural safety 31 (2), 105–112.

Donachie, M. J., 2000. Titanium: A Technical Guide. ASM international, Materials Park.

Drory, A., Apr. 2015. Failure and uses of Jaynes' principle of transformation groups. Foundations of Physics 45 (4), 439–460.

Dryburgh, P., Li, W., Pieris, D., Fuentes-Dominguez, R., Patel, R., Smith, R. J., Clark, M., 2022. Measurement of the single crystal elasticity matrix of polycrystalline materials. Acta Materialia 225, 117551.

Dyskin, A. V., 1999. On the role of stress fluctuations in brittle fracture. International Journal of Fracture 100, 29–53.

Dölle, H., Hauk, V., May 1976. Röntgenographische Spannungsermittlung für Eigenspannungssysteme allgemeiner Orientierung. HTM Journal of Heat Treatment and Materials 31 (3), 165–168.

Edmonds, A. R., 1996. Angular Momentum in Quantum Mechanics. Vol. 4. Princeton University Press, Princeton.

Eshelby, J. D., 1957. The determination of the elastic field of an ellipsoidal inclusion, and related problems. Proceedings of the Royal Society 247, 376–396.

Etingof, P., Adams, B. L., 1993. Representations of polycrystalline microstructure by n-point correlation tensors. Texture, Stress, and Microstructure 21, 17–37.

Every, A., McCurdy, A., 1992. Second and higher order elastic constants. Landolt-Börnstein Numerical Data and Functional Relationships in Science and Technology New Series Group III: Crystal and Solid State Physics 29, 743.

Fischer, G., 2003. Lineare Algebra. Vieweg, Wiesbaden.

Fokin, A., 1972. Solution of statistical problems in elasticity theory in the singular approximation. Journal of Applied Mechanics and Technical Physics 13 (1), 85–89.

Forte, S., Vianello, M., 1996. Symmetry classes for elasticity tensors. Journal of Elasticity 43, 81–108.

Frigo, M., Johnson, S. G., 2005. The design and implementation of FFTW3. Proceedings of the IEEE 93 (2), 216–231.

Fritzen, F., 2010. Microstructural modeling and computational homogenization of the physically linear and nonlinear constitutive behavior of micro-heterogeneous materials. Doctoral Thesis, Karlsruhe Institute of Technology (KIT).

Gehrig, F., Wicht, D., Krause, M., Böhlke, T., 2022. FFT-based investigation of the shear stress distribution in face-centered cubic polycrystals. International Journal of Plasticity 157, 103369.

Gnäupel-Herold, T., Jun. 2012. ISODEC: software for calculating diffraction elastic constants. Journal of Applied Crystallography 45 (3), 573–574.

Gnäupel-Herold, T., Creuziger, A. A., Iadicola, M., 2012. A model for calculating diffraction elastic constants. Journal of Applied Crystallography 45 (2), 197–206.

Greven, A., Keller, G., Warnecke, G., 2014. Entropy. Vol. 47. Princeton University Press, Princeton.

Griffiths, D. J., 2019. Introduction to Quantum Mechanics. Cambridge University Press, Cambridge.

Guedes, J.-M., Kikuchi, N., 1990. Preprocessing and postprocessing for materials based on the homogenization method with adaptive finite element methods. Comput. Methods. Appl. Mech. Engrg 83 (2), 143–198.

Guidi, M., Adams, B. L., Onat, E. T., 1992. Tensorial representation of the orientation distribution function in cubic polycrystals. Texture, Stress, and Microstructure 19 (3), 673639.

Guo, J., Fu, H., Pan, B., Kang, R., 2021. Recent progress of residual stress measurement methods: A review. Chinese Journal of Aeronautics 34 (2), 54–78.

Halmos, P. R., 2017. Finite-Dimensional Vector Spaces. Courier Dover Publications, Mineola.

Hanc, J., Tuleja, S., Hancova, M., 2004. Symmetries and conservation laws: Consequences of Noether's theorem. American Journal of Physics 72 (4), 428–435.

Hauk, V., Herlach, D., Sesemann, H., Dec. 1975. Über nichtlineare Gitterebenenabstandsverteilungen in Stählen, ihre Entstehung, Berechnung und Berücksichtigung bei der Spannungsermittlung. International Journal of Materials Research 66 (12), 734–737.

Helnwein, P., 2001. Some remarks on the compressed matrix representation of symmetric second-order and fourth-order tensors. Computer Methods in Applied Mechanics and Engineering 190 (22), 2753–2770.

Henze, N., 1997. Stochastik für Einsteiger. Vol. 4. Springer, Berlin.

Hill, R., 1963. Elastic properties of reinforced solids: some theoretical principles. Journal of the Mechanics and Physics of Solids 11 (5), 357–372.

Hill, R., 1968. On constitutive inequalities for simple materials—I. Journal of the Mechanics and Physics of Solids 16 (4), 229–242.

Huynh, D. Q., 2009. Metrics for 3D rotations: comparison and analysis. Journal of Mathematical Imaging and Vision 35 (2), 155–164.

Jaynes, E. T., 1963. Statistical Physics. Vol. 3 of Brandeis Summer Institute Lectures in Theoretical Physics. W.A.Benjamin Inc., New York.

Jaynes, E. T., Sep. 1968. Prior Probabilities. IEEE Transactions on Systems Science and Cybernetics 4 (3), 227–241.

Jaynes, E. T., Dec. 1973. The well-posed problem. Foundations of Physics 3 (4), 477–492.

Jaynes, E. T., 1978. Where do we stand on maximum entropy? In: Rosenkrantz, R. (Ed.), E.T. Jaynes: Papers on Probability, Statistics and Statistical Physics. Springer, Dordrecht.

Jänich, K., 2013. Topologie. Springer-Verlag, Berlin.

Kehrer, M. L., 2019. Thermomechanical mean-field modeling and experimental characterization of long fiber-reinforced sheet molding compound composites. Doctoral Thesis, Karlsruher Institut für Technologie (KIT).

Kocks, U., Canova, G., Jonas, J., 1983. Yield vectors in FCC crystals. Acta Metallurgica 31 (8), 1243–1252.

Kocks, U. F., Tomé, C. N., Wenk, H.-R., 2000. Texture and Anisotropy: Preferred Orientations in Polycrystals and their Effect on Materials Properties. Cambridge university press, Cambridge.

Kolmogoroff, A., 1933. Grundbegriffe der Wahrscheinlichkeitsrechnung. Springer, Berlin.

Krause, M., Böhlke, T., Jul. 2020. Maximum-entropy based estimates of stress and strain in thermoelastic random heterogeneous materials. Journal of Elasticity 141 (2), 321–348.

Krause, M., Böhlke, T., 2022. Estimating stress fluctuations in polycrystals with an improved maximum entropy method. In: 8th European Congress on Computational Methods in Applied Sciences and Engineering. CIMNE.

Krause, M., Böhlke, T., 2024. Tensorial harmonic bases of arbitrary order with applications in elasticity, elastoviscoplasticity and texture-based modeling, accepted at Mathematics and Mechanics of Solids.

Krause, M., Pallicity, T. D., Böhlke, T., 2023. Exact second moments of strain for composites with isotropic phases. European Journal of Mechanics-A/Solids 97, 104806.

Krause, M., Zürn, M., Gibmeier, J., Böhlke, T., 2024. Determination of diffraction elastic constants using the Maximum Entropy Method, under review at Journal of Elasticity.

Krawietz, A., 2013. Materialtheorie: mathematische Beschreibung des phänomenologischen thermomechanischen Verhaltens. Springer-Verlag, Berlin.

Kreher, W., 1990. Residual stresses and stored elastic energy of composites and polycrystals. Journal of the Mechanics and Physics of Solids 38 (1), 115–128.

Kreher, W., Pompe, W., 1985. Field fluctuations in a heterogeneous elastic material–An information theory approach. Journal of the Mechanics and Physics of Solids 33.5, 419–445.

Kreher, W., Pompe, W., 1989. Internal Stresses in Heterogeneous Solids. Vol. 9 of Physical Research. Akademie-Verlag, Berlin.

Kröner, E., 1958. Berechnung der elastischen Konstanten des Vielkristalls aus den Konstanten des Einkristalls. Zeitschrift für Physik 151 (4), 504–518.

Kröner, E., 1963. On the physical reality of torque stresses in continuum mechanics. Int. J. Engng. Sci 1 (2), 261–278.

Kröner, E., 1977. Bounds for effective elastic moduli of disordered materials. Journal of the Mechanics and Physics of Solids 25 (2), 137–155.

Kuhn, J., Schneider, M., Sonnweber-Ribic, P., Böhlke, T., 2020. Fast methods for computing centroidal Laguerre tessellations for prescribed volume fractions with applications to microstructure generation of polycrystalline materials. Computer Methods in Applied Mechanics and Engineering 369, 113175.

Kuhn, J., Schneider, M., Sonnweber-Ribic, P., Böhlke, T., 2022. Generating polycrystalline microstructures with prescribed tensorial texture coefficients. Computational Mechanics 70 (3), 639–659.

Lahellec, N., Suquet, P., 2007. On the effective behavior of nonlinear inelastic composites: I. Incremental variational principles. Journal of the Mechanics and Physics of Solids 55 (9), 1932 – 1963.

Larochelle, P. M., Murray, A. P., Angeles, J., Jul. 2006. A distance metric for finite sets of rigid-body displacements via the polar decomposition. Journal of Mechanical Design 129 (8), 883–886.

Lebedev, V. I., Laikov, D. N., 1999. A quadrature formula for the sphere of the 131st algebraic order of accuracy. In: Doklady Mathematics. Vol. 59. Pleiades Publishing, Ltd.

Lequeu, P., Aug. 1986. Comparison of crystallographic and continuum yield surfaces for textured polycrystals. PhD Thesis, McGill University, Montreal.

Lester, H., Aborn, R., 1925. Behavior under stress of the iron crystals. Army Ordnance 6, 1926.

Levin, V., 1967. Thermal expansion coefficients of heterogeneous materials. Mekhanika Tverdogo Tela 2, 88–94.

Lin, T. H., 1957. Analysis of elastic and plastic strains of a face-centred cubic crystal. Journal of the Mechanics and Physics of Solids 5 (2), 143–149.

Liu, I.-S., 2002. Continuum Mechanics. Advanced Texts in Physics. Springer, Berlin.

Lobos, M., Böhlke, T., 2016. On optimal zeroth-order bounds of linear elastic properties of multiphase materials and application in materials design. International Journal of Solids and Structures 84, 40–48.

Lobos Fernández, M., Böhlke, T., 2019. Representation of Hashin–Shtrikman bounds in terms of texture coefficients for arbitrarily anisotropic polycrystalline materials. Journal of Elasticity 134 (1), 1–38.

Macherauch, E., Müller, P., 1961. Das $\sin^2$(psi)-Verfahren der röntgenographischen Spannungsmessung. Z. angew. Phys 13, 305–312.

Man, C.-S., Du, W., 2022. Recasting Classical Expansion of Orientation Distribution Function as Tensorial Fourier Expansion. Journal of Elasticity , 1–23.

Man, C.-S., Huang, M., 2001. Identification of material parameters in yield functions and flow rules for weakly textured sheets of cubic metals. International Journal of Non-Linear Mechanics 36 (3), 501–514.

Mandel, J., 1965. Généralisation de la théorie de plasticité de WT Koiter. International Journal of Solids and Structures 1 (3), 273–295.

Marsden, J. E., Hughes, T. J., 1994. Mathematical Foundations of Elasticity. Dover Publications, Mineola.

Matthies, S., Humbert, M., 1995. On the Principle of a Geometric Mean of Even-Rank Symmetric Tensors for Textured Polycrystals. J. Appl. Cryst. 28 (3), 254–266.

Mori, T., Tanaka, K., 1973. Average stress in matrix and average elastic energy of materials with misfitting inclusions. Acta Metallurgica 21 (5), 571–574.

Moulinec, H., Suquet, P., 1998. A numerical method for computing the overall response of nonlinear composites with complex microstructure. Comput. Methods. Appl. Mech. Engrg 157 (1-2), 69–94.

Murray, C. E., Noyan, I. C., Feb. 1999. A modified Voigt method for calculation of the elastic constants of ensembles selected by diffraction methods. Philosophical Magazine A 79 (2), 371–389.

Mánik, T., 2021. A natural vector/matrix notation applied in an efficient and robust return-mapping algorithm for advanced yield functions. European Journal of Mechanics - A/Solids 90, 104357.

Nadeau, J. C., Ferrari, M., 2001. On optimal zeroth-order bounds with application to Hashin-Shtrikman bounds and anisotropy parameters. International Journal of Solids and Structures 38 (44-45), 7945–7965.

Nemat-Nasser, S., Hori, M., 1993. Micromechanics: Overall Properties of Heterogeneous Materials. North-Holland, Amsterdam.

Norris, A. N., 1985. A differential scheme for the effective moduli of composites. Mechanics of Materials 4 (1), 1–16.

Noyan, I. C., Cohen, J. B., 1987. Residual Stress: Measurement by Diffraction and Interpretation. Springer, New York.

Papenfuß, C., 2020. Continuum Thermodynamics and Constitutive Theory. Springer Nature Switzerland, Cham.

Pawar, R. R., Deshpande, V., 1968. The anisotropy of the thermal expansion of alpha-titanium. Acta Crystallographica Section A: Crystal Physics, Diffraction, Theoretical and General Crystallography 24 (2), 316–317.

Ponte Castañeda, P., 2002. Second-order homogenization estimates for nonlinear composites incorporating field fluctuations: I–theory. Journal of the Mechanics and Physics of Solids 50 (4), 737 – 757.

Reuss, A., 1929. Berechnung der Fließgrenze von Mischkristallen auf Grund der Plastizitätsbedingung für Einkristalle. ZAMM - Zeitschrift für Angewandte Mathematik und Mechanik 9 (1), 49–58.

Roe, R.-J., 1965. Description of crystallite orientation in polycrystalline materials. III. General solution to pole figure inversion. Journal of Applied Physics 36 (6), 2024–2031.

Rosen, B. W., Hashin, Z., 1970. Effective thermal expansion coefficients and specific heats of composite materials. Int. J. Engng. Sci. 8, 157–173.

Schneider, M., Ospald, F., Kabel, M., 2016. Computational homogenization of elasticity on a staggered grid. International Journal for Numerical Methods in Engineering 109, 693–720.

Seth, B. R., B., 1964. Generalized strain measure with applications to physical problems. In: Second-Order Effects in Elasticity, Plasticity and Fluid Dynamics. Pergamon Press, Oxford, pp. 162–172.

Shannon, C. E., 1948. A mathematical theory of communication. The Bell system technical journal 27 (3), 379–423.

Simmons, G., Wang, H., 1971. Single Crystal Elastic Constants and Calculated Aggregate Properties. MIT Press, Cambridge.

Spencer, A., 1970. A note on the decomposition of tensors into traceless symmetric tensors. International Journal of Engineering Science 8 (6), 475–481.

Taira, S., Tanaka, K., 1979. Local residual stress near fatigue crack tip. Transactions of the Iron and Steel Institute of Japan 19 (7), 411–418.

Taylor, G. I., 1938. Plastic strain in metals. J. Inst. Metals 62, 307–324.

Torquato, S., 2002. Random Heterogeneous Materials. Springer, New York.

Trauth, A., Kehrer, L., Pinter, P., Weidenmann, K., Böhlke, T., 2021. On the effective elastic properties based on mean-field homogenization of sheet molding compound composites. Composites Part C: Open Access 4, 100089.

Van Houtte, P., 1988. A comprehensive mathematical formulation of an extended Taylor–Bishop–Hill model featuring relaxed constraints, the Renouard–Wintenberger theory and a strain rate sensitivity model. Textures and Microstructures 8, 313–350.

Voigt, W., 1889. Ueber die Beziehung zwischen den beiden Elasticitätsconstanten isotroper Körper. Annalen der Physik 274 (12), 573–587.

Voigt, W., 1910. Lehrbuch der Kristallphysik. Vol. 34. BG Teubner, Leipzig.

Walpole, L. J., 1966. On bounds for the overall elastic moduli of inhomogeneous systems-I. Journal of the Mechanics and Physics of Solids 14 (3), 151–162.

Wicht, D., Schneider, M., Böhlke, T., 2020a. An efficient solution scheme for small-strain crystal-elasto-viscoplasticity in a dual framework. Computer Methods in Applied Mechanics and Engineering 358, 112611.

Wicht, D., Schneider, M., Böhlke, T., 2020b. On Quasi-Newton methods in fast Fourier transform-based micromechanics. International Journal for Numerical Methods in Engineering 121 (8), 1665–1694.

Wigner, E. P., 1931. Gruppentheorie und ihre Anwendung auf die Quantenmechanik der Atomspektren. Friedr. Vieweg & Sohn Akt.-Ges., Braunschweig.

Willis, J. R., 1977. Bounds and Self-Consistent Estimates for the Overall Properties of Anisotropic Composites. Journal of the Mechanics and Physics of Solids 25, 185–202.

Willis, J. R., 1981. Variational and related methods for the overall properties of composites. Advances in Applied Mechanics 21, 1–78.

Zeman, J., Vondřejc, J., Novák, J., Marekc, I., 2010. Accelerating a FFT-based solver for numerical homogenization of periodic media by conjugate gradients. Journal of Computational Physics 229, 8065–8071.

Zheng, Q.-S., Spencer, A., 1993. On the canonical representations for Kronecker powers of orthogonal tensors with application to material symmetry problems. International Journal of Engineering Science 31 (4), 617–635.

Schriftenreihe Kontinuumsmechanik im Maschinenbau
Karlsruher Institut für Technologie (KIT)
(ISSN 2192-693X)

Band 1 Felix Fritzen
Microstructural modeling and computational homogenization of the physically linear and nonlinear constitutive behavior of micro-heterogeneous materials.
ISBN 978-3-86644-699-1

Band 2 Rumena Tsotsova
Texturbasierte Modellierung anisotroper Fließpotentiale.
ISBN 978-3-86644-764-6

Band 3 Johannes Wippler
Micromechanical finite element simulations of crack propagation in silicon nitride.
ISBN 978-3-86644-818-6

Band 4 Katja Jöchen
Homogenization of the linear and non-linear mechanical behavior of polycrystals.
ISBN 978-3-86644-971-8

Band 5 Stephan Wulfinghoff
Numerically Efficient Gradient Crystal Plasticity with a Grain Boundary Yield Criterion and Dislocation-based Work-Hardening.
ISBN 978-3-7315-0245-6

Band 6 Viktor Müller
Micromechanical modeling of short-fiber reinforced composites.
ISBN 978-3-7315-0454-2

Die Bände sind unter www.ksp.kit.edu als PDF frei verfügbar oder als Druckausgabe bestellbar.

Band 7 Florian Rieger
Work-hardening of dual-phase steel.
ISBN 978-3-7315-0513-6

Band 8 Vedran Glavas
Micromechanical Modeling and Simulation of Forming Processes.
ISBN 978-3-7315-0602-7

Band 9 Eric Bayerschen
Single-crystal gradient plasticity with an accumulated plastic slip: Theory and applications.
ISBN 978-3-7315-0606-5

Band 10 Bartholomäus Brylka
Charakterisierung und Modellierung der Steifigkeit von langfaserverstärktem Polypropylen.
ISBN 978-3-7315-0680-5

Band 11 Rudolf Neumann
Two-Scale Thermomechanical Simulation of Hot Stamping.
ISBN 978-3-7315-0714-7

Band 12 Mauricio Lobos Fernández
Homogenization and materials design of mechanical properties of textured materials based on zeroth-, first- and second-order bounds of linear behavior.
ISBN 978-3-7315-0770-3

Band 13 Malte Schemmann
Biaxial Characterization and Mean-field Based Damage Modeling of Sheet Molding Compound Composites.
ISBN 978-3-7315-0818-2

Band 14 Jürgen Albiez
Finite element simulation of dislocation based plasticity and diffusion in multiphase materials at high temperature.
ISBN 978-3-7315-0918-9

Die Bände sind unter www.ksp.kit.edu als PDF frei verfügbar oder als Druckausgabe bestellbar.

Band 15 Maria Loredana Kehrer
Thermomechanical Mean-Field Modeling and Experimental Characterization of Long Fiber-Reinforced Sheet Molding Compound Composites.
ISBN 978-3-7315-0924-0

Band 16 Peter Hölz
A dynamic and statistical analysis of the temperature- and fatigue behavior of a race power unit – The effect of different thermodynamic states.
ISBN 978-3-7315-0988-2

Band 17 Andreas Prahs
A Gradient Crystal Plasticity Theory Based on an Extended Energy Balance.
ISBN 978-3-7315-1025-3

Band 18 Johannes Ruck
Modeling martensitic phase transformation in dual phase steels based on a sharp interface theory.
ISBN 978-3-7315-1072-7

Band 19 Hannes Erdle
Modeling of Dislocation - Grain Boundary Interactions in Gradient Crystal Plasticity Theories.
ISBN 978-3-7315-1196-0

Band 20 Johannes Görthofer
Microstructure generation and micromechanical modeling of sheet molding compound composites.
ISBN 978-3-7315-1205-9

Band 21 Daniel Wicht
Efficient fast Fourier transform-based solvers for computing the thermomechanical behavior of applied materials.
ISBN 978-3-7315-1220-2

Band 22 Juliane Lang
Thermomechanical Modeling and Experimental Characterization of Sheet Molding Compound Composites.
ISBN 978-3-7315-1232-5

Die Bände sind unter www.ksp.kit.edu als PDF frei verfügbar oder als Druckausgabe bestellbar.

Band 23 Julian Karl Bauer
Fiber Orientation Tensors and Mean Field Homogenization: Application to Sheet Molding Compound.
ISBN 978-3-7315-1262-2

Band 24 Sebastian Gajek
Deep material networks for efficient scale-bridging in thermomechanical simulations of solids.
ISBN 978-3-7315-1278-3

Band 25 Jannick Kuhn
Microstructure modeling and crystal plasticity parameter identification for predicting the cyclic mechanical behavior of polycrystalline metals.
ISBN 978-3-7315-1272-1

Band 26 Felix Ernesti
A computational multi-scale approach for brittle materials.
ISBN 978-3-7315-1285-1

Band 27 Patrick Arthur Hessman
On multi-scale modeling of fatigue in short glass fiber reinforced thermoplastics.
ISBN 978-3-7315-1398-8

Band 28 Benedikt Sterr
Machine learning aided multiscale mechanics of fiber suspensions.
ISBN 978-3-7315-11421-3

Band 29 Maximilian Krause
Local Stresses and Strains in Polycrystals.
ISBN 978-3-7315-1411-4

This work discusses various methods of calculating local stress and strain statistics of heterogeneous materials with particular focus on polycrystalline metals. The main method under consideration is the micromechanical Maximum Entropy Method, an approximation technique based on results from information theory, which predicts local stress and strains based on the macroscopic properties of a material without explicit descriptions of the microstructure. Based on the general principle of maximum entropy, we derive different versions of the technique based on different micromechanical assumptions, and evaluate these versions in terms of theoretical consistency and accuracy compared to numerical full-field simulations. To validate and extend the maximum entropy approach, we furthermore derive stress and strain statistics from homogenization theories using a variational technique, which we apply to the Singular Approximation framework to find explicit formulas which are parameterized to describe a wide range of microstructures. To facilitate numerical implementations of the theoretical approaches, we define a harmonic basis convention for tensorial spaces of arbitrary order, which allows for an efficient tensorial description of probability distributions of orientations in polycrystals.

ISSN 2192-693X
ISBN 978-3-7315-1411-4

Gedruckt auf FSC-zertifiziertem Papier